

Intelligent design of microfluidic components for Newtonian
and complex fluid systems

PhD Thesis

Konstantinos Zografos

James Weir Fluids Laboratory
Mechanical and Aerospace Engineering
University of Strathclyde, Glasgow

2017

This thesis is the result of the author's original research. It has been composed by the author and has not been previously submitted for examination which has led to the award of a degree.

The copyright of this thesis belongs to the author under the terms of the United Kingdom Copyright Acts as qualified by University of Strathclyde Regulation 3.50. Due acknowledgement must always be made of the use of any material contained in, or derived from, this thesis.

Konstantinos Zografos

December 2016

Abstract

Interest in microfluidics has increased dramatically in recent years, with applications spanning a wide range of fields. However, despite several advances, design of microfluidic devices still relies largely on trial-and-error. This thesis aims to go beyond this approach in favour of a rational design of microfluidic devices based on theoretical and numerical design rules and algorithms. More specifically, this research focuses on understanding and controlling fluid dynamics in applications involving complex non-Newtonian fluids in shear and extensional flows. Biomimetic principles and shape optimisation methods are employed to propose new designs for single-phase fluid flow. Furthermore, the single-phase numerical solver is extended to cope with two-phase systems, thus paving the way for new applications of these techniques.

Focusing on shear-flows, a biomimetic principle appropriate for fully developed flows has been extended here to be applicable for non-Newtonian fluids, described by the power-law constitutive relationship. The derivation of the principle leads to a biomimetic rule that provides the appropriate dimensions for designing customised microfluidic bifurcating networks, able to generate specific wall shear-stress gradients along consecutive generations. A range of power-law fluids is examined numerically demonstrating great agreement with theoretical predictions.

In terms of extensional flow, a range of shapes are proposed for designing microfluidic channels for studies related to the response of complex fluid systems under homogeneous strain-rate. Optimisation techniques are employed for finding the appropriate shapes to generate homogeneous extensional flows along the flow centreline of single-stream (contraction-expansion channels) and the multi-stream designs (T-channels and flow focusing devices). The optimised geometries proposed exhibit enhanced perfor-

mance compared to well defined geometrical shapes.

The in-house single phase solver used in all numerical studies is upgraded here in order to solve numerically 3D-problems related to two-phase systems described by the Phase Field method. Here, the code is validated for 2D-problems only, using a range of test-cases demonstrating a very good quantitative agreement.

Keywords: Non-Newtonian fluids, Shear-thinning and shear-thickening behaviour, Bifurcating networks, Biomimetics, Optimisation, Extensional flows, Two-phase systems

To *Bívu* ..

Nature took her away too soon but,
her smile always accompanies me
along the road ..

Live each day with truth, love, fight and creation.

Live each day as if it was your last.

*Often, during our everyday life, we magnify small
problems leaving aside and allowing to forget what an
important and great gift is life that was given to us.*

Θ. Ανεστόπουλος

Acknowledgements

At this point I would like to express my sincere gratitude to all these people that helped me and supported me all these years, those that I had the pleasure to collaborate with and those that linked my past with this amazing ride. Every single one of them added a different piece to this part of the journey to reach to its end.

The words I am able to find are not enough for me to express my deepest gratefulness to my supervisor Dr. Mónica S. N. Oliveira. She was the one who gave me the opportunity to start this amazing journey in science and to feel part of the scientific community. Her constant support and kindness always motivated me to become better. Together with her perfect guidance I believe we have managed to create a very small “dent” in the “knowledge circle” and hope for more in the future. No matter the position, it is a blessing for someone to work with a person like her. Thank you for always finding a way to add fuel in my tank.

I would like to express my deepest appreciation to Dr. Tom Scanlon for constantly encouraging me and for being always available. I owe him the comforting motto “*This is research..*” and the realisation that one always learns. Also, I would like to thank a lot Prof. Yonghao Zhang and Prof. Jason Reese for making me feel immediately part of the James Weir Fluids Laboratory group and for helping me with everything I needed.

I was lucky enough during this time to interact and collaborate with people that helped me to gain knowledge and offered me their precious time unconditionally. Therefore I am deeply grateful to Prof. Manuel Alves, Dr. Alexandre Afonso, Prof. Nigel Mottram, Dr. Edmondo Minisci, Dr. Robert Barber, Dr. George Pashos and Dr. George Kokkoris. All of them assisted me in different ways related to the subjects discussed in

this thesis and I learned a lot from them. Without their critical view some tasks would have been more difficult. Also, I wish to thank Prof. Anke Lindner from whom I always received generous support. Moreover, I would like to express my deepest appreciation to my friends and colleagues Andreia, Ferdin, Joana, Nikos, Paolo, from the JWFL group, Konstantinos, Mike and Giannis, for their positive and encouraging presence. My apologies for the times I have been fussy under the pressure of results. Finally, I would like here to thank the city that hosted me. Indeed, people make Glasgow a great city for someone to live.

Our past sometimes determines our future and therefore, I would like to thank a lot my former professors Prof. Kyriakos C. Giannakoglou, Prof. Andreas Boudouvis and Prof. Nikolaos C. Markatos for their support when I decided to start sending my first PhD applications.

I also acknowledge the financial support of the University and the James Weir Foundation in the form of the scholarship that they have provided me with.

Concluding, I am deeply grateful to my grandmother Ζωή my mother Ελένη, my father Ζωγράφο and his wife Έφη, my brother Νικόλα, my girlfriend Νάντια, my cousins Ζωή and Φανή and my beloved friends Αντρέα, Αριστεΐδη, Γιώργο, Δάφνη, Θανάση, Θωμά, Κατερίνα and Νίκο, Κωνσταντίνα and Κώστα, Μαρία and Αντρέα, Νίκη, Παναγιώτη. Each one of them greatly helped me to handle mentally the vertigo from the emotional roller coaster of these years. I feel honoured to be surrounded from such great souls and apologise for being absent ..

“.. Keep Ithaka always in your mind.

Arriving there is what you are destined for.

But do not hurry the journey at all.

Better if it lasts for years,

so that you are old by the time you reach the island,

wealthy with all you have gained on the way,

not expecting Ithaka to make you rich ..”

Ιθάκη - Κ. Π. Καβάφης

“He, who never did mistakes never tried something new..”

Albert Einstein

Contents

Abstract	ii
Acknowledgements	v
List of Figures	xii
List of Tables	xxvii
Glossary	xxx
Acronyms	xxxvii
1 Introduction	1
1.1 Motivation	1
1.2 Outline of the thesis	6
2 Theoretical Considerations	9
2.1 Fluids from “ <i>oblivion to memory</i> ”	9
2.2 Constitutive models	11
2.2.1 Fluids without memory	12
2.2.2 Fluids with memory	15
2.3 Dimensionless groups	22
3 Numerical Techniques	26
3.1 Introduction	27
3.2 Generalised Coordinates	28

3.3	Single phase solver	30
3.3.1	Governing equations	31
3.3.2	Control volume discretisation	32
3.3.3	Schemes for convection	39
3.3.4	Boundary conditions	47
3.3.5	Velocity and pressure fields coupling	49
3.3.6	Solution Procedure	51
3.4	Mesh deformations	54
3.4.1	Bezier Curves	55
3.4.2	Free Form Deformation	57
3.4.3	From B-Splines to Non-Uniform Rational B-Splines	61
3.4.4	Non-Uniform Rational B-Splines (NURBS)	67
4	Shear dominated designs	78
4.1	Introduction	79
4.2	Biomimetic design of networks for Newtonian fluids	81
4.2.1	Circular cross-section networks	82
4.2.2	Rectangular cross-section networks	84
4.3	Biomimetic design of networks for power-law fluids	86
4.3.1	Flow resistance in the bifurcating networks	89
4.4	Geometrical design considerations	92
4.5	Numerical Validation	93
4.5.1	Numerical method and problem set-up	94
4.5.2	Uniform shear-stress distribution ($X = 1$)	95
4.5.3	Positive gradients of shear-stress distribution ($X = 1.25$)	103
4.5.4	Negative gradients of shear-stress distribution ($X = 0.75$)	111
4.5.5	Effect of increasing Reynolds number	119
4.6	Synopsis	120
5	Designs for extensional flow	124
5.1	Introduction	125

5.2	Optimisation Strategy	132
5.3	Governing equations	134
5.4	Single-stream designs	135
5.4.1	Geometry definition	135
5.4.2	Designs with $CR = 8$	140
5.4.3	Designs for other contraction ratios	154
5.4.4	Pressure-driven flow vs Electro-osmotic flow	156
5.5	Multi-stream designs	158
5.5.1	T-Junction configuration	158
5.5.2	Flow-focusing configuration	173
5.6	Synopsis	185
6	From single-phase to two-phase	190
6.1	Introduction	190
6.2	Phase Field theory	193
6.2.1	Phase field approach	193
6.2.2	Governing equations	196
6.2.3	Considerations for the Cahn-Hilliard equation	197
6.3	Numerical Implementation	199
6.3.1	The Cahn-Hilliard equation	199
6.3.2	The force term	212
6.3.3	The boundary conditions	213
6.4	Validation	214
6.4.1	Test-cases with non-active surface tension	214
6.4.2	Test-cases considering active surface tension	227
6.5	Synopsis	243
7	Conclusions & Future work	246
7.1	Thesis conclusions	246
7.1.1	Design of microfluidic components	246
7.1.2	Two-phase solver	251

7.2 Future work	252
Appendices	255
Appendix A Biomimetic Design	256
A.1 Biomimetic design other aspect ratios	256
Appendix B Optimised designs	259
B.1 Converging/diverging geometry compared to converging/abrupt	259
B.2 Linear target profile	260
B.3 Velocity profiles for increasing Re for other aspect ratios	262
B.4 Other aspect ratios for the 2D optimised shape for a T-junction	263
Bibliography	265

List of Figures

1.1	Word-cloud for microfluidics.	2
1.2	Fabricated bifurcating microchannel, designed based on the biomimetic principle that is discussed in Chapter 4 , in contrast to an ESC button taken from a common keyboard.	2
2.1	Shear-stress response with increasing shear-rate for non-Newtonian fluids described by GNF models. Adapted from White [37]	13
2.2	Behaviour of viscosity with shear-rate in the log-log plot for the power-law fluid.	14
2.3	Representation of the Maxwell model as a combination of a dash-pot and a spring.	16
2.4	Representation of the Oldroyd-B model as a combination of a dash-pot in parallel with a dash-pot and a spring in series.	18
3.1	Types of grid arrangement in control volume formulation, (a) staggered grid and (b) collocated grid.	33
3.2	One-dimensional representation of the convective variable ϕ	41
3.3	Representation of the approximated solution at the faces of a CV for the one-dimensional Central Differencing Scheme.	42
3.4	Representation of the approximated solution at the faces of a CV for the one-dimensional Upwind Differencing Scheme.	44
3.5	Representation of the approximated solution at the faces of a CV for the one-dimensional QUICK scheme.	44

3.6	Bezier curve and Control Polygon	56
3.7	Object deformation using a FFD lattice.	58
3.8	Deformation in all directions using a FFD lattice.	59
3.9	Bernstein basis functions using different number of control points.	60
3.10	Bernstein basis functions for five control points and a curve with $k_s = 3$, for a uniform periodic knot vector (a), an open non-uniform (b), an open non-uniform with inner multiplicity $m_{in} = 2$ (c) and an open uniform with $m_{op} = k_s$ (d).	65
3.11	Rational basis functions for five control points and $k_s = 3$ for an open uniform knot vector with different weights.	68
3.12	Rational basis functions for six control points of order $k_s = 4$, with different weights for each control point and a uniform knot vector.	69
3.13	Different object deformations obtained by a lattice with the same number of control points, but with different properties.	70
3.14	Effect of three collinear points in the NURBS lattice.	72
3.15	Non-uniformly spaced NURBS lattice and the embedded physical domain. The <i>square</i> symbols correspond to the control points of the NURBS lattice.	73
3.16	3D deformation of an initial shape form the NURBS lattice. The small right hand image illustrates the NURBS lattice with the positions of the control points.	74
3.17	Initial uniform mesh (a) and distorted mesh-lines (b) because of the strong local properties of NURBS lattice that embeds the object.	75
3.18	Parameterised domains corresponding to (a) the desired s_2, t_2 , (b) the intermediate and distorted s_3, t_3 and (c) the final s_1, t_1	76
4.1	Bifurcation showing a parent vessel splitting into two daughter vessels.	82
4.2	Microfluidic bifurcating network with N bifurcations and the equivalent electrical circuit analogue.	91

4.3	Two dimensional view of the microfluidic bifurcating network, indicating the length set up (a) and a zoomed view at the 90° bend of the first daughter (b). The <i>dashed-dotted</i> lines indicate limiting positions of the design.	92
4.4	Indication of the locations for the evaluation of the pressure drop for each generation (only half of the network is illustrated).	93
4.5	Microfluidic bifurcating network of constant depth with 4 generations ($i = 0, 1, 2, 3$) designed for a Newtonian fluid with aspect ratio $\alpha_0 = 0.5$ and $X = 1$. The dashed-dotted line illustrates the symmetry conditions about $y = 0$	95
4.6	Numerical mesh M1 used to discretise one quarter of the geometry at the first (a) and at the second bifurcation (b), produced from Eq. (4.31) for a Newtonian fluid with aspect ratio $\alpha_0 = 0.5$ and $X = 1$	96
4.7	Normalised wall shear-stress for a Newtonian fluid along the four generations of the bifurcating network designed for a Newtonian fluid for $\alpha_0 = 0.5$ and $X = 1$ (Table 4.1).	97
4.8	Normalised flow resistance for a Newtonian fluid along the 4 generations of the bifurcating network designed for a Newtonian fluid for $\alpha_0 = 0.5$ and $X = 1$ (Table 4.1).	98
4.9	Combined contour-plot of the normalised wall shear-stress (top left part) and the normalised velocity at the centreplane (bottom right part) along the Newtonian-designed geometry (Table 4.5) for a Newtonian fluid. . .	98
4.10	Normalised average velocities along the customised bifurcating networks of each particular fluid obtained for $\alpha_0 = 0.5$, and $X = 1$	101
4.11	Normalised wall shear-stress for various fluids along the 4 generations of the bifurcating network designed for a Newtonian fluid for $\alpha_0 = 0.5$ and $X = 1$ (Table 4.1).	101
4.12	Normalised flow resistance for various fluids along the 4 generations of the bifurcating network designed for a Newtonian fluid for $\alpha_0 = 0.5$ and $X = 1$ (Table 4.1).	102

4.13 Normalised wall shear-stress along the bifurcating network for a Newtonian, shear-thinning ($n = 0.6$) and shear-thickening ($n = 1.6$) fluids, when the Newtonian designed geometry with $a_0 = 0.5$ and $X = 1.25$ is used. 104

4.14 Normalised resistance along the bifurcating network for a Newtonian, shear-thinning ($n = 0.6$) and shear-thickening ($n = 1.6$) fluids, when the Newtonian designed geometry with $a_0 = 0.5$ and $X = 1.25$ is used. 105

4.15 Normalised average velocities along the customised bifurcating networks of each particular fluid obtained for $\alpha_0 = 0.5$, and $X = 1.25$ 106

4.16 Normalised wall shear-stress along the customised bifurcating networks ($\alpha_0 = 0.5$), designed using the biomimetic principle Eq. (4.31). Two customised geometries were considered corresponding to $n = 0.6$ and $n = 1.6$ with $X = 1.25$ 108

4.17 Normalised flow resistance along the customised bifurcating networks ($\alpha_0 = 0.5$), designed using the biomimetic principle (Eq. (4.31)). Two customised geometries were considered corresponding to $n = 0.6$ and $n = 1.6$ with $X = 1.25$ 108

4.18 Contour-plots of the normalised wall shear-stress along the bifurcating networks ($\alpha_0 = 0.5$), for a power-law fluid flow with $n = 0.6$ in the Newtonian-designed geometry (Table 4.5) (a) and in the customised geometry (Table 4.7) (b) for $X = 1.25$ 109

4.19 Contour-plots of the normalised wall shear-stress along the bifurcating networks ($\alpha_0 = 0.5$), for a power-law fluid flow with $n = 1.6$ in the Newtonian-designed geometry (Table 4.5) (a) and in the customised geometry (Table 4.7) (b) for $X = 1.25$ 110

4.20 Comparison of the bifurcating networks of rectangular cross-section and inlet aspect ratio $\alpha_0 = 0.5$ created for Newtonian fluids with $L_i = 20D_{h_i}$, using different branching parameters, X 112

4.21 Normalised wall shear-stress along the network with $a_0 = 0.5$, designed for a Newtonian fluid with $X = 0.75$ 113

4.22	Normalised flow resistance (b) along the network with $a_0 = 0.5$, designed for a Newtonian fluid with $X = 0.75$	114
4.23	Normalised wall shear-stress along the customised bifurcating networks ($\alpha_0 = 0.5$), designed using the biomimetic principle (Eq. (4.31)). Two customised geometries were considered corresponding to $n = 0.6$ and $n = 1.6$ with $X = 0.75$	115
4.24	Normalised flow resistance along the customised bifurcating networks ($\alpha_0 = 0.5$), designed using the biomimetic principle (Eq. (4.31)). Two customised geometries were considered corresponding to $n = 0.6$ and $n = 1.6$ with $X = 0.75$	116
4.25	Contour-plots of the normalised wall shear-stress along the bifurcating networks ($\alpha_0 = 0.5$), for a power-law fluid flow with $n = 0.6$ in the Newtonian-designed geometry (Table 4.9) (a) and in the customised geometry (Table 4.11) (b) for $X = 0.75$	117
4.26	Contour-plot of the normalised wall shear-stress along the bifurcating networks ($\alpha_0 = 0.5$), for a power-law fluid flow with $n = 1.6$ in the Newtonian-designed geometry (Table 4.9) (a) and in the customised geometry (Table 4.11) (b) for $X = 0.75$	118
4.27	Normalised network total resistance as a function of the inlet Reynolds number (Re_0^*) defined in Eq. (4.22) for Newtonian, shear-thinning ($n = 0.6$) and shear-thickening ($n = 1.6$) fluids using the Newtonian designed geometry for $\alpha_0 = 0.5$ and $X = 1$ (Table 4.1).	119
5.1	Configuration of various single-stream designs with an abrupt contraction (a), a sudden contraction followed by a symmetric expansion (b) and a smooth symmetric converging/diverging region (c). The <i>dashed</i> rectangles illustrate the regions of interest.	126

5.2	Configuration of various multi-stream designs with a cross-slot shape (a), a T-Junction (b) and a flow-focusing device (c). The arrows indicate the direction of the bulk flow, the <i>dashed</i> rectangles illustrate the regions of interest for each configuration, and the <i>dot</i> indicates the position of the stagnation point.	129
5.3	Flow chart of the optimisation procedure.	132
5.4	Configuration of the converging/diverging geometry.	136
5.5	Ideal velocity (a) and strain-rate profiles (b) along the centreline of the flow.	136
5.6	Example of various designs obtained during the optimisation procedure: (a) Represents the shape of the initial estimation (\mathbf{Y}^0), (g) illustrates the optimised shape (\mathbf{Y}^{opt}) and (b) to (f) intermediate shapes (\mathbf{Y}^*) examined during the intermediate steps of the optimisation procedure. The <i>red square</i> symbols, illustrate the positions of the lattice control points.	139
5.7	Comparison between the optimised shape (<i>dash-dotted line</i>) and the ideal hyperbolic design (<i>continuous line</i>) discussed in Oliveira <i>et al.</i> [74] (2D, $\text{CR} = 8$, $l_c = 2w_u$, $l_\varepsilon = w_u$).	140
5.8	Velocity (a) and strain-rate (b) profiles computed for creeping flow conditions along the centreline of the flow for the optimised geometry and the ideal hyperbolic design (2D, $\text{CR} = 8$, $l_c = 2w_u$, $l_\varepsilon = w_u$). The target velocity profile is represented as a <i>continuous line</i>	141
5.9	Shapes of the optimised and the ideal hyperbolic devices (a) and strain-rate profiles along the flow centreline for the optimised devices (b) with $l_c = 4w_u$ and $l_c = 2w_u$ (2D, $\text{CR} = 8$, $l_\varepsilon = w_u$) for creeping flow conditions. Note that in (a) x and y axes are not to scale.	142

5.10 Strain-rate profiles along the flow centreline computed under creeping flow conditions for a geometry with $l_c = 2w_u$, $l_\varepsilon = w_u$, CR = 8 and (a) AR = 1, (b) AR = 2, (c) AR = 4, (d) AR = 8 and (e) AR = 32. The performance of each optimised shape is compared with the hyperbolic function (cf. Eq. (5.9)). 144

5.11 (a) Comparison of the channel boundaries obtained from 3D optimisations for creeping flow conditions for AR = 1, 2, 4, 8 and 32 and the ideal hyperbolic shape when $l_c = 2w_u$, $l_\varepsilon = w_u$ and CR = 8. (b)-(f) Contour-plots of the normalised streamwise velocity for each optimised geometry. 146

5.12 Meshes M0 (a) and M1 (b) for the optimised geometry with $l_c = 2w_u$, $l_\varepsilon = w_u$, CR = 8 and AR = 1. 148

5.13 Effect of Re on the velocity (a) and strain-rate (b) profiles computed along the flow centreline, for the optimised geometry with $l_c = 2w_u$, $l_\varepsilon = w_u$, CR = 8 and AR = 1 (Fig. 5.11), considering Newtonian fluid flow. 149

5.14 Normalised pressure drop for various Re across the contraction for a geometry with $l_c = 2w_u$, $l_\varepsilon = w_u$, CR = 8 and (a) AR = 1, (b) AR = 2, (c) AR = 4 (d) AR = 8 and (r) AR = 32. 150

5.15 Effect of Wi on the velocity (a) and strain-rate (b) profiles along the flow centreline computed for the Oldroyd-B model ($\beta = 0.5$) under creeping flow conditions, for the optimised geometry with $l_c = 2w_u$, $l_\varepsilon = w_u$, CR = 8 and AR = 1 (Fig. 5.11). 151

5.16 Effect of Wi on the velocity (a) and strain-rate (b) profiles along the flow centreline computed for a PTT fluid ($\varepsilon = 0.25, \beta = 0.01$) under creeping flow conditions, for the optimised geometry with $l_c = 2w_u$, $l_\varepsilon = w_u$ and CR = 8 for AR = 1 (Fig. 5.11). 152

5.17 Normalised pressure profile along the centreline for the Oldroyd-B model (a), the PTT model (b) and normalised pressure drop across the contraction/expansion region for both models under creeping flow conditions (c), when the optimised geometry with $l_c = 2w_u$, $l_\varepsilon = w_u$, CR = 8 and AR = 1 is used. 153

5.18 Target normalised velocity profiles (a) and nominal strain-rates (b) expected to be produced by the geometries with CR = 3, 8 and 20. 154

5.19 Strain-rate profiles along the centreline of the flow for the optimised geometry and the ideal hyperbolic design computed for creeping flow conditions (a) and normalised velocity contours for the optimised shape (CR = 3, $l_c = 2w_u$, $l_\varepsilon = w_u$ for AR = 1). 155

5.20 Strain-rate profiles along the centreline of the flow for the optimised geometry and the ideal hyperbolic design computed for creeping flow conditions (a) and normalised velocity contours for the optimised shape (CR = 20, $l_c = 2w_u$, $l_\varepsilon = w_u$ for AR = 1). 155

5.21 Configuration a T-shaped channel. The *dot* illustrates the position of the stagnation point and the *dashed-dotted* line the flow centreline of the channel. 159

5.22 Velocity (a) and strain-rate (b) target profiles along the centreline of the flow for WR = 1, $L_\perp = 4w_u$ 160

5.23 Movement of control points for the sequence of the three NURBS lattices used for optimising the T-junction (a) and the merging arrangement of the lattices (L_1, L_2 and L_3) in order to maintain the continuity of the curve (b). 161

5.24 Velocity (a) and strain-rate (b) profiles along the centreline of the flow at the outlet of the 2D, 90° bend T-shaped channel with WR = 1, under creeping flow conditions. 162

5.25 Contour-plots of the normalised y -component of the velocity of the rounded (a) and the hyperbolic (b) shaped T-channels in 2D with $WR = 1$ and $L_{\perp} = 4w_u$, under creeping flow conditions. The *dashed* straight line illustrates the position of the symmetry plane. 163

5.26 Velocity (a) and strain-rate (b) profiles along the centreline of the flow at the outlet of the 2D, rounded and hyperbolic T-channels with $WR = 1$ and $L_{\perp} = 4w_u$, under creeping flow conditions. 163

5.27 Velocity (a) and strain-rate (b) profiles along the centreline of the flow at the outlet channel of the 2D, optimised geometries with straight bottom and an optimised bottom for $WR = 1$ and $L_{\perp} = 4w_u$, under creeping flow conditions. 164

5.28 Contour-plots of the normalised y -component of the velocity of the optimised T-junction geometries for the optimised standard T-junction (a) and T-junction with cavity (b), in 2D with $WR = 1$ and $L_{\perp} = 4w_u$, under creeping flow conditions. The *dashed* straight line illustrates the position of the symmetry plane. 165

5.29 Comparison between the original abrupt and the smooth target velocity profiles (a) and corresponding strain-rate profiles (b) along the centreline of the flow at the outlet channel. 166

5.30 Velocity (a) and strain-rate (b) profiles along the centreline of the flow at the outlet channel of the 2D, optimised standard geometry for $WR = 1$, $L_{\perp} = 4w_u$ and $l_{\varepsilon} = 0.5w_u$, considering the modified target velocity profile of Eq. (5.14) under creeping flow conditions. 167

5.31 Contour-plots of the normalised y -component of the velocity of the optimised standard T-junction in 2D with $WR = 1$, $L_{\perp} = 4w_u$ and $l_{\varepsilon} = 0.5w_u$, under creeping flow conditions when the modified target velocity profile of Eq. (5.14) is used. The *dashed* straight line illustrates the position of the symmetry plane. 168

5.32 Velocity (a) and strain-rate (b) profiles along the centreline of the flow at the outlet channel of the 3D, optimised geometry with straight bottom in and for the 3D geometry designed with the 2D optimised solution for $AR = 1$, $WR = 1$, $L_{\perp} = 4w_u$ and $l_{\varepsilon} = 0.5w_u$, considering the modified target velocity profile of Eq. (5.14) under creeping flow conditions. . . . 169

5.33 Normalised y -component of the velocity contour-plot of the optimised T-junction geometry (a) and comparison with the 2D optimised shape (b), with $AR = 1$, $WR = 1$, $L_{\perp} = 4w_u$ and $l_{\varepsilon} = 0.5w_u$ under creeping flow conditions. The *dashed* straight line illustrates the position of centreline of the flow and the symmetry axis. 170

5.34 Meshes M0 (a) and M1 (b) for the optimised geometry with $AR = 1$, $WR = 1$, $L_{\perp} = 4w_u$ and $l_{\varepsilon} = 0.5w_u$ 170

5.35 Effect of Wi on the velocity (a) and strain-rate (b) profiles along the flow centreline computed for the Oldroyd-B model ($\beta = 0.5$) under creeping flow conditions, for the optimised T-junction with $AR = 1$, $WR = 1$, $L_{\perp} = 4w_u$ and $l_{\varepsilon} = 0.5w_u$ 171

5.36 Effect of Wi on the velocity (a) and strain-rate (b) profiles along the flow centreline computed for the PTT model ($\beta = 0.01$, $\varepsilon = 0.25$) under creeping flow conditions, for the optimised T-junction with $AR = 1$, $WR = 1$, $L_{\perp} = 4w_u$ and $l_{\varepsilon} = 0.5w_u$ 172

5.37 Configuration a flow-focusing channel with the *dashed-dotted* line indicating the flow centreline of the channel. 173

5.38 Contours of the normalised magnitude of the velocity in a 2D flow-focusing design with $WR = 1$ for $VR = 10$ (a), $VR = 20$ (b) and $VR = 100$ (c) under creeping flow conditions. The *vertical dashed line* indicates the flow field centreline, coinciding with the symmetry axis employed. 174

5.39 Velocity (a) and strain-rate (b) profiles for the abrupt, 2D, flow-focusing geometry with $WR = 1$ considering three different velocity ratios, $VR = 10, 20$ and 100 175

5.40 Normalised velocity (left hand side column) and strain-rate (right hand side column) profiles along the centreline of the flow for the optimised geometries with $WR = 1$, $L_{\perp} = 3w_u$ and $l_{\varepsilon} = 0.5w_u$ for $VR = 10, 20$ and 100 177

5.41 Contour-plots of the normalised velocity magnitude and streamlines obtained for the optimised flow focusing geometries under creeping flow conditions with $VR=10$ (a), $VR=20$ (b), $VR=100$ (c) and comparison of the optimised shapes obtained (d) when $WR = 1$, $L_{\perp} = 3w_u$ and $l_{\varepsilon} = 0.5w_u$ 178

5.42 Normalised velocity magnitude contour-plot of the 3D optimised, flow-focusing geometry (a) and comparison with the 2D optimised shape (b), with $AR = 1$, $WR = 1$, $VR = 20$, $L_{\perp} = 3w_u$ and $l_{\varepsilon} = 0.5w_u$. The *dashed* straight line illustrates the position of centreline of the flow and the symmetry axis. 179

5.43 Velocity (a) and strain-rate (b) profiles along the centreline of the flow for the 3D, flow-focusing, optimised geometry and for the 3D flow-focusing geometry designed with the shape of the 2D optimised solution for $AR = 1$, $WR = 1$, $VR = 20$, $L_{\perp} = 4w_u$ and $l_{\varepsilon} = 0.5w_u$, under creeping flow conditions. 180

5.44 Meshes M0 (a) and M1 (b) for the optimised geometry with $AR = 1$, $WR = 1$, $VR = 20$, $L_{\perp} = 3w_u$ and $l_{\varepsilon} = 0.5w_u$ 180

5.45 Strain-rate profiles along the flow centreline of the 3D optimised flow-focusing geometry with $AR = 1$, $WR = 1$, $L_{\perp} = 3w_u$, $l_{\varepsilon} = 0.5w_u$, optimised for $VR = 20$ under creeping flow conditions, when imposing different velocity ratios. 181

5.46 Contour-plots of the normalised velocity magnitude and streamlines obtained for the 3D optimised flow focusing geometry with $AR = 1$, $WR = 1$, $L_{\perp} = 3w_u$, $l_{\varepsilon} = 0.5w_u$, optimised for $VR = 20$ under creeping flow conditions, when imposing $VR = 1$ (a), $VR = 10$ (b), $VR = 40$ (c), $VR = 60$ (d), $VR = 80$ (e), $VR = 100$ (f). 182

5.47	Effect of Wi on the velocity (a) and strain-rate (b) profiles along the flow centreline computed for the Oldroyd-B model ($\beta = 0.50$) under creeping flow conditions, for the optimised geometry with $AR = 1$, $WR = 1$, $VR = 20$, $L_{\perp} = 3w_u$ and $l_{\varepsilon} = 0.5w_u$	184
5.48	Effect of Wi on the velocity (a) and strain-rate (b) profiles along the flow centreline computed for the PTT model ($\varepsilon = 0.25$ and $\beta = 0.50$) under creeping flow conditions, for the optimised geometry with $AR = 1$, $WR = 1$, $VR = 20$, $L_{\perp} = 3w_u$ and $l_{\varepsilon} = 0.5w_u$	184
6.1	Double well function for the free energy density model	194
6.2	Concentration profile at the interface of the two fluids.	195
6.3	Two dimensional representation of a control volume.	202
6.4	Three dimensional representation of a control volume.	206
6.5	Domain initialisation for the stretching element case. The contour corresponds to the magnitude of velocity from Eq. (6.83) and the black circle indicates the drop interface based on the 0.5-contour at $t = 0$ s.	216
6.6	Stretching of the 0.5-contour of the circular element in time for the M128 mesh, using the SMART scheme for convection. The contours correspond to u -velocity calculated from Eq. (6.83).	217
6.7	Performance of all the convective schemes for all numerical meshes at times $t = 2$ s and $t = 4$ s.	218
6.8	Performance of all the convective schemes for the most refine grid, M512, at times $t = 2$ s and $t = 4$ s.	219
6.9	Stretching of the circular element without reversing the velocity field by removing the cosine term from Eqs. (6.81) and (6.83) for all grids using the SMART scheme at times $t = 1$ s, $t = 2$ s, $t = 3$ s and $t = 4$ s.	220
6.10	Contour-plot of the concentration for the initialisation of the Rayleigh-Taylor instability problem. The top fluid (A , <i>red</i>) is heavier than the bottom fluid (B , <i>blue</i>).	222
6.11	Contour-plots of the concentration at different dimensionless times for the Rayleigh-Taylor instability when $At = 0.5$ for the M200.	224

6.12	Front positions for the lighter and heavier fluids at different dimensionless times, for the Rayleigh-Taylor instability when $At = 0.5$ for all numerical meshes considered (cf. Table 6.2), compared with the solution from Ding <i>et al.</i> [58].	225
6.13	Contour-plots of the concentration at different dimensionless times for the Rayleigh-Taylor instability when $At = 1$ for the M200.	226
6.14	Front positions for the lighter and heavier fluids at different dimensionless times, for the Rayleigh-Taylor instability when $At = 1$ for all numerical meshes considered (cf. Table 6.2).	226
6.15	Domain initialisation for the M064 mesh (cf. Table 6.3) for validating Young-Laplace formula (Eq. (6.86)).	228
6.16	Contour plot of the velocity magnitude for the various meshes considered (details in Table 6.3). The <i>dashed</i> line indicates the position of the interface (0.5-contour).	229
6.17	Evaluation of Young-Laplace formula (Eq. (6.87)) for different surface tension coefficient values for a fixed $R = 0.125$ m (a) and for different radii for a fixed $\sigma = 0.1$ Nm^{-1} (b).	232
6.18	Evaluation of Young-Laplace formula (Eq. (6.87)) for a range of density ratios, λ_ρ , when $\lambda_\eta = 1$ (a) for a range of viscosity ratios, λ_η , when $\lambda_\rho = 1$ (b) and when both λ_ρ and λ_η vary (c), for $R = 0.125$ m and $\sigma = 0.1$ Nm^{-1}	233
6.19	Contour-plots of the concentration of the oscillatory droplet at different dimensionless times	234
6.20	Combined contour-plots of the velocity magnitude (left-part) and the pressure distribution (right-part) for each frame at different dimensionless times.	236
6.21	Configuration for the shear deformation test-case. The drop is positioned in between the two parallel plates ($y = 0$) that move in opposite directions with the same velocity (a), and deforms under constant shear obtaining an ellipsoidal form (b).	237

6.22	Drop deformation in dimensionless time, evaluated using Eq. (6.88), for all numerical grids of Table 6.7, compared with the solution from Chinyoka <i>et al.</i> [263].	239
6.23	Drop deformation indicated by the 0.5-contour for various dimensionless times (a), and contour-plot of concentration together with the streamlines at $\tilde{t} = 10$ (b), for $Ca = 0.6$ and $Re = 0.3$ when $k = 5$ for M256.	239
6.24	Drop deformation in dimensionless time, evaluated using Eq. (6.88), for all numerical grids of Table 6.7, compared with the solution from Chinyoka <i>et al.</i> [263].	240
6.25	Drop deformation indicated by the 0.5-contour in dimensionless times with the arrow pointing the direction of the deformation (a), and contour-plot of concentration together with the streamlines at $\tilde{t} = 10$ (b), for $Ca = 0.6$ and $Re = 0.3$ when ϵ is constant ($k = 20$) for the M256. The <i>red</i> shape in (a) corresponds to the case of $k = 5$ at $\tilde{t} = 10$	241
6.26	Behaviour of the contour-lines at $\tilde{t} = 10$ for all three meshes when $k = 5$ (a) and for constant ϵ (b), for $Ca = 0.6$, $Re = 0.3$	242
B.1.1	Velocity (a) and strain-rate (b) profiles along the centreline of the flow for the optimised converging-diverging (<i>solid line</i>) and converging-abrupt geometries (<i>dashed line</i>).	259
B.1.2	Normalised velocity contour-plots for the optimised converging-abrupt (top-figure) and converging-diverging (bottom-figure) geometries.	260
B.2.1	Velocity (a) and strain-rate (b) profiles computed for creeping flow conditions along the centreline of the flow for the optimised geometry considering an abrupt transition profile and the ideal hyperbolic design (2D, $CR = 8$, $l_c = 2w_u$, $l_\epsilon = 0$). The target velocity profile is represented as a <i>continuous line</i>	261
B.2.2	Comparison between the optimised shapes obtained considering the abrupt transition profile (2D, $CR = 8$, $l_c = 2w_u$, $l_\epsilon = 0$), the smoothed transition profile (2D, $CR = 8$, $l_c = 2w_u$, $l_\epsilon = w_u$) and the ideal hyperbolic function.	261

B.3.1 Effect of Re on the velocity (a) and strain-rate (b) profiles computed along the flow centreline, for the optimised geometry with $l_c = 2w_u$, $l_\varepsilon = w_u$, CR = 8 for AR = 2 (Fig. 5.11c), considering Newtonian fluid flow. 262

B.3.2 Effect of Re on the velocity (a) and strain-rate (b) profiles computed along the flow centreline, for the optimised geometry with $l_c = 2w_u$, $l_\varepsilon = w_u$, CR = 8 for AR = 4 (Fig. 5.11d), considering Newtonian fluid flow. 262

B.3.3 Effect of Re on the velocity (a) and strain-rate (b) profiles computed along the flow centreline, for the optimised geometry with $l_c = 2w_u$, $l_\varepsilon = w_u$, CR = 8 for AR = 8 (Fig. 5.11e), considering Newtonian fluid flow. 263

B.3.4 Effect of Re on the velocity (a) and strain-rate (b) profiles computed along the flow centreline, for the optimised geometry with $l_c = 2w_u$, $l_\varepsilon = w_u$, CR = 8 for AR = 32 (Fig. 5.11f), considering Newtonian fluid flow. 263

B.4.1 Effect of the aspect ratio ($AR = w_u/d$) on the strain-rate profile computed along the flow centreline. The 3D geometries are designed using the 2D optimised shape for AR = 0.1, 0.2, 0.5 and 2 with WR = 1, $L_\perp = 4w_u$ and $l_\varepsilon = 0.5w_u$ considering creeping flow conditions. 264

List of Tables

2.1	Comparison between the various models discussed.	21
4.1	Geometrical parameters and dimensions of a planar bifurcating network with inlet aspect ratio $\alpha_0 = 0.5$ obtained for a Newtonian fluid ($n = 1$).	96
4.2	Mesh characteristics for a Newtonian ($n = 1$) geometry, designed for $X = 1$ and $a_0 = 0.5$	97
4.3	Geometrical parameters and dimensions of planar bifurcating networks with inlet aspect ratio $\alpha_0 = 0.5$ obtained for power-law, shear-thinning fluids with $n = 0.2, 0.4, 0.6$ and 0.8	99
4.4	Geometrical parameters and dimensions of planar bifurcating networks with inlet aspect ratio $\alpha_0 = 0.5$ obtained for power-law, shear-thickening fluids with $n = 1.2, 1.4, 1.6, 1.8$ and 2.0	100
4.5	Geometrical parameters and dimensions of planar bifurcating networks with initial aspect ratio $\alpha_0 = 0.5$ and branching parameter $X = 1.25$, designed for a Newtonian fluid.	103
4.6	Mesh characteristics for a 3D flow simulation for a Newtonian ($n = 1$) geometry, designed for $X = 1.25$ and $a_0 = 0.5$	104
4.7	Geometrical parameters and dimensions of planar networks with initial aspect ratio $\alpha_0 = 0.5$ and branching parameter $X = 1.25$, for power-law fluids with $n = 0.6$ and $n = 1.6$	107
4.8	Mesh characteristics for the power-law geometries considered ($n = 0.6$ and $n = 1.6$) geometry, designed for $X = 1.25$ and $a_0 = 0.5$	107

4.9	Geometrical parameters and dimensions of planar bifurcating networks with initial aspect ratio $\alpha_0 = 0.5$ and branching parameter $X = 0.75$, designed for a Newtonian fluid.	112
4.10	Mesh characteristics for a Newtonian ($n = 1$) geometry, designed for $X = 0.75$ and $a_0 = 0.5$	113
4.11	Geometrical parameters and dimensions of planar networks with initial aspect ratio $\alpha_0 = 0.5$ and branching parameter $X = 0.75$, for power-law fluids with $n = 0.6$ and $n = 1.6$	114
4.12	Mesh characteristics for the power-law geometries considered ($n = 0.6$ and $n = 1.6$) geometry, designed for $X = 0.75$ and $a_0 = 0.5$	115
5.1	Mesh characteristics for the 2D simulations performed with $CR = 8$ and $l_c = 2w_u$	141
5.2	Mesh characteristics for the 3D optimisations for a geometry of $l_c = 2w_u$, $l_\varepsilon = w_u$ and $CR = 8$ for $AR = 1, 2, 4$ and 8	147
5.3	Mesh characteristics for the 3D optimisations for the geometries with $l_c = 2w_u$, $l_\varepsilon = w_u$ and $AR = 1$	156
5.4	Mesh characteristics for 2D optimised geometries when $WR = 1$ and $L_\perp = 4w_u$	168
5.5	Mesh characteristics for the 3D optimised geometry when $AR = 1$, $WR = 1$, $L_\perp = 4w_u$ and $l_\varepsilon = 0.5w_u$	171
5.6	Mesh characteristics for the 2D optimised geometry when $WR = 1$, $L_\perp = 3w_u$ and $l_\varepsilon = 0.5w_u$	178
5.7	Mesh characteristics for the 3D optimised geometry with $AR = 1$, $WR = 1$, $L_\perp = 3w_u$ and $l_\varepsilon = 0.5w_u$	180
6.1	Performance of all numerical schemes for each computational mesh considered, for the stretching test of a circular element with $R = 0.15$ m.	219
6.2	Mesh characteristics for the Rayleigh-Taylor instability study.	225
6.3	Mesh characteristics for the Young-Laplace test-case for $R = 0.125$ m and $\sigma = 0.1$ Nm^{-1}	229

6.4	Variation of the interface resolution, k , for the case of a quiescent drop with $R = 0.125$ m	230
6.5	Variation of the characteristic mobility M_c for the case of a quiescent drop with $R = 0.125$ m.	231
6.6	Variation of the interface resolution, k , and the characteristic mobility, M_c , for the case of a quiescent drop with $R = 0.125$	231
6.7	Mesh characteristics for the study of the droplet deformation under constant shear with $k = 5$	238
6.8	Mesh characteristics for the study of the droplet deformation under constant shear with constant interface thickness, ϵ	240
A.1	Geometrical parameters and dimensions of planar bifurcating networks with inlet aspect ratio $\alpha_0 = 0.2$ obtained for Newtonian ($n = 1.0$) and power-law fluids ($n = 0.6, 1.6$) for $X = 1$	256
A.2	Geometrical parameters and dimensions of planar bifurcating networks with inlet aspect ratio $\alpha_0 = 0.3$ obtained for Newtonian ($n = 1.0$) and power-law fluids ($n = 0.6, 1.6$) for $X = 1$	257
A.3	Geometrical parameters and dimensions of planar bifurcating networks with inlet aspect ratio $\alpha_0 = 1.0$ obtained for Newtonian ($n = 1.0$) and power-law fluids ($n = 0.6, 1.6$) for $X = 1$	257

Glossary

Greek Letters

α	Aspect ratio, constant parameter.
α^*	Aspect ratio parameter.
β^{li}	Cofactors of the transformation matrix.
β	Viscosity ratio.
Γ	General diffusion coefficient.
$\dot{\gamma}$	Rate-of-deformation (shear-rate) tensor.
$\dot{\gamma}$	Shear-rate.
ΔP	Pressure drop.
ΔP_c	Contraction normalised pressure drop.
$\Delta \tilde{x}_i$	Dimensionless grid spacing.
δ	Interface thickness width.
ε	Extensibility parameter for the PTT.
$\dot{\varepsilon}$	Strain-rate.
$\dot{\varepsilon}_a$	Apparent strain-rate.
ϵ	Interface thickness.
ϵ_H	Hencky strain.
η	Shear viscosity.
η_0	Zero-shear viscosity.
η_p	Polymer viscosity.
η_s	Solvent viscosity.
η_E	Extensional viscosity.
I	Identity tensor.

λ	Relaxation time.
λ_r	Retardation time.
λ_ρ	Density ratio.
λ_η	Viscosity ratio.
ξ	PTT parameter.
ξ_1, ξ_2, ξ_3	Generalised coordinates.
$\bar{\xi}$	Normalised distance.
ρ	Density.
σ	Surface tension.
$\boldsymbol{\tau}$	Extra stress tensor.
$\boldsymbol{\tau}_p$	Polymer stress tensor.
$\boldsymbol{\tau}_s$	Solvent stress tensor.
τ	Wall shear-stress.
$\bar{\tau}$	Average wall shear-stress.
ϕ	Diameter, Chemical potential, General transport quantity.
ϕ_c	Characteristic chemical potential.
$\bar{\phi}$	Normalised convective variable.
$\psi(C)$	Double well function.

Roman Letters

A	Cross sectional area.
At	Atwood number.
a	Coefficients of the discretised equations.
a^*	Geometrical parameter.
\mathbf{B}_i	Control points.
B	Bottom neighbour cell.
b^{li}	Cofactor variable.
$b_{i,n}$	Bernstein basis polynomials.
b^*	Geometrical parameter.

\mathcal{C}	Flux of the Cahn-Hilliard equation.
C	Concentration, Order parameter.
Ca	Capillary number.
Cn	Cahn number.
c_p	Proportionality constant.
D	Deformation parameter.
De	Deborah number.
D_h	Hydraulic diameter.
d	Depth.
E	East neighbour cell.
El	Elasticity number.
F_X, F_Y, F_Z	Interpolation factors.
\mathbf{F}	Mass flow rate.
F	Free energy.
F_f	Mass flow rate component at each cell face.
F_{obj}	Objective function.
\mathbf{f}_{st}	Surface tension forces.
f	Fanning friction factor.
$f(\boldsymbol{\tau}_p)$	Stress function.
G	Elastic modulus.
\mathbf{g}	Gravitational acceleration.
H	Sum of the neighbouring coefficients.
h	Characteristic grid cell size.
I	Convection-diffusion integral.
I^C	Convection integral.
I^D	Diffusion integral.
J	Jacobian.

K	Power law parameter for flow in rectangular duct.
k	Consistency index, Numerical cells defining interface thickness, Basis function order.
k^*	Basis function intermediate orders.
L	Characteristic dimension, Length.
L_{\perp}	Vertical segment optimisation length.
l_c	Contraction length.
l_{ε}	Smoothing length.
M	Mobility, Basis functions.
M_c	Characteristic mobility.
m_{op}	Multiplicity.
N	Basis functions.
N_1	First normal-stress difference.
N_2	Second normal-stress difference.
N	North neighbour cell.
\mathbf{n}	Normal unit vector.
n	Power-law index.
$\mathbf{P}(s)$	Parametric curve.
\mathcal{P}_m	Power for the metabolic processes.
P_{ref}	Reference pressure.
\mathcal{P}_{tot}	Total power of a vascular system.
\mathcal{P}_v	Power for overcoming the viscous losses.
P	Cell under investigation.
Pe	Peclet number.
Po	Poiseuille number.
\mathcal{P}	Wetted perimeter.
p	Pressure, Total number of knot vectors.
Q	Flow rate.
q	Diffusive flow rate.

q	Knot vector elements.
R	Hydraulic resistance, Radius, Rational basis functions.
Re	Reynolds number.
Re*	Generalised Reynolds number.
r	Knot vector elements.
S	Total length vector.
S	Volume source (integrated over the cell centre), Bivariate rational surface basis functions.
S	South neighbour cell.
s	Parameterised coordinate.
T	Total length vector.
T_f	Total simulation time.
T	Top neighbour cell.
t	Time, Parameterised coordinate.
t_{conv}	Convection time.
t_{diff}	Diffusion time.
t_{flow}	Time of observation.
U	Characteristic velocity, Average velocity.
U_1	Perpendicular inlet average velocity.
U_2	Horizontal inlet average velocity.
u	Velocity vector.
u	Velocity, Knot vector elements.
u_w	Wall velocity.
\tilde{u}	Normalised velocity.
\tilde{u}_c	Normalised maximum contraction velocity.
\tilde{u}_u	Normalised maximum upstream velocity.
\bar{u}	Average velocity.
V	Volume.

\tilde{v}	Normalised velocity.
\tilde{v}_d	Normalised downstream velocity.
\tilde{v}_2	Normalised maximum inlet velocity.
\tilde{v}_3	Normalised maximum outlet velocity.
w	Width, Parameterised coordinate.
W	Total length vector.
W	West neighbour cell.
Wi	Weissenberg number.
w_c	Contraction width.
w_u	Upstream width.
w_{\perp}	Vertical segment width.
X	Branching parameter.
x_1, x_2, x_3	Cartesian coordinates.
\tilde{x}	Normalised x -position.
Y*	Set of control points positions.
\tilde{y}	Normalised y -position.

Subscripts

A	Fluid A.
a	Apparent.
B	Fluid B.
b	Bottom face.
c	Characteristic, contraction.
D	Downstream cell.
e	East face.
F	Neighbour cell.
f	Face direction.
f	Face.
i, j, k, l	Indices.
m	Abbreviation of metabolic, Index.

<i>n</i>	North face, Index.
P	Cell under investigation.
<i>s</i>	South face, Parametric space direction.
st	Abbreviation of “surface tension”.
<i>t</i>	Top face, Parametric space direction.
<i>tot</i>	Abbreviation of total.
U	Upstream cell.
<i>v</i>	Abbreviation of viscus.
<i>w</i>	West face, Parametric space direction.
w	Wall.

Superscripts

<i>C</i>	Abbreviation for convective.
<i>D</i>	Abbreviation for diffusive.
<i>f</i>	Face direction.
f	Face.

Acronyms

2D	Two dimensional.
3D	Three dimensional.
AR	Aspect ratio.
CAD	Computer Aided Designing.
CBC	Convection Boundedness Criterion.
CDS	Central Differencing Scheme.
CFD	Computational Fluid Dynamics.
CR	Contraction ratio.
CUBISTA	Convergent and Universaly Bounded Interpolation Scheme for the Treatment of Advection.
EDL	Electric Double Layer.
EOF	Electro-Osmotic Flow.
EVROC [™]	Extensional Viscometer Rheometer On a Chip.
FD	Finite Differences.
FE	Finite Elements.
FFD	Free Form Deformation.
FV	Finite Volume.

GNF	Generalised Newtonian Fluid.
HO	Higher Order Scheme.
HRS	High Resolution Scheme.
LHS	Left Hand Side.
LS	Level Set.
NOMAD	Nonlinear Optimization by Mesh Adaptive Direct Search.
NURBS	Non-Uniform Rational B-Splines.
NVD	Normalised Variable Diagram.
NVF	Normalised Variable Formulation.
NVSF	Normalised Variable and Space Formulation.
OS CER	Optimised Shape Cross-slot Extensional Rheometer.
PF	Phase Field.
PTT	Phan-Thien Tanner.
QUICK	Quadratic Upwind Interpolation for Convective Kinematics.
RHS	Right Hand Side.
ROJER	Rayleigh Ohnesorge Jetting Extensional Rheometry.

SIMPLE	Semi-Implicit Method for Pressure Linked Equations.
SIMPLEC	Semi-Implicit Method for Pressure Linked Equations-Consistent.
SMART	Sharp and Monotonic Algorithm for Realistic Transport.
TVD	Total Variation Diminishing.
UCM	Upper Convected Maxwell.
UDS	Upwind Differencing Scheme.
VOF	Volume Of Fluid.
VR	Velocity ratio.
WR	Width ratio.

“Science is a way of life. Science is a perspective. Science is the process that takes us from confusion to understanding in a manner that’s precise, predictive and reliable - a transformation, for those lucky enough to experience it, that is empowering and emotional.”

B. Green

Chapter 1

Introduction

1.1 Motivation

Industrial and scientific fields are eager for intelligent applications that are able to provide solutions to the increasing needs for more efficient products. Nature has always acted as a source of inspiration to technological developments, giving birth to the field of *biomimetics* and turning it into an increasingly active area of research [1]. On the other hand the (r)-evolution in computer industry and the advances in computational methods allowed researchers to employ sophisticated configurations and methods as tools to perfect their designs. The work presented in the following chapters of this thesis is influenced by these two different sources of inspiration, in order to propose designs for performing studies related to Newtonian and complex fluid systems under shear- and extension-dominated flows at the micro-scale.

The constantly growing interest nowadays around *Lab-on-a-chip* technologies is indicative of their importance and their advantages. Many scientific studies in various fields such as Biology, Chemistry, Engineering, Biotechnology and Medicine engage *microfluidic* devices to carry out complex tasks (cf. Fig. 1.1). The inherently small scales (cf. Fig. 1.2), with characteristic dimensions in the range of 1 μm - 1000 μm , bring about a number of advantages, both practical and in terms of the fluid dynamic conditions they can provide. In practical terms, they require a small amount of samples to operate (and therefore generate low amounts of waste), a significant feature espe-



Figure 1.1. Word-cloud for microfluidics.

cially for studies related to biofluids that are typically available in small quantities and pharmacological products, which tend to be expensive. These features together with the generally low-cost fabrication procedure makes them a very attractive choice [2,3]. Moreover, they provide the ability to manipulate fluids generating laminar flows using different techniques, where the external forces responsible for setting the fluid in motion in the microdevice can be applied by pressure differences, by an electric field, by a magnetic field or even by an acoustic field [2]. In this context, applications in Biotechnology and other biomedical areas have been thriving. Examples of bio applications include cell-response studies, blood flow analysis, drug delivery and tissue engineering. Faivre *et al.* [4], designed a microfabricated device that could form the base for future blood-plasma separation devices, and other micro-designs for blood fractionation have been reported [5]. Choucha-Snouber *et al.* [6] fabricated a liver-kidney co-culture mi-

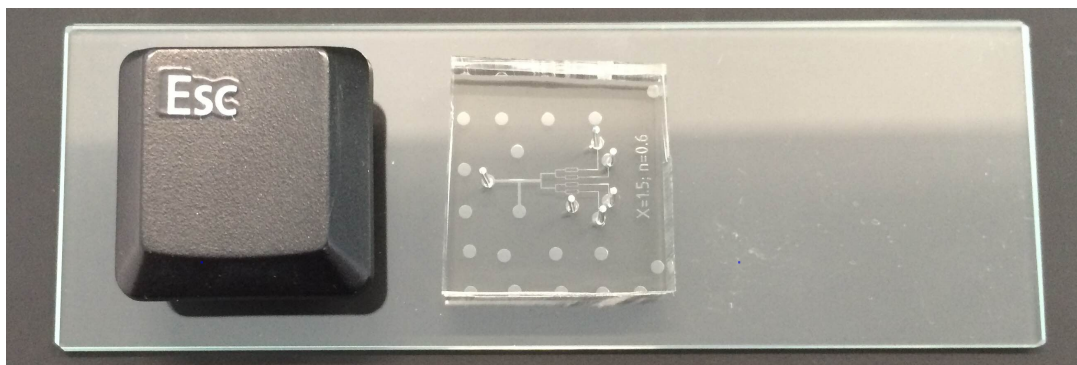


Figure 1.2. Fabricated bifurcating microchannel, designed based on the biomimetic principle that is discussed in Chapter 4, in contrast to an ESC button taken from a common keyboard.

crofluidic chip in order to probe the interaction between both organs and illustrated the advantages of using micro-chips for investigating organ-organ interactions. Moreover, they highlighted the advantage of this technology to provide *in-vitro* platforms that replicate the *in-vivo* environment, closer to what the conventional cell culture dishes are able to do. Huh *et al.* [7] described a biomimetic microsystem that is able to mimic the alveolar capillary interface of the human lung, that was providing the ability to observe complex responses such as pulmonary inflammation. The fact that microfluidic devices have increased their popularity in areas such as tissue-engineering made them also strong candidates as investigation platforms for optimised drug carriers [8], indicating their significance in future studies and developments.

Besides the popularity of microfluidics for sophisticated applications related to biological fluids, microdevices can also provide important assistance to more classical studies in fluid mechanics. Fluid flow studies have been extensively performed in large scales (macro dimensions), where typically small surface-to-volume ratios exist, and inertial forces dominate in most of the flows. An important characteristic of microfluidics lies in the fact that they provide high surface-to-volume ratios, and this offers the ability to closer investigate interesting effects, such as the elastic behaviour of viscoelastic fluids and surface interactions, while maintaining negligible inertial effects. In fact, at the macroscale the effects due to fluid elasticity are mostly revealed when highly viscous fluids were considered (to mitigate effects of inertia) [9]. As pointed out by Pipe and McKinley [10], this realisation together with the previously reported advantages, stimulated the interest for in-depth investigations that are related to the dynamics of complex fluid systems using microfabricated devices.

The remarkable effects of the non-Newtonian fluids which demonstrate elastic responses, known as *viscoelastic fluids*, have been studied using various microfluidic devices in literature. Recently Galindo-Rosales *et al.* [11] reviewed various micro-configurations that trigger viscoelastic instabilities and assist in investigating this effect. Groisman and Quake [12] designed microfluidic rectifiers and demonstrated the non-reversibility of the flow for viscoelastic fluids due to the anisotropy in the resistance when the flow was reversed. Using a similar configuration with different depths

and consisting of a sequence of hyperbolic contractions, Sousa *et al.* [13] improved the diodicity of the channels for viscoelastic fluids, by enhancing extensional effects and reducing the effects of shear. Zilz *et al.* [14] used a microfluidic serpentine channel to determine experimentally the critical conditions for the onset of a time dependent instability, and then Zilz *et al.* [15] proposed the use of these channels as micro-rheometers for measuring the relaxation time of the fluid. The fact that microfluidics can generate flows of high deformation rates for low inertia, also motivated Rodd *et al.* [16] to investigate the existence of elastic effects in microscale contraction-expansion flows. In contrast with the experiments performed by Nigen and Walters [17] using Boger fluids at the macroscale, the authors were able to demonstrate the existence of an elastic corner vortex. Recently, Drost and Westerweel [18] used two different configurations of an abrupt contraction followed by three equidistant outlets and illustrated the different kinematics in viscoelastic fluid flow. The authors pointed out that these results directly affect industrial processes such as multi-outlet extrusion flows. A variety of other types of microfluidic configurations also exist in the literature that investigate the elastic behaviour of viscoelastic fluids, such as T-channels, cross-slots and flow focusing devices. For instance, Sousa *et al.* [19] studied the onset of elastic instabilities for a range of viscoelastic fluids in a cross-slot device. They showed that depending on the concentration of the polymer, different regimes are captured which are also dependent on the aspect ratio of the design. Soulages [20] *et al.* examined the flow of a shear-thinning viscoelastic fluid employing two types of a three-dimensional T-shaped microfabricated channel, one that has a fixed stagnation point and one that is free, and reported the flow regimes where the flow patterns remain symmetric up to where they become unsteady three-dimensional. Oliveira *et al.* [21] investigated numerically the flow of viscoelastic fluids with either constant viscosity or shear-thinning behaviour under creeping flow conditions in a flow-focusing configuration, and reported strong viscoelastic effects that resulted in purely elastic instabilities. Later, Oliveira *et al.* [22] investigated both numerically and experimentally the flow of a Newtonian fluid in a flow focusing microchannel. The authors demonstrated the ability of this geometry to generate a controlled extensional flow along the flow centreline. By varying the veloc-

ity ratio of the perpendicular inlets to the horizontal inlet, a converging flow region is formed that resembles a smooth, hyperbolic contraction in which slip on the walls can be considered. Moreover it was shown that even for creeping flow conditions, the variation of velocity ratio is able to generate recirculation regions which remain symmetric around the flow centreline. For three-dimensional geometries it was shown that surrounding walls have a stabilising effect on vortex enhancement. In contrast to the behaviour of the Newtonian fluid, Oliveira *et al.* [23] investigated the flow of a Boger fluid using the same microchannel and reported various flow regimes, with the flow changing from steady symmetric to steady asymmetric and unsteady, relative to the flow centreline.

Microfluidic systems that contain two-phases are also in high demand as Lab-on-a-chip technology offers advantages to create emulsions with increased control, resulting in droplets with uniform and precise volume, making them a great platform for examining and understanding interfacial mechanisms such as break-up and coalescence [24, 25]. The necessity for configurations that offer this ability has also been pointed out by Christopher and Anna [26], with examples of possible applications, such as the use of well defined droplets as carriers for transporting sensitive cells, or their use in protein crystallisation.

It becomes evident from this brief introduction that microfluidic applications span a variety of fields and have significantly increased in importance in recent years. The concomitant increase of research in this field has led to several conceptual and practical advances. Nevertheless, the design of microfluidic devices for particular applications still largely relies on experimental trial-and-error. To fully realise the potential of microfluidics one needs to transcend this approach in favour of a more informed/rational design of devices. This thesis aims to make a contribution towards this end, by proposing theoretical and numerical design rules and algorithms that enable the design and fine-tuning of microfluidic devices to suit specific applications, more specifically to generate well defined and controlled dynamics in applications involving non-Newtonian fluids. It is attempted to reach this goal numerically, using an in-house single-phase solver [27], by employing biomimetic approaches and shape optimisation techniques

in order to propose new designs. Additionally, the large interest in studying complex fluid systems described by two fluid phases, triggered the motivation of this research to update the numerical single-phase solver to a two-phase solver, aiming to provide an extra tool for assisting future experimental studies.

1.2 Outline of the thesis

This thesis refers to numerical studies that are related to microfluidics, focusing on the investigation of the flow behaviour of complex fluid systems. The first aim is to generate and propose possible device configurations that can produce specific and well controlled flow dynamics for applications of Lab-on-a-chip platforms. This is achieved by employing biomimetic and optimisation techniques. The second objective is to implement appropriate numerical tools that will allow for such design and optimisation techniques to be extended to systems involving two-phase flows.

The work undertaken had as an outcome three (3) publications, two (2) in international journals and one (1) in a conference proceedings, drawing mostly from the results presented in [Chapters 4](#) and [5](#). Moreover, parts of this research have been presented in ten (10) conferences (oral and poster presentations). Due to the diversity of topics addressed in this thesis it was decided that each chapter would begin with an individual literature review, thus guiding the reader to the specific issues discussed in that chapter.

The main interest of this thesis, motivating all the individual studies and numerical implementations performed, is the examination of the flow of non-Newtonian fluids. [Chapter 2](#) serves as an introductory section to the non-Newtonian fluids world introducing the main properties and the characteristics of the fluid models that are considered in the subsequent chapters. The discussion is narrowed to the models considered in this work and cannot be regarded as a complete representation of all the existing models in the scientific literature. Important dimensionless numbers used are also introduced at the end of this chapter.

The majority of the numerical studies presented in this thesis are based on an in-

house numerical code that does not consist of an original work of this research. The basic features of the computational fluid dynamics solver are presented in the first part of [Chapter 3](#), but for more in-depth information regarding the solver procedures, the reader is addressed to the references given within. The second part of [Chapter 3](#) details the numerical procedure implemented for shape manipulation, an essential technique to employ shape optimisation techniques.

Inspired by an important biomimetic principle related to the configuration of the vascular network, [Chapter 4](#) presents a study which offers the ability to design microfluidic bifurcating networks that can generate well defined conditions at each consecutive generation. Initially the theoretical considerations behind the biomimetic design rule are proposed, extending the current theory to microdevice applications (that normally use rectangular channels of constant depth) for use with non-Newtonian fluids that exhibit shear-thinning and shear-thickening behaviour. The design rule is then validated by extensive three dimensional numerical simulations and the results are found to be in very good agreement with theory. A critical assessment of its capabilities and limitations is also included. This research has been published in “*Microfluidics Nanofluidics*” [28], and in the proceedings of the “*4th Micro and Nano Flows Conference*” [29].

In [Chapter 5](#), motivated by the importance of extensional dominated flows, various configurations have been optimised to provide a region of homogeneous extension rate employing the numerical codes presented in [Chapter 3](#). The configurations are separated into single-stream and multi-stream designs and are optimised based on the same demand, to produce strong extensional flows of constant strain-rate along the flow centreline. Various geometries have been considered, both in two and three dimensions, illustrating that the different dynamics affect the final shapes where a single, global solution is not achievable. The study related to the optimised configurations for the single-stream designs has been published in “*Biomicrofluidics*” [30]. A future publication which includes the optimised multi-stream designs is under preparation.

[Chapter 6](#) demonstrates the numerical implementation of a two-phase solver, built on top of the single-phase solver presented in the first part of [Chapter 3](#). The first

part of [Chapter 6](#) introduces the method considered for modelling two-phase systems as well as its advantages and limitations, followed by a detailed description of the three dimensional numerical implementation in the context of the already available single-phase solver. The last part of the chapter contains the two dimensional validation of the two-phase implementation, where a very good approximation for various benchmark cases studied is illustrated and additionally particularities of the method are discussed.

In the last chapter of this dissertation ([Chapter 7](#)), the major outcomes and the main conclusions of the work undertaken are reported, and suggestions for further investigations and future developments are discussed.

Chapter 2

Theoretical Considerations

In this introductory chapter, the fundamental differences between Newtonian and non-Newtonian fluid are highlighted and important rheological characteristics of non-Newtonian fluids are discussed. The reader is introduced to the constitutive models considered in this thesis, which are used to define the extra stress tensor in order to express mathematically a variety of different responses observed in non-Newtonian fluid flows. In addition, the set of dimensionless numbers used to categorise the flow throughout this thesis are presented and their meaning is discussed based on the underlying physics.

2.1 Fluids from “*oblivion to memory*”

Fluids exist almost everywhere in our daily life and possess a significant role that is of great and vital importance for all living organisms. Their great significance in life always intrigued and motivated scientists and engineers for acquiring a better understanding and detailed insight regarding their properties, either from a chemical or a mechanical point of view [31]. The mechanical manipulation of fluids has been essential since ancient times, with engineering achievements such as water management being substantial for human evolution and assisting in the formation of large civilisa-

tions. The first studies related to fluid mechanics date back to the times of ancient Greeks and around 250 BC, where Archimedes shouted the famous “*Ευρηκα*” (Eureka) and reported in his work “*On Floating Bodies*” the law of buoyancy. The progress in the field of fluid mechanics since then has been enormous, with various methods and models proposed for studying fluid systems of either one or more phases. The great impact of the Navier-Stokes equations on the analysis of various problems related to fluid mechanics gave rise to a massive list of scientific studies [31].

The wide diversity of fluids ranging from those with “*natural*” origin, such as water, blood, saliva and other biofluids, to those “*human made*”, like drugs, shampoo, food products and cosmetics, results in a variety of behaviours under the same flow conditions, due to the inherently different mechanical properties that arise from their individual chemical composition [31]. Based on their behaviour under shear they are classified in two major categories, which divides them into *Newtonian* and *non-Newtonian* fluids.

In 1928, Bingham and Reiner based on the motto of the Greek philosopher Heraclitus, “*Τα πάντα ρεῖ*” (everything flows), established a new scientific field named Rheology which focuses on the study of flow and deformation of non-Newtonian fluids [32]. However, in rheological studies it is common to compare the behaviour of a non-Newtonian fluid to the equivalent of a Newtonian fluid (under the same flow conditions), in order to extract important conclusions related to the properties of the former and attempt to define the underlying mechanisms that are responsible for their inherent differences. These different responses are also expressed mathematically with the inclusion of appropriate relationships that define the stress tensor, called *constitutive equations*. These equations suitably relate the stress tensor with quantities related to the deformation [33], and replace or couple the expression of the Newtonian behaviour in the equation of motion.

2.2 Constitutive models

For a fluid that is Newtonian, its resistance to the applied forces is described by the Newtonian constitutive equation:

$$\boldsymbol{\tau} = \eta \dot{\boldsymbol{\gamma}} \quad (2.1)$$

where $\boldsymbol{\tau}$ is the stress tensor, η is the dynamic viscosity (hereafter called viscosity for simplicity) of the fluid and $\dot{\boldsymbol{\gamma}} = \nabla \mathbf{u} + (\nabla \mathbf{u})^T$ is the rate-of-deformation or shear-rate tensor. This relationship states that the shear stresses are linearly proportional to the gradient of velocity, with the constant of proportionality being the shear viscosity, which gives a measure of the fluid's resistance to shear flow. For Newtonian fluids the viscosity does not depend on the shear rate.

Fluids that deviate from Newton's law of viscosity are known as non-Newtonian fluids, also called complex fluids. A wide variety of non-Newtonian fluids exists, where some of them appear to be solids but are not¹, others which display non-constant viscosity that varies with the applied force and therefore the stress tensor can no longer be expressed by the linear relationship of Eq. (2.1) (e.g. shear-thinning/thickening fluids), others which behave both as viscous fluids and as elastic solids, illustrating the existence of “*fluid memory*” to the applied deformation (e.g. polymer melts) [34]. In order for the motion of these fluids to be predicted, alternative constitutive models should be employed which either comprise, or replace the Newtonian constitutive equation completely [31, 35]. Based on the type of models and the predictions they offer, for the purposes of this work non-Newtonian fluids are subdivided in two major classes. The first follows the *generalised Newtonian fluid* (GNF) approach for which the effects of elasticity are not important. These models refer to fluids that are purely viscous but in which the viscosity is no longer constant but depends on the deformation rate.

¹In 1927 Thomas Parnell initiated the experiment known as “*Pitch drop experiment*”, in order to persuade his students that solid-like objects are actually fluids that have different properties, i.e. fluids of very high viscosities, and to highlight the importance of the timescale of observation. For achieving that, he placed inside a sealed funnel a sample of heated pitch and allowed it to rest for three years. In 1930, the neck of the sealed funnel was released and the first drop fell after eight years. Today, only nine drops have fallen and the ninth fell in 2014.

These models are able to predict the variation of viscosity and therefore the impact of this effect on the flow field. The second class considered deals with models that aim to capture the elastic behaviour of *viscoelastic fluids*, illustrating how they are influenced by the recent history of applied deformation. Viscoelastic fluids can have constant viscosity (known as Boger fluids in honour of David Boger [36]) but can also exhibit shear-thinning behaviour. Therefore, a range of models with different levels of complexity exists. Some of these models can capture only the elastic responses whereas, others are able to predict also the additional shear-thinning feature.

This chapter is not intended to be an extensive literature review on non-Newtonian constitutive models, but a brief introduction to the models used throughout this thesis, providing some insight of their capabilities and limitations.

2.2.1 Fluids without memory

The models based on the GNF approach focus on the prediction of the variation of the fluid's viscosity with shear-rate and its implications on the fluid flow behaviour. In [Fig. 2.1](#) various different behaviours of generalised Newtonian fluids are illustrated in terms of the developed shear-stress as a function of the applied shear-rate, and are juxtaposed to the expected linear response of a Newtonian fluid. More specifically, the curve labelled "*shear-thickening*" corresponds to dilatant fluids that demonstrate the ability to increase their resistance while the applied force is increased. It can be seen that the local slope of the curve, which corresponds to the fluid's viscosity, is increased as the applied shear-rate is increased. Fluids of this type are not the most common, but can describe the behaviour of concentrated suspensions, which find applications in body armour technology for example [38, 39]. The opposite behaviour is observed in fluids labelled as "*shear-thinning*", for which their viscosity, and consequently their resistance, decreases as the applied force is increased. Examples of fluids which exhibit shear-thinning behaviour include polymer solutions and blood, for which this characteristic is inherently related to its functionality and the fact that it has to travel along the entire vascular system of the human body. Finally, the last type of GNF illustrated in [Fig. 2.1](#) corresponds to fluids that act like solids when at rest, but start to flow when

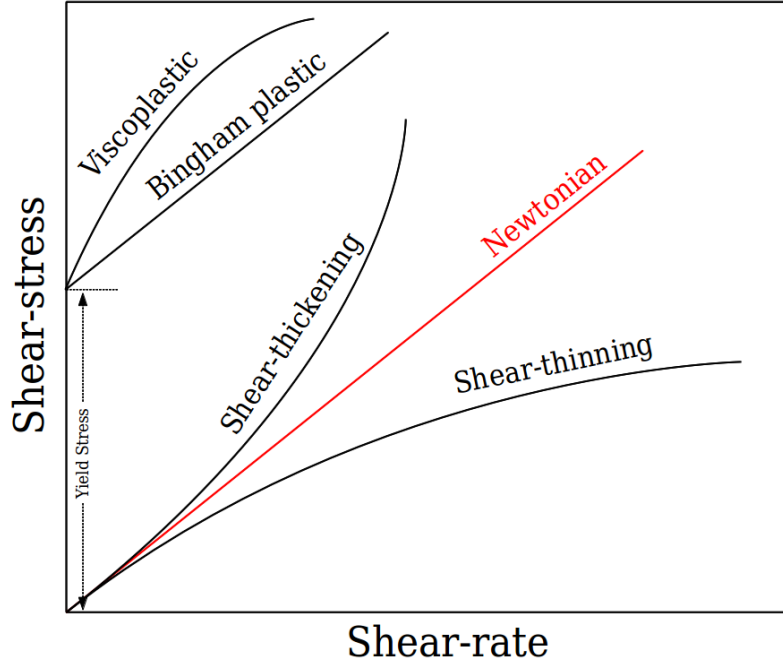


Figure 2.1. Shear-stress response with increasing shear-rate for non-Newtonian fluids described by GNF models. Adapted from White [37].

the applied stress exceeds a specific threshold value, called *yield stress*. Above the yield stress, these fluids can demonstrate either Newtonian behaviour with a shear-thinning apparent viscosity ($\tau/\dot{\gamma}$) and are labelled as “*Bingham plastics*”, or they can show shear-thinning behaviour and are labelled as “*Viscoplastic*” fluids. Examples of these types of fluids are toothpaste and mayonnaise.

The constitutive equations for all fluids mentioned so far can be expressed using a generalised approach of the Newtonian constitutive equation (Eq. (2.1)) as

$$\boldsymbol{\tau} = \eta(\dot{\gamma})\dot{\boldsymbol{\gamma}} \quad (2.2)$$

where the viscosity is now considered as a scalar function of the magnitude of the shear-rate tensor $\dot{\gamma} = |\dot{\boldsymbol{\gamma}}| = \sqrt{\frac{1}{2}(\dot{\boldsymbol{\gamma}} : \dot{\boldsymbol{\gamma}})}$, and its definition is decided by the user and the application for which is intended [34].

Arguably, one of the most famous models that can predict the variation of viscosity with the imposed shear-rate is the power-law or Ostwald de-Waele model [31, 34].

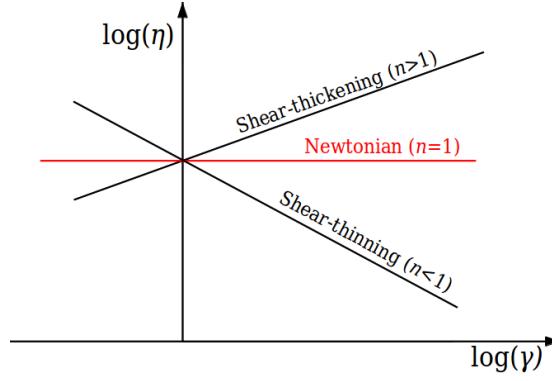


Figure 2.2. Behaviour of viscosity with shear-rate in the log-log plot for the power-law fluid.

Based on the GNF approach, viscosity is considered a function of the shear-rate and is expressed by the relationship:

$$\eta(\dot{\gamma}) = k\dot{\gamma}^{n-1} \quad (2.3)$$

where k (Pa s^n) is the consistency index that is related to the magnitude of viscosity and n is the power-law index that generates the desired behaviour. Figure 2.2 shows the $\log(\eta)$ versus $\log(\dot{\gamma})$ diagram described by Eq. (2.3). When the value of the power-law index is equal to unity, $n = 1$, the power-law model describes the Newtonian behaviour with the viscosity remaining constant independently of the applied deformation. On the other hand, when $n < 1$, the viscosity of the fluid decreases with applied shear-rate, describing fluids that exhibit shear-thinning behaviour; while for $n > 1$ the fluid becomes more viscous with increased shear-rate, describing a shear-thickening fluid.

Usually, a fitting to experimental data is performed for determining the parameters k and n of the power-law model in order to generate the correct/desired behaviour using Eq. (2.3). This empirical model has been found very useful in engineering applications due to its simplicity and the convenience provided to produce analytical expressions, and has been widely applied to investigate high shear-rate flows [34]. However, this model is limited by the inability of its parameters to be efficiently related with molecular weight and solution concentration, it does not contain any information for the elastic response of non-Newtonian fluids and fails to describe changes in the variation of viscosity for very small and large shear-rates [31].

There are various other models which follow the GNF approach [31, 33, 40]. Among

them is the Carreau-Yasuda model and the Bingham model. The first one can also predict shear-thinning and shear-thickening behaviour and contains five parameters that need to be controlled in order to evaluate the viscosity variation curve [31, 34]. In contrast to the power-law fluid, the viscosity curve predicted by the Carreau-Yasuda predicts a high and a low plateau for the shear viscosity at low and high shear-rates, respectively. The Bingham model is used for predicting the behaviour of Bingham fluids which exhibit yield stress, below which the fluid does not flow. Once the value of the yield-stress is achieved, the model predicts a linear increase of the stress with increased shear-rate, similarly to the response of a Newtonian fluid.

In the course of this thesis, only the power-law model for simplicity will be considered when dealing with inelastic non-Newtonian fluids.

2.2.2 Fluids with memory

Non-Newtonian fluids exhibit a number of impressive behaviours, which cannot be predicted by the previously presented category of GNF models. The origin of these effects is due to the existence of a partial or otherwise fading memory upon the history of the deformation [34], and the fluids of this category are known as viscoelastic fluids. Effects such as the climbing of a viscoelastic fluid on the rod that is used to stir it, known as the “*Weissenberg effect*”; the “*elastic recoil*” of a polymeric fluid in a Poiseuille flow when suddenly the flow ceases; the well known effect in the polymeric industry of the swelling of the extrudate when it exits from a die to the air, otherwise called “*Die swell*”, highlight important features related to viscoelasticity. All of them reveal the existence of normal-stresses in flows of viscoelastic fluids and the presence of a finite time, called *relaxation time*, that the fluid needs in order to relax from the effects of the applied stresses. A major difference between a viscoelastic fluid, such as a polymeric solution or melt, and a Newtonian fluid is that when the former is subjected to a shearing flow it will demonstrate a non-zero *first normal difference*, $N_1 = \tau_{11} - \tau_{22}$, and a non-zero *second normal difference*, $N_2 = \tau_{22} - \tau_{33}$ (for a Newtonian fluid $N_1 = N_2 = 0$). This means that for a polymeric liquid, together with the applied shear-stress an additional tension is applied along the streamwise direction, on account of the stretching of the

polymer molecules along the streamlines [31].

It is obvious that the category of non-Newtonian fluids includes an extensive list of fluids, which may exhibit very different behaviours. Currently, a single model is not able to describe the whole variety of different responses and a wide range of constitutive models, which include time derivatives of stress/shear-rate, is now available for modelling viscoelastic behaviour. In this thesis, the constitutive relations expressed by the Oldroyd-B and Phan-Thien and Tanner (PTT) models are considered,(cf. [Chapter 5](#)) and are presented below.

i) Upper Convected Maxwell model (UCM)

In 1867, the first empirical approach to represent viscoelasticity was mathematically presented by Maxwell in his studies related to gases [41]. His approach influenced all studies related to viscoelasticity and formed the starting point for a range of models developed subsequently, including the Oldroyd-B and the PTT models.

For a shearing flow, Maxwell suggested that fluids indicating elastic behaviour should be expressed by Newton's law of viscosity together with Hooke's law of elasticity as:

$$\tau_{21} + \frac{\eta_0}{G} \frac{\partial \tau_{21}}{\partial t} = \eta_0 \dot{\gamma}_{21} \quad (2.4)$$

where η_0 is constant viscosity parameter or zero-shear viscosity and G is the scalar constant called elastic modulus. This behaviour can be represented schematically by a combination of a dash-pot and a spring in series as shown in [Fig. 2.3](#). The dash-pot represents the resisting behaviour of the fluid due to viscous forces, whereas the spring denotes the elastic response to the applied displacement. This empirical relationship is valid only for small displacement gradients, borrowing the ability of an elastic solid to

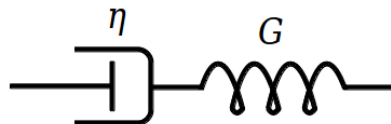


Figure 2.3. Representation of the Maxwell model as a combination of a dash-pot and a spring.

“remember” its previous state, and can be generalised in tensor form as [31, 34]:

$$\boldsymbol{\tau} + \lambda \frac{\partial \boldsymbol{\tau}}{\partial t} = \eta_0 \dot{\boldsymbol{\gamma}} \quad (2.5)$$

where $\lambda = \eta_0/G$ is the relaxation time of the fluid.

The Maxwell model is valid for time dependent flows with small displacement gradients, while at steady state reverts back to Newton’s law of viscosity ($\partial \boldsymbol{\tau} / \partial t \rightarrow 0$). Although it contains information on the history of the deformation it is not able to predict non-zero normal-stress differences in shear flows, since it is a linear model that is proportional only to the rate-of-deformation tensor, which has zero diagonal coefficients under shear flow [34]. Additionally, this model is not able to predict shear-thinning, but most importantly Eq. (2.5) is not free from superposed rotations and therefore, it is not frame invariant due to the time derivative of the stress tensor [34].

In order to surpass the invariance problem of the Maxwell tensor form, the time derivative of the stress tensor may be replaced by its *upper convected derivative* [31, 42, 43], yielding:

$$\lambda \overset{\nabla}{\boldsymbol{\tau}} + \boldsymbol{\tau} = \eta_p \dot{\boldsymbol{\gamma}} \quad (2.6)$$

where the upper convected derivative of the stress tensor is here written as in Morrison [34]:

$$\overset{\nabla}{\boldsymbol{\tau}} = \frac{\partial \boldsymbol{\tau}}{\partial t} + \mathbf{u} \cdot \nabla \boldsymbol{\tau} - (\nabla \mathbf{u})^T \cdot \boldsymbol{\tau} - \boldsymbol{\tau} \cdot \nabla \mathbf{u} \quad (2.7)$$

The viscosity notation in Eq. (2.6) was changed from η_0 to η_p , which corresponds to the polymeric viscosity. The UCM model is the simplest viscoelastic model used in rheological studies since it contains only two parameters that need to be considered, the relaxation time and the polymeric viscosity. When $\lambda = 0$, Eq. (2.6) resembles the Newtonian constitutive relation. The UCM model contains information of the stretching history and additionally is able to predict a non-zero first normal-stress difference, but it does not present shear-thinning behaviour and second normal-stress difference [34].

ii) Oldroyd-B model

After the proposal of the linear Maxwell model, other more complex models were created by considering the inclusion of other convected derivatives and non-linear strain tensors [34]. Following this approach, the Jeffreys model [31] was introduced where the time derivative of $\dot{\gamma}$ was included (compare with Eq. (2.4)):

$$\tau_{21} + \lambda \frac{\partial \tau_{21}}{\partial t} = \eta_0 \left(\dot{\gamma}_{21} + \lambda_r \frac{\partial \dot{\gamma}_{21}}{\partial t} \right) \quad (2.8)$$

where λ_r is the retardation time, a time scale that refers to the time needed for the stresses to build-up [34]. Similarly to the Maxwell model, the time derivative of the strain-rate tensor in Jeffreys model should be replaced by the convected derivative in order to become frame-invariant, resulting in the Oldroyd-B model:

$$\lambda \overset{\nabla}{\tau} + \tau = \eta_0 (\dot{\gamma} + \lambda_r \overset{\nabla}{\dot{\gamma}}) \quad (2.9)$$

The zero-shear viscosity η_0 is considered as the total viscosity, and is expressed by the sum of its two counterparts (the solvent viscosity, η_s , and the polymeric viscosity, η_p) as $\eta_0 = \eta_s + \eta_p$. This model can be schematically described as a dash-pot (solvent) in parallel with a series which contains a spring and a dash-pot (polymer), as shown in Fig. 2.4.

The stress tensor of a system described by Eq. (2.9) can therefore be expressed as

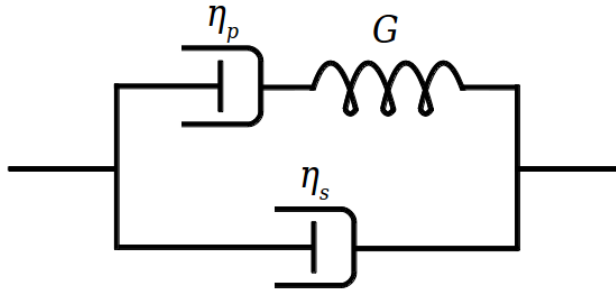


Figure 2.4. Representation of the Oldroyd-B model as a combination of a dash-pot in parallel with a dash-pot and a spring in series.

the sum of the solvent component, τ_s (Newtonian), and the polymeric component, τ_p :

$$\boldsymbol{\tau} = \boldsymbol{\tau}_s + \boldsymbol{\tau}_p \quad (2.10)$$

Using Eq. (2.10) in Eq. (2.9) and knowing that the retardation time λ_r is considered as a combination of the relaxation time, the total viscosity and the solvent viscosity, $\lambda_r = \lambda\eta_s/\eta_0$ [35, 43], it can be shown that the polymeric stress component is evaluated by:

$$\lambda \overset{\nabla}{\boldsymbol{\tau}}_p + \boldsymbol{\tau}_p = \eta_p \dot{\boldsymbol{\gamma}} \quad (2.11)$$

It is clear from Eq. (2.11) that if the solvent contributions in Eq. (2.10) are considered negligible (i.e. $\eta_s = 0$), then the Oldroyd-B model is identical to the UCM model.

Similarly to the UCM model, the Oldroyd-B model predicts non-zero first normal differences but it fails to predict second normal differences and capture the shear-thinning behaviour [31, 35]. However, it can be used for investigating the flow of polymer solutions composed of different solvent and polymer concentrations and has therefore found applications in studies related to Boger fluids [44, 45]. An important drawback of the Oldroyd-B model (as well as for the UCM model), is that in steady state elongational flows the tensile stresses can grow infinitely resulting in an extensional viscosity (η_E) that is unbounded [31, 35, 43]. In general, as is discussed by Owens and Philips [35], more complex constitutive equations for viscoelastic fluids can be considered by adding extra terms to the Oldroyd-B model.

iii) Phan-Thien and Tanner model

Inspired by the network theory of polymeric fluids, for which a polymer is represented by a network of macromolecules with strong local attractions, Phan-Thien and Tanner [46] proposed a non-linear model known as PTT that has the following general form:

$$\lambda \overset{\nabla}{\boldsymbol{\tau}}_p + f(\boldsymbol{\tau}_p) \boldsymbol{\tau}_p + \frac{\lambda \xi}{2} (\dot{\boldsymbol{\gamma}} \cdot \boldsymbol{\tau}_p + \boldsymbol{\tau}_p \cdot \dot{\boldsymbol{\gamma}}) = \eta_p \dot{\boldsymbol{\gamma}} \quad (2.12)$$

where $f(\boldsymbol{\tau}_p)$ is a function of the polymeric stress tensor that can take either a linear form [46]:

$$f(\boldsymbol{\tau}_p) = 1 + \frac{\lambda\varepsilon}{\eta_p} \text{Tr}(\boldsymbol{\tau}_p) \quad (2.13)$$

or an exponential form [47]:

$$f(\boldsymbol{\tau}_p) = \exp\left(\frac{\lambda\varepsilon}{\eta_p} \text{Tr}(\boldsymbol{\tau}_p)\right) \quad (2.14)$$

where $\text{Tr}(\boldsymbol{\tau}_p)$ is the trace of polymeric stress tensor, ξ is related to the non-affine movement of the polymeric network and provides additional information regarding the slip between the molecular network and the continuum medium [48], while ε is the extensibility parameter that affects the elongational properties of the fluid and sets an upper bound to the extensional viscosity [46, 48, 49]. The variation of the extensional viscosity is affected by the choice of $f(\boldsymbol{\tau}_p)$. When Eq. (2.13) is considered, the extensional viscosity is found to increase monotonically until it approaches a plateau value for increasing strain-rates. On the contrary, when Eq. (2.14) is employed the PTT model predicts an extensional viscosity that attains a maximum value and then decreases to a plateau for increasing strain-rates [50].

The studies performed here consider that $\xi = 0$, which corresponds to the simplified version of the PTT model:

$$\lambda \overset{\nabla}{\boldsymbol{\tau}}_p + f(\boldsymbol{\tau}_p) \boldsymbol{\tau}_p = \eta_p \hat{\boldsymbol{\gamma}} \quad (2.15)$$

Moreover, when $\varepsilon = 0$ and $\xi = 0$, Eq. (2.15) reduces to the Oldroyd-B model. Additionally, if $\eta_s = 0$ then the UCM model is recovered.

The advantage of the PTT model over the Oldroyd-B and the UCM models is that it is able to predict shear-thinning behaviour in both its forms (Eq. (2.12) or Eq. (2.15)). Moreover, in its full version ($\xi \neq 0$) it is able to capture non-zero first and second normal differences, whereas in its simplified version predicts only a first normal difference [48, 49]. Table 2.1 compares the various models discussed in terms of the parameters required and their capabilities and limitations.

Table 2.1. Comparison between the various models discussed.

Model	η_s	λ	ε	ξ	η_p	N_1	N_2	η	η_E
Newtonian	✓	0	0	0	0	0	0	C	$\alpha\eta$
UCM	0	✓	0	0	✓	✓	0	C	U
Oldroyd-B	✓	✓	0	0	✓	✓	0	C	U
simplified PTT	✓	✓	✓	0	✓	✓	0	St	B
PTT	✓	✓	✓	✓	✓	✓	✓	St	B

C Constant

B Bounded

U Unbounded

St Shear-thinning

α For uniaxial extensional flow $\alpha=3$, For planar extensional flow $\alpha=4$

2.3 Dimensionless groups

In the following chapters various dimensionless quantities are used. These include dimensionless numbers related to geometrical scaling, and dimensionless numbers which provide meaningful insight into different physical mechanisms, important for the flows considered in this work.

i) Reynolds number

The *Reynolds number* (Re) is an ubiquitous dimensionless number used in fluid dynamics and for Newtonian fluid flows it is used to provide important information regarding the flow regime. The Reynolds number gives a measure between inertial and viscous forces:

$$\text{Re} = \frac{\text{inertial forces}}{\text{viscous forces}} = \frac{\rho UL}{\eta} \quad (2.16)$$

where U is the characteristic velocity of the fluid and L is the characteristic dimension. Depending on the problem, appropriate quantities for U and L are chosen. For non-Newtonian fluids where the shear viscosity is not constant, modifications are applied to the Reynolds number definition, as it will be discussed in [Chapter 4](#) where flows of power-law fluids are considered.

ii) Deborah number

The rheological behaviour of non-Newtonian fluids with viscoelastic behaviour cannot be described by the Reynolds number alone and additional dimensionless numbers need to be defined. One of such dimensionless numbers is called the *Deborah number* (De) and was introduced in 1964 by Reiner [\[32\]](#). Inspired by the words of Prophetess Deborah “*The mountains flowed before the Lord*” he defined De as

$$\text{De} = \frac{\text{time of relaxation}}{\text{time of observation}} = \frac{\lambda}{t_{flow}} \quad (2.17)$$

Literally, Deborah number links to Heraclitus belief that everything flows given an appropriate time scale of the observer. Following Bird *et al.* [\[31\]](#), the two limiting cases

for De are evident. If $De \rightarrow 0$, then the flow of the polymer is qualitatively similar to that of a Newtonian fluid ($\lambda \simeq 0$), since the polymer molecules are more or less in their equilibrium state. Conversely, if the experiment happens very fast, $De \rightarrow \infty$, then the polymer molecules will not have enough time to change configuration and the fluid will behave similarly to a Hookean solid. The time of observation is usually related to the characteristic time of deformation and therefore various definitions can be used, generalised as:

$$De = \frac{\lambda U}{L} \quad (2.18)$$

where U/L defines the characteristic deformation.

As pointed out by Poole [51], considering that in fully developed flows or viscometric flows, such as steady shear, the deformation process becomes infinite then from the original definition given in Eq. (2.17) one can state that De is zero. It is therefore suggested the inclusion of an additional dimensionless group for characterising the effects of viscoelasticity.

iii) **Weissenberg number**

The dimensional analysis performed by White [52] considering a second order fluid, gave rise to three dimensionless numbers. The ubiquitous Reynolds number, a viscoelastic ratio number related to the higher order terms of the kinematic tensor for the second order fluid and the *Weissenberg number* (Wi). Bird *et al.* [31], also pointed the existence of more than two characteristic numbers for some flow problems, the Weissenberg number being one of them.

Various discussions have taken place in the field of Rheology about the correct use of De and Wi [51, 53, 54]. Based on the derivation of White [52], Poole [51] rationalised the significance of addressing the Weissenberg number, as a characteristic quantity that represents the ratio between elastic and viscous forces:

$$Wi = \frac{\text{elastic forces}}{\text{viscous forces}} = \lambda \dot{\gamma} \quad (2.19)$$

As such, it has been argued that Wi is appropriate for characterising the viscoelastic

effects of the fluid and De is appropriate for categorising unsteady viscoelastic fluid flows [51].

***iv)* Elasticity number**

Although for the majority of viscoelastic fluid flows at the microscale inertial effects are usually small, the *Elasticity number* (El) is used to indicate the balance between inertial and elastic forces and is defined as the ratio of the Weissenberg number to the Reynolds number:

$$\text{El} = \frac{\text{elastic forces (Wi)}}{\text{inertial forces (Re)}} = \frac{\lambda\eta}{\rho L^2} \quad (2.20)$$

It is interesting to note that El is independent of the kinematics and depends only on the geometric and fluid properties. The benefits of using microfluidic devices with complex, non-Newtonian fluids is clear from a careful analysis of the relevant dimensionless numbers. Small Reynolds numbers are easily achieved at these scales, where at the same time the generated deformations are large as discussed in [Chapter 1](#). Consequently, high De and Wi can be attained, leading to high elasticity numbers and providing the ability to investigate elastic-driven effects associated with viscoelastic fluid flows [9, 10].

***v)* Capillary number**

When investigating multiphase flow problems, one of the most commonly met dimensionless number² is the *capillary number* (Ca). It is employed to provide a measurement of the balance between viscous forces and capillary stresses (surface tension forces) [55, 56], defined as

$$\text{Ca} = \frac{\text{viscous forces}}{\text{capillary stresses}} = \frac{\eta U}{\sigma} \quad (2.21)$$

²The complexity of multiphase flows has as result a variety of dimensionless numbers that are responsible for reporting the balance between existing forces (gravity, inertial, etc). In this thesis only the ones used are reported.

where σ is the surface tension coefficient. As mentioned in [Chapter 1](#), in microfluidic flows viscous forces are usually considered greater than inertial forces. Hence, the importance of this dimensionless number when investigating multiphase two-phase flows in microfluidic configurations is apparent.

vi) Atwood number

The *Atwood number* (At) is a dimensionless number that is usually employed when investigating the occurrence of instabilities across the interface of two fluids, due to the differences between their densities [\[55\]](#) (cf. Rayleigh-Taylor instability in [Section 6.4](#)), and is defined as

$$\text{At} = \frac{\rho_A - \rho_B}{\rho_A + \rho_B} \quad (2.22)$$

where ρ_A is the density of the heavier fluid and ρ_B the density of the lighter fluid.

vii) Cahn number

In [Chapter 6](#) the implementation and validation of a two-phase solver based on the Phase Field method and the Cahn-Hilliard equation is discussed. As it will be shown, for this approach the interface thickness between the fluid phases needs to be specified. A dimensionless number that relates the length of the interface thickness to the characteristic length scale of the problem under investigation is the *Cahn number* (Cn) [\[57, 58\]](#):

$$\text{Cn} = \frac{\epsilon}{L} \quad (2.23)$$

where ϵ is the imposed interface thickness. The desired condition is $\text{Cn} \rightarrow 0$ in order to approach the sharp interface limit.

“If I have seen further it is by standing on the shoulders of giants..”

I. Newton

Chapter 3

Numerical Techniques

In this chapter, a description of the in-house single phase solver used for the computational fluid dynamics simulations conducted in the context of the present thesis is discussed together with the mesh deformation code that was implemented for manipulating the computational grids. The chapter is divided in two parts. In the first part, the numerical procedure employed for discretising the equations of motion in order to study numerically the flow of Newtonian and non-Newtonian fluids is outlined. The reader is introduced to the Finite Volume method and to important modifications related to the use of a collocated grid arrangement. Some additional important characteristics of the current solver are discussed as these are the basis for the code development for multiphase flows discussed in [Chapter 6](#). The second part describes the theoretical background of a mesh deformation technique that was borrowed from computer graphics, and which was implemented in order to manipulate the numerical grids generated by a basic mesh generator, offering the ability to perform shape optimisation studies.

3.1 Introduction

In the field of computational fluid dynamics (CFD), the numerical investigation of fluid flows and relevant phenomena presented in [Chapter 2](#) requires the appropriate treatment of the governing partial differential equations which principally depends on the *discretisation* method considered. In CFD, a variety of numerical methods are used for discretising the equations of motion. Arguably, the most important and most frequently used are the Finite Differences (FD), the Finite Volumes (FV) and the Finite Elements (FE) methods. These methods are strongly influenced by the *numerical grid*, which consists of a discrete representation of the physical domain under investigation and can be either *structured* or *unstructured*.

Briefly, the FD methods have been widely used in the past because of their inherent ability to be easily applied to any type of numerical grids used [59]. The transformation of the partial differential equations, is done by simply applying Taylor expansion series at the nodes of the numerical grid. The FV methods consider the numerical grid to be composed by finite numerical cells, commonly referred to as *control-volumes*, which comprise a specific volume. The equations describing the problem of interest are integrated over each control volume, and then based on Gauss's theorem are transformed into algebraic equations between adjacent control-volume centres, where all values need to be calculated [59, 60]. Additionally, their inherent conservation properties due to the requirement for evaluating volume fluxes and other variables on the faces of each control-volume, make them suitable for a great range of applications investigated with numerical simulations [61]. Finally, the FE methods consider control-elements similar to control-volumes. For two dimensions (2D) the control-elements usually have triangular or quadrilateral shapes, whereas in three dimensions (3D) they assume the shape of tetrahedra, bricks or prisms [59]. In each of the control-elements, the so-called *shape-functions* are employed for approximating the numerical solution. These functions are usually linear or quadratic polynomials and fulfil specific requirements depending on the problem solved [62, 63]. Together with a set of weighting functions, the shape-functions are integrated in the global domain, resulting in a set of algebraic equations

that describes the problem of interest [64]. Here, the FV method is considered and all the terms of the equations describing the problems studied are discretised in this way.

This chapter is organised as follows. In [Section 3.2](#), the transformation from the Cartesian orthogonal system to a generalised coordinate system is presented. Furthermore, the discretisation of the equations of motion for the in-house single-phase CFD solver, appropriate for viscoelastic fluid flows, is discussed in [Section 3.3](#). It is mentioned that the single phase solver is later upgraded to consider elements of a second phase using the Phase Field method and is presented analytically in [Chapter 6](#). The basic considerations introduced here are then employed for the implementation of the two phase solver. In [Section 3.4](#), an overview of the implemented mesh deformation code used for the shape optimisations studies discussed in [Chapter 5](#), is presented.

3.2 Generalised Coordinates

Engineering applications make use of geometrical configurations that often have complex shapes better described by curves rather than linear, orthogonal shapes. The numerical study of flows inside or around these geometries, requires the solution of the appropriate set of equations using the numerical grid which discretises the physical object. Therefore, the use of a Cartesian coordinate system for expressing the derivatives of scalar, vector or tensor quantities may be insufficient and the transformation into a generalised non-orthogonal coordinate system is preferred [65].

The very well known Cartesian system (physical system) is described by the orthogonal basis written in vector form as $\mathbf{x}=(x_1, x_2, x_3)$, where the indices $i = 1, 2, 3$ correspond to each one of the three directions. Similarly, a generalised coordinate system is described by the basis $\boldsymbol{\xi}=(\xi_1, \xi_2, \xi_3)$, which is not necessarily orthogonal. When the Cartesian coordinate system is transformed into the generalised coordinate system, $\boldsymbol{\xi}=\boldsymbol{\xi}(\mathbf{x})$, every coordinate of the latter is expressed as a function of the former. The differential of the new coordinate system gives:

$$d\xi_i = \frac{\partial \xi_i}{\partial x_1} dx_1 + \frac{\partial \xi_i}{\partial x_2} dx_2 + \frac{\partial \xi_i}{\partial x_3} dx_3 \quad (3.1)$$

or in Einstein notation:

$$d\xi_i = \frac{\partial \xi_i}{\partial x_j} dx_j \quad (3.2)$$

where the repeated indices $j = 1, 2, 3$ indicate the summation of the terms. [Equations \(3.1\)](#) and [\(3.2\)](#) can also be presented in matrix format:

$$\begin{bmatrix} d\xi_1 \\ d\xi_2 \\ d\xi_3 \end{bmatrix} = \underbrace{\begin{bmatrix} \frac{\partial \xi_1}{\partial x_1} & \frac{\partial \xi_1}{\partial x_2} & \frac{\partial \xi_1}{\partial x_3} \\ \frac{\partial \xi_2}{\partial x_1} & \frac{\partial \xi_2}{\partial x_2} & \frac{\partial \xi_2}{\partial x_3} \\ \frac{\partial \xi_3}{\partial x_1} & \frac{\partial \xi_3}{\partial x_2} & \frac{\partial \xi_3}{\partial x_3} \end{bmatrix}}_{\Xi} \begin{bmatrix} dx_1 \\ dx_2 \\ dx_3 \end{bmatrix} \quad (3.3)$$

Considering now the inverse transformation from the generalised coordinate system into the physical coordinates, $\mathbf{x}=\mathbf{x}(\boldsymbol{\xi})$, the equivalent relationship in Einstein notation is

$$dx_i = \frac{\partial x_i}{\partial \xi_j} d\xi_j \quad (3.4)$$

and in matrix form:

$$\begin{bmatrix} dx_1 \\ dx_2 \\ dx_3 \end{bmatrix} = \underbrace{\begin{bmatrix} \frac{\partial x_1}{\partial \xi_1} & \frac{\partial x_1}{\partial \xi_2} & \frac{\partial x_1}{\partial \xi_3} \\ \frac{\partial x_2}{\partial \xi_1} & \frac{\partial x_2}{\partial \xi_2} & \frac{\partial x_2}{\partial \xi_3} \\ \frac{\partial x_3}{\partial \xi_1} & \frac{\partial x_3}{\partial \xi_2} & \frac{\partial x_3}{\partial \xi_3} \end{bmatrix}}_X \begin{bmatrix} d\xi_1 \\ d\xi_2 \\ d\xi_3 \end{bmatrix} \quad (3.5)$$

where $J = \det(X)$, is the Jacobian of the transformation. In order for [Eqs. \(3.3\)](#) and [\(3.5\)](#) to be valid, the derivative matrices should satisfy the relationship $\Xi = (X)^{-1}$. Therefore, the elements of matrix Ξ are related to the elements of X by the following:

$$\Xi_{ij} = \frac{(-1)^{i+j} M_{ji}}{J} \quad (3.6)$$

where M_{ji} is the minor determinant of X . The numerator of the fraction in the right-hand side of [Eq. \(3.6\)](#) is the so called cofactor:

$$\beta^{ij} = (-1)^{i+j} M_{ji} \quad (3.7)$$

Using [Eqs. \(3.6\)](#) and [\(3.7\)](#) and following Oliveira [\[66\]](#) and Ferzinger and Perić [\[59\]](#), the

required transformation rules for the time and space derivatives are:

$$\frac{\partial}{\partial t} = \frac{1}{J} \frac{\partial}{\partial t} J \quad (3.8)$$

$$\frac{\partial}{\partial x_j} = \frac{\partial}{\partial \xi_l} \frac{\partial \xi_l}{\partial x_j} = \frac{1}{J} \frac{\partial}{\partial \xi_l} \beta^{lj} \quad (3.9)$$

An illustrative example of the transformation rule is applied on the generalised transport equation of a dependent variable ϕ , expressed in Einstein notation, for the Cartesian coordinate system:

$$\frac{\partial}{\partial t}(\rho\phi) + \frac{\partial}{\partial x_j}(\rho u_j \phi) = \frac{\partial}{\partial x_j}(\Gamma \frac{\partial \phi}{\partial x_j}) + S_\phi \quad (3.10)$$

where u_j denotes the velocity along each direction, ρ is the density, Γ is the general diffusion coefficient and S_ϕ corresponds to the added sources. Applying the transformation rules, Eq. (3.10) can be expressed in generalised coordinates as

$$\frac{\partial}{\partial t}(J\rho\phi) + \frac{\partial}{\partial \xi_l}(\rho u_j \phi \beta^{lj}) = \frac{\partial}{\partial \xi_l} \left(\frac{\Gamma}{J} \frac{\partial \phi}{\partial \xi_m} \beta^{mj} \right) + JS_\phi \quad (3.11)$$

3.3 Single phase solver

The in-house CFD solver used for the numerical studies in [Chapters 4](#) and [5](#), is applicable for single-phase, incompressible and isothermal flows for Newtonian and non-Newtonian fluids, and is briefly discussed here. This numerical approach has been extensively validated both in studies of Newtonian and non-Newtonian, viscoelastic fluid flows and its great performance can be attested by the quality of results in various scientific publications [[27](#), [28](#), [67–79](#)]. The principles of the solver implementation were first discussed in Pinto [[80](#)] and then have been updated and thoroughly discussed in Oliveira [[66](#)], Oliveira *et al.* [[27](#)], Oliveira and Pinho [[49](#)] and in Alves [[65](#)]. Since the single-phase solver was further upgraded during the present work to include a second phase as discussed in [Chapter 6](#), only a brief description of the major parts of the implementation is presented here for completeness and for introducing to the finite volume discretisation method followed.

3.3.1 Governing equations

The basic set of equations used for investigating the motion of a Newtonian or a non-Newtonian fluid has been presented theoretically in [Chapter 2](#). Since the general coordinates are adopted, the transformation of the equations of motion to the new system is provided here. Using the transformation rules described by [Eqs. \(3.8\)](#) and [\(3.9\)](#), the continuity equation for an incompressible fluid is expressed as

$$\frac{\partial}{\partial \xi_l}(\rho u_i \beta^{li}) = 0 \quad (3.12)$$

and in a similar manner, the momentum equation is given by

$$\frac{\partial}{\partial t}(J \rho u_i) + \frac{\partial}{\partial \xi_l}(\rho u_j u_i \beta^{lj}) = -\frac{\partial}{\partial \xi_l}(p \beta^{li}) + \frac{\partial}{\partial \xi_l}(\beta^{lj} \tau_{ij}) + J \rho g_i \quad (3.13)$$

where, τ_{ij} corresponds to the total stress tensor and is evaluated by the sum of the polymeric and the Newtonian stresses (cf. [Eq. \(2.10\)](#)):

$$\tau_{ij} = \tau_{p,ij} + \tau_{s,ij} \quad (3.14)$$

To complete the set of equations an appropriate constitutive equation for the extra stress tensor in [Eq. \(3.13\)](#) needs to be added for each particular case studied, as discussed in [Chapter 2](#). For this brief description of the implementation, the simplified-PTT fluid is considered (cf. [Section 2.2.2](#)) and is expressed in generalised coordinates:

$$\begin{aligned} \lambda \frac{\partial}{\partial t}(J \tau_{p,kk}) + J f(\tau_{p,kk}) \tau_{p,ij} + \lambda \frac{\partial}{\partial \xi_l}(u_k \beta^{lk} \tau_{p,ij}) = \lambda \left[\frac{\partial}{\partial \xi_l}(u_j \beta^{lk} \tau_{p,ik}) + \right. \\ \left. \frac{\partial}{\partial \xi_l}(u_i \beta^{lk} \tau_{p,kj}) \right] + \eta_p \left[\frac{\partial}{\partial \xi_l}(u_i \beta^{lj}) + \frac{\partial}{\partial \xi_l}(u_j \beta^{li}) \right] - \frac{2}{3} \eta_p \frac{\partial}{\partial \xi_l}(u_k \beta^{lk} \delta^{ij}) \end{aligned} \quad (3.15)$$

where the stress function, $f(\tau_p)$, is expressed by the linear version:

$$f(\tau_{p,kk}) = 1 + \frac{\lambda \varepsilon}{n_p} \tau_{p,kk} \quad (3.16)$$

As explained in Oliveira [27], for numerical simulations with the FV method the diffusion term in the momentum equation has the important role to promote stability. In the generalised form of the momentum equation, the ordinary diffusion term does not appear explicitly and thus, it was included in both sides of Eq. (3.13), to enhance stability:

$$\begin{aligned} \frac{\partial}{\partial t}(J\rho u_i) + \frac{\partial}{\partial \xi_l}(\rho u_j u_i \beta^{lj}) - \frac{\partial}{\partial \xi_l}\left(\frac{\eta}{J} \frac{\partial u_i \beta^{lj} \beta^{lj}}{\partial \xi_l}\right) = \\ - \frac{\partial}{\partial \xi_l}(p\beta^{li}) + \frac{\partial}{\partial \xi_l}(\beta^{lj} \tau_{ij}) + J\rho g_i - \frac{\partial}{\partial \xi_l}\left(\frac{\eta}{J} \frac{\partial u_i \beta^{lj} \beta^{lj}}{\partial \xi_l}\right) \end{aligned} \quad (3.17)$$

where, η is the total viscosity of the fluid, $\eta = \eta_s + \eta_p$. The indices l of the cofactors of the ordinary diffusion terms do not indicate summation over the terms, but rather the direction of the derivative for the generalised coordinate. The term in the left hand side (LHS) of the equation is treated implicitly whereas the term on the right hand side (RHS) is treated explicitly, with both being mutually cancelled when the steady state solution is attained.

3.3.2 Control volume discretisation

In the control volume formulation the locations of both the volume centres and the centres of the volume faces are employed for the discretisation. Adopting the usual notation, the cell under investigation is named “P” and its neighbours are called based on their orientation relevant to the interrogated cell centre as “E” (east), “W” (west), “N” (north), “S” (south), “T” (top) and “B” (bottom). Following the same notation, the faces of the examined control volume are expressed with the small letters e , w , n , s , t and b .

There are two common different approaches that depend on the arrangement of the grid and which consequently affect the discretisation procedure. These arrangements of the numerical mesh are the *staggered* arrangement and the *collocated* arrangement [59]. When staggered grids are employed, the vector quantities such as velocities, are evaluated at the faces of the control volumes and scalar variables such as pressure and temperature, are evaluated at the cell centres as shown in Fig. 3.1a. Conversely,

when the collocated arrangement is considered both the scalar and vector quantities are evaluated at the cell centres as shown in Fig. 3.1b.

The arrangement of the staggered grid was widely used in the past since it was providing a strong coupling between the velocities and the pressure gradients [59]. Using this arrangement it was illustrated by Patankar [60], that the generation of a possible checkerboard pattern for the pressure field could be completely avoided, in contrast to the regular collocated approach. Based on the configuration of the staggered arrangement, Patankar and Spalding [81] introduced the Semi-Implicit Method for Pressure Linked Equations (SIMPLE), a powerful procedure that couples effectively the pressure gradients evaluated through the continuity equation with the velocities calculated from momentum equation. After the pioneering work of Patankar and Spalding [81], similar procedures, which are improvements of SIMPLE, have been suggested and can be found in many textbooks related to the Finite Volume discretisation method [59–61, 64]. In this work, the SIMPLEC procedure, introduced by Van Doormal and Raithby [82], is considered and is discussed in Section 3.3.6.

Although staggered grids are powerful and widely applied, their use is limited to Cartesian systems [59, 83, 84]. When the geometry is complex, as in the majority of the

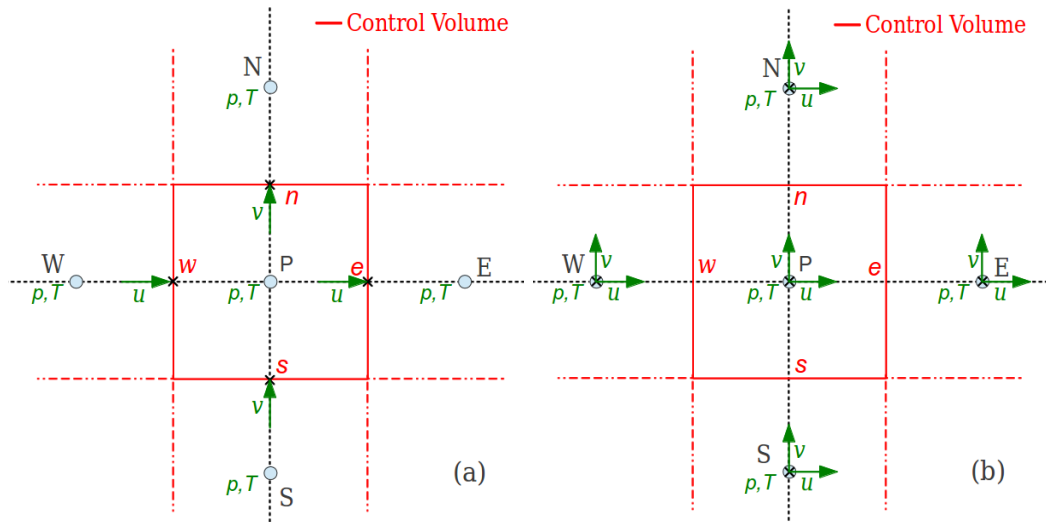


Figure 3.1. Types of grid arrangement in control volume formulation, (a) staggered grid and (b) collocated grid.

engineering applications, staggered grids are problematic. Coordinate transformation is not easily applied because of the increased number of interpolations that need to be performed in order to achieve good resolution [59,61]. Another important consequence of the staggered grids usage is the large needs of computational memory, since the appropriate information for each of the velocity components and the scalar variables needs to be stored at different locations [61]. This obviously becomes more demanding when dealing with 3D flows. On the other hand, collocated grids are easily transferred in a generalised coordinate system and the drawback of the possible checkerboard pattern for the pressures is surpassed with the Rhie-Chow interpolation scheme [85], which enables the use of SIMPLE and its descendants for coupling the pressure and velocity field. All these facts made collocated grids the standard approach nowadays when using Finite Volume methods, and the same arrangement is adopted here.

The partial differential equations that describe the problem under consideration are integrated over each control volume P (cf. Fig. 3.1b), and together with the use of Gauss theorem the discretised expressions are produced [59,60]. The set of the governing equations solved by the CFD solver consists of the continuity equation (Eq. (3.12)), the momentum equation (Eq. (3.17)) and the appropriate constitutive relation for the stresses (Eq. (3.15)). Since the discretisation of these equations does not consist an original work of the author of this thesis, only some important issues related to the the discretisation of the continuity and the momentum equations are mentioned here, in order to introduce to the reader the notation adopted in the two-phase implementation presented in Chapter 6. The discretisation of the terms of the stress constitutive equation is not shown and details can be found in Oliveira *et al.* [27] and in Alves [65].

i) Continuity discretisation

Expanding the generalised differential form of the continuity equation to all terms, Eq. (3.12) is written as

$$\begin{aligned} \frac{\partial}{\partial \xi_1} (\rho u_1 \beta^{11} + \rho u_2 \beta^{12} + \rho u_3 \beta^{13}) + \frac{\partial}{\partial \xi_2} (\rho u_1 \beta^{21} + \rho u_2 \beta^{22} + \rho u_3 \beta^{23}) \\ + \frac{\partial}{\partial \xi_3} (\rho u_1 \beta^{31} + \rho u_2 \beta^{32} + \rho u_3 \beta^{33}) = 0 \end{aligned} \quad (3.18)$$

Following the standard procedure, Eq. (3.18) is integrated over the control volume P and together with the use of Gauss's theorem ¹ can be re-written as

$$\begin{aligned} & \left(\rho u_1 \beta^{11} A + \rho u_2 \beta^{12} A + \rho u_3 \beta^{13} A \right)_w^e + \left(\rho u_1 \beta^{21} A + \rho u_2 \beta^{22} A + \rho u_3 \beta^{23} A \right)_s^n \\ & + \left(\rho u_1 \beta^{31} A + \rho u_2 \beta^{32} A + \rho u_3 \beta^{33} A \right)_b^t = 0 \end{aligned} \quad (3.19)$$

where A corresponds to the surface area of each particular face. The terms in the brackets, represent the mass flow rates which enter and exit the control volume. Considering as an example the integral at the east face, the component, F_e , of the mass flow rate \mathbf{F} , normal to the east face is expressed as

$$F_e = \rho_e A_e (u_1 \beta^{11} + u_2 \beta^{12} + u_3 \beta^{13})_e \quad (3.20)$$

or²

$$F_e = \rho_e (u_1 b^{11} + u_2 b^{12} + u_3 b^{13})_e \quad (3.21)$$

similar expressions are employed at the w , n , s , t and b faces. Hence, as explained in Oliveira [66] and in Oliveira *et al.* [27], Eq. (3.19) can be expressed in a compact form:

$$\sum_{f=1}^6 \left(\sum_i \rho \tilde{u}_{i,f} b_f^{fi} \right) = \sum_{f=1}^6 F_f = 0 \quad (3.22)$$

where $f = 1, 2$ or 3 corresponds to each direction and denotes values that are evaluated at the faces, f . The additional notation $\tilde{u}_{j,f}$ indicates that Rhie and Chow [85]

¹Also referred to as the divergence theorem:

$$\int_V \nabla \cdot \mathbf{F} dV = \int_S \mathbf{F} \cdot \mathbf{n} dS$$

² As explained in Peric [86], the variables b^{li} are evaluated from the product $b_{li} = \beta^{li} A_f$ where f indicates the appropriate face. As an example:

$$\beta_e^{11} A_e = \frac{1}{\delta \xi_2 \delta \xi_3} \left(\delta(x_2)_2 \delta(x_3)_3 - \delta(x_3)_2 \delta(x_2)_3 \right) \delta \xi_2 \delta \xi_3 = b^{11}$$

with $\delta(x_k)_m$ referring to the variation of coordinate k along the direction m .

interpolation scheme is employed [27], which is discussed in [Section 3.3.5](#).

ii) Momentum discretisation

The same procedure as in the discretisation of continuity is applied, where each of the terms in [Eq. \(3.17\)](#) is integrated over a control volume as presented above. The terms on the LHS of the generalised equation are treated implicitly, whereas the terms on the RHS are all evaluated as sources and treated explicitly.

• **Inertia term**

The integration of the inertia term results in:

$$\int_{V_P} \frac{\partial}{\partial t} (J\rho u_i) dV_P = \left(\frac{u_i^{(n)} - u_i^{(n-1)}}{\Delta t} \right)_P \rho_P V_P \quad (3.23)$$

where a first order scheme is applied for discretising the time derivative. The index n indicates the current time level and has not been included in the terms discussed next. For the discretisation, the relationship $J\delta\xi^1\xi^2\xi^3 = \delta V$ was employed [59].

• **Convection term**

The integration of the convective term results in:

$$\int_{V_P} \frac{\partial}{\partial \xi_i} (\rho u_j u_i \beta^{lj}) dV_P = \sum_{f=1}^6 \left(\sum_j \rho u_{j,f} b_f^{lj} \hat{u}_{i,f} \right) = \sum_{f=1}^6 F_f \hat{u}_{i,f} \quad (3.24)$$

where \hat{u} is the convection velocity and F_f corresponds to the mass flow rate component at each cell face. In the control volume formulation it is known that the central difference scheme for discretising the convected variable is not appropriate [59, 60]. Therefore, the different notation \hat{u} , is used for indicating that this term is evaluated using different differencing schemes as will shown in [Section 3.3.3](#).

• **Ordinary diffusion term**³

The ordinary diffusion term, acting at the normal direction of the faces is discretised as follows:

$$\int_{V_P} \frac{\partial}{\partial \xi_l} \left(\frac{\eta}{J} \frac{\partial u_i \beta^{lj} \beta^{lj}}{\partial \xi_l} \right) dV_P = \sum_{f=1}^6 \left[\frac{\eta_f}{V_f} \left(\sum_j b_f^{lj} b_f^{lj} \right) [\Delta u_i]_f^f \right] \begin{cases} \text{LHS: as is} \\ \text{RHS} \rightarrow S_{u_i-\text{diffusion}} \end{cases} \quad (3.25)$$

where V_f is a face pseudo-volume [27, 66]. In Eq. (3.17), the term on the LHS is added in the resulting coefficients of the discretisation and the term on the RHS is accounted in the source term.

- **Pressure gradient term**⁴

The discretised pressure gradient term is expressed as:

$$\int_{V_P} \frac{\partial}{\partial \xi_l} (p \beta^{li}) dV_P = \sum_{l=1}^3 b_f^{li} [\Delta p]_l^P \rightarrow S_{u_i-\text{pressure}} \quad (3.26)$$

The contribution of the pressure gradients is added at the sources of the momentum equation.

- **Stress divergence term**

The stress tensor is evaluated from the appropriate constitutive equation and is discretised in the momentum equation as

$$\int_{V_P} \frac{\partial}{\partial \xi_l} (\beta^{lj} \tau_{ij}) dV_P = \sum_{f=1}^6 b_f^{fj} \tilde{\tau}_{ij,f} \rightarrow S_{u_i-\text{stress}} \quad (3.27)$$

The approach followed is similar to the velocity discretisation applied for the continuity equation Eq. (3.22). The stresses need to be evaluated at the faces of the control volumes and the symbol $\tilde{\tau}_{ij,f}$ indicates that a special interpolation technique is employed. As discussed in detail in Oliveira *et al.* [27], the use of a linear interpolation scheme

³ In Oliveira *et al.* [27] the notation $[\Delta \Phi]_f^f = \Phi_F - \Phi_P$ corresponds to the evaluation of the derivative at the face f, considering the cell centre P and its neighbour F along the direction of the derivative.

⁴ In Oliveira *et al.* [27] the notation $[\Delta \Phi]_f^P = \Phi_{f^+} - \Phi_{f^-}$ corresponds to the evaluation of the derivative at the cell centre P, using the values at the faces f^+ and f^- of the control volume along the positive and negative directions of the desired derivative.

between the cell-centre values for the evaluation of the stresses at the faces, may result in a lack of connectivity between the stresses and the velocity field. It was illustrated that a checkerboard pattern of the velocity field, may result in the correct field for the stresses. Therefore, the use of a special interpolation scheme was suggested in the same manner as Rhie and Chow interpolation [85] is used for coupling the velocity and pressure fields. The use of this scheme results in the coupling between the two fields since the face stresses are also coupled to the velocities at the cell centres.

- **Gravity term**

The discretisation of the momentum is completed with the discretised gravity terms:

$$\int_{V_P} J \rho g_i dV_P = V_P \rho g_i \rightarrow S_{u_i-\text{gravity}} \quad (3.28)$$

The gravity terms are added to the sources as done previously for all terms in the RHS of Eq. (3.17).

The form of the final numerical system that needs to be solved after all terms are discretised, has a linear algebraic form and is described in many textbooks related to Finite Volumes [59–61, 64]. As illustrated in Oliveira *et al.* [27], the numerical scheme for the momentum equation is completed by gathering all above discretised terms and solving numerically the system:

$$a_P u_{i,P} - \sum_F a_F u_{i,F} = S_{u_i} + \frac{\rho V_P}{\Delta t} u_{i,P}^{(n-1)} \quad (3.29)$$

where the coefficient a_P contains the contributions from all its neighbours and the previous time step:

$$a_P = \sum_F a_F + \frac{\rho V_P}{\Delta t} \quad (3.30)$$

The coefficients a_F , contain the convection and diffusion contributions a_F^C and a_F^D for the neighbour cells, with the former depending on the direction of the flow:

$$a_F = a_F^C + a_F^D \quad \text{where} \quad \begin{cases} a_F^C = +F_f \text{ for } f^- \\ a_F^C = -F_f \text{ for } f^+ \end{cases} \quad (3.31)$$

Finally, the total source term S_{u_i} holds the contribution from all the sources discussed above:

$$S_{u_i} = S_{u_i\text{-pressure}} + S_{u_i\text{-stress}} + S_{u_i\text{-gravity}} + S_{u_i\text{-diffusion}} \quad (3.32)$$

Following a similar procedure, the constitutive equation for the stresses (Eq. (3.15)) is discretised, which can be found in detail in Alves [65] and therefore is not repeated here. After all terms are discretised, the algebraic equation that needs to be solved for evaluating the stresses, is represented in a similar way as Eq. (3.29) :

$$a_{\text{P}}^{\tau} \tau_{ij,\text{P}} - \sum_{\text{F}} a_{\text{F}}^{\tau} \tau_{ij,\text{F}} = S_{\tau_{ij}} + \frac{\lambda_{\text{P}} V_{\text{P}}}{\Delta t} \tau_{ij,\text{P}}^{(n-1)} \quad (3.33)$$

3.3.3 Schemes for convection

The discretised form of the convective terms for any transport problem with convection results in simple expressions like that shown in Eq. (3.24) for the discretised momentum equation. Although their treatment seems relatively easy, since only the value of the convective variable at the faces of the control volume is required, the performance of the numerical solver strongly depends on the choice of the numerical scheme used to evaluate the face values.

Over the years a wide variety of numerical schemes has been proposed for treating the numerical problems associated with convection terms, including the first-order *upwind differencing scheme* (UDS), second-order schemes such as the *central differencing scheme* (CDS) or improvements of UDS, and *higher order* schemes (HO) like the *quadratic upwind interpolation for convective kinematics* (QUICK) suggested by Leonard [87]. These schemes have been widely used in order to investigate a variety of numerical problems and their performance has been extensively reported in the literature [59–61, 64]. Although important, each one suffers from different problems as it will briefly present in the following sections, which made them less desirable to use. However, they formed the base for more accurate numerical schemes, commonly known as *high resolution schemes* (HRS).

The need for HRS in order to treat more accurately convective variables, led to

the generation of various tools appropriate for monitoring and controlling their performance. Harten [88] introduced the *total variation diminishing* framework (TVD), for solving numerically partial differential equations for convection. As it will be shown in the next subsections, UDS was found to be unconditionally stable but suffers from artificial diffusion while on the other hand, CDS is conditionally stable, and HO schemes have shown unbounded behaviour⁵ [59, 61, 89]. Therefore, TVD was introducing an approach where the use of appropriate flux limiters was producing numerical schemes that performed in between UDS and CDS [61] while at the same time the boundedness criterion is enforced. Later, the very useful tool of the *normalised variable framework* (NVF) was introduced by Leonard [89, 90], an approach that was generating the *normalised variable diagram* (NVD). The NVF methodology is considering that the numerical grids are uniform and thus, Darwish and Moukalled [91] extended this approach to non uniform meshes introducing the *normalised variable and space formulation* (NVSF). Expressing the numerical schemes for convection in the NVD, important insight for their characteristics and their performance is provided. Together with the NVD, the convection boundedness criterion CBC proposed by Gaskell and Lau [92] should be considered, which demands that the appropriate function for the evaluation of the convective variable at the cell face (ϕ_f) should exhibit a monotonic behaviour [61, 92].

In order to discuss the characteristics and differences between the various numerical schemes, the one-dimensional problem for convection is employed, presented schematically in Fig. 3.2, together with the one-dimensional, discretised convective terms of the generalised transport equation (cf. Eq. (3.11)) for a general transported variable ϕ :

$$\int_{V_P} \frac{\partial}{\partial \xi_l} (\rho u_j \phi \beta^{lj}) dV_P = \sum_{f=1}^2 \left(\sum_j \rho \tilde{u}_{j,f} b_f^{fj} \hat{\phi} \right) = \sum_{f=1}^2 F_f \hat{\phi}_f = F_{f+} \hat{\phi}_{f+} - F_{f-} \hat{\phi}_{f-} \quad (3.34)$$

The cell centre P in Fig. 3.2 is located at a distance ξ_P from the origin and corresponds

⁵ A numerical scheme for convection is said to be unbounded due to the fact that it illustrates oscillatory behaviour in regions where convection is characterised by steep gradients, and additionally tends to produce solutions that exhibit undershoots/overshoots [61].

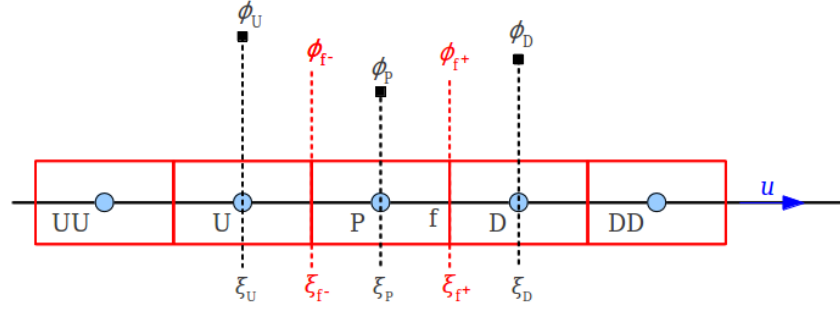


Figure 3.2. One-dimensional representation of the convective variable ϕ .

to the interrogated cell for which the convective variable ϕ needs to be calculated at the cell face, f , located at a distance ξ_f . The abbreviations D and U correspond to the computational cells *downstream* and *upstream* of the flow respectively, located similarly at distances ξ_D and ξ_U .

The NVSF approach [91] is adopted in the following discussion, for presenting the expressions used for the evaluation of the convective variables at the cell face ϕ_f . According to this methodology ϕ_f is generally expressed as a function:

$$\phi_f = f(\phi_P, \phi_U, \phi_D, \xi_P, \xi_U, \xi_D, \xi_f) \quad (3.35)$$

In order to produce the NVD diagram, the normalisation rules for the variable and the space values applied are:

$$\bar{\phi} = \frac{\phi - \phi_U}{\phi_D - \phi_U} \quad ; \quad \bar{\xi} = \frac{\xi - \xi_U}{\xi_D - \xi_U} \quad (3.36)$$

and Eq. (3.35) can be simplified in terms of a normalised function that depends only on the grid spacing and the value of the convected variable at the cell centre:

$$\bar{\phi}_f = f(\bar{\phi}_P, \bar{\xi}_P, \bar{\xi}_f) \quad (3.37)$$

Additionally the CBC suggests that in order to reduce any unphysical oscillations to the

approximation of the convective property at the cell face, an HRS should be bounded:

$$\bar{\phi}_f = \bar{\phi}_P \quad \text{if } \bar{\phi}_P \notin [0, 1] \quad (3.38)$$

and exhibit a monotonic behaviour between the values of the convective property at the cell centre, ϕ_P , and at the downstream centre, ϕ_D , expressed in a normalised form as

$$\bar{\phi}_P \leq \bar{\phi}_f \leq 1 \quad \text{if } \bar{\phi}_P \in [0, 1] \quad (3.39)$$

The numerical studies presented in [Chapters 4 to 6](#) are performed considering HRS for the treatment of the convective terms. Here, a brief description of the basic numerical schemes employed is given but more in-depth information about the performance of lower and higher order schemes can be found in [\[59, 61, 65\]](#).

i) Central Differencing Scheme

Arguably, the most obvious choice for approximating the value of a convective quantity ϕ_f at the face of a control volume, is the use of linear interpolation between the nodal values ϕ_P and ϕ_D , as shown schematically in [Fig. 3.3](#). This approach is known in numerical methods as the central differencing scheme (CDS), naturally produced by a Taylor series formulation and is very well known for its second order of accuracy. Despite the inherent second order accuracy of the scheme, it was shown that it can only be used under specific conditions due to the fact that it can generate unrealistic results

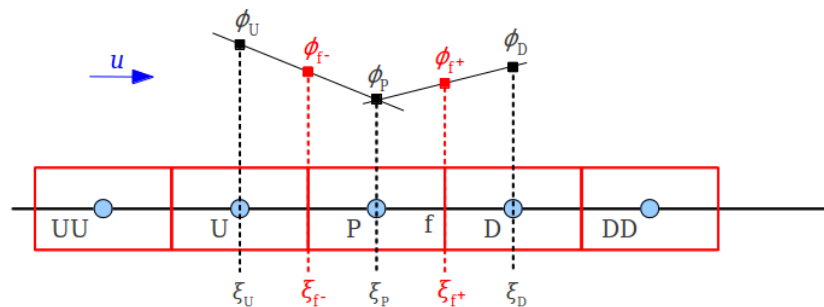


Figure 3.3. Representation of the approximated solution at the faces of a CV for the one-dimensional Central Differencing Scheme.

[60]. Applying linear interpolation between the interrogated cell and its downstream neighbour, the convective variable at the face can be evaluated by:

$$\phi_{f^+} = \phi_P \left(1 - \frac{\xi_{f^+} - \xi_P}{\xi_D - \xi_P} \right) + \phi_D \left(\frac{\xi_{f^+} - \xi_P}{\xi_D - \xi_P} \right) \quad (3.40)$$

where for a uniform mesh $(\xi_{f^+} - \xi_P)/(\xi_D - \xi_P) = 0.5$. Equation (3.40) can be further expressed as:

$$\frac{\phi_{f^+} - \phi_U}{\phi_D - \phi_U} = \frac{\phi_P - \phi_U}{\phi_D - \phi_U} + \frac{\phi_D - \phi_P}{\phi_D - \phi_U} \left(\frac{\xi_{f^+} - \xi_P}{\xi_D - \xi_P} \right) \quad (3.41)$$

The CDS can be therefore expressed in the NVSF using the relationships of Eq. (3.36):

$$\bar{\phi}_{f^+} = \frac{\bar{\xi}_{f^+} - \bar{\xi}_P}{1 - \bar{\xi}_P} + \left(\frac{1 - \bar{\xi}_{f^+}}{1 - \bar{\xi}_P} \right) \bar{\phi}_P \quad (3.42)$$

The major drawback of the CDS is its inability to identify the flow direction [64]. The linear interpolation scheme applied, results in a value at the cell face that is dependent from P, U and the mesh spacing. For example, for the case of a highly convective flow using a uniform mesh, ϕ_{f^+} depends equally on ϕ_P and ϕ_D . This is not realistic since one would expect that ϕ_P would influence ϕ_{f^+} more than ϕ_D . Following that, it was shown that the CDS can lead to unrealistic results and should be limited to flows that are characterised by low convection [60, 61].

ii) Upwind Differencing Scheme

The inability of the CDS scheme to yield realistic results for moderate to highly convective flows as discussed above, promoted the use of UDS for approximating convective flows. The UDS approach is shown schematically in Fig. 3.4, where it can be seen that the value of the convective variable at the cell face is completely influenced by the flow direction. This is expressed as

$$\phi_{f^+} = \phi_P \quad (3.43)$$

The expression of Eq. (3.43) in the NVSF is simply:

$$\bar{\phi}_{f^+} = \bar{\phi}_P \quad (3.44)$$

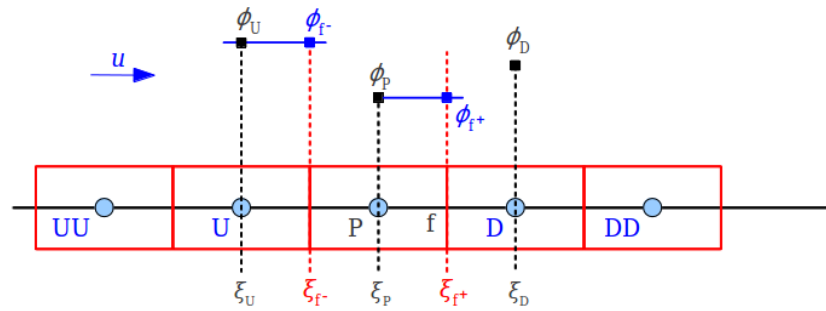


Figure 3.4. Representation of the approximated solution at the faces of a CV for the one-dimensional Upwind Differencing Scheme.

Although UDS is only first order accurate, it produces more realistic numerical solutions than CDS for convection problems. It is found to be the only numerical scheme that is unconditionally stable, however it suffers from artificial diffusion [59].

iii) Quadratic Upwind Interpolation for Convective Kinematics

The best representative of HO numerical schemes, QUICK, was proposed in 1979 by Leonard [87] and was based on the idea that convective values at the cell faces could be approximated using a parabolic function for the interpolation instead of a straight line (CDS and UDS), as shown schematically in Fig. 3.5. The QUICK scheme found great success in numerical simulations due to its third order accuracy and formed the basis for a range of high resolution schemes developed later. The advantage, in contrast with the UDS and CDS, is that with this methodology the face value, ϕ_{f^+} , is evaluated using information for the convected variable not only from P and D but also from the

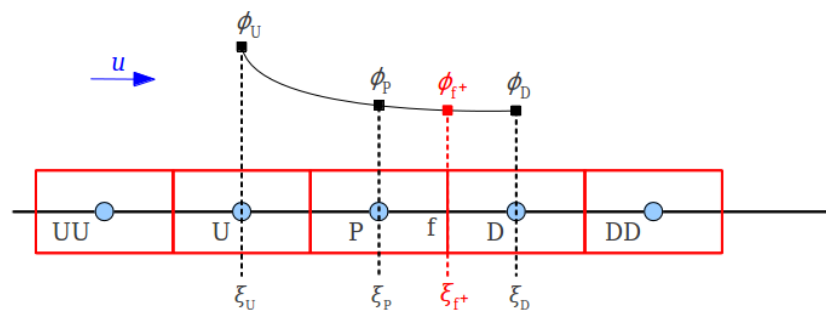


Figure 3.5. Representation of the approximated solution at the faces of a CV for the one-dimensional QUICK scheme.

upstream cell U:

$$\phi_{f^+} = \phi_U + \frac{(\xi_{f^+} - \xi_U)(\xi_{f^+} - \xi_P)}{(\xi_D - \xi_U)(\xi_D - \xi_P)}(\phi_D - \phi_U) + \frac{(\xi_{f^+} - \xi_U)(\xi_D - \xi_{f^+})}{(\xi_P - \xi_U)(\xi_D - \xi_P)}(\phi_P - \phi_U) \quad (3.45)$$

after doing some mathematical re-arrangements and by employing the normalisation rules from Eq. (3.36), the QUICK scheme is translated in the NVSF as

$$\bar{\phi}_{f^+} = \frac{\bar{\xi}_{f^+} - \bar{\xi}_P}{1 - \bar{\xi}_P} \bar{\xi}_{f^+} + \frac{\bar{\xi}_{f^+}(1 - \bar{\xi}_{f^+})}{\bar{\xi}_P(1 - \bar{\xi}_P)} \bar{\phi}_P \quad (3.46)$$

Despite the QUICK scheme's enhanced performance, it was shown that it exhibits oscillations when the flow conditions are highly convective [61, 89].

iv) High Resolution Schemes

Higher order schemes exhibit oscillatory solutions when the gradients of the convective property are steep due to the fact that they are unbounded [61] and can produce local maxima (or minima). It was shown by Gaskell and Lau [92], and Leonard [90], that the desired behaviour for a numerical scheme is to be monotonic in the normalised region $\bar{\phi}_P \in [0, 1]$ of the NVD diagram. Since a high resolution scheme cannot preserve monotonicity by its nature, the numerical tools discussed above are employed (TVD, NVD, CBC) in order to overcome this problem and control in the most appropriate way the continuous function or the sets of functions employed.

Various schemes have been reported in literature but here only the *sharp and monotonic algorithm for realistic transport* (SMART) scheme proposed by Gaskell and Lau [92] and the *convergent and universally bounded interpolation scheme for the treatment of advection* (CUBISTA) scheme proposed by Alves *et al.* [93], are discussed because of the relevance to the problems tackled in this work. Both SMART and CUBISTA are based on QUICK scheme retaining its advantages, but additionally they bound QUICK's unbounded behaviour by following the CBC approach (cf. Eqs. (3.38) and (3.39)), providing as a consequence less oscillatory solutions. Their comparison in the NVD diagram and detailed discussion can be found in Alves *et al.* [93] and in Alves [65].

After employing the normalisation rules of (Eq. (3.36)), the SMART scheme can be expressed in the NVSF as

$$\bar{\phi}_{f^+} = \begin{cases} \frac{\bar{\xi}_{f^+}(1 - 3\bar{\xi}_P + 2\bar{\xi}_{f^+})}{\bar{\xi}_P(1 - \bar{\xi}_P)} \bar{\phi}_P & \text{if } 0 < \bar{\phi}_P < \frac{\bar{\xi}_P}{3} \\ \frac{\bar{\xi}_{f^+} - \bar{\xi}_P}{1 - \bar{\xi}_P} \bar{\xi}_{f^+} + \frac{\bar{\xi}_{f^+}(1 - \bar{\xi}_{f^+})}{\bar{\xi}_P(1 - \bar{\xi}_P)} \bar{\phi}_P & \text{if } \frac{\bar{\xi}_P}{3} \leq \bar{\phi}_P \leq \frac{\bar{\xi}_P}{\bar{\xi}_{f^+}} (1 + \bar{\xi}_{f^+} - \bar{\xi}_P) \\ 1 & \text{if } \frac{\bar{\xi}_P}{\bar{\xi}_{f^+}} (1 + \bar{\xi}_{f^+} - \bar{\xi}_P) < \bar{\phi}_P < 1 \\ \bar{\phi}_P & \text{elsewhere} \end{cases} \quad (3.47)$$

It can be seen that the core of the SMART scheme maintains the QUICK approach. The same function (cf. Eq. (3.46)) is employed for evaluating the convective variable on the control volume face, when $\frac{\bar{\xi}_P}{3} \leq \bar{\phi}_P \leq \frac{\bar{\xi}_P}{\bar{\xi}_{f^+}} (1 + \bar{\xi}_{f^+} - \bar{\xi}_P)$. However, in contrast with QUICK, SMART is bounded by the addition of the extra functions below and above as shown in Eq. (3.47). The addition of these functions is responsible for the less oscillatory behaviour of SMART scheme.

Following the same ideas, the CUBISTA scheme has been proposed by Alves *et al.* [93] and is expressed in the NVSF as

$$\bar{\phi}_{f^+} = \begin{cases} \left[1 + \frac{\bar{\xi}_{f^+} - \bar{\xi}_P}{3(1 - \bar{\xi}_P)} \right] \frac{\bar{\xi}_{f^+}}{\bar{\xi}_P} & \text{if } 0 < \bar{\phi}_P < \frac{3\bar{\xi}_P}{4} \\ \frac{\bar{\xi}_{f^+} - \bar{\xi}_P}{1 - \bar{\xi}_P} \bar{\xi}_{f^+} + \frac{\bar{\xi}_{f^+}(1 - \bar{\xi}_{f^+})}{\bar{\xi}_P(1 - \bar{\xi}_P)} \bar{\phi}_P & \text{if } \frac{3\bar{\xi}_P}{4} \leq \bar{\phi}_P \leq \frac{1 + 2(\bar{\xi}_{f^+} - \bar{\xi}_P)}{2\bar{\xi}_{f^+} - \bar{\xi}_P} \bar{\xi}_P \\ 1 - \frac{1 - \bar{\xi}_{f^+}}{2(1 - \bar{\xi}_P)} (1 - \bar{\phi}_P) & \text{if } \frac{1 + 2(\bar{\xi}_{f^+} - \bar{\xi}_P)}{2\bar{\xi}_{f^+} - \bar{\xi}_P} \bar{\xi}_P < \bar{\phi}_P < 1 \\ \bar{\phi}_P & \text{elsewhere} \end{cases} \quad (3.48)$$

It can be seen that, as for the SMART scheme, the core of CUBISTA uses QUICK interpolation (second inequality interval in Eq. (3.48)) but considers different functions to the first and last intervals. As mentioned by the authors, CUBISTA was developed respecting both the TVD constraints and the CBC, in contrast with SMART that respects only the CBC. They compared those two schemes among others by performing a set of specific numerical tests (i.e. pure advection of a scalar for a step profile) and found that CUBISTA performs similarly to SMART, with the latter being less diffusive. However, the main purpose of their study was to propose a new convection scheme appropriate for discretising the convective terms in studies of viscoelastic fluids. When

it comes to these kind of flows, the CUBISTA scheme was found to perform much better than SMART in terms of convergence for implicit solution methods for both fine and coarse meshes.

v) Final remark

Once the desired scheme is chosen and the normalised variable $\bar{\phi}_{f+}$ is evaluated at the cell face following the NVSF framework, it is then reverted back to dimensional form by

$$\phi_{f+} = \bar{\phi}_{f+}(\phi_D - \phi_U) + \phi_U \quad (3.49)$$

The single phase solver follows the deferred correction approach, proposed by Khosla and Rubin [94]. According to this approach instead of using directly the discretised equations produced by the use of high resolution schemes in the momentum equation, the convective fluxes are replaced by the expression:

$$F_{f+}\phi_{f+}^{HRS} = F_{f+}\phi_{f+}^{UDS} - F_{f+}(\phi_{f+}^{UDS} - \phi_{f+}^{HRS}) \quad (3.50)$$

where the terms with the superscript UDS denote that the values are evaluated at the cell face based on the upwind scheme. The first term in the RHS of Eq. (3.50) is treated implicitly and is added at the coefficients in the LHS of Eq. (3.29), whereas the second term is evaluated explicitly and is added in the sources on the RHS of Eq. (3.29) [59]. This procedure has the advantage that numerical stability is promoted due to the use of UDS [65], while no additional effort is needed in order to treat the chosen HRS implicitly, and the method facilitates in the use of less computer memory [91, 93].

3.3.4 Boundary conditions

The set of algebraic expressions responsible for evaluating numerically the fluid flow presented previously is completed by setting the appropriate boundary conditions for the problem studied. Here, the boundary conditions that need to be specified are those for the inlets, outlets, walls and symmetric planes of the domain and are briefly discussed.

- **Inlet conditions**

When the numerical study corresponds to cases where inlet conditions are required, all quantities need to be prescribed. Velocities and stresses can be designated by either well defined profiles from existing analytical solutions or they can just be initialised using a uniform constant value.

- **Outlet conditions**

The lack of knowledge of the flow behaviour at the outlets of a configuration which is investigated numerically, is forcing one to place the boundaries as far as possible from the region of interest. That way the propagation of possible numerical errors to the region of interest is avoided and do not affect the solution of the flow field. In this work, zero stream-wise gradients are considered for the velocities and the stresses. They are applied by considering that the outlet cell face has the same value as the boundary cell centre. Please note that the velocities at the outlets are additionally adjusted to ensure that the overall mass is conserved. For the pressure, linear extrapolation is employed for its evaluation at the boundary faces using the values calculated at the two cell centres upstream of the boundary [27, 65].

- **Symmetry conditions**

There are many examples of flows that are symmetric. The numerical advantage of these kind of flows is that one can employ symmetry boundary conditions and split the domain in two or more symmetric parts, solving only for one of them. That way, the computational cost can be greatly reduced. At a symmetric boundary the convective fluxes of all quantities ($\mathbf{u}, \boldsymbol{\tau}, \phi$) are zero, and all diffusive fluxes must also vanish.

As discussed in Oliveira *et al.* [27] and with more details in Oliveira [66] and in Alves [65], the reflection rule is employed for evaluating the velocity, stresses and scalar fields on symmetry planes. The use of a symmetric fiction cell is considered for the correct evaluation of vectors and tensors at the cell faces which are located on the symmetry plane. For all scalar quantities, zero gradient is used with the variable values on the symmetry plane being equal to their values at the boundary cell centres.

- **Wall conditions**

The last boundary condition considered is related to the walls that confine the domain. Usually the walls are stationary or they can be set to motion with a specific velocity. Considering that viscous fluids stick to the solid boundary (i.e. no slip condition applied) it can be generally expressed as:

$$u_{i,f} = u_{i,w} \quad (3.51)$$

Regarding the pressure a zero gradient profile is employed, while for the stresses a Couette approximation is considered together with the appropriate viscometric functions for each viscoelastic fluid [65].

3.3.5 Velocity and pressure fields coupling

The possibility of an unrealistic checkerboard pattern field for pressure that could result in the correct velocity field was illustrated by Patankar [60]. The use of “different grids in one” was promoted for this particular reason and resulted in the so called staggered arrangement. The choice of this arrangement has benefited by the great performance of the SIMPLE algorithm [81], which was introduced for linking the pressure and velocity fields.

The basic idea of SIMPLE is based on the ascertainment that the momentum equation can be solved only when the pressure field is given. If an incorrect pressure field is applied, then the resulting velocity field will not satisfy the continuity equation. Starting from a guessed velocity and pressure fields, the convective fluxes are evaluated and the momentum equation is solved, resulting in a new velocity field that in general does not satisfy the continuity equation. Then, a pressure correction equation is applied through the continuity equation, which in turn results in a corrected pressure field that is used to correct the velocities [60, 64, 81]. This procedure is repeated in an iterative manner, until the pressure field generates a velocity field that satisfies continuity.

The success of SIMPLE for staggered grids together with the major problem of the collocated arrangement to predict correct velocity values for an unrealistic pres-

sure pattern, was one of the major reasons for discarding the use of collocated meshes. However, the usefulness of the collocated arrangement in engineering applications, motivated Rhie and Chow to suggest a special interpolation scheme [85] which enabled the use of SIMPLE for this arrangement.

The discretised expressions of the momentum equation at the cell P and its neighbour F are:

$$a_P u_{i,P} = H_P(u_i) + S_{P,u_i-\text{rest}} - \sum_{l=1}^3 b_P^{li} [\Delta p]_l^P + \frac{\rho V_P}{\Delta t} u_{i,P}^{(n-1)} \quad (3.52)$$

and

$$a_F u_{i,F} = H_F(u_i) + S_{F,u_i-\text{rest}} - \sum_{l=1}^3 b_F^{li} [\Delta p]_l^F + \frac{\rho V_F}{\Delta t} u_{i,F}^{(n-1)} \quad (3.53)$$

where it can be seen that the sources related to pressures (cf. Eq. (3.26)) have been excluded from the total sources of Eq. (3.29), while $H_P(u_i)$ and $H_F(u_i)$ contain the sum of the neighbouring coefficients of P and F respectively. Following the same idea, the discretised momentum equation at the face is expressed by

$$a_f \tilde{u}_{i,f} = H_f(u_i) + S_{f,u_i-\text{rest}} - \sum_{l=1}^3 b_f^{li} [\Delta p]_l^f + \frac{\rho V_f}{\Delta t} u_{i,f}^{(n-1)} \quad (3.54)$$

Rhie and Chow suggested that each of the terms in Eq. (3.54) can be expressed as an arithmetic average of each equivalent term from Eqs. (3.52) and (3.53). With this approach, the velocity at the cell face is evaluated by performing linear interpolation of the momentum equations at the nodal positions and moreover, the face velocities are linked to nodal pressures mimicking the staggered arrangement approach [59, 61, 95]. This idea was implemented in Issa and Oliveira [96], and Oliveira *et al.* [27], as

$$\bar{a}_f \tilde{u}_{i,f} = \bar{H}_f(u_i) + \bar{S}_{u_i-\text{rest}} - b_f^{li} [\Delta p]_f^f - \overline{\sum_{l \neq f} b^{li} [\Delta p]_l} + \overline{\left(\frac{\rho V}{\Delta t} \right)} \tilde{u}_{i,f}^{(n-1)} \quad (3.55)$$

where the overbar denotes the arithmetic average of the equivalent terms from the known discretised momentum equations at P and F. As it can be seen from the discretised form of Eq. (3.26), the pressure gradients along the normal face directions are

evaluated by the values of pressure at the faces, using the nodal pressures. Subtracting from Eq. (3.55) all averaged terms from the combination of Eqs. (3.52) and (3.53), the velocity used at the faces in Eq. (3.22) for evaluating the convective fluxes becomes⁶

$$\tilde{u}_{i,f} = \frac{\overline{a_f u_{i,f}} + \overline{b_f^{fi} [\Delta p]_f} - b_f^{fi} [\Delta p]_f + \overline{\left(\frac{\rho V}{\Delta t}\right)_f \tilde{u}_{i,f}^{(n-1)}} + \overline{\left(\frac{\rho V}{\Delta t} u_i^{(n-1)}\right)_f}}{\bar{a}_f} \quad (3.56)$$

The same idea considering this special interpolation scheme was suggested by Oliveira *et al.* [27], for treating a similar decoupling observed between the stress field and the velocity field when collocated meshes are employed. The discretisation of the divergence of the stress field (cf. Eq. (3.27)) in the momentum equation, which is added as a source term, employs interpolated values of the stresses at the faces of the control cell, taken from the cell centre values. Following that, Oliveira and Pinho [67] suggested an improved version which is able to treat better abrupt changes in mesh spacing:

$$\begin{aligned} \tilde{\tau}_{ij,f} = & \overline{\tau_{ij,f}} - \left(B'_{fj} [\Delta u_i]_f + B'_{fi} [\Delta u_j]_f - \frac{2}{3} \eta_p \sum_{k=1}^3 b'_{fk} [\Delta u_k]_f \delta_{ij} \right) \\ & + \left(\tilde{B}'_{fj} [\Delta u_i]_f + \tilde{B}'_{fi} [\Delta u_j]_f - \frac{2}{3} \eta_p \sum_{k=1}^3 \tilde{b}'_{fk} [\Delta u_k]_f \delta_{ij} \right) \end{aligned} \quad (3.57)$$

where

$$\begin{aligned} B'_{fj} = & \frac{\eta_p b_{fj} + \lambda \sum_{k=1}^3 b_{fk} \tau_{ki}}{a_P^\tau} \quad \text{and} \quad b'_{fi} = \frac{b_{fi}}{a_P^\tau} \\ \tilde{B}'_{fj} = & \frac{\left(\eta_p b_{fj} + \lambda \sum_{k=1}^3 b_{fk} \tau_{ki} \right)_f}{V_f (a_P^\tau / V_p)} \quad \text{and} \quad \tilde{b}'_{fi} = \frac{b_{fi}^f}{V_f (a_P^\tau / V_p)} \end{aligned} \quad (3.58)$$

3.3.6 Solution Procedure

When all the terms from continuity (Eq. (3.12)), momentum (Eq. (3.17)) and constitutive (Eq. (3.15)) equations are discretised, the linear algebraic system of Eqs. (3.29)

⁶ The symbol f underneath the overbar indicates that the variable is the arithmetic mean of P and F cells at the face. When not underneath the overbar, the derivative is evaluated using the differencing scheme between the cells P and F (i.e. $[\Delta \Phi]_f = \Phi_F - \Phi_P$).

and (3.33) that needs to be solved is assembled. As mentioned previously, Patankar and Spalding [81] proposed the SIMPLE algorithm, an iterative procedure that generates a pressure-velocity correction procedure. The underlying idea of SIMPLE is to link pressure and velocity fields through the continuity equation. Starting from an initial guess of the pressure field $p^{(*)}$ (predictor stage), the generated velocities from the solution of the momentum equation will not necessarily satisfy the continuity Eq. (3.22). Therefore, by attaching the pressure field in the continuity equation the pressures are corrected (corrector stage), which in turn corrects the velocities. After the velocities are corrected, the transport equation of any other quantity is evaluated. This procedure is repeated until the correct pressure field is computed and the velocities that satisfy Eq. (3.22) are generated. Various improvements of this procedure have been suggested. Van Doormal and Raithby [82] proposed the SIMPLEC, algorithm which is considered here. The major difference is the treatment of the term from the momentum relationships in the corrector stage, which is neglected in the SIMPLE algorithm, due to the fact that its inclusion would lead to complex numerical expressions [60]. In SIMPLEC this approximation follows a more appropriate procedure [59, 86] and as a result the under-relaxation for the pressure solution used in SIMPLE, is no longer required. In the current solver, the SIMPLEC algorithm is modified in order to account for the solution of the stress constitutive equation as described in Oliveira *et al.* [27].

For studying complex fluids an additional stress-relation equation is needed since Newton's law of viscosity is no longer valid as discussed in Chapter 2. Considering that the stress tensor is symmetric, the stress field results in six equations, and the modified SIMPLEC algorithm implies that the algebraic equation for the stresses is solved prior to the momentum equations. Therefore the six stress components are evaluated through the solution of:

$$a_{\text{P}}^{\tau} \tau_{ij,\text{P}}^* - \sum_{\text{F}} a_{\text{F}}^{\tau} \tau_{ij,\text{F}}^* = S_{\tau_{ij}} \quad (3.59)$$

where the calculation of stresses is done at the new time step ($\tau_{ij,\text{P}}^*$), whereas the source terms ($S_{\tau_{ij}}$) and coefficients (a_{P}^{τ} , a_{F}^{τ}) are evaluated using the previous time step. For

reducing the terms appearing in the equations, those terms related to the previous time step for both the constitutive and momentum discretised expressions are inserted in the sources.

When the stress field is evaluated, the momentum equation is solved based on the guessed pressure field p^* and the new stresses τ_{ij}^* , estimating the velocities ⁷:

$$\left(\sum_{\text{F}} a_{\text{F}} + S_{\text{P}} + \frac{\rho V_{\text{P}}}{\Delta t}\right) u_{i,\text{P}}^* - \sum_{\text{F}} a_{\text{F}} u_{i,\text{F}}^* = S'_{u_i} - \sum_{l=1}^3 b_{\text{P}}^{li} [\Delta p^*]_l^{\text{P}} \quad (3.60)$$

where S'_{u_i} are all remaining sources from Eq. (3.32) with the exception of the pressure sources, which are extracted. The resulting velocities u_i^* are not expected in general to satisfy the continuity equation, Eq. (3.22), and the new fluxes at the faces, F_{f}^* , are evaluated using the Rhie and Chow interpolation technique presented in Section 3.3.5.

Considering now that an updated pressure field p^{**} will generate velocities u^{**} that satisfy both momentum and continuity equations, then the old values should be corrected as

$$p^{**} = p^* + p' \quad \text{and} \quad u^{**} = u^* + u' \quad (3.61)$$

Therefore, the momentum equations for the updated velocities can be approximated by

$$\left(\sum_{\text{F}} a_{\text{F}} + S_{\text{P}}\right) u_{i,\text{P}}^* + \frac{\rho V_{\text{P}}}{\Delta t} u_{i,\text{P}}^{**} - \sum_{\text{F}} a_{\text{F}} u_{i,\text{F}}^* = S'_{u_i} - \sum_{l=1}^3 b_{\text{P}}^{li} [\Delta p^{**}]_l^{\text{P}} \quad (3.62)$$

Note that only the pressure field and the time dependent term are updated [27, 86] to the new time level. Subtraction of Eqs. (3.60) and (3.62), generates the appropriate relationships for the corrected velocities u'_{P} , which depend on the corrected pressure drops:

$$\frac{\rho V_{\text{P}}}{\Delta t} u'_{i,\text{P}} = - \sum_{l=1}^3 b_{\text{P}}^{li} [\Delta p']_l^{\text{P}} \quad (3.63)$$

and result the appropriate expressions for the mass flux corrections F'_{f} [86]. Since the

⁷The sources contain the stress divergence term from Eq. (3.27), which is evaluated based on the special interpolation presented in Section 3.3.5 for coupling the stress field with the velocity field. The interpolation is considering the previously, new-time, computed stress field τ_{ij}^* .

updated velocities are satisfying continuity, it can be written that:

$$\sum_{f=1}^6 F_f^{**} = \sum_{f=1}^6 (F_f^* + F_f') = 0 \quad (3.64)$$

The combination of Eqs. (3.63) and (3.64) results in the algebraic equation for the pressures that is produced from the continuity equation:

$$a_P^p p_P' - \sum_F a_F^p p_F' = - \sum_{f=1}^6 F_f^* \quad (3.65)$$

where $a_P^p = \sum_F a_F^p$ and $a_F^p = \rho(\sum_j b_f^{lj} b_f^{lj}) / (\overline{\rho V / \Delta t})_f$

Therefore, the solution of Eq. (3.65) gives the pressure field correction p' , which in turn will result in the correction of the velocities (Eq. (3.63)) and the variables in the new time step will be updated (cf. Eq. (3.61)). This procedure continues iteratively until a desired convergence is obtained.

3.4 Mesh deformations

The ability to manipulate geometrical objects and generate different versions of their initial form was always of great interest in engineering fields. However, geometric modelling of sophisticated objects that can produce specific and well controlled characteristics is many times a difficult task. The majority of geometries under investigation in scientific or industrial applications are often defined by complex functions, which may be difficult to apply using programming techniques.

The numerical investigation of fluid flow for Newtonian or non-Newtonian fluids in this study, is achieved based on the numerical implementation presented in the previous section (Section 3.3). The implicit Finite Volume flow-solver presented, is coupled with a block-structured mesh generator, responsible for discretising the physical geometry under investigation. The output of the mesh generator contains all the appropriate information such as nodal position, grid spacings, cell connectivities and more, which are required by the flow-solver for evaluating the flow field correctly.

The mesh generator maps the desired physical space (x_1, x_2, x_3) on to the generalised non-orthogonal system (ξ_1, ξ_2, ξ_3) , following the very well known procedure for proper mesh discretisation of geometries with “awkward” shapes [59, 97], and reverts it back to the physical space employing the isoparametric quadratic functions [98]. However, applying non-linear shapes in practice is not straightforward and for that reason, techniques commonly used in computer graphics were employed in order to manipulate the linear block-structured meshes. Computer graphic techniques are used by many commercial CFD packages and Computer Aided Designing (CAD) for generating, modifying or optimising geometries for engineering purposes. Among these, Free Form Deformation (FFD) and the Non-Uniform Rational B-Splines (NURBS) techniques are the most popular parametric representations [97, 99, 100] used for that purpose.

A numerical code using NURBS was implemented in this work and employed in Chapter 5 for finding the best possible shape in the shape optimisations performed. Here, starting from the predecessors of NURBS (e.g. Bezier curves, FFD and B-splines), their mathematical formulation is described and their characteristics are discussed.

3.4.1 Bezier Curves

The very well known parametric Bezier curves were invented in the early 1960’s by Pierre Bezier, an engineer at Renault car company. Bezier used these parametric curves mainly for car design but also for designing aircraft wings. Bezier’s approach was later found very useful in shape optimisations of an airfoil [101, 102] and machinery blades [103]. Mathematically, a parametric Bezier curve is defined as

$$\mathbf{P}(s) = \sum_{i=0}^n \mathbf{B}_i b_{i,n}(s) \quad 0 \leq s \leq 1 \quad (3.66)$$

where $b_{i,n}$ corresponds to the Bernstein basis polynomials or blending functions, \mathbf{B}_i refers to the control points that define the parametric curve, s is the parametric space coordinate, the index n indicates the degree of the basis function and the index i corresponds to the number of control points that form the control polygon of Fig. 3.6.

The Bernstein polynomial is evaluated using the formula:

$$b_{i,n}(s) = \binom{n}{i} s^i (1-s)^{n-i} \quad (3.67)$$

where the binomial coefficient is evaluated as

$$\binom{n}{i} = \frac{n!}{i!(n-i)!} \quad (3.68)$$

with $b_{i,n}(s) = 0$ if $i \notin \{0, \dots, n\}$. Some important properties of the Bezier curves are [99]:

- The basis functions, $b_{i,n}(s)$, are real.
- The degree of the polynomial, n , that defines the curve segment is always one less ⁸ than the number of control polygon points, \mathbf{B}_i .
- The curve follows the shape of the control polygon.
- The first and last points on the curve are coincident with the first and last points of the control polygon.
- The tangent vectors at the start and the end of the curve have the same direction as the first and the last polygon spans.

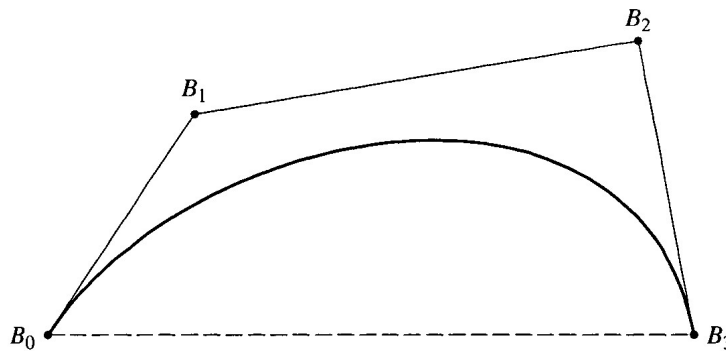


Figure 3.6. Bezier curve and Control Polygon

⁸Note that the numbering of the control points starts from $i = 0$. Therefore for example a control polygon of 4 points will have Bernstein polynomial of degree $n = 3$.

- The curve is contained between the convex hull defined by the control polygon.
- The curve is invariant to any affine transformation.

As inferred from Eq. (3.66), the degree of the curve depends on the number of control points that define the control polygon. This characteristic of Bernstein polynomials limits the flexibility of the resulting curve since the only way to reduce or increase the degree of the resulting curve is by reducing or increasing the number of control points, respectively [99,100]. Bernstein polynomials have two important properties [104]: first, they satisfy the following recursion formula:

$$b_{i,n}(s) = (1-s)b_{i,n-1}(s) + sb_{i-1,n-1}(s) \quad (3.69)$$

with $b_{0,0}(s) \equiv 0$; second, for a given value of parameter s the sum of the polynomials is equal to unity.

$$\sum_{i=0}^n b_{i,n}(s) = 1 \quad (3.70)$$

3.4.2 Free Form Deformation

Sederberg and Parry [105] introduced the Free Form Deformation technique as a tool for modelling and deforming objects either globally or locally. To exemplify the FFD technique one can consider a parallelepiped mesh that surrounds a physical flexible object, forming an outer lattice that is responsible for deforming the embedded object, as illustrated in Fig. 3.7. The flexible object is initially surrounded by the FFD lattice (Fig. 3.7a) and then by moving the control points of the lattice, the object is deformed (Fig. 3.7b).

The Free Form Deformation technique is based on the Bezier curves, discussed in Section 3.4.1. The deformations are defined by parametric functions, the values of which are determined by the location of control points [106], and are defined mathematically in terms of a trivariate Bernstein polynomial tensor product. Any point \mathbf{X} of the physical object with (x_1, x_2, x_3) coordinates at the physical space is transferred to the

parametric space (s,t,w) following the relationship [105]:

$$\mathbf{X} = \mathbf{X}_0 + s\mathbf{S} + t\mathbf{T} + w\mathbf{W} \quad (3.71)$$

where \mathbf{S} , \mathbf{T} and \mathbf{W} represent the vectors of the total length of the embedded object at each direction. The parameterised coordinates are evaluated using the following equations:

$$s = \frac{\mathbf{T} \times \mathbf{W} \cdot (\mathbf{X} - \mathbf{X}_0)}{\mathbf{T} \times \mathbf{W} \cdot \mathbf{S}} \quad t = \frac{\mathbf{S} \times \mathbf{W} \cdot (\mathbf{X} - \mathbf{X}_0)}{\mathbf{S} \times \mathbf{W} \cdot \mathbf{T}} \quad w = \frac{\mathbf{S} \times \mathbf{T} \cdot (\mathbf{X} - \mathbf{X}_0)}{\mathbf{S} \times \mathbf{T} \cdot \mathbf{W}} \quad (3.72)$$

From Eq. (3.72), one can realise that the nominator corresponds to the total length of the physical object along each direction and therefore, for any point interior to the lattice the parametric coordinates are in the range $0 \leq s, t, w \leq 1$. The locations of the lattice control points (nodes of the FFD mesh in Fig. 3.7) are defined by

$$\mathbf{B}_{ijk} = \mathbf{X}_0 + \frac{i}{l}\mathbf{S} + \frac{j}{m}\mathbf{T} + \frac{k}{n}\mathbf{W} \quad (3.73)$$

where l , m , and n refer to the number of the desired elements (spacings) in each direction, and $0 \leq i \leq l$, $0 \leq j \leq m$ and $0 \leq k \leq n$ are the indices holding the appropriate numbering of the control points. From Eq. (3.73) it can be deduced that all control points are equally distributed, resulting always to a uniform lattice.

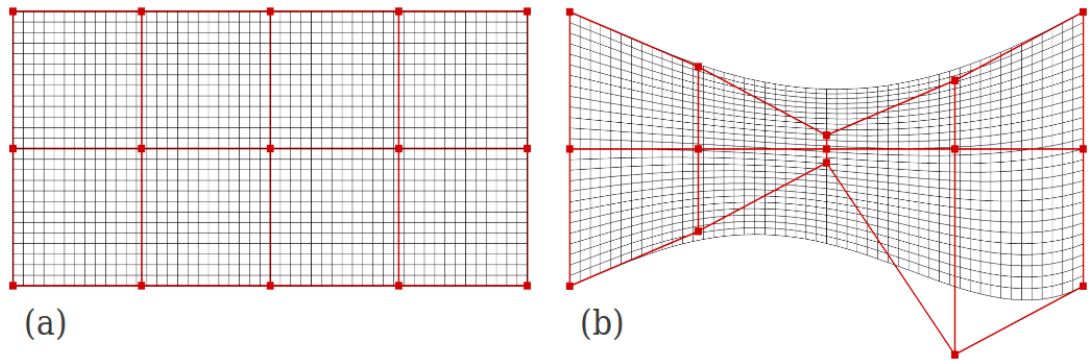


Figure 3.7. Initial shape of the object embedded by the FFD lattice (a) and deformed object after the movement of the lattice control points (b). The *squares* at nodal positions of the FFD lattice correspond to the lattice control points.

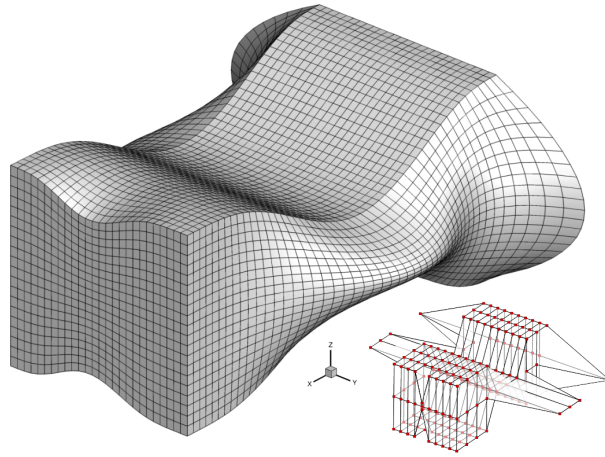


Figure 3.8. 3D deformation of an initial rectangular object from the FFD lattice. The small right hand image illustrates the positions of the 3D lattice control points.

After the control points are specified, the deformation of the object can be achieved by simply moving the control points from their initially defined position. The deformation is then applied to the embedded object through the evaluation of the trivariate Bernstein polynomial vector:

$$\mathbf{X} = \sum_{i=0}^l \binom{l}{i} (1-s)^{l-i} s^i \left\{ \sum_{j=0}^m \binom{m}{j} (1-t)^{m-j} t^j \left\{ \sum_{k=0}^n \binom{n}{k} (1-w)^{n-k} w^k \mathbf{B}_{ijk} \right\} \right\} \quad (3.74)$$

Comparing Eqs. (3.67) and (3.74), it is clear that the deformations produced by the FFD technique are based on the Bezier curves. Figure 3.8, presents a 3D deformation of the embedded object based on Eq. (3.74), with the inset figure illustrating the movement of the control points of the lattice, for obtaining the resulting shape.

Figure 3.9 presents the basis functions for an one-dimensional case with control polygons consisted of 2, 3, 5 and 7 control points, similarly to Rogers [99]. One can notice two things. Each control point has an area of dominance, defined by the Bernstein polynomials, with the first and last points always attaining the maximum value at the beginning and at the end of the parameterised space. This is in agreement with an important feature of Bezier curves in which the first and last control points are forced to coincide with the curve. Moreover, it can be seen that as an adjacent point starts to affect the representation of the curve, the equivalent Bernstein polynomial value starts

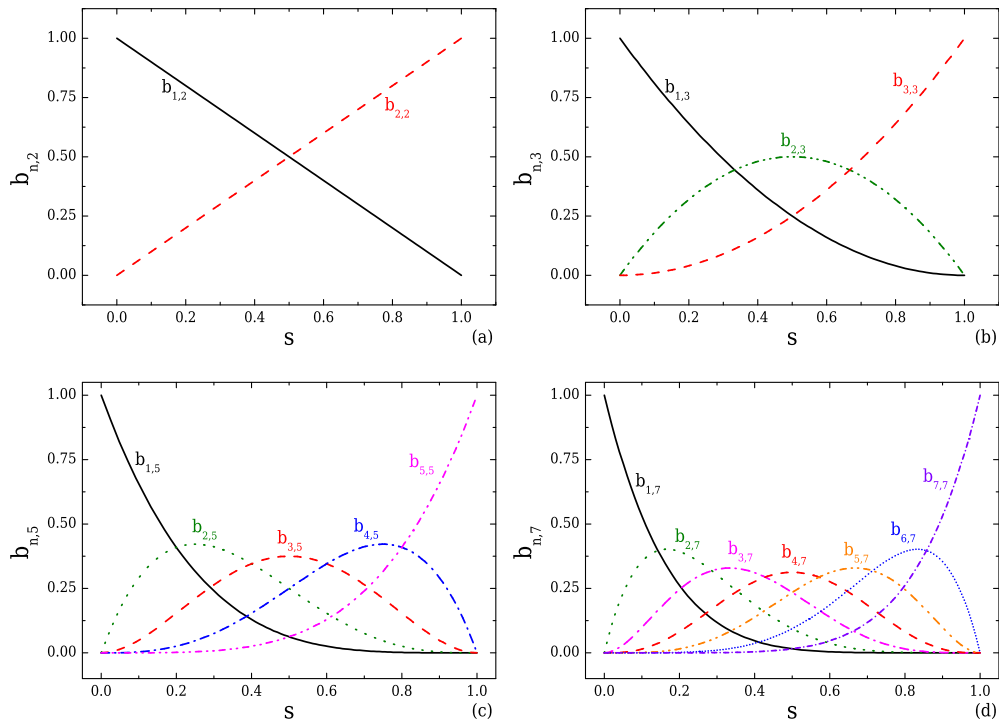


Figure 3.9. Bernstein basis functions for two control points, $n = 1$ (a); three control points, $n = 2$ (b); five control points, $n = 4$ (c), and seven control points, $n = 6$ (d).

to increase to a value defined by the remaining neighbouring points, as imposed by Eq. (3.70).

Although Free Form Deformation is a great, straightforward and easy to program technique that generates smooth curves, uniformity of the lattice limits the ability of applications. One can only surpass this uniformity limitation by employing simultaneously various lattices consisting of different nodal spacings, which enclose partially the object at different locations. However, complex deformations usually require a large number of points [106]. As the number of control points is increased, the grade of the Bernstein polynomials also increases and therefore, the computational cost is increased [99, 107]. Finally, the restriction of the method to use only the Bernstein functions for different deformations results in the generation of a specific type of curves, which can only be affected by the number of control points. This will be further discussed in the following sections. However, even more important is the fact that the final curve is significantly affected by the position of all control points, which influence *globally* the nature of the

curve [99,100], as it can be seen by the non-zero values of the Bernstein polynomials.

3.4.3 From B-Splines to Non-Uniform Rational B-Splines

The requirement to be able to control the deformation of the object “locally” and the drawbacks of FFD technique in this respect (mainly because of the limited flexibility of the Bernstein polynomials), led to the need for an alternative approach and promoted the use of another set of functions called B-splines. It is noted that B-splines consider the Bernstein polynomials as a special case [99,100].

Here, for each control point the range of effect on the parameter space (s) varies along a specified segment, defined by the so called *knot vectors*, which can also be manipulated. As a result, the basis functions can now have zero values and the position of the control points affect only a desired part of the parameter space, for which the basis functions are non-zero. At the same time, the grade of the polynomial basis now not only depends by the number of control points, but also depends on the number of knot vectors. This section provides the most important information for B-spline theory, which assists in describing the functionality of NURBS. More detailed material can be found in Les Piegl [100], Farin [104] and Rogers [99].

i) B-Spline definition

A B-Spline curve is defined by the following relationship:

$$\mathbf{P}(s) = \sum_{i=1}^n \mathbf{B}_i N_{i,k_s}(s) \quad s_{min} \leq s < s_{max} \quad , \quad 2 \leq k_s \leq n \quad (3.75)$$

where, as previously, \mathbf{B}_i corresponds to the equivalent control point coordinates of the control polygon which is defined by n total control points and $n - 1$ linear segments; N_{i,k_s} are the normalized B-spline basis functions and k_s is the order of the basis functions, which have a degree of $k_s - 1$. Moreover, a curve designed by B-splines is everywhere C^{k_s-2} continuous [99]. Comparing Eqs. (3.66) and (3.75) there is an obvious similarity in both mathematical expressions which generate the curves $\mathbf{P}(s)$.

In order to evaluate the B-spline basis functions on Eq. (3.75), the Cox de Boor

[108] recursive formula is employed, as this is arguably the most efficient for computer implementation [100]:

$$N_{i,1}(s) = \begin{cases} 1 & u_i \leq s < u_{i+1} \\ 0 & \text{otherwise} \end{cases} \quad (3.76)$$

$$N_{i,k_s^*}(s) = \frac{s - u_i}{u_{i+k_s^*-1} - u_i} N_{i,k_s^*-1}(s) + \frac{u_{i+k_s^*} - s}{u_{i+k_s^*} - u_{i+1}} N_{i+1,k_s^*-1}(s) \quad (3.77)$$

where u_i are the elements of the desired knot vector, which will be presented in the next section, and $2 \leq k_s^* \leq k_s$ refer to the intermediate and final orders of the evaluated basis functions.

Similarly to the Bernstein polynomials, one of the basic properties of B-spline basis functions is that for any parameter s , the total sum of the functions is equal to unity:

$$\sum_{i=1}^n N_{i,k_s}(s) = 1 \quad (3.78)$$

where, as previously, each basis function $N_{i,k_s}(s)$ has positive values, but now can also be zero for a specific span. For the Bernstein polynomials, $b_{i,n}(s) \approx 0$ only if a large number of points is used (cf. Fig. 3.9), whereas for B-Splines, $N_{i,k_s}(s)$ can be zero depending on the type of knot vectors and the fact that $N_{i,1}(s) = 0$ if $s \notin [u_i, u_{i+1})$ (as shown later in Fig. 3.10). Overall, since the mathematical structure of B-Splines is the same as the Bezier curves, the control polygon formed by the control points controls completely the curve, which is obliged to follow its shape.

ii) Knot Vectors

The set of the real numbers in the interval $[u_1, u_p]$ corresponds to the knot vectors which are the most important parameters of B-splines. The choice of a knot vector sequence influences significantly the B-spline basis functions, and consequently the form of the curve. This interval is responsible for the range and the type of influence each function has upon the parameter space [109], and thus, the effect each control point has on the curve. Moreover, the type of the vector has a significant effect upon the continuity of the resulting curve.

The basic requirement a knot sequence should always obey is $u_i \leq u_{i+1}$. The total number p of the real numbers forming the knot vector sequence is defined by the sum of the desired basis function order k_s , and the number of the control points (n) which define the control polygon:

$$p = k_s + n \tag{3.79}$$

The two major categories which classify the knot vectors are the *periodic* and the *open* knot vectors [99]. The difference in the structure between these two classifications is that the periodic knot vectors always have p number of knots with increasing knot values in the form:

$$[u_1, u_2, \dots, u_{p-1}, u_p] \quad , \quad u_i \leq u_{i+1} \tag{3.80}$$

whereas, the open knot vectors have a compulsory multiplicity, m_{op} , in the beginning and at the end of the vector sequence of the total p number of knots, equal to the desired grade k_s of the basis functions:

$$\underbrace{[u_1, \dots, u_{k_s}, \dots, u_{p-k_s+1}, \dots, u_p]}_{m_{op}} \quad , \quad u_1 = \dots = u_{k_s} \quad \text{and} \quad u_{p-k_s+1} = \dots = u_p \tag{3.81}$$

The two main categories are further subdivided in uniform and non-uniform sequences. Periodic uniform knot vectors form a sequence of equally increasing real numbers, as in the following example for a knot vector ($p = 8$) which is appropriate for a control polygon with five control points ($n = 5$) and basis functions of third order ($k_s = 3$):

$$[1 \ 2 \ 3 \ 4 \ 5 \ 6 \ 7 \ 8]$$

While for the same example, open-uniform knot vectors have equally spaced internal values and a multiplicity, $m_{op} = k_s$, only at the beginning and at the end of the sequence as

$$[\underbrace{0 \ 0 \ 0}_{k_s = 3} \ 1 \ 2 \ \underbrace{3 \ 3 \ 3}_{k_s = 3}]$$

Unlike uniform vectors, for non-uniform the vector elements u_i are unequally spaced and they can additionally exhibit a multiplicity m_{in} at the internal knots, like it is shown

below for the same case ($p = 8$) of a control polygon with five control points ($n = 5$) and basis functions of third order ($k_s = 3$) for a periodic sequence:

$$[0 \quad 2.1 \quad \overbrace{3.4 \quad 3.4}^{m_{\text{in}}} \quad 5.2 \quad 5.2 \quad 6.9 \quad 7]$$

or for an open sequence:

$$[\underbrace{0 \quad 0 \quad 0}_{k_s = 3} \quad \overbrace{2.3 \quad 2.3}^{m_{\text{in}}} \quad \underbrace{3 \quad 3 \quad 3}_{k_s = 3}]$$

By using multiple interior knot values one can generate cusps in the curve introducing reduced differentiability for the basis functions where the curve is $C^{k_s - m_{\text{in}} - 1}$ continuous [99, 100].

All these different types of knot sequences generate curves of a different kind and therefore, unlike the FFD technique, the existence of the knot vectors offers an additional tool for manipulating the curve. Knot vector values are usually used in normalized form to be consistent with the parameterised domain $s \in [0, 1]$. From this point and onwards, all knot vectors will be represented considering that $u_i \in [0, 1]$.

Figure 3.10 illustrates four different B-Spline basis functions, generated for a control polygon defined by five control points ($n = 5$) for an order $k_s = 3$, considering different knot vectors. Figure 3.10a, shows the form of the five basis functions (one for each control point) when a periodic uniform knot vector is used. It can be seen that all functions have the same form with an apparent periodicity on the way they act on the parameter space. For this particular case, it can be seen that Eq. (3.78) is not valid at the start and the end points of the parameter space and only holds in the interval $u_i \in [2/7, 5/7]$. This in fact affects the curve representation, with the first and last control points not coinciding with curve [100]. Therefore, the periodic knot vectors are not used and are only reported here as an alternative tool.

Figures 3.10b to 3.10c display the different distribution of the basis functions when open knot vectors are used. It can be seen, that Eq. (3.78) is valid for all three cases in the full parameter space. Although a non-uniform open vector is considered for the

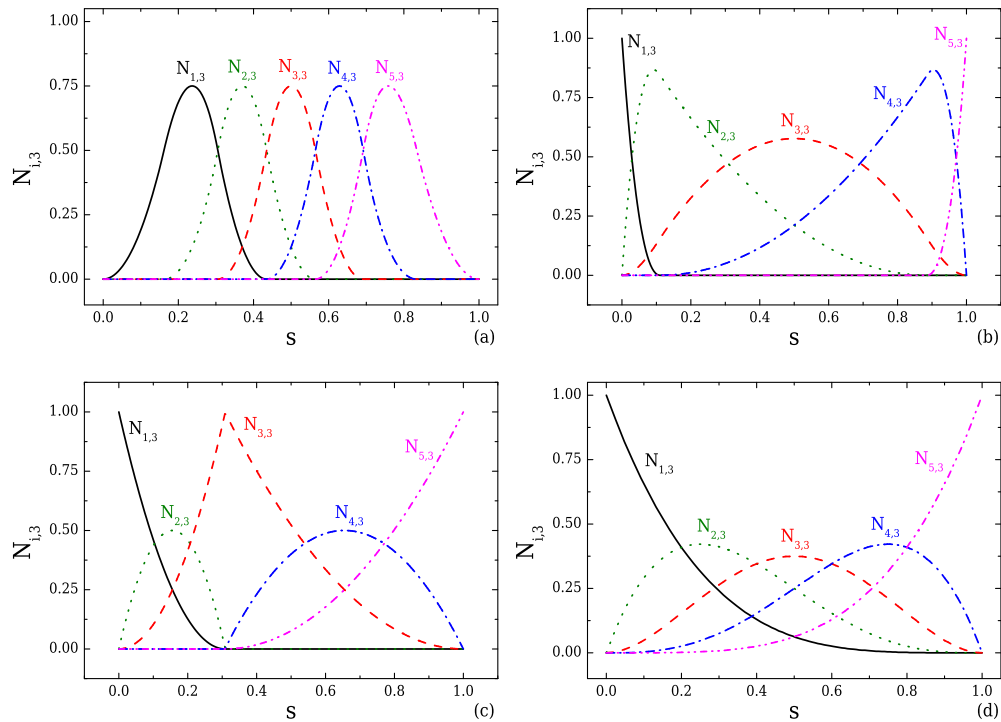


Figure 3.10. Bernstein basis functions for five control points and a curve with $k_s = 3$, for a uniform periodic knot vector $[0, 1/7, 2/7, 3/7, 4/7, 5/7, 6/7, 1]$ (a), an open non-uniform $[0, 0, 0, 0.4/3, 2.6/3, 1, 1, 1]$ (b), an open non-uniform $[0, 0, 0, 1/3, 1/3, 1, 1, 1]$ with inner multiplicity $m_{in} = 2$ (c) and an open uniform $[0, 0, 0, 0, 1, 1, 1, 1]$ with $m_{op} = k_s$ (d).

case of Fig. 3.10b, the functions are distributed symmetrically since the knot vectors are spaced symmetrically. On the other hand in Fig. 3.10c, the inner multiplicity of the knot vector results the cusp in $N_{3,3}$ and the non-uniform nature of the sequence to an asymmetric distribution of the functions in the parameter space. Finally in Fig. 3.10d, the special case when B-splines are reproducing Bezier curves and the basis functions N_{i,k_s} are equal to Bernstein polynomials is shown (compare with Fig. 3.9c). This is achieved for an open uniform knot vector when the desired order k_s is equal to the number of control points n .

These examples illustrate the ability provided by the B-Splines to generate different curves by following different approaches. Clearly, very important is the fact that one can manipulate the generated curve keeping the same number of control points by changing only the knot vectors or the order k_s of the basis functions.

iii) B-Spline Surfaces

Moving to two-dimensional (2D) objects, the appropriate equations for generating and manipulating surfaces using the B-spline theory is briefly explained here. A surface designed by a B-spline lattice (similarly to FFD), is mathematically defined by the following relationship [99]:

$$\mathbf{Q}(s, t) = \sum_{i=1}^n \sum_{j=1}^m \mathbf{B}_{i,j} N_{i,k_s}(s) M_{j,k_t}(t) \quad (3.82)$$

$$s_{min} \leq s < s_{max} \quad , \quad 2 \leq k_s \leq n$$

$$t_{min} \leq t < t_{max} \quad , \quad 2 \leq k_t \leq m$$

where similarly to Eq. (3.75), N_{i,k_s} and M_{j,k_t} are the B-spline basis functions acting on the the two parameterised directions s , t , respectively. The total control points, n and m , considered along each direction form the 2D control lattice, with the desired order of the basis functions imposed by k_s and k_t . As previously the Cox de Boor [108] recursive formula is employed for evaluating the basis functions N_{i,k_s} and M_{j,k_t} :

$$N_{i,1}(s) = \begin{cases} 1 & u_i \leq s < u_{i+1} \\ 0 & \text{otherwise} \end{cases} \quad (3.83)$$

$$N_{i,k_s^*}(s) = \frac{s - u_i}{u_{i+k_s^*-1} - u_i} N_{i,k_s^*-1}(s) + \frac{u_{i+k_s^*} - s}{u_{i+k_s^*} - u_{i+1}} N_{i+1,k_s^*-1}(s) \quad (3.84)$$

$$M_{j,1}(t) = \begin{cases} 1 & v_j \leq t < v_{j+1} \\ 0 & \text{otherwise} \end{cases} \quad (3.85)$$

$$M_{j,k_t^*}(t) = \frac{t - v_j}{v_{j+k_t^*-1} - v_j} M_{j,k_t^*-1}(t) + \frac{v_{j+k_t^*} - t}{v_{j+k_t^*} - v_{j+1}} M_{j+1,k_t^*-1}(t) \quad (3.86)$$

where u_i and v_j are the knot vectors elements for both directions and as previously, $2 \leq k_s^* \leq k_s$ and $2 \leq k_t^* \leq k_t$ represent the order of the evaluated basis functions.

As in the case of one dimension, the shape and the character of the curve are significantly influenced by the knot vectors, u_i and v_j which need not be the same

[99, 100], i.e one can be a periodic vector and the other have an open form. More significantly, the special case of Bezier curves and surfaces and thus the FFD method, is reproduced when the number of control points is equal to the order of the desirable basis functions for each direction, and the knot vectors for each direction are open uniform with multiplicity $m_{\text{op}}^s = k_s = n$ and $m_{\text{op}}^t = k_t = m$.

3.4.4 Non-Uniform Rational B-Splines (NURBS)

Non-Uniform Rational B-splines are currently the basic tool for representing and modelling curves and surfaces in computer graphics, and for that it is used by the majority of CAD programs [110–112]. The mathematical formulation of NURBS used in this work is based on rational B-splines, and they have been proven a very useful tool for geometrical modelling [109, 111–115]. An extensive analysis about the analytical functions and properties of NURBS information can be found in Piegl and Tiler [100], Rogers [99] and Dimas and Briasoulis [112].

i) NURBS Curves

To obtain a NURBS curve, the number of control points B_i that form the control polygon for a B-spline must be defined together with the desired order, k_s , of the polynomial basis functions and the resulted knot vector. Then the curve is mathematically defined as

$$\mathbf{P}(s) = \sum_{i=1}^n \mathbf{B}_i R_{i,k_s}(s) \quad s_{\min} \leq s < s_{\max} \quad (3.87)$$

where $R_{i,k_s}(s)$ are the rational basis functions, defined from the following relationship:

$$R_{i,k_s}(s) = \frac{w_i N_{i,k_s}(s)}{\sum_{i=1}^n w_i N_{i,k_s}(s)} \quad w_i \geq 0 \quad (3.88)$$

with $N_{i,k_s}(s)$ being the B-Spline basis functions as previously (cf. Eq. (3.77)), and w_i the weight that each control point has for affecting the curve. The ability to use different weight for each control point is one of the major differences relative to B-Splines, since one can determine the level of influence that each control point has on the curve.

Rational basis functions are a generalisation of B-spline basis functions and hold the majority of the characteristics of B-Splines [99,112]. Consequently, for each rational basis function $R_{i,j}$ the summation for any parameter s , should be equal to unity similarly to Eq. (3.78):

$$\sum_{i=1}^{n+1} R_{i,k_s}(s) = 1 \tag{3.89}$$

In Fig. 3.11 the rational basis functions $R_{i,3}$ for $n = 5$ control points and $k_s = 3$ are plotted for various weight values for the control point B_3 , while the remaining points have constant and equal to unity weights. Figure 3.11a shows that when $w_3 = 0$, the rational function $R_{3,3}$ is zero and thus, the control point B_3 will have no influence upon the final shape of the curve which will be completely controlled by the remaining four points which dominate the parameterised space. As the weight of B_3 is increased, the effect of $R_{3,3}$ and therefore the influence of the position of the control point B_3 ,

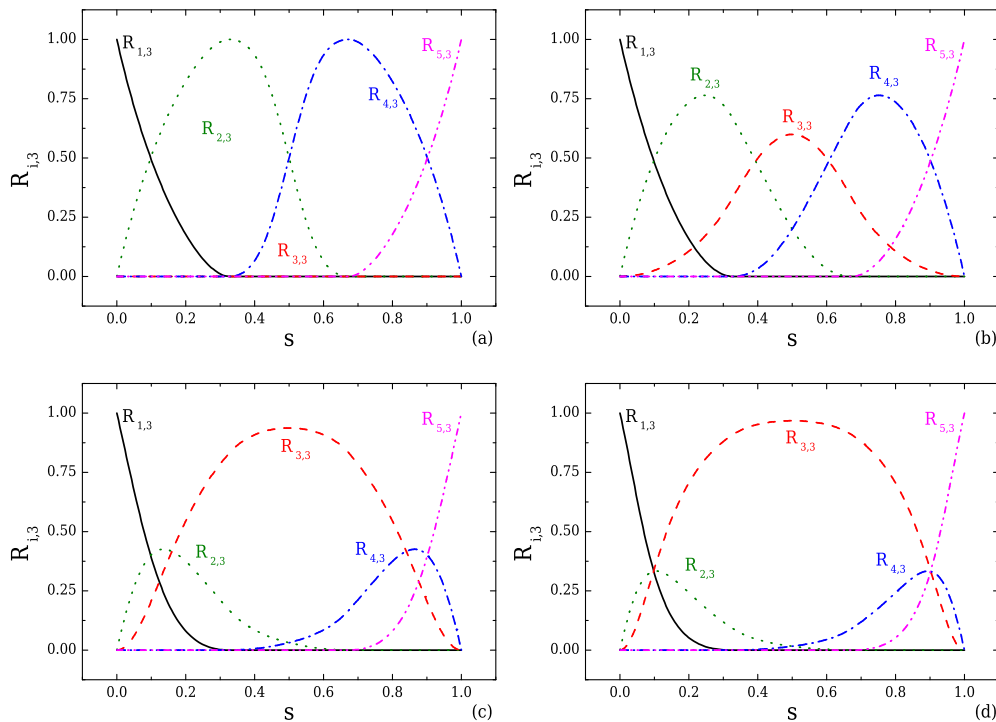


Figure 3.11. Rational basis functions for five control points and $k_s = 3$ for an open uniform knot vector $[0 \ 0 \ 0 \ 1/3 \ 2/3 \ 1 \ 1 \ 1]$ for $w_3 = 0$ (a), $w_3 = 0.5$ (b), $w_3 = 5$ (c), and $w_3 = 10$ (d).

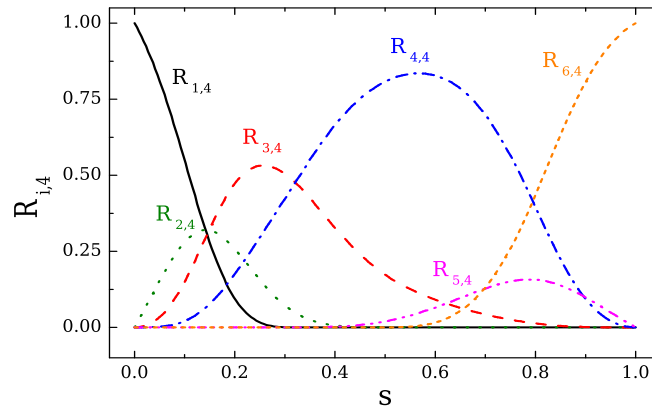


Figure 3.12. Rational basis functions for six control points of order $k_s = 4$, with different weights for each control point and a uniform knot vector $[0 \ 0 \ 0 \ 0 \ 1/3 \ 2/3 \ 1 \ 1 \ 1 \ 1]$.

will affect the final shape. For the cases of Figs. 3.11c and 3.11d the weight of B_3 is much larger than the remaining and its movements will affect a large part of the parameterised domain. Figure 3.12 illustrates a case where the weight of every control point is different. Therefore, it is clear that one has many options when using NURBS for generating and manipulating curves with the additional advantage of controlling the influence of each control point individually. When all the weights are equal to unity it is clear from Eqs. (3.75) and (3.88) that $R_{i,k_s}(s) \equiv N_{i,k_s}(s)$. Therefore with NURBS, the Bernstein polynomial basis can be reproduced when the knot vector is open uniform with $m_{op} = k_s = n$ and $w_i = 1$ [99, 100].

ii) NURBS Surfaces

The mathematical formulation of NURBS in 2D to manipulate and generate surfaces is obtained by a similar expression to that used for the B-Splines (cf. Eq. (3.82)) as

$$\mathbf{Q}(s, t) = \sum_{i=1}^n \sum_{j=1}^m \mathbf{B}_{i,j} S_{i,j}(s, t) \quad (3.90)$$

The variable $S_{i,j}(s, t)$ corresponds to the bivariate rational surface basis functions, evaluated by

$$S_{i,j}(s, t) = \frac{w_{i,j} N_{i,k_s}(s) M_{j,k_t}(t)}{\sum_{i=1}^n \sum_{j=1}^m w_{i,j} N_{i,k_s}(s) M_{j,k_t}(t)} \quad (3.91)$$

where $N_{i,k_s}(s)$ and $M_{j,k_t}(t)$ are the B-Spline basis functions evaluated using the Cox de Boor formula in Eqs. (3.83) to (3.86) and $w_{i,j}$ is the weight of each control point $B_{i,j}$. For a NURBS surface the sum of the rational basis functions for any value of the parameters s, t should be equal to unity:

$$\sum_{i=1}^n S_{i,j}(s, t) = 1 \quad (3.92)$$

where $S_{i,j}(s, t)$ is a direct product of the basis functions $N_{i,k_s}(s)$, $M_{j,k_t}(t)$ and not a product of the rational basis function, of each parameter space s, t , given from equation Eq. (3.88). Thus, it will have similar analytical and geometrical properties to the non-rational counterparts [99].

In a similar manner to the deformation applied by a two dimensional FFD lattice, presented in Section 3.4.2, a variety of different deformations can be obtained as shown in Fig. 3.13 for a two dimensional NURBS lattice. The lattice which surrounds the object is uniform and consists of $(n \times m) = (5 \times 2)$ control points and every point that

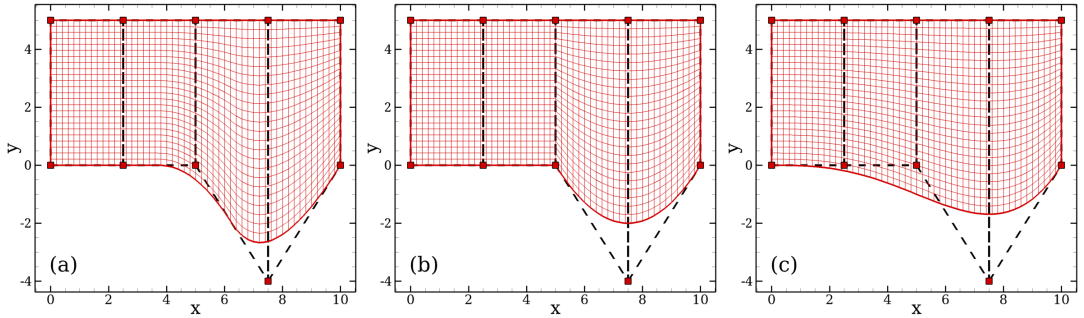


Figure 3.13. Different object deformations obtained by a lattice with the same number of control points $(n \times m) = (5 \times 2)$ but with different properties. The vector along the y-direction is an open uniform with $k_s = 2$ for all cases whereas along x-direction (a) $k_s = 3$, $u_p = [0 \ 0 \ 0 \ 1/3 \ 2/3 \ 1 \ 1 \ 1]$, (b) $k_s = 3$, $u_p = [0 \ 0 \ 0 \ 1/2 \ 1/2 \ 1 \ 1 \ 1]$ with inner multiplicity $m_{in} = 2$ (c) and $u_p = [0 \ 0 \ 0 \ 0 \ 1 \ 1 \ 1 \ 1]$ with $m_{op} = k_s = n$ (corresponding to FFD).

is moved from its initial position results in a deformation to the embedded object. Although the number of control points (n, m) , their weights $(w_{i,j})$ and the lattice deformation are the same for all three cases, the order of the basis polynomials and the knot vectors are different, resulting in different object deformations. Additionally, for all cases the same conditions are applied along the y -direction and consequently for the t parameter space, where an open uniform vector is considered, $u_q = [0 \ 0 \ 1 \ 1]$, for $m = 2$ and $k_t = 2$. The deformation in Fig. 3.13a is obtained by an open uniform vector $u_p = [0 \ 0 \ 0 \ 1/3 \ 2/3 \ 1 \ 1 \ 1]$, considered along the s parameter space for basis functions of order $k_s = 3$ whereas, the deformation in Fig. 3.13b is resulted by an open uniform vector $u_p = [0 \ 0 \ 0 \ 1/2 \ 1/2 \ 1 \ 1 \ 1]$, with an internal multiplicity $m_{in} = 2$ along the s parameter space and basis functions of order $k_s = 3$. It can be seen that as discussed above, the internal multiplicity introduces a span of zero length. Therefore, the support of the function is reduced and results in a sudden deformation with a form of a cusp [99,100]. The continuity is affected locally [99], forcing the curve to obtain a local discontinuity since $C^{k_s-m_{in}-1} = C^0$ around $s = 1/2$, which results in the cusp observed at $x = 5$. On the contrary, for the open uniform vector of Fig. 3.13a the line continuity is preserved. Finally the deformation in Fig. 3.13c is generated by the special case where $m_{op} = k_s = n$ and thus, $u_p = [0 \ 0 \ 0 \ 0 \ 1 \ 1 \ 1 \ 1]$, employing that way the Bernstein basis functions for deforming the object which produce Bezier curves. Consequently, for this case the two dimensional NURBS lattice performs as an FFD lattice. The internal mesh-lines are also affected by the point movement as can be seen that for all three cases of Fig. 3.13. Similarly to the FFD technique, the mesh-lines are affected by all control points. For example it can be seen that the imposed discontinuity in Fig. 3.13b vanishes for the mesh lines that are closer to the control points along $y = 5$.

Concluding, an important ability of the convex hull of NURBS is that three or more collinear points in the control point lattice, will force the curve to coincide with a part of the control polygon. This characteristic is very useful when there is a need for the boundary to be exactly in a desired position, as in the case of the studies presented in Chapter 5. An example is shown in Fig. 3.14 for the case of

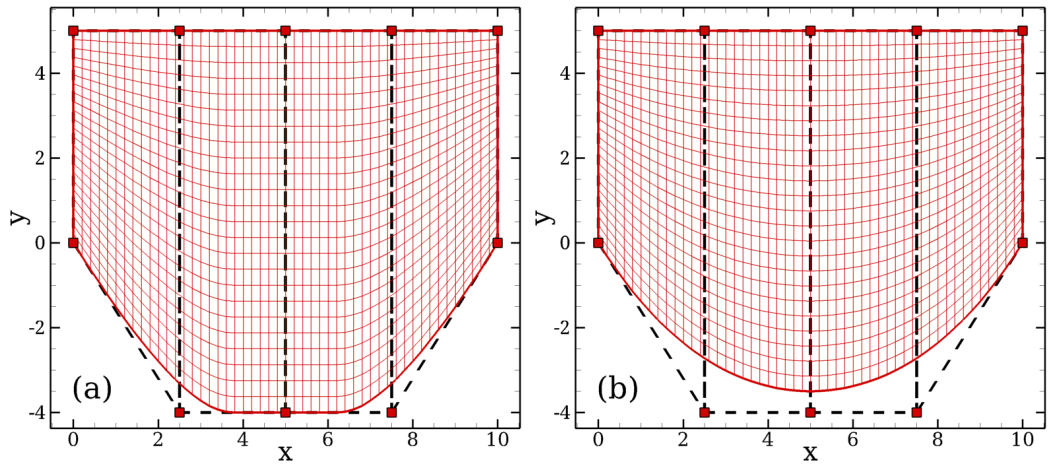


Figure 3.14. Effect of three collinear points of the NURBS lattice with $(n \times m) = (5 \times 2)$ and different properties. The vector along the y-direction is an open uniform with $ks = 2$ for all cases whereas along x-direction (a) $ks = 3$, $u_p = [0 \ 0 \ 0 \ 1/3 \ 2/3 \ 1 \ 1 \ 1]$, (b) and $u_p = [0 \ 0 \ 0 \ 0 \ 1 \ 1 \ 1 \ 1]$ with $m_{op} = ks = n$ (corresponding to FFD).

$u_p = [0 \ 0 \ 0 \ 1/3 \ 2/3 \ 1 \ 1 \ 1]$ and $ks = 3$ in which the curve coincides with a part of the control polygon when using NURBS (Fig. 3.14a), while for the FFD technique ($u_p = [0 \ 0 \ 0 \ 0 \ 1 \ 1 \ 1 \ 1]$), the curve will coincide only with the last points of the polygon as expected (Fig. 3.14b).

All these examples and the corresponding comparisons with the FFD technique indicate that for design purposes NURBS are more precise and the deformation applied can be directed and controlled in a more versatile way. For any designer who uses NURBS or B-splines it is clear that the designing tools and options for manipulating the embedded objects and obtaining the desired shapes are plentiful.

iii) Three dimensional design using NURBS

Lamousin and Waggenspack [107], influenced by the FFD technique of Sederberg and Parry [105], introduced a similar approach where a deformable lattice is used for embedding the physical object and deforming it. Figure 3.15 illustrates a non-uniform NURBS lattice used to surround the physical object. The 3D NURBS lattice is formed by the control points $B_{i,j,k}$ at the physical space (x,y,z) which have weights $w_{i,j,k}$. Additionally, three open uniform knot vectors are employed, one for each parametric

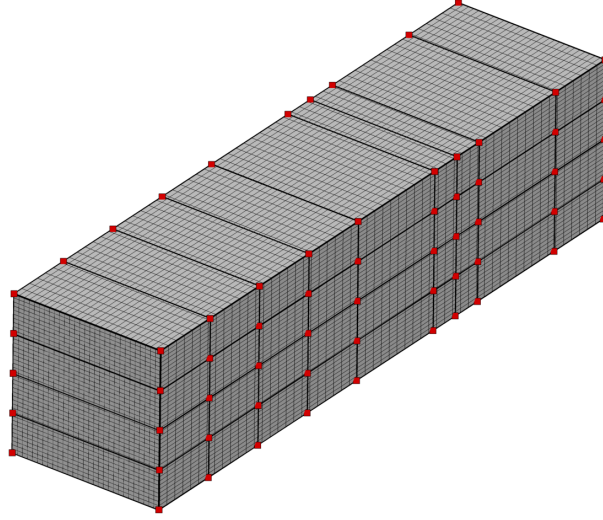


Figure 3.15. Non-uniformly spaced NURBS lattice and the embedded physical domain. The *square* symbols correspond to the control points of the NURBS lattice.

direction (s, t, w) for controlling the distribution of the basis functions and therefore the region of influence of each control point. As previously, by moving each control point from its initial position, the embedded object is deformed based on the extension of Eq. (3.90) in the 3D space:

$$\mathbf{Q}(s, t, w) = \sum_{i=1}^n \sum_{j=1}^m \sum_{k=1}^l \mathbf{B}_{i,j,k} S_{i,j,k}(s, t, w) \quad (3.93)$$

with

$$S_{i,j,k}(s, t, w) = \frac{w_{i,j,k} N_{i,k_s}^1(s) N_{j,k_t}^2(t) N_{i,k_w}^3(w)}{\sum_{i=1}^n \sum_{j=1}^m \sum_{k=1}^l w_{i,j,k} N_{i,k_s}^1(s) N_{j,k_t}^2(t) N_{i,k_w}^3(w)} \quad (3.94)$$

where as previously k_s , k_t , k_w correspond to the order of basis functions used at each parametric coordinate s , t , w and $N_{i,k_s}^1(s)$, $N_{j,k_t}^2(t)$, $N_{i,k_w}^3(w)$ are the B-spline basis polynomial functions, which as usual are evaluated using the Cox de Boor [108] formula (cf. Eqs. (3.83) and (3.85) to (3.86) for 2D). For each parametric coordinate s , t and w a knot vector sequence consisted by p , q and r total elements is defined, based on the number of control points placed along each direction and the desired order of the basis

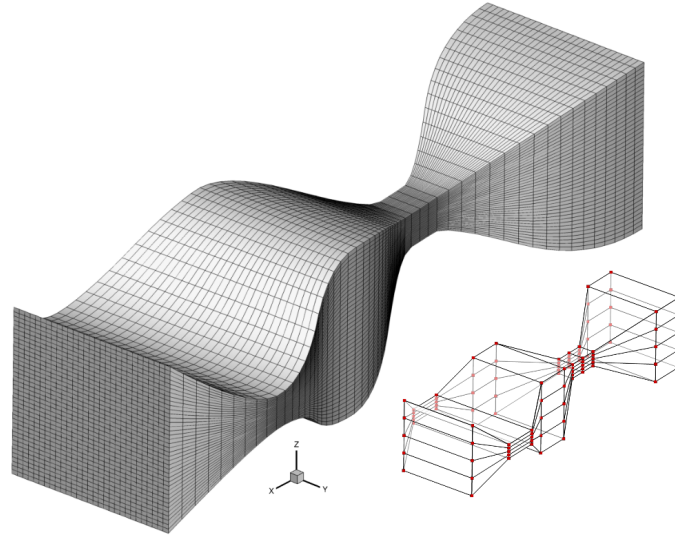


Figure 3.16. 3D deformation of an initial shape from the NURBS lattice. The small right hand image illustrates the NURBS lattice with the positions of the control points.

functions:

$$p = n + k_s \quad , \quad q = m + k_t \quad , \quad r = l + k_w \quad (3.95)$$

A change of the lattice control points position results the deformation of the embedded object as shown in Fig. 3.16, and in a similar way as was done for the FFD technique. However, the deformation obtained using a NURBS lattice is calculated from Eq. (3.93). As noted before, the knot vectors controlling the deformation along each direction are not necessarily the same [99], and are only chosen based on designing needs. The polynomial functions defined for each directions at the parameter space s, t, w , can be of a different order.

***iv)* NURBS parameterised domain: effect on mesh characteristics**

As mentioned previously, techniques like FFD and NURBS originate from computer graphics science, a field that is interested mostly in shape deformation. In CFD however, numerical simulations are performed to examine physical phenomena in the domain and are strongly influenced by the quality of the numerical grid that discretises the physical domain under investigation [97]. As discussed, NURBS technique is a great tool for designing, manipulating and optimising shapes of engineering interest. By manipulating

the shape of an object using this technique, one also changes the parameterised domain of the numerical grid which is strongly influenced by the local properties of NURBS [110].

Figures 3.17a and 3.17b, demonstrate the distortion of the mesh of the initial uniform spaced domain, immediately after a uniform NURBS lattice is used to surround the object. It can be seen that although the boundaries remain unaffected since there is no control point movement, the interior mesh lines (cf. Fig. 3.17b) are packed to the centre of the domain, resulting in a bad quality mesh. The lattice is composed by $(n \times m)=(5 \times 5)$ control points with $w_{i,j} = 1$, while the basis functions considered at each direction are of the same order $k_s = k_t = 3$ and their influence is controlled by the same open uniform knot vector.

Yu and Soni [110] proposed a solution for this effect of NURBS by considering the usage of a parameterisation scheme. Considering a 2D domain, the use of an iterative algorithm was presented that employs three parameterised domains: (s_1, t_1) , (s_2, t_2) and (s_3, t_3) . These domains are appropriate for generating a modified parameterised domain that will result in the desired numerical mesh. The domain (s_2, t_2) is related to the parameterised spaces before the NURBS lattice surrounds the desired object and is, therefore, evaluated in the beginning of the parameterisation procedure and remains unchanged throughout. The domain (s_3, t_3) is related to the shifted parameterised space when the lattice is applied and contains the information for the shifted inner mesh-lines. Finally, the domain (s_1, t_1) is associated with the final and desired mesh-line

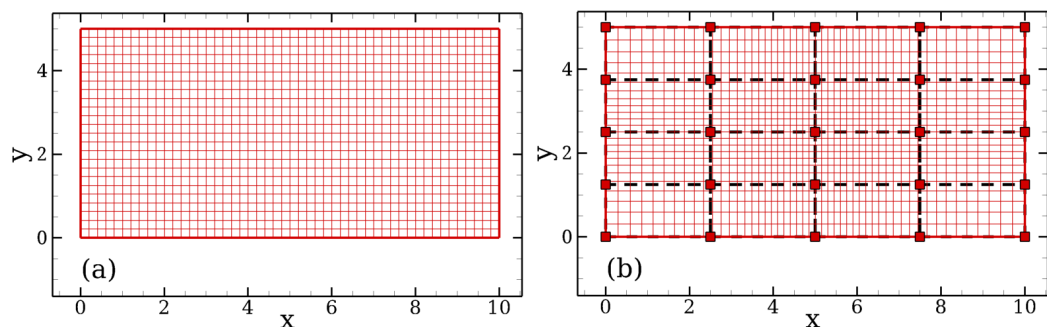


Figure 3.17. Initial uniform mesh (a) and distorted mesh-lines (b) because of the strong local properties of NURBS lattice that embeds the object.

distribution, which is then used for applying the deformations of the lattice on the object.

Using as an example the 2D uniform numerical grid of Fig. 3.17a, assuming that it consists of $n_{tot} = n_x \times n_y$ total nodes, in order to obtain a mesh of the same quality instead of the distorted mesh of Fig. 3.17b the procedure proposed by Yu and Soni [110] has two steps: first, it is considered that $(s_1, t_1) = (s_3, t_3)$; second, based on the absolute difference at each nodal position between s_2 and s_3 , $|ds| = |s_2(ip) - s_3(ip)|$, the nodal values of s_1 are updated as:

$$s_1(ip) = \begin{cases} s_1(ip) & \text{if } |ds| < \varepsilon \\ s_1(ip) + ds(s_1(ip) - s_1(ip - 1)) & \text{if } |ds| > \varepsilon, ds < 0 \\ s_1(ip) + ds(s_1(ip + 1) - s_1(ip)) & \text{if } |ds| > \varepsilon, ds > 0 \end{cases} \quad (3.96)$$

where the index ip holds the global numbering of each node ($ip = i_x + (i_y - 1)n_{tot}$, $1 < i_x < n_x$ and $1 < i_y < n_y$) and ε corresponds to a specific tolerance. The iterative procedure is repeated starting from the updated values of the parameterised space s_1 until the desired tolerance is reached. The same procedure is applied for the parameterised t -space and for the parameterised w -space when the domain is 3D (s, t, w) . Figure 3.18 illustrates all three parameterised domains $((s_1, t_1), (s_2, t_2)$ and $(s_3, t_3))$ that prevent the mesh distortion of Fig. 3.17b, and will result in a numerical grid as in Fig. 3.17a. The parameterised domain shown in Fig. 3.18a, holds the values for the

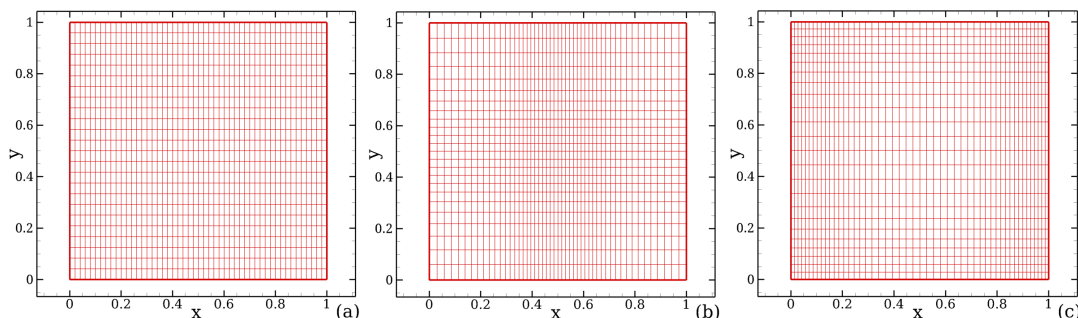


Figure 3.18. Parameterised domains corresponding to (a) the desired s_2, t_2 , (b) the intermediate and distorted s_3, t_3 and (c) the final s_1, t_1 used for obtaining a uniform mesh as in Fig. 3.17a.

(s_2, t_2) domain and remains as is (corresponding to the good-quality/desired initial domain). The intermediate domain (s_3, t_3) , shown in Fig. 3.18b, changes during the iterative procedure based on Eq. (3.96). When the iterative procedure is over, the appropriate parameterised domain (s_1, t_1) that will generate a good-quality/desired grid is obtained, as shown in Fig. 3.18c. Examining the mesh lines of the final parameterised domain (s_1, t_1) , it is clear that they are distributed in such a way to counter the effect of the distorted domain (s_3, t_3) forcing the basis functions to generate a uniformly distributed mesh.

This parameterisation scheme is crucial for the cases where the NURBS lattice is non-uniform since the distortion will be more enhanced. An uneven spatial distribution of the lattice control points will generate a more intense packing of the mesh-lines at the location where the lattice control points are closer.

“Nature uses only the longest threads to weave her patterns, so that each small piece of her fabric reveals the organization of the entire tapestry.”

R. Feynman

Chapter 4

Shear dominated designs

A design rule based on a biomimetic principle inspired directly from natural bifurcating systems is proposed here. The solution of the biomimetic set of equations provides the appropriate dimensions for designing microfluidic bifurcating networks, able to generate specific and well controlled characteristics. The background theory related to the biomimetic design considers that the flow is fully developed and is extended here to consider power-law fluids, introduced in [Section 2.2.1](#). The applicability of the theory is investigated numerically considering extensive three dimensional numerical simulations for both power-law and Newtonian fluids. Three basic configurations are considered for the validation, employing networks that are able to generate constant, positive and negative shear-stress gradients and are examined under creeping flow conditions unless stated otherwise.

Part of the results have been published in:

K. Zografos, R. W. Barber, D. Emerson and M. S. N. Oliveira, “*A design rule for constant depth microfluidic networks for power law fluids*”, *Microfluid Nanofluid*, vol. **19**, pp. 737-749, 2015.

K. Zografos, R. W. Barber, D. R. Emerson, and M. S. N. Oliveira, “*Constant depth microfluidic networks based on a generalised Murray’s law for Newtonian and power-law fluids.*”, in *Proceedings of the 4th Micro and Nano Flows Conference*, 2014.

4.1 Introduction

Over millions of years, biological systems have evolved through the numerous trial-and-error procedures of natural selection to perfect design solutions that often surpass those developed by Man. The field of *biomimetics* has turned into an increasingly active area of research that studies and imitates naturally-inspired systems in order to advance modern technology through the use of innovative materials and geometrical optimisation.

In this chapter, biomimetic principles are used for the design and optimisation of bifurcating fluid distribution networks. Branching networks are numerous in natural systems and can be found in many processes which are often responsible for controlling fluids that present complex rheological behaviour. Examples include the vascular system that drives blood and other vital substances throughout the body, the oxygen transfer system in the human lungs, or the water transport through the xylem in the bifurcating networks of plants and trees [116].

Microfluidics offers the possibility of mimicking the natural environment at the dimensional scale of many biological processes [117]. Hence, bifurcating microfluidic devices may find applications in many processes, such as blood-plasma separation [118–120], which exploits the plasma skimming concept in which red blood cells concentrate in the high flow rate region away from walls [4]. Another example is the use of micro-fabricated branching networks to design applications that can artificially assist the gas exchange between blood and air in the respiratory system of the human body [121,122].

The ability of microfluidics to provide adequate and controlled flow conditions may also benefit areas such as stem cell research [123] and tissue engineering [124,125]. Microfluidics could assist studies related to the deformability of red blood cells [126] and those investigating blood flow mechanisms, providing important information for diagnosing diseases and treating patients [127]. As recently pointed out by DesRochers *et al.* [128], micro-fabricated networks can be used as 3D cell culture micro-environments, in order to generate cell interactions that are unlikely to be replicated in 2D techniques, providing suitable conditions to carry out studies related to kidney diseases. In

addition, bifurcating structures offer the ability to carry out many experiments in parallel, a characteristic referred to as “scaling out”. An example of this is the exposure of shear sensitive cells to different flow conditions being investigated simultaneously in a single experiment. Microfluidic bifurcating networks have also been used by various authors in biological and chemical applications to generate precise concentration gradients [129–132] due to their superior performance compared with conventional techniques, or as micro-structure evaporators, for which better and more accurate designs are essential in order to achieve the best possible performance [133]. Recently, Liao *et al.* [134] fabricated a microfluidic bifurcating network based on Murray’s law [135], in order to perform as a planar reactor for water purification. The authors compared the performance of the biomimetic channel with a non-biomimetic designed configuration and reported a more efficient degradation procedure. Moreover, the importance of fluid flows in microfluidic bifurcating networks and the need to exploit the advantages provided, influenced Damiri and Bardaweel to propose a design theory that considers Newtonian fluid flow in microfluidic branching channels [136]. Their theory was able to predict the average wall shear-stress and the hydraulic resistance along the network.

Most of the scientific fields of interest referred to previously require the handling of non-Newtonian fluids that exhibit shear-dependent viscosity (i.e. shear-thinning or shear-thickening behaviour). Hence, it is of great interest to develop customised designs that offer the ability to control the flow of these fluids in lab-on-a-chip networks by generating precise shear-stress distributions at the walls and specific flow resistances along the microfluidic networks to suit a particular application.

In this chapter, a biomimetic rule based on the optimum relationship expressed by Murray [135] is proposed for designing manifolds that can produce desired flow characteristics for non-Newtonian, power-law fluids in microfluidic planar devices of rectangular cross-section. In Sections 4.2 and 4.3 a theoretical analysis of the design rule is presented, leading to the basic set of equations that needs to be solved for designing an appropriate manifold. Section 4.4 discusses some considerations related to the geometrical set up, and in Section 4.5 the validity of the biomimetic rule is examined, using numerical simulations and focusing on the estimation of the average shear-stress

at the walls of each generation and the flow resistance along the bifurcating networks. Concluding remarks are summarised in [Section 4.6](#), where further improvements of the final design are also discussed.

4.2 Biomimetic design of networks for Newtonian fluids

In 1926, Murray [135] investigated the blood flow in the vascular system of living organisms, considering they are composed of branches of circular cross-section. Inspired by the generalised principle of the maintenance of steady states, he discussed the applicability of the *principle of minimum work* in order to express quantitative laws, able to provide useful information for a biological system. In his studies he proposed that the total power, \mathcal{P}_{tot} , of a vascular system should be considered as a combination of two main processes. Initially the organism has to spend an amount of energy, for overcoming the viscous losses due to the blood transfer in the circulatory system (corresponding to a power \mathcal{P}_v), whereas an additional amount of energy should be provided for maintaining the vital metabolic processes (corresponding to a power \mathcal{P}_m), expressed as the “*cost of blood volume*”:

$$\mathcal{P}_{tot} = \mathcal{P}_v + \mathcal{P}_m \quad (4.1)$$

Based on the assumption that the flow is fully developed everywhere in the vascular system and that each segment is defined by a length L and a diameter ϕ , then the power per unit length, \mathcal{P}_v , can be expressed with the use of the Hagen-Poiseuille equation as

$$\mathcal{P}_v = \frac{128\eta Q^2}{\pi\phi^4} \quad (4.2)$$

where Q is the flow rate and η is the fluid viscosity. Murray assumed that the power of the metabolic processes per unit length is associated to the volume of the segment and expressed as

$$\mathcal{P}_m = \frac{b\pi\phi^2}{4} \quad (4.3)$$

where b is a metabolic parameter. Following this analysis and based on the assumption of the minimum work principle he suggested that, “*The amount of biological work*

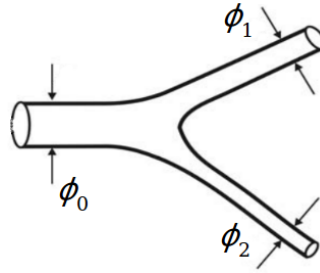


Figure 4.1. Bifurcation showing a parent vessel splitting into two daughter vessels.

required to operate and maintain the system should be minimised through an optimum design” [135]:

$$\frac{d\mathcal{P}_{tot}}{dr} = -\frac{1024\eta Q^2}{\pi\phi^5} + b\pi\phi = 0 \quad (4.4)$$

and derived the optimum relationship between the segment’s optimum diameter and the flow rate:

$$Q = M\phi^3 \quad (4.5)$$

where $M = \pi/32\sqrt{b/\eta}$.

Using Eq. (4.5), mass conservation and considering that a parent segment with a diameter ϕ_0 splits into two daughter branches with diameters ϕ_1 and ϕ_2 (cf. Fig. 4.1), the optimum relationship between the diameters of the parent and daughter vessels becomes:

$$\phi_0^3 = \phi_1^3 + \phi_2^3 \quad (4.6)$$

This relationship is now known as Murray’s law and states that the cube of the diameter of the parent vessel is equal to the sum of the cubes of the diameters of the daughter vessels.

4.2.1 Circular cross-section networks

Murray’s original relationship was derived for fully developed flow of Newtonian fluids in circular ducts to match the basic shape of most biological distribution systems, such as the vascular system, and can be considered as a particular case of constructal theory [137, 138]. Considering a symmetric bifurcating network where $\phi_1 = \phi_2$ it follows

from Eq. (4.6) that

$$\phi_0^3 = 2\phi_1^3 \quad (4.7)$$

Emerson *et al.* [139] and Barber and Emerson [140] generalised Murray's law for designing microfluidic manifolds intended to produce specific fluidic conditions. They modified relationship (Eq. (4.7)) and introduced the use of a geometrical *branching parameter*, X :

$$X = \frac{\phi_0^3}{2\phi_1^3} \quad (4.8)$$

It is obvious that for $X = 1$, Murray's law for symmetric bifurcating systems is recovered, but there is an additional range of relationships between the parent and the consecutive generations that can be achieved when $X \neq 1$. If the value of the parameter X is held constant through the branching network, then it can be shown that the diameter of generation i is given by

$$\phi_i = \frac{\phi_0}{(2X)^{i/3}} \quad (4.9)$$

where the index $i = 0, 1, 2, \dots, N$ refers to the number of each generation in the network. It should be noticed that for the cases of $X \neq 1$ Murray's assumption of the principle of minimum work is no longer valid and Eq. (4.9) allows us to create customised manifolds for applications that require particular flow conditions, in particular in terms of shear-stress gradients or flow resistance along the branching network.

For a symmetric system, the volumetric flow rate halves at each bifurcation. Therefore, for generation i , the volumetric flow rate is given by

$$Q_i = 2^{-i}Q_0 \quad (4.10)$$

Considering the fundamental relationship between the flow rate and the average velocity $Q_i = \bar{u}_i A_i$, where A_i is the cross-sectional area of each segment i , Eq. (4.10) is rearranged to correlate the average velocities at each segment with the inlet mean velocity as

$$\bar{u}_i = \bar{u}_0 2^{-i} \frac{A_0}{A_i} \quad (4.11)$$

Using Eqs. (4.9) and (4.11), the mean flow velocity for each generation, \bar{u}_i , can be then expressed as a function of the branching parameter and the inlet mean velocity:

$$\bar{u}_i = \bar{u}_0 \left(\frac{1}{2} X^2 \right)^{i/3} \quad (4.12)$$

The wall shear-stress for fully developed laminar flow in a circular pipe can be written (see White [37]) as follows:

$$\tau = \frac{8\eta\bar{u}}{\phi} \quad (4.13)$$

Substituting Eqs. (4.9) and (4.12) into Eq. (4.13) the wall shear-stress in each segment is then expressed as a function of the wall shear-stress developed at the inlet channel, τ_0 and the branching parameter, X resulting in

$$\tau_i = \tau_0 X^i \quad (4.14)$$

Equation (4.14) clearly shows that if Murray's law is obeyed ($X = 1$), then the magnitude of the wall shear-stress remains constant at every point in the branching hierarchy, whereas by changing the value of X , it is possible to introduce an element of control into the shear-stress distribution.

4.2.2 Rectangular cross-section networks

Microfluidic manifolds used in lab-on-a-chip applications are typically fabricated using techniques such as soft- or photo-lithography, and wet or dry etching, resulting in networks with non-circular cross-sections of constant depth. The main difference is that for a circular pipe the stress distribution at the walls is uniform since the fully developed velocity profile is the same in all azimuthal directions. On the contrary, for non-circular channels the velocity profiles for a fully developed flow depend on the aspect ratio, resulting in a variation of the wall shear-stress along the wetted perimeter. In order to overcome this characteristic, Emerson *et al.* [139] extended Murray's law for Newtonian fluids to non-circular ducts of rectangular and trapezoidal cross-sections

by taking into account the mean wall shear-stress:

$$\bar{\tau}_i = \bar{\tau}_0 X^i \quad (4.15)$$

The average wall shear-stress $\bar{\tau}$ is related to the Fanning friction factor, f as [37]

$$\bar{\tau} = \frac{1}{2} \rho \bar{u}^2 f = \frac{1}{2} \rho \bar{u}^2 \frac{\text{Po}}{\text{Re}} = \frac{\eta \bar{u} \text{Po}}{2 D_h} \quad (4.16)$$

where f is defined as the ratio of the Poiseuille number, Po , and the Reynolds number, Re , with ρ being the density and D_h the hydraulic diameter of the channel, defined as $D_h = 4 \times \text{area}/\text{wetted perimeter}$. It should be mentioned that for a circular channel where $\phi \equiv D_h$, Eq. (4.13) is recovered from Eq. (4.16) with $\text{Po} = 16$.

For a rectangular cross-sectional geometry, the average velocity in segment i of the symmetric bifurcating network is related to the inlet mean velocity in the same way as previously (see Eq. (4.11)). Alternatively, combining Eqs. (4.15) and (4.16) the velocity relationship can be expressed as

$$\bar{u}_i = \bar{u}_0 \frac{\text{Po}_0 D_{h_i}}{\text{Po}_n D_{h_0}} \quad (4.17)$$

Emerson *et al.* [139], combined Eqs. (4.11) and (4.14) and derived the following biomimetic equation for designing microfluidic bifurcating networks for Newtonian fluids:

$$\alpha_i (1 + \alpha_i) \text{Po}(\alpha_i^*) = (2X)^i \alpha_0 (1 + \alpha_0) \text{Po}(\alpha_0^*) \quad (4.18)$$

with α_i being the aspect ratio of each generation i , defined as the ratio of the channel's depth, d , to its width, w_i ($\alpha_i = d/w_i$) and the parameter α_i^* is defined depending on the value of α_i such as

$$\alpha_i^* = \begin{cases} d/w_i & \text{if } d \leq w_i \\ w_i/d & \text{if } d > w_i \end{cases} \quad (4.19)$$

indicating that when $\alpha_i > 1$, the fraction should be inverted.

4.3 Biomimetic design of networks for power-law fluids

As discussed in the previous section, the biomimetic rule proposed by Emerson *et al.* [139] for Newtonian fluids has the advantage of enabling the design of manifolds to control the flow within in order to generate specific shear-stress distributions along the microfluidic network (i.e. $X \neq 1$). This relationship is extended further here to consider non-Newtonian fluids described by the power-law model introduced in Section 2.2.1.

As discussed, flows of power-law fluids differ from Newtonian fluids in many ways because the viscosity can no longer be considered constant and independent of the shear-rate. Power-law fluids are described by the Ostwald de-Waele model, in which the viscosity is not constant but rather is a function of shear-rate:

$$\eta(\dot{\gamma}) = k\dot{\gamma}^{n-1} \quad (4.20)$$

As noted previously, k is the consistency index and is related to the magnitude of the viscosity, and n is the power-law index. When $n = 1$ the Newtonian behaviour is recovered with the viscosity being independent of the shear-rate, while for $n < 1$ the fluid is shear-thinning (the viscosity is decreasing as the shear-rate is increased), and for $n > 1$ the fluid is shear-thickening (the fluid becomes more viscous as the deformation rate is increased).

By analogy with Eq. (4.16) for Newtonian fluids, the mean wall shear-stress for a power-law fluid in a circular duct can be expressed as

$$\bar{\tau} = \frac{1}{2}\rho\bar{u}^2 f = \frac{1}{2}\rho\bar{u}^2 \frac{16}{\text{Re}^*} \quad (4.21)$$

where $\text{Po} = 16$ and Re^* is the generalised Reynolds number for a power-law fluid, defined as [141]

$$\text{Re}^* = \frac{\rho\bar{u}^{2-n}D_h^n}{8^{n-1}K} \quad (4.22)$$

As demonstrated by Kozicky *et al.* [142], for a power-law fluid flow in an arbitrary

cross-sectional duct, K is given by

$$K = k \left(b^* + \frac{a^*}{n} \right)^n \quad (4.23)$$

where the variables a^* and b^* are parameters that depend on the aspect ratio of the geometry examined. For the flow of a Newtonian fluid ($n = 1$) in a circular duct, the parameters should be set as $a^* = 1/4$ and $b^* = 3/4$, yielding the correct value of $Po = 16$ [143]. For rectangular channels of constant depth, these parameters can be evaluated by solving the following set of equations:

$$a^* = \frac{1}{2 \left(1 + \frac{1}{\alpha_i^*} \right)^2} \frac{1}{\left[1 + 4 \sum_{j=0}^{\infty} \frac{(-1)^{j+1}}{\left(\frac{2j+1}{2} \pi \right)^3} \frac{1}{\cosh\left(\frac{2j+1}{2} \pi \alpha_i^* \right)} \right]} \quad (4.24)$$

and

$$a^* + b^* = \frac{1}{2 \left(1 + \frac{1}{\alpha_i^*} \right)^2} \frac{3}{\left[1 - \frac{192}{\pi^5} \frac{1}{\alpha_i^*} \sum_{j=1,3,5,\dots}^{\infty} \frac{1}{j^5} \tanh\left(\frac{j\pi\alpha_i^*}{2} \right) \right]} \quad (4.25)$$

As for the case of the Newtonian biomimetic rule the same holds here, with the Eqs. (4.24) and (4.25) only being valid when the width of the channel is greater than or equal to the depth of the channel (i.e. $\alpha_i \leq 1$). For obtaining the values for $\alpha_i \geq 1$, the fraction of the aspect ratio should be inverted (i.e. Eq. (4.19)). It can be realised that the geometrical parameters, a^* and b^* , act as correction factors for the Poiseuille number, with Po depending on the geometry and thus on a^* and b^* . For the specific case of Newtonian fluid flow ($n = 1$), these parameters will produce the correct value of Po in a rectangular cross-section provided that $Po = fRe = 16(a^* + b^*)$.

Considering a circular duct, Po is constant regardless of the diameter, and the wall shear-stress distribution is uniform. This is not the case for non-circular ducts, where the wall stresses vary along the perimeter, with Po depending on the channel's aspect ratio. Consequently, the Poiseuille number needs to be evaluated for each different cross-section considered. Using Eqs. (4.21) and (4.22), the fully-developed mean shear-stress

along any branch of the network can be written as

$$\bar{\tau}_i = \frac{8^n \bar{u}_i^n K_i}{D_{h_i}^n} \quad (4.26)$$

Substituting Eq. (4.26) into Eq. (4.15), yields:

$$\frac{\bar{u}_i^n K_i}{D_{h_i}^n} = \frac{\bar{u}_0^n K_0}{D_{h_0}^n} X^i \quad (4.27)$$

Considering a symmetric network where the flow halves at each bifurcation, then

$$\bar{u}_i^n = \left(\frac{Q_i}{A_i}\right)^n = \left(\frac{2^{-i} Q_0}{A_i}\right)^n \quad (4.28)$$

where A_i refers to the cross-sectional area of generation i .

The combination of Eqs. (4.27) and (4.28), together with the definition of the hydraulic diameter, D_h , gives:

$$K_i \left(\frac{\mathcal{P}_i}{2A_i^2}\right)^n = K_0 \left(\frac{\mathcal{P}_0}{2A_0^2}\right)^n (2^n X)^i \quad (4.29)$$

where \mathcal{P}_i is the wetted perimeter of each generation. Eq. (4.29) is further expanded to

$$\frac{(w_i + d)^n}{(w_i d)^{2n}} K_i = \frac{(w_0 + d)^n}{(w_0 d)^{2n}} K_0 (2^n X)^i \quad (4.30)$$

where by employing the definition of the aspect ratio, $\alpha_i = d/w_i$, and after some mathematical rearrangements the following biomimetic rule is derived:

$$\alpha_i^n (1 + \alpha_i)^n \left(b_i^* + \frac{\alpha_i^*}{n}\right)^n = \alpha_0^n (1 + \alpha_0)^n \left(b_0^* + \frac{\alpha_0^*}{n}\right)^n (2^i)^n X^i \quad (4.31)$$

An important observation is that the proposed biomimetic design rule is a function of the power law index of the fluid, but is independent of other fluid properties, such as density.

The solution of the set of Eqs. (4.24), (4.25) and (4.31), allows the design of bifurcating manifolds of rectangular cross-sectional areas both for power-law and Newtonian fluids. For a desired power-law fluid and a known value of the power-law index, the

biomimetic design rule can be used to produce solutions in two different ways. Considering a bifurcating network with a specific number of generations and a specific value of the branching parameter X , Eq. (4.31) can either be solved by using the desired inlet (parent) geometrical characteristics (α_0) and generating the appropriate values for each generation, or starting from the geometrical characteristics of the last generations (α_n) and producing the appropriate values for all the rest. Depending on the chosen value of the branching parameter, a geometry that generates specific shear-stress distributions along each consecutive generation will be designed. For the case of $X = 1$, Murray's law is obeyed and the manifolds will produce identical average wall stresses in each segment of the network (see Eq. (4.15)) considering that the flow is fully-developed. By varying X , one is able to design customised manifolds with different shear-stress distributions along the network, depending on the needs of each specific application.

4.3.1 Flow resistance in the bifurcating networks

One of the most important issues when designing microfluidic manifolds is the estimation of the total flow resistance and the pressure distribution. Based on Hartnett and Kostic [144], Son [145] reported the following relationship between the flow rate and pressure drop along a rectangular channel for power-law fluid flow:

$$\left(\frac{\Delta P}{2L}\right) \left(\frac{wd}{w+d}\right) = \left[\left(\frac{6Q}{wd^2}\right) \left(1 + \frac{d}{w}\right) \left(\frac{2}{3}\right)\right]^n k \left(b^* + \frac{a^*}{n}\right)^n \quad (4.32)$$

Equation (4.32) is solved for Q^n and by expressing its value for the i^{th} segment of the network, gives:

$$Q_i^n = \left(\frac{\Delta P_i D_{hi}}{4L_i K_i}\right) \left(\frac{A_i D_{hi}}{8}\right)^n \quad (4.33)$$

Multiplying Eq. (4.26) on both sides by A_i^n and substituting the expression of the flow rate from Eq. (4.33), the average wall shear-stress becomes:

$$\bar{\tau}_i = \frac{\Delta P_i D_{hi}}{4L_i} \quad (4.34)$$

resulting in the fundamental relationship between the shear-stress and the pressure drop at each segment.

In biological systems, the length of an individual segment of a branching hierarchy is observed frequently to follow a *proportionality* to its diameter, as discussed by West [146]. In order to extend Murray's law to non-circular microchannels, Emerson [139] proposed that this biological principle can be generalised for non-circular cross-sections by assuming that the length of each vessel is proportional to its hydraulic diameter. The same assumption has also been proposed in other research on transport networks [147, 148].

The importance of this assumption is reflected on the additional information that the proposed design rule is able to provide, regarding the pressure drop distribution along the bifurcating network. Substituting equation Eq. (4.34) in Eq. (4.15), the pressure drop at generation i can be related to the pressure drop of the parent channel by

$$\frac{\Delta P_i D_{h_i}}{4L_i} = \frac{\Delta P_0 D_{h_0}}{4L_0} X^i \quad (4.35)$$

Considering that

$$\frac{L_i}{D_{h_i}} = \frac{L_0}{D_{h_0}} = c_p \quad (4.36)$$

where c_p is the proportionality constant, more information regarding the expected pressure drops in the network can be provided by the relationship:

$$\Delta P_i = \Delta P_0 X^i \quad (4.37)$$

The hydraulic resistance, R_i , of each segment can be evaluated by the ratio of the corresponding pressure drop, ΔP_i , to the equivalent flow rate, Q_i :

$$R_i = \frac{\Delta P_i}{Q_i} \quad (4.38)$$

Recalling that for a symmetric bifurcating network Eq. (4.10) is valid, then by substituting Eq. (4.38) into Eq. (4.37), the resistance of a single segment of generation i can be related to the flow resistance in the inlet channel ($i = 0$) and the branching

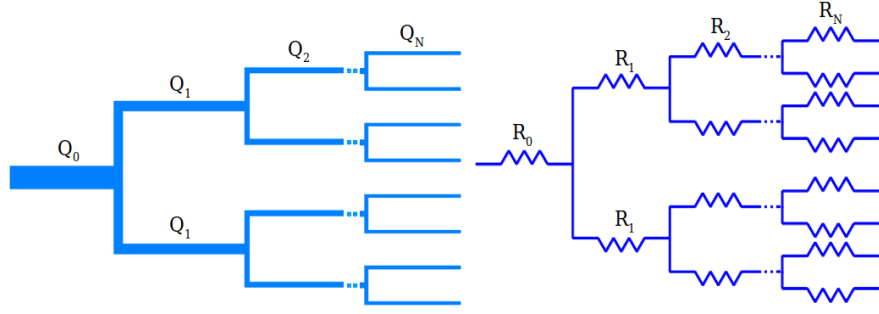


Figure 4.2. Microfluidic bifurcating network with N bifurcations and the equivalent electrical circuit analogue.

parameter by

$$\frac{R_i}{R_0} = (2X)^i \quad (4.39)$$

analogous the Newtonian case reported by Emerson *et al.* [139].

Furthermore, taking into consideration that a branching network can be represented by an electrical circuit analogue [149] as shown in Fig. 4.2, the total resistance between the inlet and the end of the segment at generation i can be written as

$$R_{tot_i} = R_0 + \frac{R_1}{2} + \dots + \frac{R_i}{2^i} \quad (4.40)$$

Moreover, for a symmetric bifurcating network composed of $N + 1$ consecutive generations, the total flow resistance in the design can be written as

$$R_{tot_N} = R_0 + \frac{R_1}{2} + \dots + \frac{R_i}{2^i} + \dots + \frac{R_N}{2^N} = R_0 \sum_{i=0}^N X^i \quad (4.41)$$

where R_{tot_N} refers to the total resistance between the inlet (at the start of generation $i = 0$) and the outlet (at the end of the channel in generation $i = N$). Expanding the series on the right hand side of Eq. (4.41), the total network resistance may be expressed as

$$R_{tot_N} = \begin{cases} R_0 (X^{N+1} - 1) / (X - 1), & X \neq 1 \\ R_0 (N + 1), & X = 1 \end{cases} \quad (4.42)$$

4.4 Geometrical design considerations

The strategies followed for designing the bifurcating networks using the proposed rule may vary. However, there are some geometrical restrictions that need to be addressed. These are discussed here, together with an illustration of the strategy that was chosen in this study.

For a desired bifurcating network of constant depth, d , described by the branching parameter X , and considering the fluid of interest characterised by the desired power-law index n , Eq. (4.31) can be solved by employing a root finding method to produce a set of appropriate widths, w_i , for each generation i . Equation (4.31) is solved either by defining the dimensions of the parent channel (w_0, d) or by imposing the values of the desired last generation (w_N, d). Here, it was decided to specify the dimensions of the parent channel and for a wanted number of consecutive generations, a simple code was developed based on the bisection method [150] and is employed to generate the

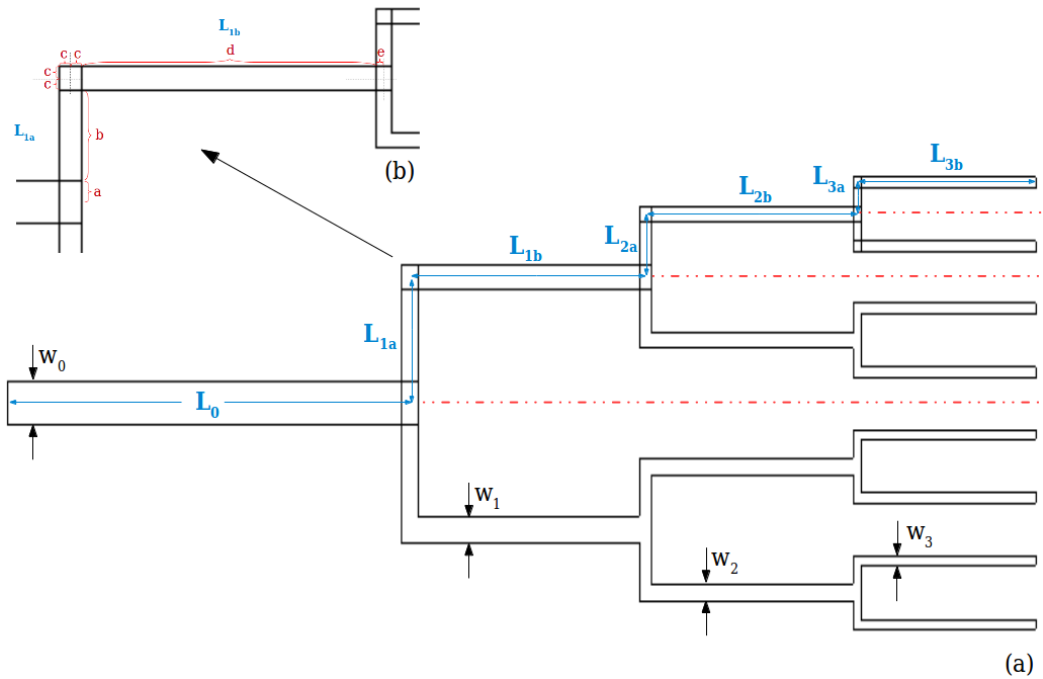


Figure 4.3. Two dimensional view of the microfluidic bifurcating network, indicating the length set up (a) and a zoomed view at the 90° bend of the first daughter (b). The *dashed-dotted* lines indicate limiting positions of the design.

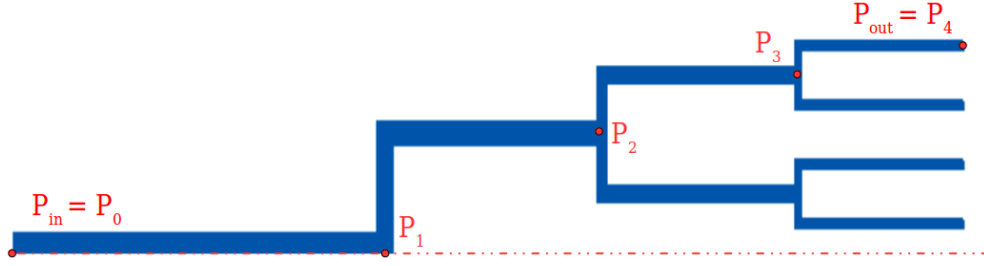


Figure 4.4. Indication of the locations for the evaluation of the pressure drop for each generation (only half of the network is illustrated).

solutions for each case considered.

In order to ensure that the flow fully develops in every segment, it was decided to set the length at each generation as $L_i = 20D_{h_i}$, for all the cases studied. Additionally, all designs contain a total number of four consecutive generations ($N = 4$). Figure 4.3 indicates how the lengths are distributed along the entire network. It is important that the lengths $L_{i,b}$ are large enough so that the flow becomes fully developed. Additionally, care must be taken to avoid clashing of the segments (limiting positions are indicated by *dashed-dotted* lines in Fig. 4.3), which is controlled by the lengths $L_{i,a}$. The total lengths of the segments are evaluated from the centres of the merging blocks at the beginning of each bifurcation, up to the centre point of the merging block of the upcoming bifurcation. That way $L_{i,a} + L_{i,b} = 20D_{h_i}$, with the vertical length $L_{i,a}$ set as $L_{i,a} = a + b + c$ and the horizontal length $L_{i,b}$ as $L_{i,b} = c + d + e$, as indicated in Fig. 4.3b.

These points, shown in Fig. 4.4, have also been used as reference in the validation of Eq. (4.40) and the evaluation of the pressure differences for each microfluidic network studied (cf. Section 4.5).

4.5 Numerical Validation

Computational fluid dynamics simulations have been performed to examine the applicability of the biomimetic rule expressed from Eq. (4.31) and its ability to produce the correct dimensions for bifurcating microfluidic networks of rectangular cross-sectional area, that will produce known and desired flow characteristics defined by Eqs. (4.15)

and (4.40).

4.5.1 Numerical method and problem set-up

The flow is considered to be laminar, incompressible and isothermal and is solved numerically using the continuity and momentum equations together with the power-law stress-strain constitutive equation:

$$\nabla \cdot \mathbf{u} = 0 \quad (4.43)$$

$$\rho \left(\frac{\partial \mathbf{u}}{\partial t} + \mathbf{u} \cdot \nabla \mathbf{u} \right) = -\nabla p + \nabla \cdot \boldsymbol{\tau} \quad (4.44)$$

$$\boldsymbol{\tau} = k \dot{\gamma}^{n-1} \dot{\gamma} \quad (4.45)$$

where p is the pressure, $\boldsymbol{\tau}$ is the extra stress tensor, $\dot{\gamma}$ is the shear-rate tensor and $\dot{\gamma}$ is the magnitude of the shear-rate tensor (cf. Section 2.2.1).

The governing equations are solved using the in-house numerical code, based on a fully implicit finite volume method discussed in Section 3.3, using collocated meshes [27]. The convective terms are discretised using the CUBISTA high resolution scheme [93] (cf. Section 3.3.3), while the diffusive terms employ a central difference scheme. The time-dependent terms in the momentum equation are discretised using a first-order implicit Euler scheme.

A uniform velocity is applied at the inlet of the designs and the developed flow field is studied considering creeping flow conditions ($\text{Re} \rightarrow 0$) unless stated otherwise, since it is a reasonable approximation in microfluidics. Additionally, in order to reduce the computational demands of the problem, symmetry boundary conditions are considered along the xy - and xz - centreplanes (cf. Fig. 4.5), simulating that way only one quarter of the complete geometry.

As mentioned, all networks considered have four consecutive generations of constant depth, d , as typically found in microfluidics applications, with the length of each segment being proportional to its hydraulic diameter ($L_i = 20D_{hi}$). For the cases examined a depth of $d = 125\mu\text{m}$ was assumed, and the inlet channel ($i = 0$) width was

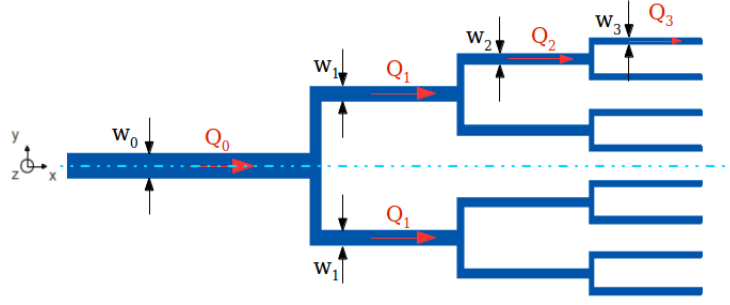


Figure 4.5. Microfluidic bifurcating network of constant depth with 4 generations ($i = 0, 1, 2, 3$) designed for a Newtonian fluid with aspect ratio $\alpha_0 = 0.5$ and $X = 1$. The dashed-dotted line illustrates the symmetry conditions about $y = 0$.

taken to be $w_0 = 250\mu\text{m}$, resulting in an inlet aspect ratio of $\alpha_0 = d/w_0 = 0.5$, unless stated otherwise. Numerical computations were performed for several values of the branching parameter, X , and for a range of power-law indices, n , that vary from shear-thinning to shear-thickening behaviour ($n = [0.2, 2.0]$) considering a consistency index of $k = 10^{-3} \text{ N s}^n \text{ m}^{-2}$. As shown in the following sections, different values of X and n , result in different sized networks and thus the number of cells of the numerical meshes used to discretise the physical domains depend on the flow geometry. Two different meshes (M0 and M1) are considered in each case in order to examine the dependence of the final solution on the numerical grid. More information about the meshes is given in the following sections.

Finally, for all the cases considered, the validity of Eq. (4.15) and the ability to generate a desired distribution of average wall shear-stress throughout the network is evaluated by averaging the shear-stresses developed at the wetted perimeter of the channel at each branch, on a fixed x -position where the flow is fully developed.

4.5.2 Uniform shear-stress distribution ($X = 1$)

The biomimetic design rule gives the ability to design microfluidic bifurcating networks in which the average wall shear-stress for a fully developed flow, remains constant throughout the entire system, obeying the principle of minimum work. Considering $X = 1$ and $\alpha_0 = 0.5$ the biomimetic design set of Eqs. (4.24), (4.25) and (4.31) is solved for Newtonian and power-law fluids.

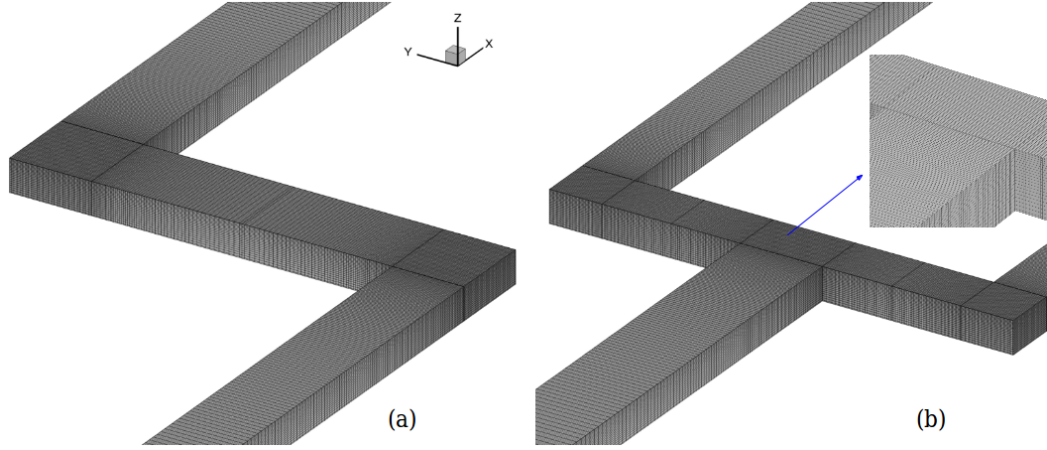


Figure 4.6. Numerical mesh M1 used to discretise one quarter of the geometry at the first (a) and at the second bifurcation (b), produced from Eq. (4.31) for a Newtonian fluid with aspect ratio $\alpha_0 = 0.5$ and $X = 1$.

Starting from the case of a Newtonian fluid ($n = 1$) for a channel with an inlet aspect ratio, $\alpha_0 = 0.5$, the geometrical characteristics for each consecutive generation are evaluated and given in Table 4.1. The evaluated dimensions for the Newtonian fluid are in agreement with those presented by Emerson *et al.* [140]. The numerical mesh M1 used for discretising the physical domain is composed by 32 blocks consisting of 2,362,416 computational cells in total, with more details given in Table 4.2. Figure 4.6a illustrates the mesh M1 in the region of the first bifurcation, whereas Fig. 4.6b displays the domain discretisation in the region of the second bifurcation.

In Fig. 4.7, the comparison between theory and computational predictions for the normalised average wall shear-stress distribution along the bifurcating network is presented. A very good agreement between theoretical Eq. (4.15) and numerical predictions

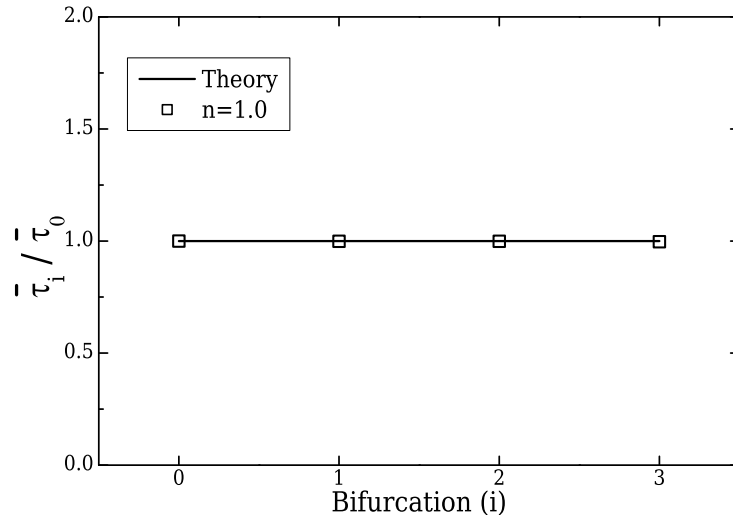
Table 4.1. Geometrical parameters and dimensions of a planar bifurcating network with inlet aspect ratio $\alpha_0 = 0.5$ obtained for a Newtonian fluid ($n = 1$).

i	w_i (μm)	d_i (μm)	α_i	Dh_i (μm)	a^*	b^*
$n = 1.0$						
0	250.0	125.0	0.500	166.7	0.2439	0.7278
1	143.3	125.0	0.872	133.6	0.2134	0.6794
2	91.8	125.0	1.361	105.9	0.2186	0.6884
3	62.5	125.0	2.000	83.3	0.2439	0.7278

Table 4.2. Mesh characteristics for a Newtonian ($n = 1$) geometry, designed for $X = 1$ and $a_0 = 0.5$.

Mesh	$\delta x_{min}/D_{h0}$	$\delta y_{min}/D_{h0}$	$\delta z_{min}/D_{h0}$	Number of Cells
M0	0.018	0.018	0.018	1,599,318
M1	0.013	0.013	0.013	2,362,416

is found, similarly to the results reported by Emerson *et al.* [139] and Barber and Emerson [140]. The relative error between the CFD calculations for $n = 1$ and the theoretical predictions was found to be less than 0.4%. Furthermore, Fig. 4.8 demonstrates the linear variation of the normalised resistance, validating the expected theoretical results from Eq. (4.40). In Fig. 4.9 a combined contour-plot of the normalised wall shear-stress and the normalised velocity distribution is given with the *dashed-dotted* line indicating the symmetry planes about $y = 0$ and $z = 0$. The left half about xz -plane illustrates the wall stress distribution as the Newtonian fluid advances towards the last generations. It is clear that the actual stresses are not constant along the widths of each face. Hence, the need to use the average wall shear-stress in contrast to the case of a network of circular cross-section, where the local wall stresses on the whole wetted perimeter of each segment are the same. The right half of Fig. 4.9 about the xz -plane, shows the distribution of the normalised velocity magnitude at the centreplane of the domain


Figure 4.7. Normalised wall shear-stress for a Newtonian fluid along the four generations of the bifurcating network designed for a Newtonian fluid for $\alpha_0 = 0.5$ and $X = 1$ (Table 4.1).

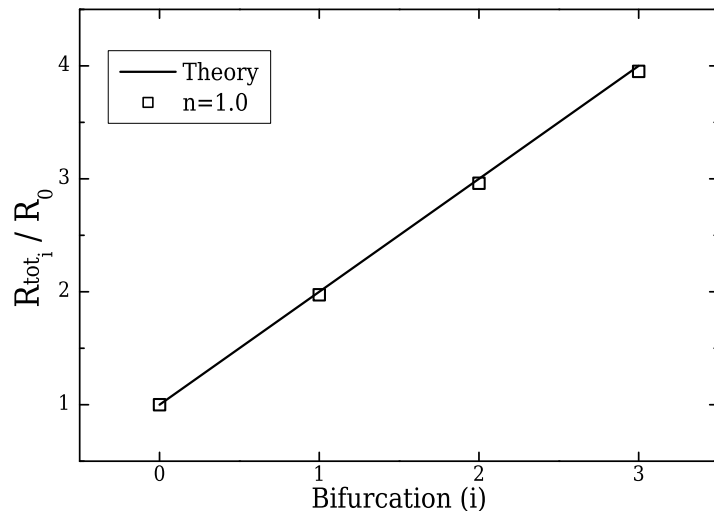


Figure 4.8. Normalised flow resistance for a Newtonian fluid along the 4 generations of the bifurcating network designed for a Newtonian fluid for $\alpha_0 = 0.5$ and $X = 1$ (Table 4.1).

($z = 0$), where it attains its maximum values.

The results illustrated above are evaluated using the more refined mesh M1. It

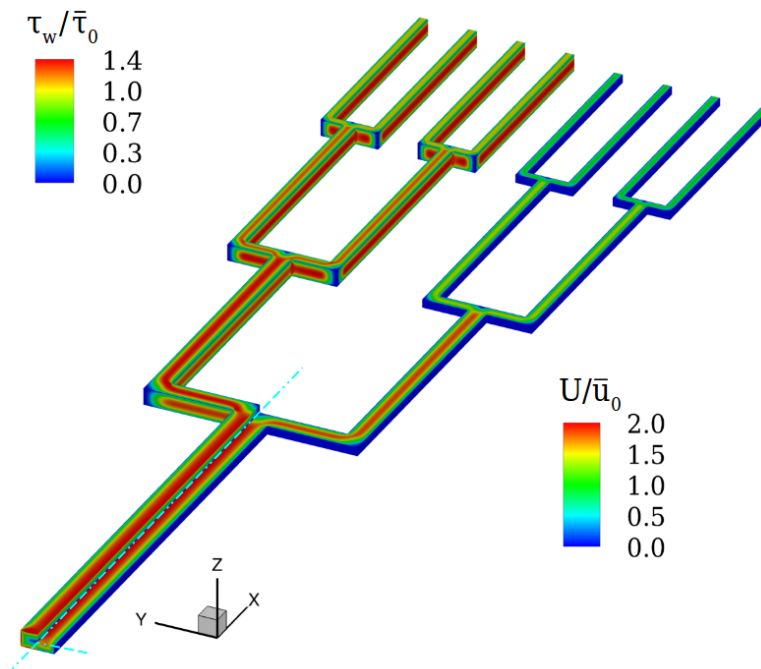


Figure 4.9. Combined contour-plot of the normalised wall shear-stress (top left part) and the normalised velocity at the centreplane (bottom right part) along the Newtonian-designed geometry (Table 4.5) for a Newtonian fluid. *Dashed-dotted* lines indicate the symmetry planes about $y = 0$ and $z = 0$.

should be noted that comparing to the studies performed by Emerson *et al.* [139] and Barber and Emerson [140], the mesh used here is approximately two times more refined and symmetry conditions are applied both along y - and z -directions.

The comparison between the solutions obtained from the numerical meshes M0 and M1 (cf. Table 4.2) are found to be in a very good agreement, since the maximum deviation reported is less than 0.5% for the shear-stresses and 0.1% for the total resistance in the microfluidic network.

For non-Newtonian fluids, the biomimetic set of equations was solved for various power-law fluids, ranging from highly shear-thinning to shear-thickening behaviour resulting in the geometrical parameters given in Tables 4.3 and 4.4, respectively. Comparing the geometrical dimensions obtained for the Newtonian fluid (Table 4.1) with the

Table 4.3. Geometrical parameters and dimensions of planar bifurcating networks with inlet aspect ratio $\alpha_0 = 0.5$ obtained for power-law, shear-thinning fluids with $n = 0.2, 0.4, 0.6$ and 0.8 .

i	w_i (μm)	d_i (μm)	α_i	D_{hi} (μm)	a^*	b^*
$n = 0.2$						
0	250.0	125.0	0.500	166.7	0.2439	0.7278
1	140.9	125.0	0.887	132.5	0.2131	0.6788
2	90.8	125.0	1.377	105.2	0.2191	0.6892
3	62.5	125.0	2.000	83.3	0.2439	0.7278
$n = 0.4$						
0	250.0	125.0	0.500	166.7	0.2439	0.7278
1	142.0	125.0	0.880	133.0	0.2132	0.6791
2	91.3	125.0	1.370	105.5	0.2189	0.6889
3	62.5	125.0	2.000	83.3	0.2439	0.7278
$n = 0.6$						
0	250.0	125.0	0.500	166.7	0.2439	0.7278
1	142.6	125.0	0.876	133.2	0.2133	0.6792
2	91.5	125.0	1.366	105.7	0.2187	0.6886
3	62.5	125.0	2.000	83.3	0.2439	0.7278
$n = 0.8$						
0	250.0	125.0	0.500	166.7	0.2439	0.7278
1	143.0	125.0	0.874	133.4	0.2133	0.6793
2	91.7	125.0	1.363	105.8	0.2187	0.6885
3	62.5	125.0	2.000	83.3	0.2439	0.7278

Table 4.4. Geometrical parameters and dimensions of planar bifurcating networks with inlet aspect ratio $\alpha_0 = 0.5$ obtained for power-law, shear-thickening fluids with $n = 1.2, 1.4, 1.6, 1.8$ and 2.0 .

i	w_i (μm)	d_i (μm)	α_i	D_{hi} (μm)	a^*	b^*
$n = 1.2$						
0	250.0	125.0	0.500	166.7	0.2439	0.7278
1	143.6	125.0	0.871	133.6	0.2134	0.6794
2	91.9	125.0	1.360	105.9	0.2186	0.6883
3	62.5	125.0	2.000	83.3	0.2439	0.7278
$n = 1.4$						
0	250.0	125.0	0.500	166.7	0.2439	0.7278
1	143.7	125.0	0.870	133.7	0.2134	0.6795
2	92.0	125.0	1.359	106.0	0.2185	0.6883
3	62.5	125.0	2.000	83.3	0.2439	0.7278
$n = 1.6$						
0	250.0	125.0	0.500	166.7	0.2439	0.7278
1	143.8	125.0	0.869	133.8	0.2134	0.6795
2	92.1	125.0	1.358	106.0	0.2185	0.6882
3	62.5	125.0	2.000	83.3	0.2439	0.7278
$n = 1.8$						
0	250.0	125.0	0.500	166.7	0.2439	0.7278
1	143.9	125.0	0.868	133.8	0.2135	0.6795
2	92.1	125.0	1.357	106.1	0.2185	0.6882
3	62.5	125.0	2.000	83.3	0.2439	0.7278
$n = 2.0$						
0	250.0	125.0	0.500	166.7	0.2439	0.7278
1	144.0	125.0	0.868	133.8	0.2135	0.6795
2	92.1	125.0	1.357	106.1	0.2185	0.6882
3	62.5	125.0	2.000	83.3	0.2439	0.7278

dimensions computed for all power-law fluids, it is clear that the differences between all customised geometries are small. The maximum deviation reported is 1.7% in w_1 , between the Newtonian design and the shear-thinning limiting case of $n = 0.2$. A preliminary analysis comparing the behaviour of a Newtonian, a shear-thinning ($n = 0.6$) and a shear-thickening ($n = 1.6$) fluid is shown in [Fig. 4.10](#), where the expected average velocities that should develop at each segment of the customised geometries for each case indicate that the behaviour of the various fluids is expected to be similar

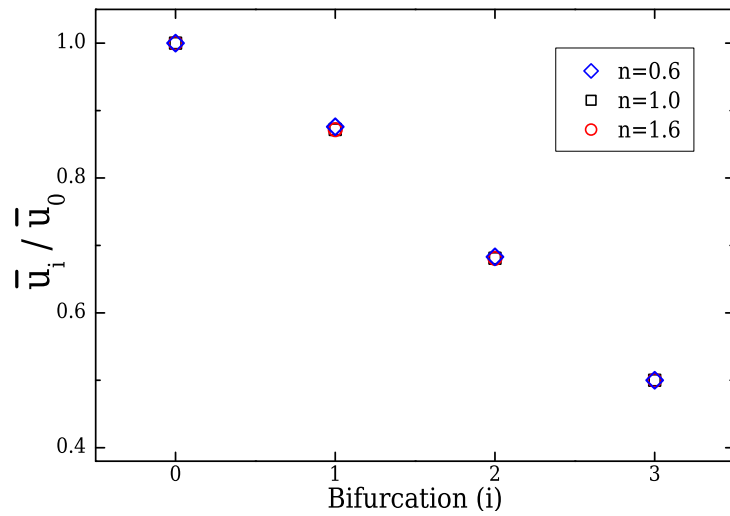


Figure 4.10. Normalised average velocities along the customised bifurcating networks of each particular fluid obtained for $\alpha_0 = 0.5$, and $X = 1$.

when using the Newtonian-designed geometry. Therefore, assuming that the geometry obtained for a Newtonian fluid ($n = 1$) will generate equivalent responses for the power-law fluids, the same geometry (Table 4.1) can be employed for examining the flow characteristics of different fluids with power-law indices ranging from $n = 0.2$ (shear-thinning) to $n = 2.0$ (shear-thickening).

In Fig. 4.11 a comparison between the desired behaviour (theory) and computa-

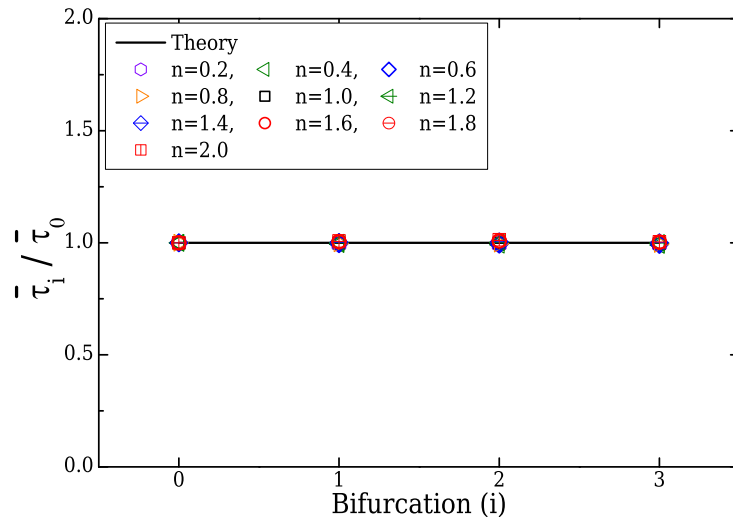


Figure 4.11. Normalised wall shear-stress for various fluids along the 4 generations of the bifurcating network designed for a Newtonian fluid for $\alpha_0 = 0.5$ and $X = 1$ (Table 4.1).

tional predictions for the normalised average wall shear-stress distribution along the bifurcating network is shown. In agreement with the assumption of similar responses, it can be seen that although the geometry was designed for Newtonian fluids, it also works well for the power-law fluids. Clearly, the response of both shear-thinning and shear-thickening fluids is similar to the Newtonian fluid, yielding a uniform average wall shear-stress along the network segments ($\bar{\tau}_i \simeq \bar{\tau}_0$). More specifically, for the shear-thickening fluid with $n = 2.0$, a maximum deviation of 1.35% from the Newtonian behaviour is reported, while for the shear-thinning fluid with $n = 0.2$, the maximum deviation is less than 1%. Additionally, Fig. 4.12 shows the total flow resistance, computed using Eq. (4.40) as described in Section 4.4, at each consecutive generation. The total flow resistance can be seen to vary linearly for all fluids thereby corroborating the good agreement between theory and numerical results for both the power-law and Newtonian fluids.

The outcome of the numerical study of the channels designed for $X = 1$ and $\alpha_0 = 0.5$ results in an interesting universality, which can be a great advantage for experimental studies, since the same microfluidic network can be used for a range of fluids.

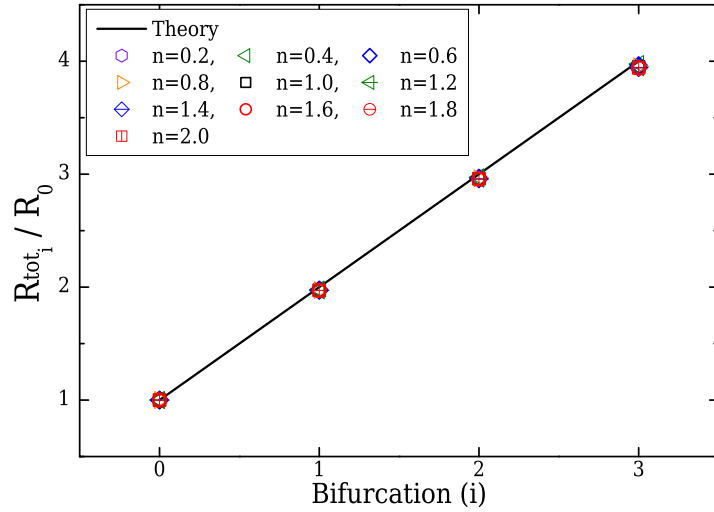


Figure 4.12. Normalised flow resistance for various fluids along the 4 generations of the bifurcating network designed for a Newtonian fluid for $\alpha_0 = 0.5$ and $X = 1$ (Table 4.1).

4.5.3 Positive gradients of shear-stress distribution ($X = 1.25$)

When the value of the branching parameter differs from unity ($X \neq 1$), the geometries generated by solving the biomimetic set of equations for a desired inlet (or outlet) aspect ratio are expected to compose manifolds able to produce well-defined shear-stress gradients. The ability to generate non-uniform, but known, shear-stress gradients is one of the advantages of the proposed biomimetic design, since a variety of applications exist which would benefit from being able to control the applied stresses along the network. For example applications in the field of tissue engineering and in other bioengineering fields which deal with shear sensitive biosamples, fall in this category. It should be noted though, that for $X \neq 1$, the principle of minimum work is no longer satisfied. Here, the case of $X = 1.25$ is considered corresponding to a positive gradient of the shear-stress distribution along the network (Eq. (4.15)). As previously, an investigation of the fluids response is performed, considering the flow of a Newtonian, a shear-thinning (with $n = 0.6$) and a shear-thickening (with $n = 1.6$) fluid.

Starting with the case of a Newtonian fluid, the characteristics of the customised geometry with $\alpha_0 = 0.5$ and $X = 1.25$ are provided in Table 4.5. Comparing this new configuration with the previously discussed case for $X = 1$ (Table 4.1), it is clear that the geometries exhibit large differences in the widths of each generation. It should be noticed that the rate at which the widths are changing when $X = 1.25$ is steeper, resulting in narrower channels, as a consequence of the requirement to produce increasing shear-stress gradients. Additionally, in order to maintain the proportionality between

Table 4.5. Geometrical parameters and dimensions of planar bifurcating networks with initial aspect ratio $\alpha_0 = 0.5$ and branching parameter $X = 1.25$, designed for a Newtonian fluid.

i	w_i (μm)	d_i (μm)	α_i	D_{h_i} (μm)	a^*	b^*
$X = 1.25$						
0	250.0	125.0	0.500	166.7	0.2439	0.7278
1	123.0	125.0	1.016	124.0	0.2121	0.6771
2	71.4	125.0	1.751	90.9	0.2332	0.7120
3	44.2	125.0	2.828	65.3	0.2796	0.7736

Table 4.6. Mesh characteristics for a 3D flow simulation for a Newtonian ($n = 1$) geometry, designed for $X = 1.25$ and $a_0 = 0.5$.

Mesh	$\delta x_{min}/D_{h0}$	$\delta y_{min}/D_{h0}$	$\delta z_{min}/D_{h0}$	Number of Cells
M0	0.012	0.012	0.021	1,598,641
M1	0.010	0.010	0.010	2,442,069

the lengths and the hydraulic diameters of each segment ($L_i = 20D_{hi}$; Eq. (4.36)), the length of each consecutive generation and thus the total length of the microfluidic network is affected, becoming smaller for the particular case of $X = 1.25$. The length of the inlet channel is the only that remains unchanged, independently of the value of the branching parameter as the imposed D_h is kept constant.

Using a similar approach as in Section 4.5.2, the geometry obtained for a Newtonian fluid is considered initially and the characteristics of a Newtonian fluid flow are examined. Then, the same geometry is used for analysing the flow of power-law fluids. The geometry is, as previously, discretised by a mesh M1 consisting of 32 blocks and 2,442,069 cells (cf. Table 4.6). Figure 4.13 illustrates the normalised average wall shear-stress in each consecutive generation of a network designed for a Newtonian fluid with $X = 1.25$. For the case of $n = 1$, the CFD results are in very good agreement with

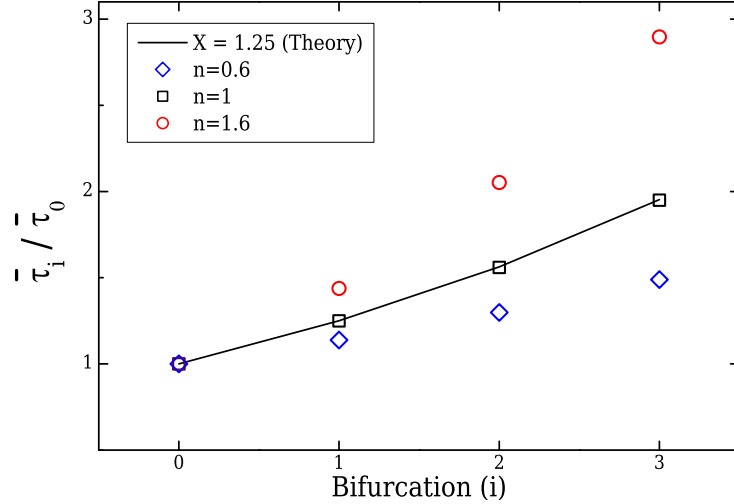


Figure 4.13. Normalised wall shear-stress along the bifurcating network for a Newtonian, shear-thinning ($n = 0.6$) and shear-thickening ($n = 1.6$) fluids, when the Newtonian designed geometry with $a_0 = 0.5$ and $X = 1.25$ is used.

the results presented by Emerson *et al.* [139] and Barber and Emerson [140], as well as with the biomimetic principle (Eq. (4.15)), resulting in a maximum deviation of less than 0.5%. Finally, the comparison of the numerical solutions obtained using the two meshes, M0 and M1, results in a maximum deviation for the normalised stresses at the last bifurcation that is less than 0.5%, whereas the total resistance is found to deviate at most 0.1%.

Clearly, when $X = 1.25$, the average wall shear-stress increases at each consecutive generation, resulting in a positive gradient along the network as imposed by setting the branching parameter to a value greater than unity ($X > 1$) in the biomimetic design rule. However, unlike the equivalent case for $X = 1$, the use of the Newtonian geometry produces very different shear-stress distributions along the network for each power-law fluid examined as shown in Fig. 4.13, and the channel can no longer be considered as universal. The flow dynamics for the three fluids considered are considerably different and the power-law fluids do not display the desired behaviour when flowing in the Newtonian-designed geometry. This is also highlighted from the deviations in the resistances shown in Fig. 4.14.

The deviating responses for $X = 1.25$ when the Newtonian geometry is used can

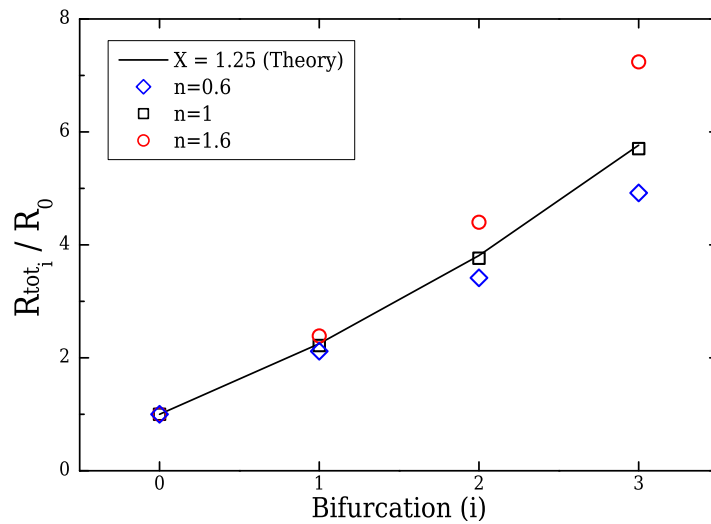


Figure 4.14. Normalised resistance along the bifurcating network for a Newtonian, shear-thinning ($n = 0.6$) and shear-thickening ($n = 1.6$) fluids, when the Newtonian designed geometry with $a_0 = 0.5$ and $X = 1.25$ is used.

be explained by the normalised average velocities that are expected to be developed at each branch of the network. Unlike the case of $X = 1$, where the average velocity ratios (\bar{u}_i/\bar{u}_0) along the bifurcating networks are similar for both the Newtonian and power-law fluids (cf. Fig. 4.10), for $X = 1.25$, the average velocities required for generating the desired wall shear-stress gradient for each fluid are clearly very different, as presented in Fig. 4.15.

When the shear-thinning fluid ($n = 0.6$) is flowing in the Newtonian geometry for $X = 1.25$, it is consistently exposed to lower average velocities in each consecutive generation when compared to its customised geometry. The result is to develop smaller shear-stresses at the walls and thus, to present a behaviour that is under-predicting the desired positive shear-stress distribution. Moreover, this behaviour is obviously affecting the development of the total resistance in the microfluidic network, as illustrated in Fig. 4.14. On the other hand, the shear-thickening fluid is exposed to higher average velocities when the Newtonian geometry is used, leading to high shear-stress ratios as the fluid thickens (as shown in Fig. 4.13). Consequently, the total resistance in the same microfluidic network will be higher than the one proposed by the biomimetic design (cf. Fig. 4.14).

In summary, when the network is designed for a Newtonian fluid for $X > 1$ and

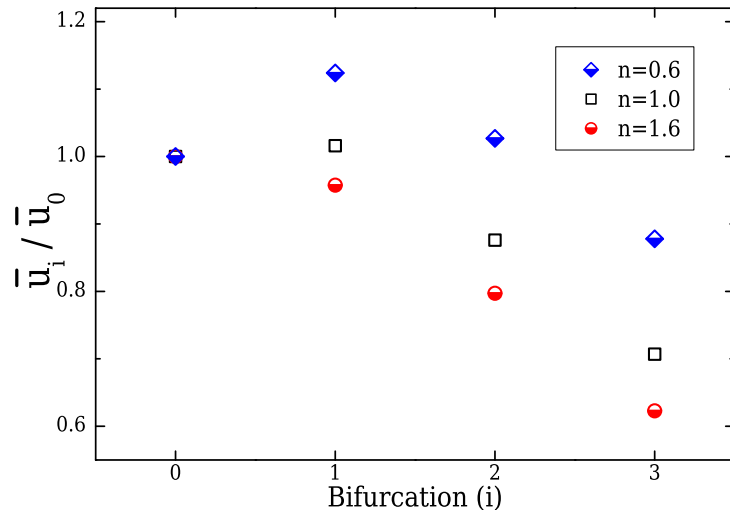


Figure 4.15. Normalised average velocities along the customised bifurcating networks of each particular fluid obtained for $\alpha_0 = 0.5$, and $X = 1.25$

Table 4.7. Geometrical parameters and dimensions of planar networks with initial aspect ratio $\alpha_0 = 0.5$ and branching parameter $X = 1.25$, for power-law fluids with $n = 0.6$ and $n = 1.6$.

i	w_i (μm)	d_i (μm)	α_i	D_{h_i} (μm)	a^*	b^*
$n = 0.6$						
0	250.0	125.0	0.500	166.7	0.2439	0.7278
1	111.2	125.0	1.124	117.7	0.2130	0.6788
2	60.9	125.0	2.054	81.9	0.2463	0.7312
3	35.6	125.0	3.511	55.4	0.3055	0.8021
$n = 1.6$						
0	250.0	125.0	0.500	166.7	0.2439	0.7278
1	130.6	125.0	0.957	127.7	0.2122	0.6773
2	78.4	125.0	1.594	96.4	0.2268	0.7020
3	50.2	125.0	2.492	71.6	0.2655	0.7566

$\alpha_0 = 0.5$, the power-law fluid behaviour diverges from the Newtonian response and the geometries designed for Newtonian fluids are not appropriate for applications that require handling power-law fluids. Thus, customised geometries for each power-law fluid should be used. The appropriate dimensions composing each bifurcating network are presented in [Table 4.7](#). Clearly, the geometrical characteristics for $n = 0.6$, $n = 1.6$ and for the Newtonian fluid are different, with the width of the last bifurcation for the $n = 0.6$ geometry deviating approximately 20% from the Newtonian case.

Numerical simulations have been performed to validate the applicability of the biomimetic design rule. The biomimetic networks for $n = 0.6$ and $n = 1.6$ are discretised using two different meshes (M0 and M1), with their details provided in [Ta-](#)

Table 4.8. Mesh characteristics for the power-law geometries considered ($n = 0.6$ and $n = 1.6$) geometry, designed for $X = 1.25$ and $a_0 = 0.5$.

Mesh	$\delta x_{min}/D_{h_0}$	$\delta y_{min}/D_{h_0}$	$\delta x_{min}/D_{h_0}$	Number of Cells
$n = 0.6$				
M0	0.013	0.013	0.021	1,480,955
M1	0.010	0.010	0.015	2,335,977
$n = 1.6$				
M0	0.016	0.016	0.019	1,584,681
M1	0.013	0.013	0.014	2,354,671

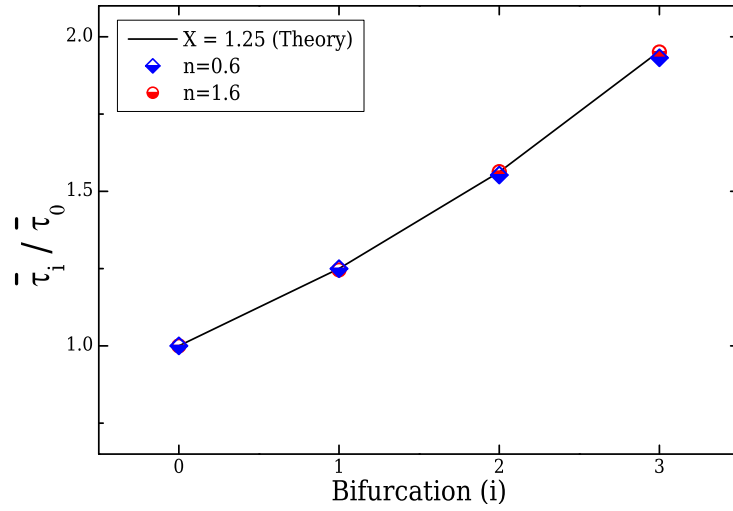


Figure 4.16. Normalised wall shear-stress along the customised bifurcating networks ($\alpha_0 = 0.5$), designed using the biomimetic principle Eq. (4.31). Two customised geometries were considered corresponding to $n = 0.6$ and $n = 1.6$ with $X = 1.25$.

ble 4.8. Figure 4.16 shows that when the customised geometries are designed using Eq. (4.31) (yielding the dimensions provided in Table 4.7) both shear-thinning and shear-thickening fluids obey the biomimetic principle, by yielding the predicted tangential shear-stress distributions with a maximum deviation of 1% for the shear-thinning fluid at the last generation. At the same time, the differences in the widths of each

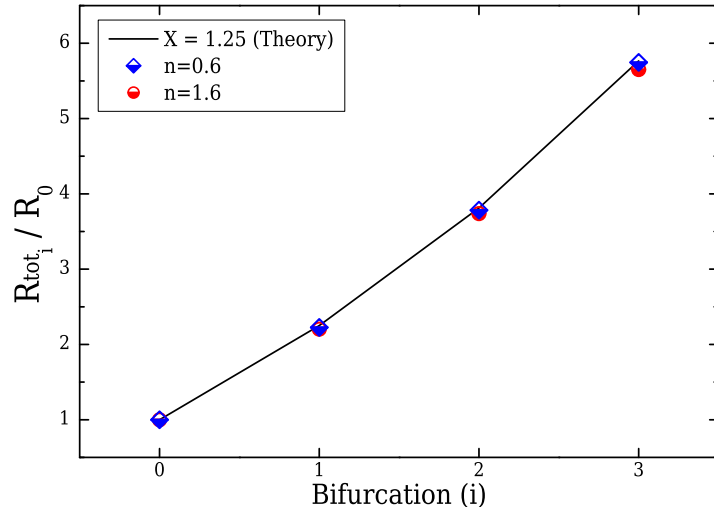


Figure 4.17. Normalised flow resistance along the customised bifurcating networks ($\alpha_0 = 0.5$), designed using the biomimetic principle (Eq. (4.31)). Two customised geometries were considered corresponding to $n = 0.6$ and $n = 1.6$ with $X = 1.25$.

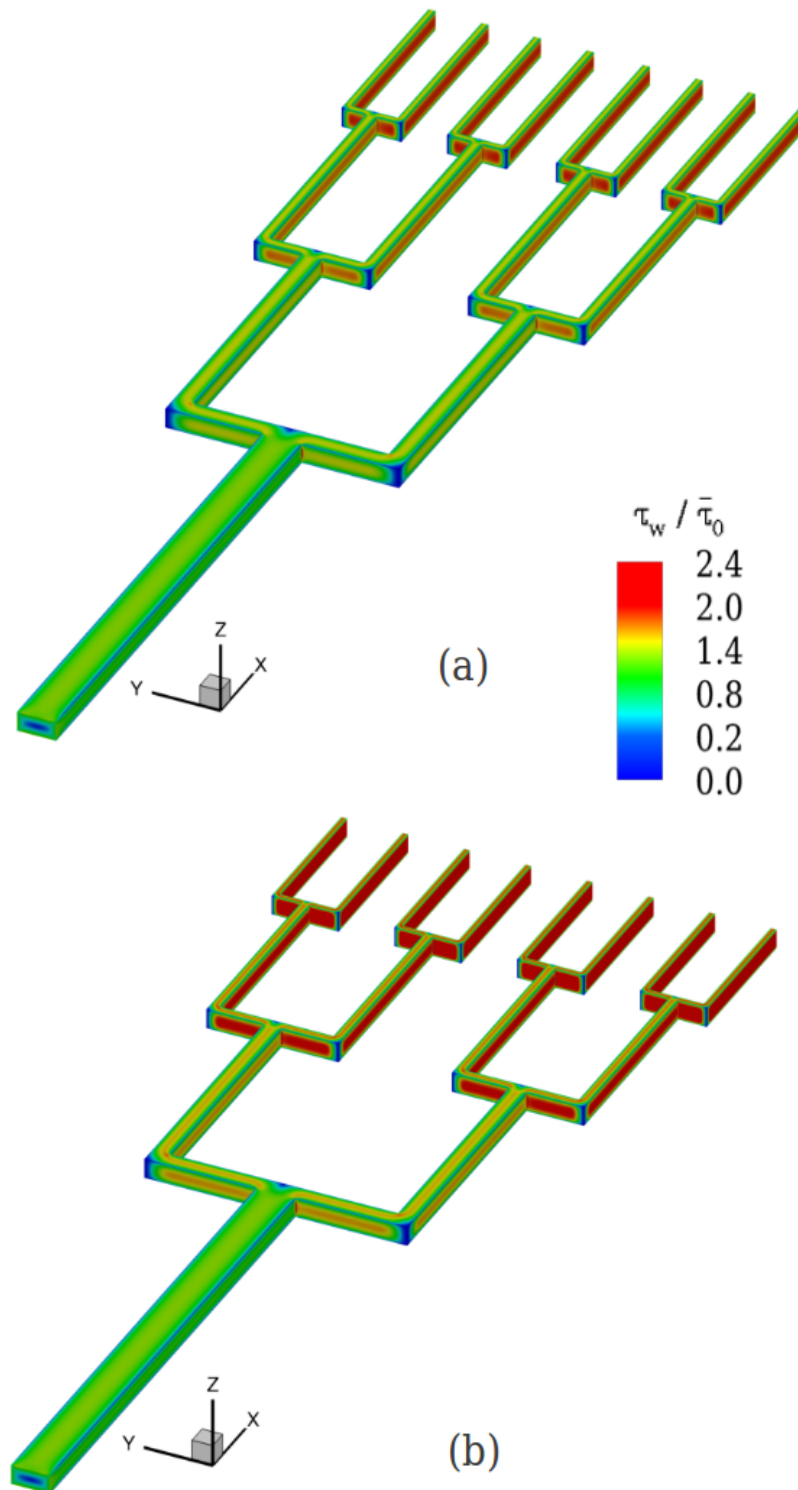


Figure 4.18. Contour-plots of the normalised wall shear-stress along the bifurcating networks ($\alpha_0 = 0.5$), for a power-law fluid flow with $n = 0.6$ in the Newtonian-designed geometry (Table 4.5) (a) and in the customised geometry (Table 4.7) (b) for $X = 1.25$.

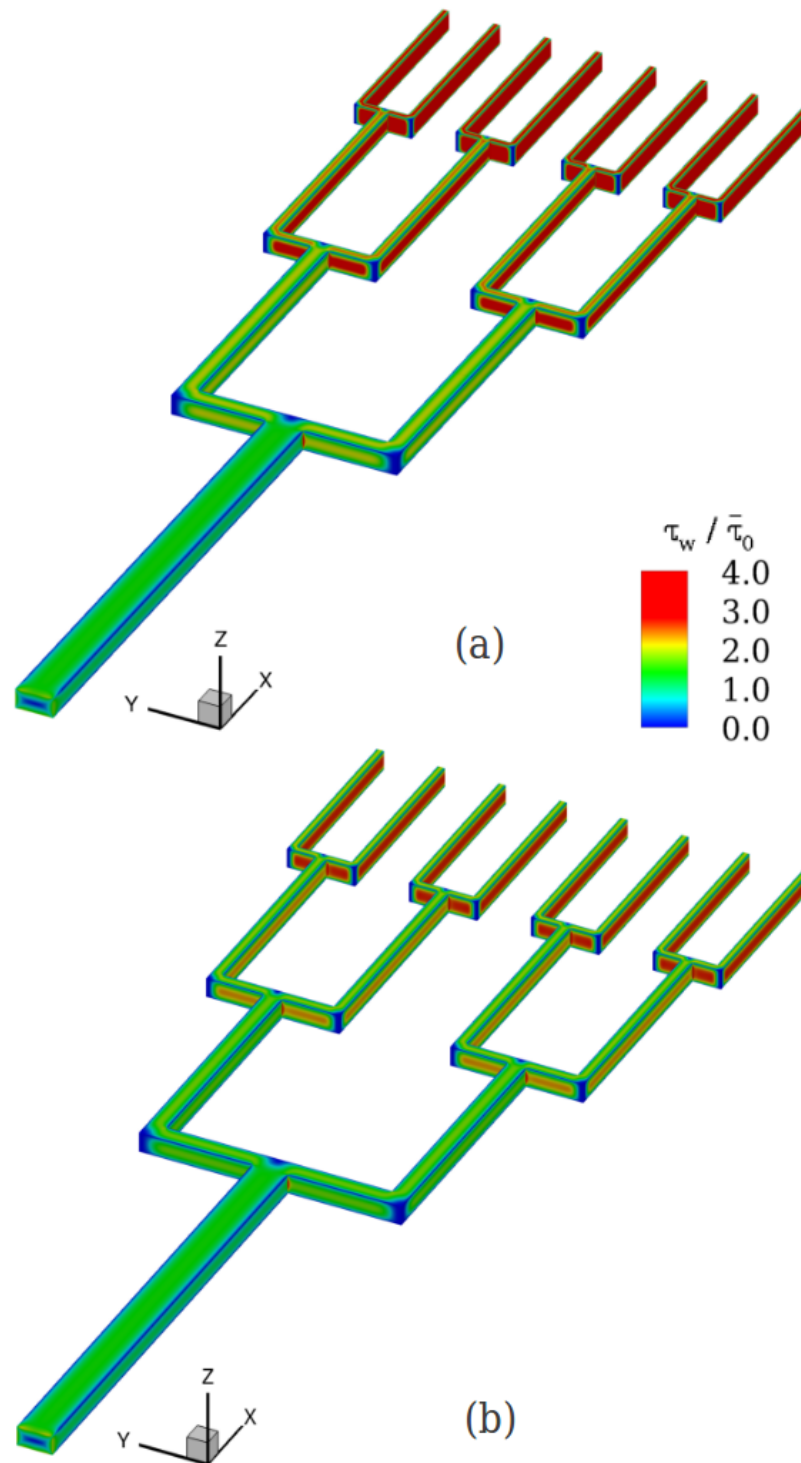


Figure 4.19. Contour-plots of the normalised wall shear-stress along the bifurcating networks ($\alpha_0 = 0.5$), for a power-law fluid flow with $n = 1.6$ in the Newtonian-designed geometry (Table 4.5) (a) and in the customised geometry (Table 4.7) (b) for $X = 1.25$.

design are reflected on the lengths of each generation and considering the proportionality assumption, the flow resistances along the networks shown in Fig. 4.17 demonstrate that the biomimetic rule is in good agreement with theory. A maximum deviation of 2% is reported for the case of the shear-thickening fluid in the last (outlet) generation of the network. Additionally, the maximum deviation between the two numerical solutions obtained for M0 and M1 is found to be 0.6% for the normalised stresses at the last bifurcation of the geometry designed for the shear-thinning fluid, and validates the applicability of the biomimetic rule for both power-law designs.

A comparison between the normalised wall shear-stress distribution along the microfluidic networks in the Newtonian-designs and in the customised geometries for the shear-thinning ($n = 0.6$) and shear-thickening ($n = 1.6$) fluids are shown in the contour-plots of Figs. 4.18 and 4.19, respectively, when $X = 1.25$. As mentioned earlier, for both cases the microfluidic networks have the same inlet aspect ratio of $\alpha_0 = 0.5$ and thus the same normalised wall shear-stress distribution in the inlet channel ($i = 0$), but only the customised geometries generate the desired gradients of the shear-stresses in the subsequent generations. An additional interesting feature considering “truly” creeping flow conditions, is that if the flow is inversed and imposed by the last generations of the design, instead of the parent branch as done so far, then the network will perform as a design which generates negative gradients of the average tangential shear-stress. As such, channels with $X > 1$ can be considered as *dual-performance* microfluidic networks, able to assist in studying the equivalent inverse problem by using only one network.

4.5.4 Negative gradients of shear-stress distribution ($X = 0.75$)

Here, the case where the branching parameter is set to be smaller than unity ($X < 1$) is examined, in order to produce negative shear-stress gradients. An inlet aspect ratio $\alpha_0 = 0.5$ is considered, and the branching parameter is set to $X = 0.75$. Table 4.9 illustrates the appropriate dimensions for the Newtonian-designed geometry. Comparing the widths predicted for $X = 0.75$ with the ones presented for the cases of $X = 1$ (Table 4.1) and $X = 1.25$ (Table 4.5) when a Newtonian fluid is considered ($n = 1$), it

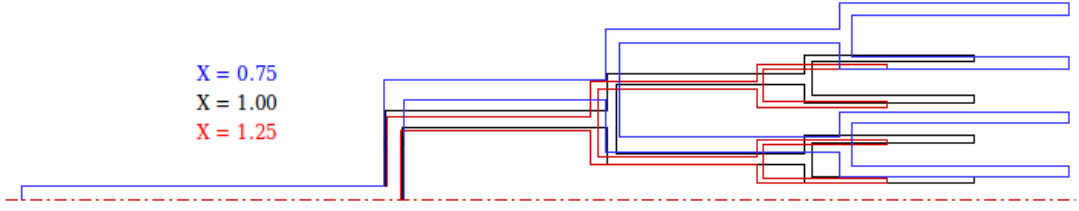


Figure 4.20. Comparison of the bifurcating networks of rectangular cross-section and inlet aspect ratio $\alpha_0 = 0.5$ created for Newtonian fluids with $L_i = 20D_{h_i}$, using different branching parameters, X .

is clear that the geometries exhibit large differences in the widths of each consecutive generation. Based on the proportionality assumption and considering that for all the cases studied the length of each generation is set to be $L_i = 20D_{h_i}$, the total length of each microfluidic network is also affected. [Figure 4.20](#) presents a comparison between the three geometries produced for the different branching parameters for the case of a Newtonian fluid, when the same proportionality is used. Evidently, since the same width and aspect ratio are considered for the inlet branch (α_0), its length, L_0 , is the same for all three cases, but daughter channels differ significantly depending on the branching parameter.

Examining the Newtonian case, the geometry composed of the dimensions of [Table 4.9](#) has been generated, consisting 32 blocks and discretised by 2,373,252 computational cells (cf. [Table 4.10](#)). The computational results for the mean tangential shear-stress throughout the network when $n = 1$, are shown in [Fig. 4.21](#), exhibiting good agreement with theory and a maximum deviation of less than 0.6%. The solution is also found to be independent from the mesh size since the performance of M0 and

Table 4.9. Geometrical parameters and dimensions of planar bifurcating networks with initial aspect ratio $\alpha_0 = 0.5$ and branching parameter $X = 0.75$, designed for a Newtonian fluid.

i	w_i (μm)	d_i (μm)	α_i	D_{h_i} (μm)	a^*	b^*
$X = 0.75$						
0	250.0	125.0	0.500	166.7	0.2439	0.7278
1	177.7	125.0	0.704	146.8	0.2205	0.6917
2	132.0	125.0	0.947	128.4	0.2123	0.6775
3	101.7	125.0	1.230	112.1	0.2150	0.6823

Table 4.10. Mesh characteristics for a Newtonian ($n = 1$) geometry, designed for $X = 0.75$ and $a_0 = 0.5$.

Mesh	$\delta x_{min}/D_{h0}$	$\delta y_{min}/D_{h0}$	$\delta z_{min}/D_{h0}$	Number of Cells
M0	0.023	0.023	0.020	1,514,623
M1	0.018	0.018	0.018	2,373,252

M1 is experiencing a maximum deviation of 0.20% in terms of the normalised stresses. The validity of this outcome is again reinforced by the evaluation of the flow resistance along the microfluidic network displayed in Fig. 4.22, where the numerical results follow once again the theoretical trend.

Moving forward to the investigation of the power-law fluids, the universality of the Newtonian geometry has been investigated using the shear-thinning fluid with $n = 0.6$ and the shear-thickening fluid with $n = 1.6$, as done previously for the case of $X = 1.25$. Figures 4.21 and 4.22 report also the response of the power-law fluids in the Newtonian designed geometry, indicating a deviating response compared to the Newtonian fluid. This behaviour is analogous but opposite to that exhibited for the case of $X = 1.25$. Here, the shear-thinning fluid experiences higher average shear-stresses at the walls of the microfluidic network, whereas the shear-thickening fluid experiences lower average

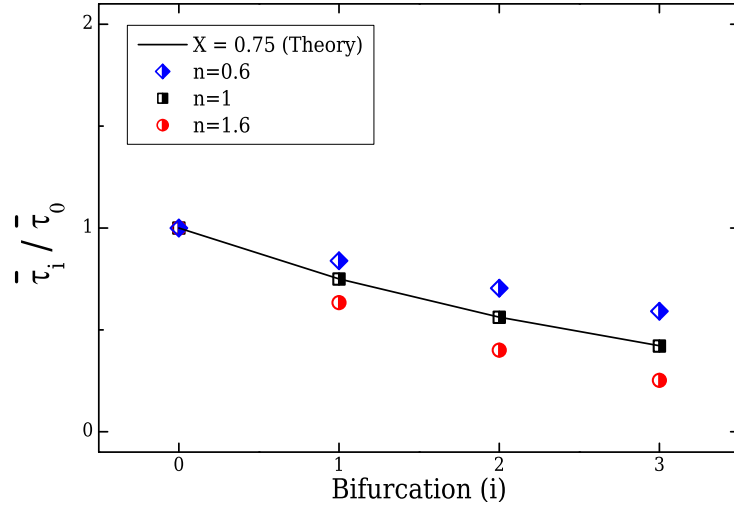


Figure 4.21. Normalised wall shear-stress along the network with $a_0 = 0.5$, designed for a Newtonian fluid with $X = 0.75$.

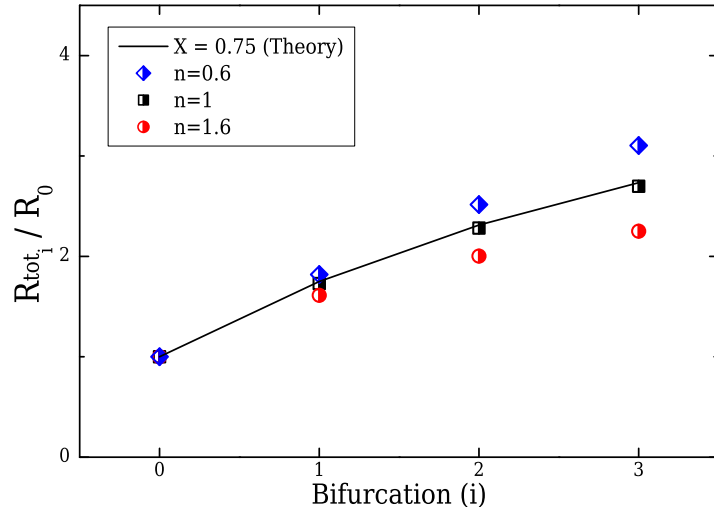


Figure 4.22. Normalised flow resistance (b) along the network with $a_0 = 0.5$, designed for a Newtonian fluid with $X = 0.75$.

shear-stresses. Obviously, this deviating response is reflected in a significant deviation on the resistances along the Newtonian-design shown in Fig. 4.22, in a similar fashion to the $X = 1.25$ case.

In order to design bifurcating networks that will predict the desirable negative average shear-stress gradients for each fluid, the biomimetic set of equations was solved. The appropriate dimensions of the customised geometries for each power-law fluid studied

Table 4.11. Geometrical parameters and dimensions of planar networks with initial aspect ratio $\alpha_0 = 0.5$ and branching parameter $X = 0.75$, for power-law fluids with $n = 0.6$ and $n = 1.6$.

i	w_i (μm)	d_i (μm)	α_i	Dh_i (μm)	a^*	b^*
$n = 0.6$						
0	250.0	125.0	0.500	166.7	0.2439	0.7278
1	207.1	125.0	0.604	155.9	0.2293	0.7059
2	173.9	125.0	0.719	145.5	0.2195	0.6900
3	148.1	125.0	0.844	135.6	0.2141	0.6806
$n = 1.6$						
0	250.0	125.0	0.500	166.7	0.2439	0.7278
1	164.1	125.0	0.762	141.9	0.2172	0.6859
2	114.8	125.0	1.088	119.7	0.2126	0.6780
3	84.2	125.0	1.485	100.6	0.2227	0.6953

Table 4.12. Mesh characteristics for the power-law geometries considered ($n = 0.6$ and $n = 1.6$) geometry, designed for $X = 0.75$ and $a_0 = 0.5$.

Mesh	$\delta x_{min}/D_{h0}$	$\delta y_{min}/D_{h0}$	$\delta x_{min}/D_{h0}$	Number of Cells
$n = 0.6$				
M0	0.027	0.027	0.022	1,576,801
M1	0.024	0.023	0.020	2,337,532
$n = 1.6$				
M0	0.019	0.020	0.020	1,763,561
M1	0.017	0.018	0.018	2,438,079

are given in [Table 4.11](#).

The meshes used to discretise each geometry consist of 32 blocks, with the shear-thinning design being discretised by 2,337,532 computational cells and the shear-thickening by 2,438,079 (cf. [Table 4.12](#)). [Figure 4.23](#) demonstrates that when the appropriate designs are used, the power-law fluids obey the biomimetic principle and produce the desired average shear-stresses at the networks walls. The maximum deviation is reported for the shear-thickening fluid and is less than 0.8%. Furthermore, the validity of the biomimetic design is verified by the evaluation of the flow resistances at each bifurcation, being in agreement with [Eq. \(4.40\)](#) as shown in [Fig. 4.24](#), with a maximum

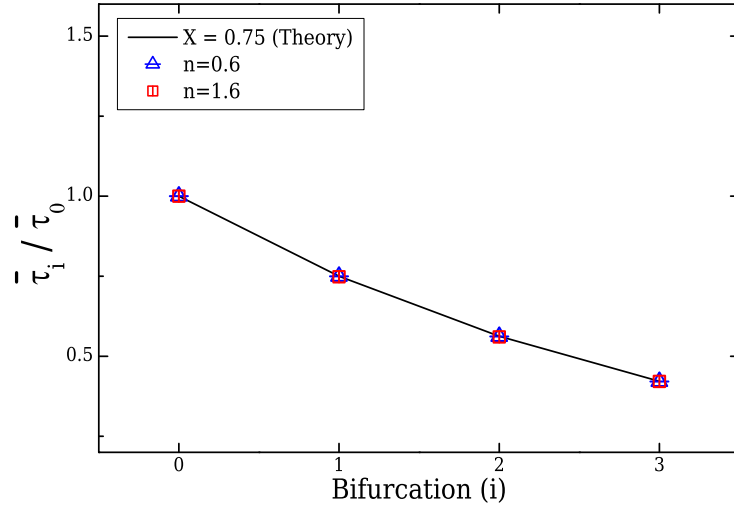


Figure 4.23. Normalised wall shear-stress along the customised bifurcating networks ($\alpha_0 = 0.5$), designed using the biomimetic principle ([Eq. \(4.31\)](#)). Two customised geometries were considered corresponding to $n = 0.6$ and $n = 1.6$ with $X = 0.75$.

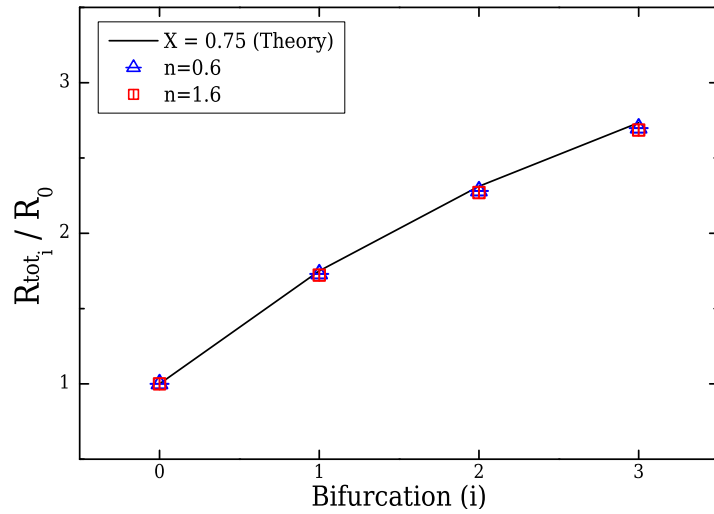


Figure 4.24. Normalised flow resistance along the customised bifurcating networks ($\alpha_0 = 0.5$), designed using the biomimetic principle (Eq. (4.31)). Two customised geometries were considered corresponding to $n = 0.6$ and $n = 1.6$ with $X = 0.75$.

deviation being 1% for the shear-thickening fluid. Very good agreement is also found when the equivalent M0 meshes are considered, with a maximum reported deviation of 0.20% for the normalised shear-stresses when $n = 0.6$.

Figures 4.25 and 4.26 illustrate a comparison of the the contour-plots for the normalised wall shear-stress distribution developed along the microfluidic networks when the Newtonian-design and the customised geometries are employed for the shear-thinning ($n = 0.6$) and shear-thickening ($n = 1.6$) fluids, respectively, for the case of $X = 0.75$. As discussed previously for the $X = 1.25$ case, reversing the flow direction by imposing the fluid of interest by what were previously outlets of the design, the network will perform now as a system that generates positive gradients of the tangential shear-stress.

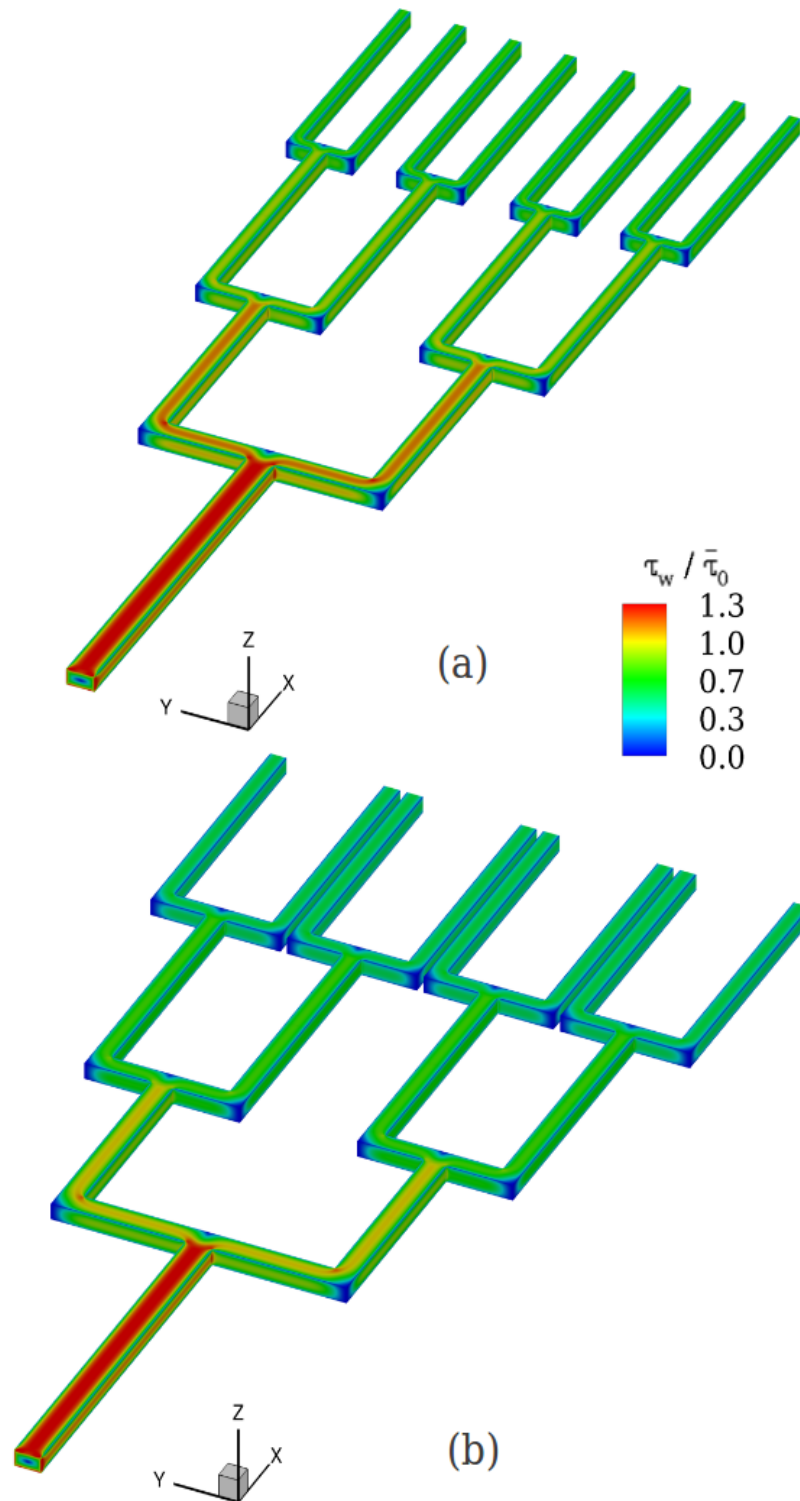


Figure 4.25. Contour-plots of the normalised wall shear-stress along the bifurcating networks ($\alpha_0 = 0.5$), for a power-law fluid flow with $n = 0.6$ in the Newtonian-designed geometry (Table 4.9) (a) and in the customised geometry (Table 4.11) (b) for $X = 0.75$.

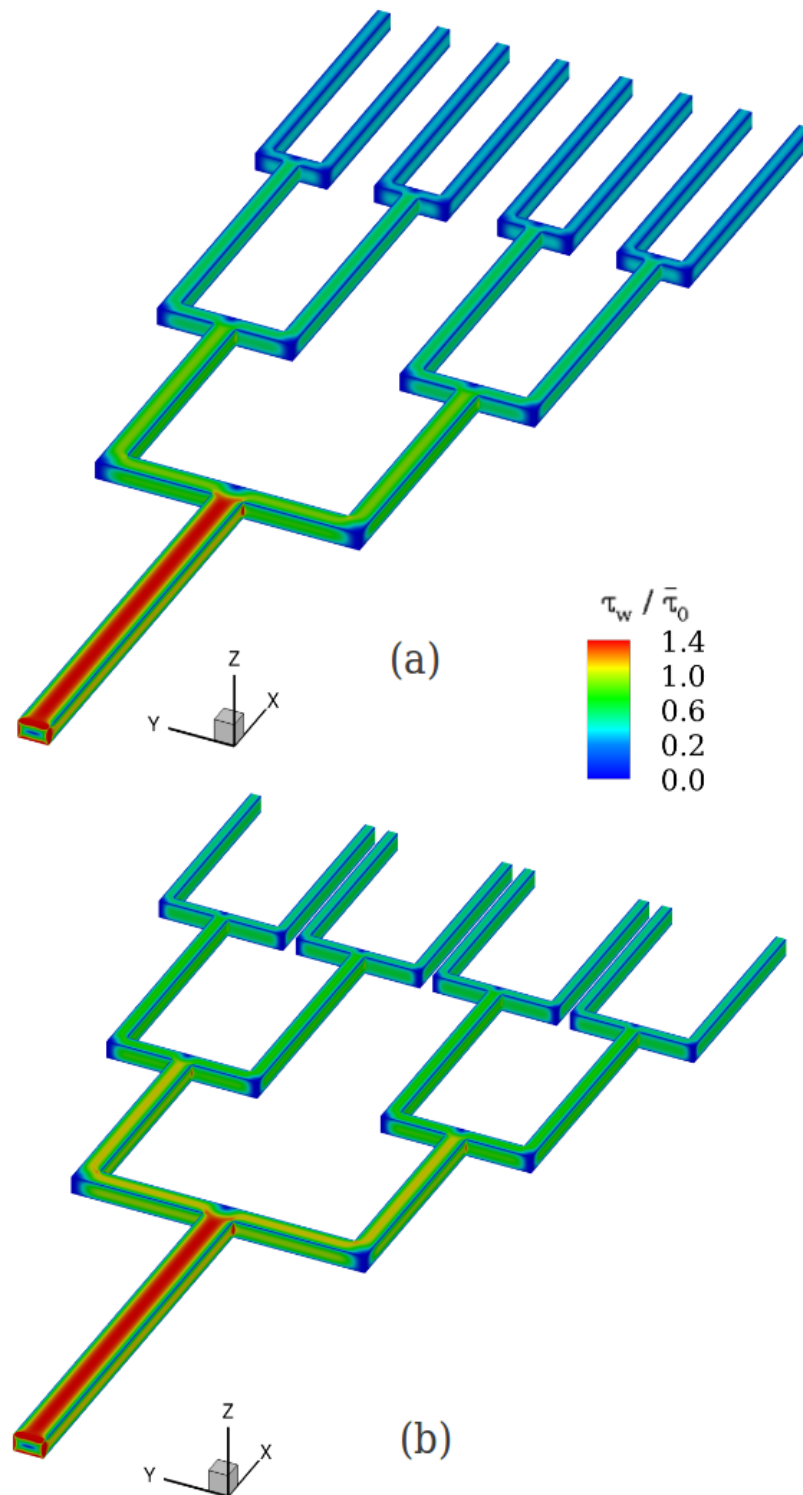


Figure 4.26. Contour-plot of the normalised wall shear-stress along the bifurcating networks ($\alpha_0 = 0.5$), for a power-law fluid flow with $n = 1.6$ in the Newtonian-designed geometry (Table 4.9) (a) and in the customised geometry (Table 4.11) (b) for $X = 0.75$.

4.5.5 Effect of increasing Reynolds number

The theoretical analysis described in detail in [Section 4.2](#) and the biomimetic design rule proposed for generating microfluidic networks that will produce known and well defined flow characteristics are based on the assumption that flow is laminar and manages to fully develop in each branch. This fact combined with the typical type of flows in microfluidics led to the assumption of considering creeping flow conditions in all previously discussed numerical simulations. Although low Reynolds numbers are easily achieved at the microscale, imposing a “truly” creeping flow experimentally is not possible and therefore, it is important to know the limit of validity of our design rule as the Reynolds number is increased. [Figure 4.27](#) shows a comparison of the normalised total network resistance for increasing Reynolds number obtained for Newtonian, shear-thinning ($n = 0.6$) and shear-thickening ($n = 1.6$) fluids in the bifurcating network designed for a Newtonian fluid ([Table 4.1](#)).

For Reynolds numbers up to a value of $Re_0^* = 30$, the CFD results are in good agreement with theory for all fluids tested, with a maximum relative error of approxi-

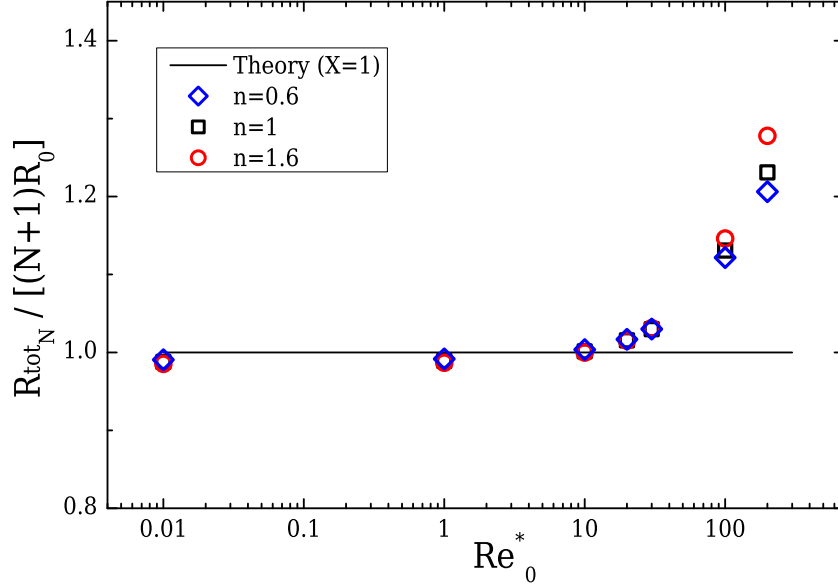


Figure 4.27. Normalised network total resistance as a function of the inlet Reynolds number (Re_0^*) defined in [Eq. \(4.22\)](#) for Newtonian, shear-thinning ($n = 0.6$) and shear-thickening ($n = 1.6$) fluids using the Newtonian designed geometry for $\alpha_0 = 0.5$ and $X = 1$ ([Table 4.1](#)).

mately 2%. However, when the imposed flow rate is increased, the CFD results clearly over-predict the theoretical resistance where a deviating behaviour with a relative error between 12% -14% for $Re_0^* = 100$ is reported for all fluids.

It should be noted that as the flow rate is increased, the flow is unable to reach a fully developed state in the branches of each generation, with secondary flows reported at the first bifurcation. All networks considered in this work exhibit abrupt, 90°, bends and it is likely that by designing a smoother configuration higher Re could be achieved, while maintaining the desired performance. Furthermore, the value of L/D_h was set to 20, and by increasing this value it is expected that the limits of validity in terms of Re_0^* will also increase. However, it should be mentioned that increasing the length in practical applications is not always viable as the increase in pressure might endanger the integrity of lab-on-a-chip devices.

4.6 Synopsis

A biomimetic design rule for constructing bifurcating microfluidic networks with rectangular cross-sectional areas is proposed and is based on the biological principle that was first expressed by Murray [135]. As described in Section 4.2, Murray’s law was originally derived considering a fully developed flow of Newtonian fluids in circular ducts under laminar flow conditions. Emerson *et al.* [139] and Barber and Emerson [140] extended Murray’s law to consider non-circular cross-sectional areas typical of microfluidic applications. Here, the biomimetic rule was extended further for designing microfluidic networks suitable for use with power-law fluids, in which the viscosity is shear-rate depended.

Designing manifolds using the new biomimetic rule offers the ability to generate customised flow characteristics for both power-law and Newtonian fluids. For a given application, the proposed design rule is able to provide control over the flow field and, in particular, over the wall shear-stress distribution along the network, by carefully selecting a branching parameter which governs the change in channel dimensions at each bifurcation.

When the value of the branching parameter is equal to unity ($X = 1$), the principle of minimum work underlying Murray's law is obeyed. For microfluidic networks with an inlet aspect ratio $\alpha_0 = 0.5$, the biomimetic design rule generates geometries for Newtonian and power-law fluids with power-law index in the range $[0.2 - 2.0]$ that exhibit negligible differences. This universality in terms of geometry is particularly useful for experimental purposes, since the same device can be used effectively for different fluids. However, a preliminary investigation when $\alpha_0 = 0.2$ or 0.3 (dimensions are given in Appendix A.1) showed that this universality is no longer valid and customised geometries should be considered for each particular power-law index. Therefore further examination is suggested if other values of α_0 are requested. It should be noted that although the ratios of the average wall shear-stresses are the same along the network for Newtonian and power-law fluids, the magnitude of the wall shear-stresses depends on the particular fluid flow conditions.

When gradients of wall shear-stresses along the bifurcating network are required (i.e. $X \neq 1$) different geometries must be used for each power-law fluid in order to achieve the desired flow characteristics. In this case, the biomimetic rule allows us to create customised geometries which provide the desired flow field with well known characteristics. Moreover these geometries have the advantage of dual-performance under creeping flow conditions, meaning that by reversing the flow the exact opposite behaviour can be studied.

The proposed designs are valid when fully-developed flow is reached in each generation of the network, and therefore creeping flow conditions have been considered throughout this study, which is a good approximation for most microfluidic flows. However, obtaining truly creeping flow is not possible and thus the limits of the design were tested in terms of Reynolds numbers in order to guide experiments. The numerical calculations conducted show that for $Re_0^* \gtrsim 30$ care should be taken as the results start to deviate from the predictions. In particular, the microfluidic networks designed exhibit 90° bends and a limitation is imposed in terms of the Reynolds number that can be used. An improvement to the current design would involve the use of smoother corners, or Y-junction shaped bifurcations where friction losses would be reduced.

The aim of the proposed biomimetic approach is to offer a design rule for microfluidic networks that may benefit research areas which require devices capable of better controlling the shear-stress field. Examples such as stem cell research, where there is a need for tuning the microenvironment around stem cells in various ways, and applications requiring separation (e.g. blood-plasma extraction, which is highly influenced by the properties of the flow field), may benefit from using customised bifurcating geometries. Another interesting study would involve investigations related to deformation history. The behaviour of a viscoelastic fluid, a droplet or a cell could be examined in channels where the stress is increasing with a very well defined and known distribution. This way, as the element of interest propagates in the interior of the network the deformation history from the previous branches should be considered.

A preliminary experimental investigation¹ (results not shown here) has shown that the flow behaviour is sensitive to large errors in the dimensions of the fabricated networks relative to the theoretical biomimetic design. Although achieving the same level of accuracy in the manufactured lab-on-a-chip devices as compared to the numerical geometrical set-up is not an easy task, care should be taken in the choice of fabrication methods to ensure enough accuracy for the rule to be approximated satisfactorily. To validate the designs experimentally, ideally one would like to measure the wall shear stresses along the network. However, measuring directly the wall shear-stresses is difficult experimentally. To overcome this issue, a solution of shear sensitive λ -DNA, for which the behaviour under shear is well-understood, is currently being used as a bio sensor to test the distinct stresses imposed by geometries generated using the design rule. By observing the individual behaviour of such molecules and the respective degree of deformation along the consecutive channels of each network, it has been verified that the geometries impose the desired stress gradients along the network as predicted by the biomimetic rule, demonstrating the potential of using the customised microfluidic networks for testing shear sensitive biological materials under well-controlled wall

¹Ph.D. student Joana Fidalgo currently investigates experimentally the validity of the proposed biomimetic rule and seeks for further interesting applications that will benefit from the use of microfluidic bifurcating networks. The work has not yet been submitted for publication.

shear-stresses [151].

There are additional applications of these microfluidic networks that could prove useful. In this work an equal split of the flow at the beginning of each generation was considered. It could be interesting if the flow is allowed to split asymmetrically at the first bifurcation and maintain the symmetric split in the remaining generations. By doing this, different conditions can be applied in the two halves of the design. The biomimetic rule will not be valid for the parent segment (although can still be correlated to the flow conditions at former branches). This could provide the ability to monitor simultaneously the behaviour of the desired sample under different flow conditions. Also, it is well reported that the effect of elastic turbulence can assist in micro-mixing [9]. Given the flow behaviour and the ability to generate curved streamlines in these type of microfluidic networks, they could potentially form a microfluidic platform to be used to enhance passive micro-mixing [152].

Chapter 5

Designs for extensional flow

In this chapter, several configurations appropriate for performing measurements under homogeneous extensional flows are proposed. These configurations are subdivided here in two categories; those that operate based on the characteristics of a flow with a single-stream and those that employ multiple inlet streams (two or three). Common standard shapes are shown not to perform ideally, failing to produce the desired homogeneous extension. Using optimisation techniques various, more efficient, shapes are proposed and further investigated. Initially, the single-stream designs with a contraction/expansion region are examined, and their performance is compared to the well-known hyperbolic shape. A variety of optimised geometries has been proposed for three dimensional configurations with different aspect ratios, due to the different kinematics produced as a consequence of wall effects. Finally, for the multi-stream cases, the performance of T-junctions and flow-focusing devices is examined and new optimised shapes, which are able to generate specific and desired characteristics are proposed.

Part of the chapter results have been published in:

K. Zografos, F. Pimenta, M. A. Alves and M. S. N. Oliveira, “*Microfluidic converging-diverging channels for homogeneous extensional deformation*”, *Biomicrofluidics*, vol. **10**, 043508, 2016

5.1 Introduction

A large amount of industrial processes and scientific investigations dealing with Newtonian and non-Newtonian fluids are characterised by the existence of strong extensional flows. There is a current demand for appropriate devices capable of assisting in the investigation of the extensional behaviour and the characterisation of extensional material properties of fluids of interest, in particular those exhibiting complex rheological behaviour, such as polymer solutions or various biofluids [153, 154]. Unlike Newtonian fluid flows - in which the extensional viscosity is proportional to the shear viscosity (Trouton ratios of 3 or 4 for uniaxial and planar extension, respectively) - viscoelastic fluid flows often lead to significantly larger flow resistance due to strong extensionally-thickening effects, with Trouton ratios that can be orders of magnitude greater than for Newtonian fluids [154]. This makes thorough experimental characterisation of extensional properties of viscoelastic fluids crucial in various contexts, ranging from fundamental studies to industrial applications, aiming to: accurately describe and predict their behaviour; effectively control their flow; design efficient and safe devices/fluidic components; detect subtle dissimilarities in their composition (e.g. for product quality control); provide quality-assurance of final products (e.g. in polymer or food processing industries).

Lab-on-a-chip platforms have been proven a very powerful tool in the context of extensional flows of complex fluids [16, 153]. The characteristic small length scales ($1\mu\text{m}$ - $1000\mu\text{m}$) of microfluidic devices allow the generation of large deformations and deformation rates for relatively small flow rates, enhancing mechanical properties that might otherwise be masked by inertial effects in macro-scale flows. The small amount of sample needed to operate the microfluidic devices and their ability to reproduce precisely controlled, three dimensional environments, make them a promising candidate over other techniques used conventionally in biomedical research [155, 156]. Examples include studies of cell responses, molecular stretching, as well as droplet deformation and other inter-facial studies [157–161]. Pipe and McKinley [10], pointed out the importance of microfluidic technology and the advantages offered for investigat-

ing and characterising the rheological behaviour of viscoelastic fluids [10] both under shear and extensional deformation. Later, Galindo-Rosales *et al.* [153] reviewed various micro-fabricated configurations for potential use in experimental studies related to elongational flows and highlighted the relevance of microfluidics in the context of extensional rheometry. Recently, Haward [154], reviewed and reported the advantages of microfluidic configurations which generate stagnation point flows in studies related to extensional rheology.

Here, the configurations employed for performing studies related to extensional flows are distinguished in two categories based on their operating simplicity. The first category contains these geometries in which only a single-stream needs to be controlled, such as *contraction/expansions*. The second refers to these geometries where two or more streams are responsible for generating the flow conditions within the device, such as *T-Junctions* and *flow-focusing* devices.

Arguably, the most frequently single-stream designs used for studying extensional flows are those that incorporate an abrupt contraction or a symmetric abrupt contraction/expansion (see Fig. 5.1a and 5.1b). Despite their geometric simplicity and their manufacturing ease they produce flows characterised by a combination of strong shear effects close to the walls and strong extensional effects along the centreline region in the vicinity of the contraction [162]. Such entry flows have been established as one of the most appropriate geometries for benchmarking the efficiency of computational methods for non-Newtonian fluids [35, 71, 163] and have been extensively used experimentally for investigating the mechanisms of fluid elasticity [16, 162, 164, 165], where the “excess” pressure drop due to extensional flow in the contraction is correlated to

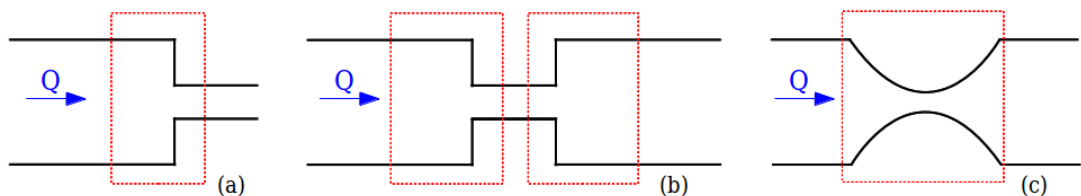


Figure 5.1. Configuration of various single-stream designs with an abrupt contraction (a), a sudden contraction followed by a symmetric expansion (b) and a smooth symmetric converging/diverging region (c). The *dashed* rectangles illustrate the regions of interest.

important viscoelastic normal-stress effects [166]. However, due to their inefficiency to produce homogeneous extension conditions are unlikely to establish a considerable region of constant strain-rate [167]. As with shear viscosity measurements, where shear rheometers generate a constant shear-rate canonical flow, which allows the measurement of the shear viscosity as a function of shear-rate, for an extensional rheometer constant extension rate would be ideal for investigating extensional properties of the fluids [153].

Smooth contraction/expansion geometries such as hyperbolic shaped microchannels (cf. Fig. 5.1c), were among those configurations suggested for this purpose, and have been discussed in the reviews by Galindo-Rosales *et al.* [153] and Haward [154] on extensional flows. The idea of constrained converging flows was proposed by Cogswell [168, 169], in order to enforce elongation and assist in rheological measurements of polymer melts under extensional flow. James *et al.* [170] introduced the principles of a hyperbolic converging rheometer pointing out its advantage to generate constant strain-rates along the centreline of the flow. Later, Oliveira *et al.* [74] were among the first to consider a micro-fabricated hyperbolic configuration as a potential microfluidic rheometer and studied its performance both numerically and experimentally, using a Newtonian fluid. A detailed study of the flow kinematics in a hyperbolic contraction followed by an abrupt expansion was presented and they pointed out the difficulty in distinguishing extensional from shearing effects within the contraction, with the flow being non-homogeneous and the developed strain-rate deviating from the ideal uniform profile. The same configuration was later used for estimating the apparent extensional viscosity of polyethylene oxide solution [171], for investigating the flow of low viscosity Boger fluids [172] and also for mimicking flows along stenoses in the human micro-circulatory system using blood analogue solutions [173]. Similar configurations to this type of converging/diverging geometries have been used to study the deformability of white blood cells [174] and of red blood cells under strong extensional flow, for potential use in diagnosis of blood diseases [175–177]. Ober *et al.* [166] and Keshavarz and McKinley [178], extended the study on the use of hyperbolic channels for rheological purposes by considering a micro-channel with a symmetric hyperbolic contrac-

tion/expansion used in the commercially available “Extensional Viscometer-Rheometer-On-a-Chip” (EVROC™). The device includes four pressure sensors along the length of the channel for separately evaluating the pressure drop due to shear effects in the fully-developed regions upstream and downstream of the contraction, where the flow is fully-developed, and the pressure drop across the hyperbolic contraction/expansion. It was intended that by subtracting these two pressure drops, it would be possible to evaluate the extra pressure drop due to elastic normal stresses alone. However, the authors reported that the configuration used produced a non-homogeneous flow field, with entrance and exit effects resulting in a region characterised by a combination of shear and elongational characteristics. In addition, Keshavarz and McKinley [178] reported that EVROC will not perform efficiently for low viscosity dilute polymer solutions, since the hyperbolic contraction is affected by non-linear inertial effects. The authors suggested instead the use of Rayleigh Ohnesorge Jetting Extensional Rheometry (ROJER) technique that was originally introduced for this reason [179].

On the contrary, multi-stream configurations have lately increased their popularity in studies related to polymer solutions, multiphase systems, biofluids and cell responses [154]. This includes geometries such as cross-slots, T-junctions and flow-focusing devices. Taylor [180], was the first to introduce the *four-roll mill* design, a configuration consisting of four cylinders able to rotate inside a confined domain. The device had the ability to generate different flow kinematics and assisted Taylor’s studies on the deformation and break-up of a droplet. Later Hudson *et al.* [181], reported the significance of stagnation point flows and inspired by the ability of Taylor’s device to generate flows of this kind, introduced the *microfluidic trap* which was the first microfluidic equivalent of the four-roll mill device. This device consisted of six opposing channels in an asymmetrical, chiral, arrangement. By imposing the appropriate flow rates one could generate a stagnation point flow varying from pure extension to nearly pure rotation. An improved version of the microfluidic trap, was proposed by Lee *et al.* [182], where four inlet and four outlet channels were arranged symmetrically and joined to a central cavity, able to generate a stagnation flow. The authors illustrated numerically and experimentally that the device was able to generate flows that varied

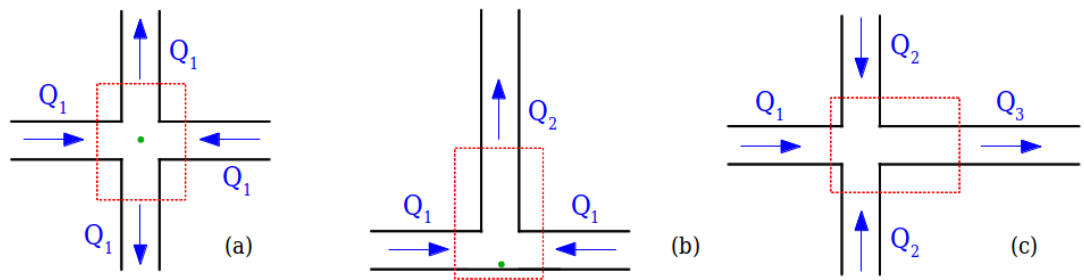


Figure 5.2. Configuration of various multi-stream designs with a cross-slot shape (a), a T-Junction (b) and a flow-focusing device (c). The arrows indicate the direction of the bulk flow, the *dashed* rectangles illustrate the regions of interest for each configuration, and the *dot* indicates the position of the stagnation point.

from purely rotational to purely extensional.

In the recent review by Haward [154], the significance of the cross-slot configuration is pointed and its advantages over other designs are discussed. Cross-slots shown schematically in Fig. 5.2a, exhibit a simpler design than those discussed so far. They are composed of four intersecting channels with two opposing inlets and two opposing outlets. They are easier to control and are able to generate strong stagnation point flows. They have found great success in investigating elastic instabilities of polymer solutions either experimentally [183,184] or numerically [79,185,186], they can be used to trap and investigate single-molecule responses [161,187,188] of interest to disease diagnostics and they can potentially assist in mixing techniques for flows with small Reynolds numbers [189]. A major characteristic of stagnation point flows is that either fluid elements are subjected to high velocity gradients for a limited time as they pass through the surrounding region of the stagnation point, or fluid elements trapped at the stagnation point are subjected to high strain-rates for undefined time. With that idea in mind and based on the simplicity of cross-slot designs, Alves [190] introduced the “peculiar” optimal shape of an optimised cross-slot, named OSCER (Optimised Shape Cross-slot Extensional Rheometer), by demonstrating numerically its ability to generate homogeneous extension along the centrelines of the flow field for both Newtonian and viscoelastic fluids. Haward *et al.* [77] fabricated and studied experimentally the performance of the optimised cross-slot, demonstrating the good performance of the OSCER device for both Newtonian and low viscosity polymer solutions, validating

its potential for extensional rheology measurements. The same configuration has been later employed for investigating the rheological properties of hyaluronic acid [191] while, a variety of three dimensional optimised shapes have been tested in Galindo-Rosales *et al.* [192].

Another configuration able to create a stagnation point flow is the T-junction, shown schematically in Fig. 5.2b. Their operation is simpler than the cross-slot device, with the fluid injected into the device either by the two opposing channels and ejected by the single perpendicular, or alternatively the two opposed channels serve as outlets and the flow is imposed by the perpendicular channel. These geometries have found applications in interfacial studies where droplet generation or break-up are investigated [193–195], in studies related to elastic instabilities [20], in DNA molecule stretching [196] exploiting the formation of a stagnation point, and they have been proposed as potential configurations for microfluidic rheometers [197] and micromixers [198, 199]. However, the capabilities of these shapes for rheological purposes have not been thoroughly explored so far [153].

Another geometry that can be employed for performing extensional flow studies is the flow-focusing design, which in contrast to the cross-slot and the T-junction configurations, does not exhibit a stagnation point. Similarly to the cross-slot, the flow-focusing design consists of four orthogonal intersecting channels, but has three inlets and only one outlet (cf. Fig. 5.2c). An important characteristic of this type of geometry is that it can minimise the shear effects due to fluid-wall interactions. The lubricant fluid that is injected in the two opposing channels shapes the third stream with the fluid of interest that is introduced through the perpendicular channel, generating a region of shear-free, elongational flow [153]. The converging flow of the fluid of interest is reminiscent of the flow produced by the single-stream hyperbolic channel [21–23]. The main advantage in this case is that different strains can be applied using the same geometry by only changing the inlet flow rate ratio of the lubricant fluid to the fluid of interest. On the contrary, for the constrained type of flow produced in the hyperbolic geometry this can only happen with the use of different geometries. This microfluidic device has been mostly considered in studies related to droplet formation and investigation of the

filament pinch-off for Newtonian and polymeric immiscible fluids [200,201], for studies related to the destabilising effects of the thread formations for highly viscous miscible and immiscible fluids [202] and also finds applications in drug delivery, for creating degradable microparticles [203].

In summary, the basic advantage of single-stream relative to multi-stream configurations is their intrinsic simplicity, resulting in designs with only one inlet and one outlet. For those cases, the Hencky strain is dictated by the geometrical configuration and the nominal strain-rate can be controlled by varying the volumetric flow rate of a single-stream instead of at least three streams which are required to be controlled for cross-slot and flow-focusing devices, and two for the T-junction, making them very practical for experimental studies. On the other hand, the possibility of having stagnation point flows (as for example in the cross-slot) and of generating a variety of different flow conditions (e.g. variation of Hencky strain in a single flow-focusing device), together with the ability to obtain a region of essentially shear-free elongational flow [154,190] increases the interest around multi-stream designs.

The aim of this chapter is to investigate the flow kinematics in both single-stream and multi-stream configurations of interest and propose improved designs based on a numerical optimisation strategy to produce a region of homogeneous extensional flow. More specifically, for single-stream designs the performance of symmetric converging/diverging channels with hyperbolic shape is investigated and optimisation techniques are employed in order to overcome the challenge of non-homogeneity that was reported in Oliveira *et al.* [74] and in Ober *et al.* [166]. Three different contraction ratios (CR) are investigated for both two and three dimensions. The aim is to optimise the shape of a converging/diverging channel to generate ideal strain-rate profiles along the centreline of the flow for use in elongational studies of macromolecules (e.g. DNA) or cells and for potential use as an extensional rheometer. For multi-stream designs, the shape of a T-junction and of a flow-focusing configuration is optimised, to generate a constant strain-rate profile along the centreline downstream of the junction. For all the optimisation studies performed, the mesh deformation technique of NURBS [107], discussed in Section 3.4, is employed. The mesh deformations are applied by equally

weighted control points constricted by an open uniform knot vector.

The chapter is organised as follows: initially, the optimisation procedure is presented in Section 5.2 and the equations of motion in Section 5.3. In Section 5.4, single-stream configurations are studied. The ideal velocity and strain-rate profiles that are used as targets in the optimisation procedure are provided, the optimised configurations are presented and their capabilities and limitations are assessed. Section 5.5 presents the optimisation study for each multi-stream configuration considered (i.e. the T-junction and the flow-focusing). Finally, in Section 5.6 the results of this study are summarised and further improvements are discussed.

5.2 Optimisation Strategy

The optimisation procedure is described schematically in the flow chart of Fig. 5.3. An iterative procedure combining an automatic mesh generation routine and the fluid flow solver discussed in Section 3.3 are coupled with an optimiser, allowing to determine numerically the appropriate boundary shape of the device for a prescribed flow field as it will be shown later.

The outcome of each CFD simulation from every set \mathbf{Y}^* represents a single solution of a general unknown *objective* function. Here, the value of the objective function is defined as a cell-average velocity difference evaluation between the ideal behaviour and

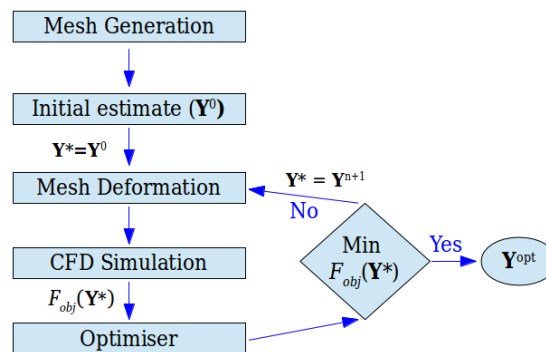


Figure 5.3. Flow chart of the optimisation procedure.

the CFD results expressed by

$$F_{obj} = \sum_i |\tilde{u}_i - \tilde{u}_{target,i}| \Delta \tilde{x}_i \quad (5.1)$$

where $\tilde{u}_{target,i}$ is the desired dimensionless velocity value in each computational cell i required to obtain the ideal velocity profile; \tilde{u}_i is the dimensionless velocity evaluated from the CFD solver at each i -cell along the centreline of the flow and $\Delta \tilde{x}_i$ is the streamwise dimensionless spacing of the computational cell i . Since for each of the single-stream and multi-stream designs considered the desired velocity profiles used as targets are different, they will be presented in the relevant section.

The optimisation procedure responsible for the optimised shape generation depends on the nature of the objective function which is non-linear and therefore not easy to solve. In this work, the freely available derivative-free optimiser NOMAD (Nonlinear Optimization by Mesh Adaptive Direct Search) [204–206] is employed. The NOMAD optimiser is based on the Mesh Adaptive Direct Search algorithm and is specially designed in order to deal with non-linear constrained optimisation problems.

As indicated in Fig. 5.3, an initial estimate \mathbf{Y}^0 of the lattice design points is given as input to the mesh generation program for creating the initial discretised geometry. Each one of these points is then responsible for the geometrical deformation of the numerical mesh as discussed in Section 3.4.4. A single point movement is translated into a deformation of the numerical mesh, applied via the NURBS deformation lattice in which the object is embedded. Depending on the case under investigation the mesh deformation procedure considers either a single NURBS lattice (single-stream designs) or a sequence of joined lattices (multi-stream designs). After the geometry is generated/deformed, the flow solver computes the corresponding flow field, from which the value of a single objective function, F_{obj} , is calculated. The current $F_{obj}(\mathbf{Y}^*)$ is then examined by the optimiser and a new set \mathbf{Y}^{n+1} is produced by the optimiser, which is used to generate a new geometry. The aim of the optimiser is to minimise the value of the objective function, approximating the desired velocity profile by minimising Eq. (5.1) ideally for a small number of F_{obj} evaluations, to reduce the computational costs

associated with the optimisation procedure. When a minimum of F_{obj} is approached, the final optimised solution \mathbf{Y}^{opt} is obtained. It is noted that the optimiser used in this work does not guarantee that the global optimum solution is always achieved, since a local minimum can be found. However, different initial estimates \mathbf{Y}^0 allows to obtain good results.

5.3 Governing equations

The CFD simulations performed for each evaluation of the objective function consider a laminar, incompressible and isothermal fluid flow, solving numerically the continuity and momentum equations:

$$\nabla \cdot \mathbf{u} = 0 \quad (5.2)$$

$$\rho \left(\frac{\partial \mathbf{u}}{\partial t} + \mathbf{u} \cdot \nabla \mathbf{u} \right) = -\nabla p + \nabla \cdot \boldsymbol{\tau} \quad (5.3)$$

where ρ is the fluid density, \mathbf{u} is the velocity vector, p is the pressure and $\boldsymbol{\tau}$ is the extra-stress tensor. For all optimisations creeping flow conditions ($\text{Re} \rightarrow 0$) are considered, which are a reasonable approximation for microfluidic studies. Therefore, except from a small number of CFD simulations presented in [Section 5.4.2](#), the convective terms in the momentum equation are neglected.

For viscoelastic fluid flow, two models were tested, namely the Oldroyd-B and the linear form of the PTT model [46], both discussed in [Section 2.2.2](#). The Oldroyd-B model is used to assess the response of viscoelastic fluids with constant shear viscosity (Boger fluids), whereas the PTT model was used because of its additional ability to predict shear-thinning behaviour. Both models are expressed by the compact form of the simplified Phan-Thien and Tanner constitutive equation ($\xi = 0$):

$$\lambda \overset{\nabla}{\boldsymbol{\tau}}_p + f(\boldsymbol{\tau}_p) \boldsymbol{\tau}_p = \eta_p (\nabla \mathbf{u} + \nabla \mathbf{u}^T) \quad (5.4)$$

where $\overset{\nabla}{\boldsymbol{\tau}}_p$ is the upper-convected derivative of the polymeric component of the extra-stress tensor, $\boldsymbol{\tau}_p$, η_p is the polymer viscosity ($\eta_p = 0$ for Newtonian fluids) and λ is the fluid relaxation time. For the stress function, $f(\boldsymbol{\tau}_p)$, the linear function of the trace of

the polymeric stress tensor [Eq. \(2.13\)](#) is considered:

$$f(\boldsymbol{\tau}_p) = 1 + \frac{\lambda\varepsilon}{\eta_p} \text{Tr}(\boldsymbol{\tau}_p) \quad (5.5)$$

It is reminded, that when $\varepsilon = 0$, the Oldroyd-B model is recovered and the steady state extensional viscosity becomes unbounded. The extra-stress tensor in the momentum equations is decomposed in two parts, the solvent and the polymeric components:

$$\boldsymbol{\tau} = \eta_s(\nabla\mathbf{u} + \nabla\mathbf{u}^T) + \boldsymbol{\tau}_p \quad (5.6)$$

where η_s corresponds to the solvent viscosity. Additionally, for both viscoelastic models the ratio of the solvent viscosity, η_s , to the total zero shear viscosity, η_0 , known as solvent viscosity ratio, β , needs to be defined. The total zero shear viscosity is defined as the summation of the solvent and the polymeric viscosities, $\eta_0 = \eta_s + \eta_p$. In the PTT model, we consider $\beta = 0.01$ and $\varepsilon = 0.25$, which are typical values for concentrated polymer solutions, whereas for the Oldroyd-B model the viscosity ratio was set at $\beta = 0.50$ representative of a constant-viscosity Boger fluid.

The fluid flow is solved numerically using the in-house implicit finite volume CFD solver described in [Section 3.3](#), developed for collocated meshes [\[27,207\]](#). The convective terms in the momentum and constitutive equations are discretised using the CUBISTA high-resolution scheme [\[93\]](#), while the diffusive terms are discretised with central differences. The transient term in the momentum and constitutive equations are evaluated using a first-order implicit Euler scheme. It is noted that since only steady-state solutions are desired, the lower order of accuracy of the transient term is irrelevant, as this term vanishes when steady-state is approached.

5.4 Single-stream designs

5.4.1 Geometry definition

In this section the flow in a single-stream, converging/diverging channel is examined, in which the flow enters the inlet with a flow rate Q (and an average velocity, U_u) as

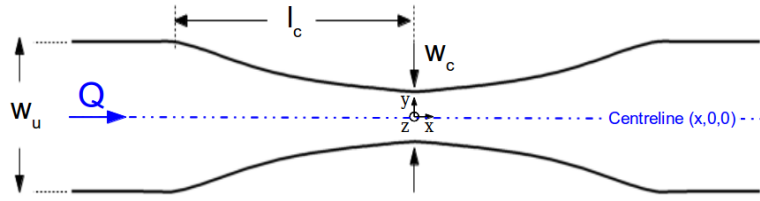


Figure 5.4. Configuration of the converging/diverging geometry.

shown in Fig. 5.4, and is driven towards the outlet of the device. The primary aim is to find the optimised shape that is able to produce a wide region of constant strain-rate, $\dot{\epsilon} = \partial u / \partial x$, along the centreline of the flow.

As discussed in James *et al.* [170] and in James [208], when the fluid flows through the contraction the velocity along the centreline of the flow, u , will ideally start to increase linearly as shown in Fig. 5.5a, reaching a maximum value at the throat of the contraction/expansion region. In the same manner the fluid velocity is expected to decrease linearly in the symmetric diverging part. This ideal behaviour results in a region of strong extension, where the strain-rate should remain constant along the centreline of the flow as shown in Fig. 5.5b. The geometry is characterised by an upstream width, w_u , and a contraction width, w_c , (cf. Fig. 5.4) which define the contraction ratio $CR = w_u/w_c$, the length of the contraction, l_c and produces a total extension, described by the value of Hencky strain, $\epsilon_H = \ln(CR)$.

Typically the cross-sections of microfluidic platforms are not circular, but exhibit a rectangular shape with constant depth. In the converging part of the contraction,

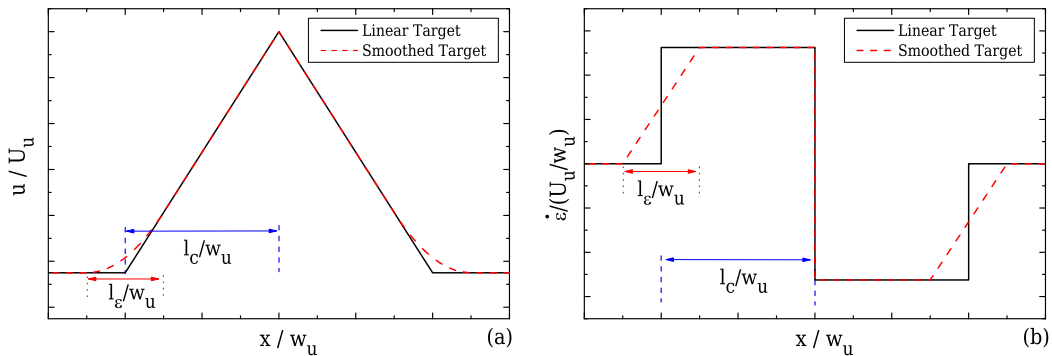


Figure 5.5. Ideal velocity (a) and strain-rate profiles (b) along the centreline of the flow.

the lateral walls approach each other creating a narrow region where fluid elements are submitted to stretching deformation. As such, the channel aspect ratio (AR) defined as $AR = w_u/d$ (where d is the depth of the device) varies significantly along the streamwise direction within the contraction region. This, together with typical abrupt or short-length hyperbolic configurations reported in the literature [74, 166], lead to non-ideal flow kinematics with a non-homogeneous strain-rate along the centreline. This drawback is overcome by employing optimisation techniques and searching for a design that can produce homogeneous strain-rate along the centreline to obtain the ideal profiles illustrated in Fig. 5.5. The choice of a symmetric converging/diverging contraction is based on the fact that this configuration has the potential to provide a constant strain-rate along the entire length of the contraction/expansion, with a positive strain-rate in the converging region and a negative value in the expansion region, where the stretching and relaxation processes can be analysed under homogeneous flow conditions. A smooth contraction followed by an abrupt expansion configuration, similar to Oliveira *et al.* [74], would generate a large undershoot of the strain-rate in the vicinity of the expansion plane, due to the sudden decrease of the velocity along the centreline, which would not be ideal for devices intended to produce homogeneous extension. A brief comparison of these two configurations is given in Appendix B.1.

Geometries with three different contraction ratios are investigated, resulting in devices characterised by different Hencky strains. More specifically, the cases with an upstream width that is three, eight and twenty times larger than the contraction width ($CR = 3, 8$ and 20) are considered. A more detailed study is presented in Section 5.4.2 for the intermediate case of ($CR = 8$). For this case, various three dimensional designs are reported depending on the AR, in the range of $1 \leq AR \leq 32$. It was found that the choice of the depth of the device affects significantly the final shape. Moreover, the operational limitation for each of the designs is investigated in terms of Reynolds numbers. The optimised design for a device $AR = 1$ is further employed for investigating the response of viscoelastic fluids. For the cases with $CR = 3$ and $CR = 20$ the 3D optimised shapes for $AR = 1$ under creeping flow conditions are also reported.

For all cases studied, the contraction length is correlated to the upstream width

with the use of a factor n_1 , such that $l_c = n_1 w_u$. However, for the case of $CR = 8$ the effect of using different contraction lengths on the final optimised designs is also reported, highlighting the importance of this choice.

The envisioned ideal flow field in the converging/diverging geometries corresponds to a linear velocity profile along the centreline. However, this profile imposes instantaneous step changes in the strain-rate at the beginning and at the end of the contraction, as illustrated in Fig. 5.5b. This limiting behaviour is not possible in reality because the gradient of the velocity profile is a continuous function and therefore we consider a smooth transition in the velocity profile that is first order differentiable and which yields a linear transition in the strain-rate profile (cf. Fig. 5.5b) except at the throat, $x/w_u = 0$. The performance of the unrealistic, abrupt transition profile is also examined and a comparison is given in Appendix B.2.

The general form of the target velocity profile is given in Eq. (5.7), and holds for both 2D or 3D geometries. It considers a smooth transition of the velocity when the fluid enters the converging part and exits the diverging part of the channel. The smoothing of the target profile is achieved by employing a region of length l_ϵ , which is correlated to the upstream width by the use of a factor n_2 , such that $l_\epsilon = n_2 w_u$. For the cases studied here, we considered $n_2 = 1$. In this transition region, the velocity is expressed by a second-order polynomial as shown in Fig. 5.5a.

$$\tilde{u} = \begin{cases} \tilde{u}_u & \text{if } \tilde{x} \leq -n_1 - \frac{n_2}{2} \\ f_2 \left[\tilde{x} + n_1 + \frac{n_2}{2} \right]^2 + \tilde{u}_u & \text{if } -n_1 - \frac{n_2}{2} < \tilde{x} < -n_1 + \frac{n_2}{2} \\ f_1 \tilde{x} + \tilde{u}_c & \text{if } -n_1 + \frac{n_2}{2} \leq \tilde{x} \leq 0 \\ -f_1 \tilde{x} + \tilde{u}_c & \text{if } 0 \leq \tilde{x} \leq n_1 - \frac{n_2}{2} \\ f_2 \left[\tilde{x} - n_1 - \frac{n_2}{2} \right]^2 + \tilde{u}_u & \text{if } n_1 - \frac{n_2}{2} < \tilde{x} < n_1 + \frac{n_2}{2} \\ \tilde{u}_u & \text{if } \tilde{x} \geq n_1 + \frac{n_2}{2} \end{cases} \quad (5.7)$$

All symbols with tilde represent normalised values, such that $\tilde{x} = x/w_u$, $\tilde{u} = u/U_u$, where U_u is the average upstream velocity, and the dimensionless parameters f_1 and f_2 are given by $f_1 = (\tilde{u}_c - \tilde{u}_u)/n_1$ and $f_2 = (\tilde{u}_c - \tilde{u}_u)/2n_1n_2$, respectively. The resulting

normalised strain-rate profiles corresponding to Eq. (5.7) are given by

$$\dot{\epsilon}/(U_u/w_u) = \begin{cases} 0 & \text{if } \tilde{x} \leq -n_1 - \frac{n_2}{2} \\ 2f_2[\tilde{x} + n_1 + \frac{n_2}{2}] & \text{if } -n_1 - \frac{n_2}{2} < \tilde{x} < -n_1 + \frac{n_2}{2} \\ f_1 & \text{if } -n_1 + \frac{n_2}{2} \leq \tilde{x} \leq 0 \\ -f_1 & \text{if } 0 \leq \tilde{x} \leq n_1 - \frac{n_2}{2} \\ 2f_2[\tilde{x} - n_1 - \frac{n_2}{2}] & \text{if } n_1 - \frac{n_2}{2} < \tilde{x} < n_1 + \frac{n_2}{2} \\ 0 & \text{if } \tilde{x} \geq n_1 + \frac{n_2}{2} \end{cases} \quad (5.8)$$

It is noted that, when no smoothing is desired ($n_2 = 0$; $l_\epsilon = 0$), the intervals of the smoothed function drop to zero, yielding only the linear velocity profile.

Figure 5.5b shows that the smooth target velocity profile of Eq. (5.7) produces a linear increase/decrease of the strain-rate along the centreline of the flow at the beginning/end of the contraction/expansion region, instead of the step profile. At the contraction throat ($\tilde{x} = 0$) there is a discontinuity in the strain-rate profile, but given the small total width of the channel, the target profile is reasonably well approximated as will be shown.

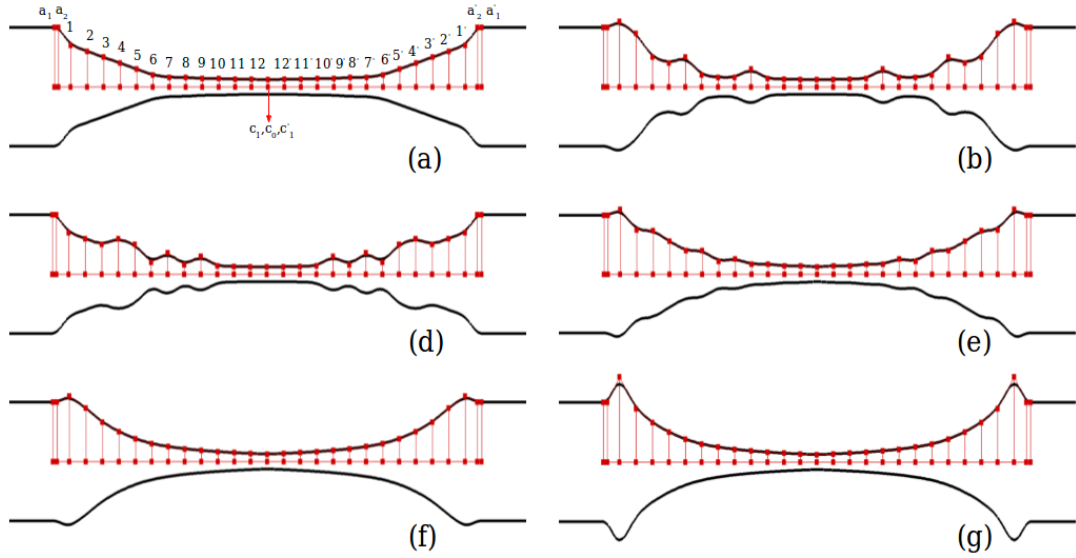


Figure 5.6. Example of various designs obtained during the optimisation procedure: (a) Represents the shape of the initial estimation (\mathbf{Y}^0), (g) illustrates the optimised shape (\mathbf{Y}^{opt}) and (b) to (f) intermediate shapes (\mathbf{Y}^*) examined during the intermediate steps of the optimisation procedure. The red square symbols, illustrate the positions of the lattice control points.

Figure 5.6 illustrates various configurations generated during the optimisation procedure. The NURBS deformation lattice, which is responsible for the generation of the optimal shape consists of $31 \times 2 \times 2$ total control points. Each deformation \mathbf{Y}^* imposed by the optimiser is applied by the 12 inner control points located in the converging part (cf. Fig. 5.6a), and the same deformation is applied to the equivalent points of the symmetric diverging part (indicated by the prime symbol in Fig. 5.6a). An important fact is that two in-line points are placed at the beginning (a_1 and a_2) and at the end (a'_1 and a'_2) of the contraction region in order to maintain the boundary continuity [99] and three collinear points (c_1 , c_0 and c'_1) are placed in the middle of the contraction in order to force the boundary to be exactly at the desired position (c_0) to match with the desired contraction ratio.

5.4.2 Designs with CR = 8

i) Optimised design in 2D

Here, the optimisation results for a 2D Newtonian fluid flow are presented, considering a constant contraction length, $l_c = 2w_u$. The shape obtained from the optimisation is shown in Fig. 5.7 and is compared with the ideal hyperbolic shape for unidimensional flows. Here, the expression suggested in Oliveira *et al.* [74] is used for designing the walls

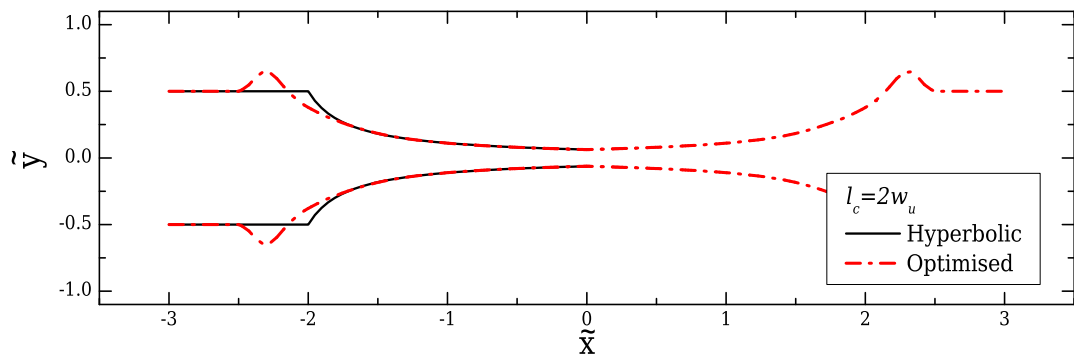


Figure 5.7. Comparison between the optimised shape (*dash-dotted line*) and the ideal hyperbolic design (*continuous line*) discussed in Oliveira *et al.* [74] (2D, CR = 8, $l_c = 2w_u$, $l_\varepsilon = w_u$).

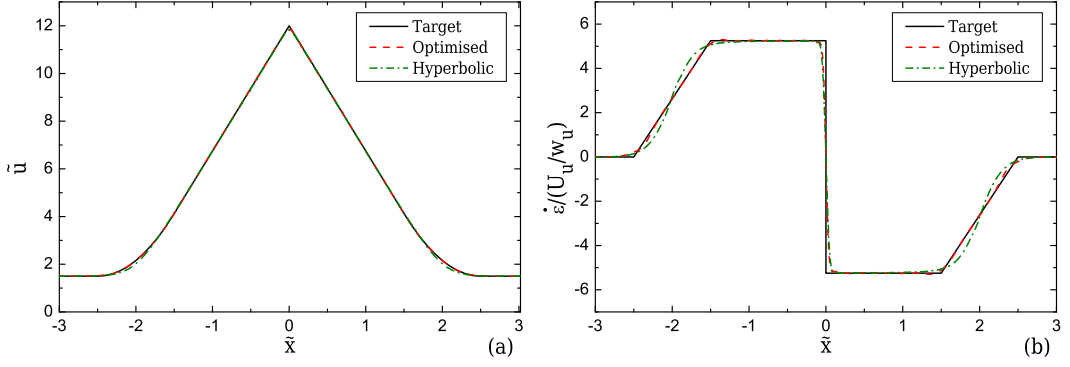


Figure 5.8. Velocity (a) and strain-rate (b) profiles computed for creeping flow conditions along the centreline of the flow for the optimised geometry and the ideal hyperbolic design (2D, CR = 8, $l_c = 2w_u$, $l_e = w_u$). The target velocity profile is represented as a *continuous line*.

of the hyperbolic-shaped device. The exact expression considered here is the following:

$$|\tilde{y}| = \begin{cases} [2\text{CR}(1 - |\tilde{x}|\frac{w_u - w_c}{l_c})]^{-1} & \text{for } |\tilde{x}| \leq n_1 \\ 1/2 & \text{for } |\tilde{x}| > n_1 \end{cases} \quad (5.9)$$

The generated velocity and the strain-rate profiles along the centreline of the flow are shown in Figs. 5.8a and 5.8b, respectively. It can be seen that both the optimised and the hyperbolic designs perform well. The optimised shape exhibits shifts at the beginning and at the end of the contraction/expansion region (Fig. 5.7), resulting in a better approximation of the desired strain-rate profile in the transition regions as can be seen in the strain-rate profiles shown in Fig. 5.8b.

The optimised solution is obtained using a base mesh M0. In order to assess the dependence of the optimised solution on the mesh refinement, besides M0, a refined mesh M1 was employed (Table 5.1) and a very good agreement between the computed velocity profiles is reported for both meshes, with the maximum deviation in the strain-rate being less than 0.5%.

Table 5.1. Mesh characteristics for the 2D simulations performed with CR = 8 and $l_c = 2w_u$.

Mesh	$\delta x_{min}/w_c$	$\delta y_{min}/w_c$	#Computational Cells
M0	0.045	0.045	4862
M1	0.023	0.023	19448

ii) Effect of contraction length

The choice of the contraction length l_c is crucial for the performance of the device, since it has a direct effect on the total residence time of the sample of interest. Additionally, its choice affects directly the final shape of the optimised device. The results obtained for two different imposed lengths, $l_c = 2w_u$ and $l_c = 4w_u$, are shown in Fig. 5.9a. As the contraction length decreases, the optimisation procedure produces geometries with larger deviations from the hyperbolic shape at the start and the end of the converging/diverging region. Conversely, as the length of the contraction is increased, the optimisation procedure predicts optimal shapes approaching the ideal hyperbolic geometry. This finding is particularly important for experimentalists wishing to use the hyperbolic function for designing their microfluidic geometries, or for applications that are especially built for studying specific properties under extensional flow. For example, in studies where a large strain history is required, the hyperbolic shape will in fact perform well, providing a reasonable approximation to the linear velocity profile. However, when it comes to applications where stretch should be fast and in a short length of the device, the use of optimisation for obtaining a more appropriate design with enhanced performance is suggested.

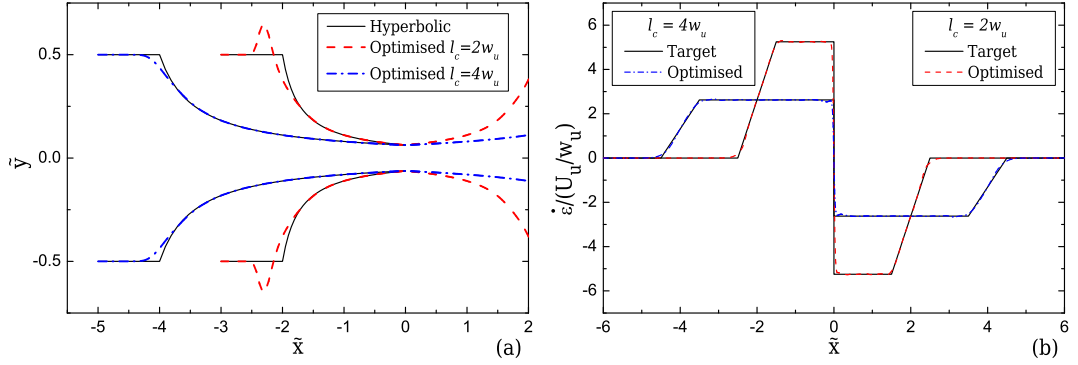


Figure 5.9. Shapes of the optimised and the ideal hyperbolic devices (a) and strain-rate profiles along the flow centreline for the optimised devices (b) with $l_c = 4w_u$ and $l_c = 2w_u$ (2D, CR = 8, $l_\varepsilon = w_u$) for creeping flow conditions. Note that in (a) x and y axes are not to scale.

iii) Effect of channel depth

When the devices have low to moderate depths, as is typical in microfluidic platforms, three dimensional effects due to wall interactions need to be taken into account. In such cases, the flow dynamics are different and the optimised shape obtained for 2D flow will not be adequate. Here, the effect of aspect ratio on the optimised shape of the geometry is investigated, considering the same contraction length, $l_c = 2w_u$. More specifically, the cases of a 3D geometry with a square cross-sectional area in the middle of the contraction/expansion region ($AR = 8$), another with a square cross-sectional area at the inlet ($AR = 1$) and two intermediate cases with $AR = 2$ and $AR = 4$ are considered. In addition, the case of $AR = 32$ which results in a very shallow channel that approaches Hele-Shaw flow is also examined.

In order to reduce the cost of the CFD simulations required at every optimisation step for finding the shape that will produce the desired constant strain-rate regions along the flow centreline, symmetry conditions along xy - and xz -centreplanes have been considered. That way, only a quarter of the full geometry was simulated. The target profiles for the 3D cases were created by evaluating the maximum velocity from the fully-developed velocity profiles upstream and in the middle of the contraction along the centreline ($y = 0, z = 0$), using the analytical solution given for each AR [37]:

$$u(y, z) = \frac{12Q}{\pi^3 ab} \frac{\sum_{i=1,3,\dots}^{\infty} (-1)^{\frac{i-1}{2}} \left[1 - \frac{\cosh(i\pi z/2a)}{\cosh(i\pi b/2a)} \right] \frac{\cos(i\pi y/2a)}{i^3}}{1 - \frac{192a}{\pi^5 b} \sum_{i=1,3,\dots}^{\infty} \frac{\tanh(i\pi b/2a)}{i^5}} \quad (5.10)$$

where Q is the flow rate and a, b , are the half-width and half-depth of the channel cross-section respectively.

Initially, the performance of the hyperbolic shape was examined for all aspect ratios and the corresponding strain-rate profiles along the flow centreline are shown in Fig. 5.10. It can be seen that the hyperbolic geometry does not generally perform as well as for the 2D cases, exhibiting large deviations from the desired target profile, especially for the two intermediate cases of $AR = 2$ (Fig. 5.10b), $AR = 4$ (Fig. 5.10c) and

the shallow channel with $AR = 32$ (Fig. 5.10e). The use of the hyperbolic shape was derived by James [208] considering an axisymmetric converging channel. The characteristic shape of the cross-sectional areas of microfluidic devices is usually rectangular. For 3D planar channels, the varying rectangular cross-section results in velocity pro-

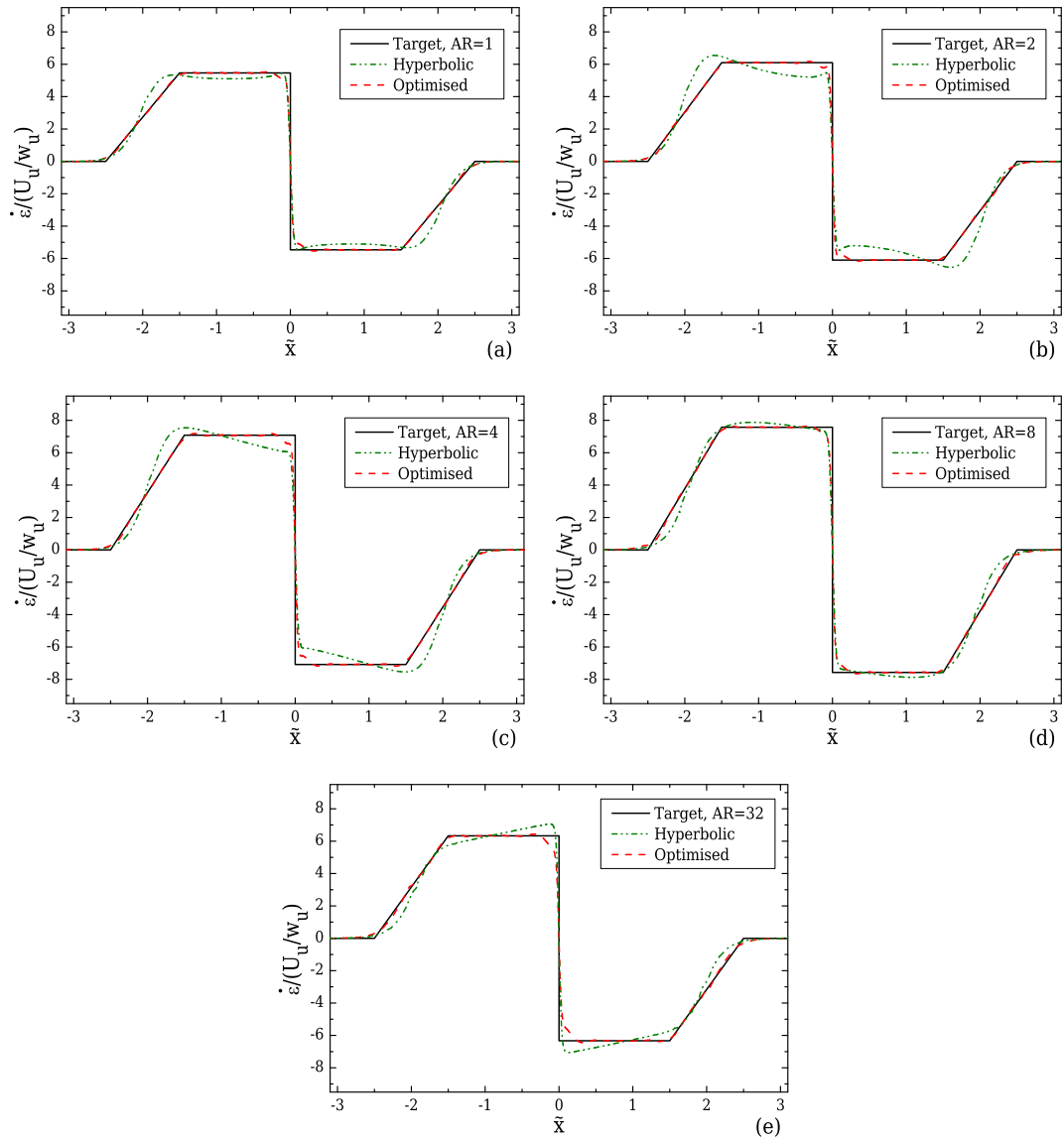


Figure 5.10. Strain-rate profiles along the flow centreline computed under creeping flow conditions for a geometry with $l_c = 2w_u$, $l_\varepsilon = w_u$, $CR = 8$ and (a) $AR = 1$, (b) $AR = 2$, (c) $AR = 4$, (d) $AR = 8$ and (e) $AR = 32$. The performance of each optimised shape is compared with the hyperbolic function (cf. Eq. (5.9)).

files that are not necessarily the same in both transverse directions but depend on the local aspect ratio, which explains this deviation. Considering the upstream velocity profiles along the centreplanes xz and xy for the case of $AR = 1$, both profiles will be the identical since $d = w_u$. However, as the fluid flows towards the middle of the contraction and the width of the channel decreases, the profile on the xz -plane will gradually become more flattened than the xy -profile, reaching a maximum difference in the throat of the contraction/expansion region. A similar but inverse behaviour is found in the case of $AR = 8$, with the velocity profile in the xy -plane exhibiting a more flattened region close to the centreline when compared to the profile in the xz -plane in the region upstream of the contraction and identical velocity profiles in both planes at the throat, where $d = w_c$. Finally, for the limiting case of $AR = 32$ the velocity profile along the xy -plane will be more flattened than the equivalent of the xz -plane along the entire domain, reaching their minimum difference at the throat. The gradual transitions for $AR = 1$ (local $AR \leq 1$) and $AR = 8$ (local $AR \geq 1$) result in some deviation in the strain-rate profiles as shown in [Figs. 5.10a](#) and [5.10d](#). These deviations are more pronounced for the two intermediate cases of $AR = 2$ and $AR = 4$, as shown in [Figs. 5.10b](#) and [5.10c](#), where the local aspect ratio varies from above one upstream of the contraction to below one at the throat of the contraction/expansion region. For the case of $AR = 32$, clearly the transition region needs to be corrected in order to obtain the desired velocity gradient.

The optimised shapes for each aspect ratio are presented and compared with the hyperbolic shapes in [Fig. 5.11](#). Clearly, the boundaries are deformed according to the different flow kinematics in each geometry, exhibiting different sizes in the shifts of the boundary upstream of the start of the converging region (the same applies to the symmetric end of the contraction/expansion). A similar behaviour was also found by Galindo-Rosales *et al.* [[192](#)], where a variety of optimised shapes for the cross-slot configuration have been proposed, depending on the various aspect ratios and leg-lengths investigated. The maximum shift of the boundary relative to the hyperbolic case, is approximately 16% for $AR = 1$, 42% for $AR = 2$, 35% when $AR = 4$, 68% for $AR = 8$ and 12% for $AR = 32$. More importantly, there are significant differences between the

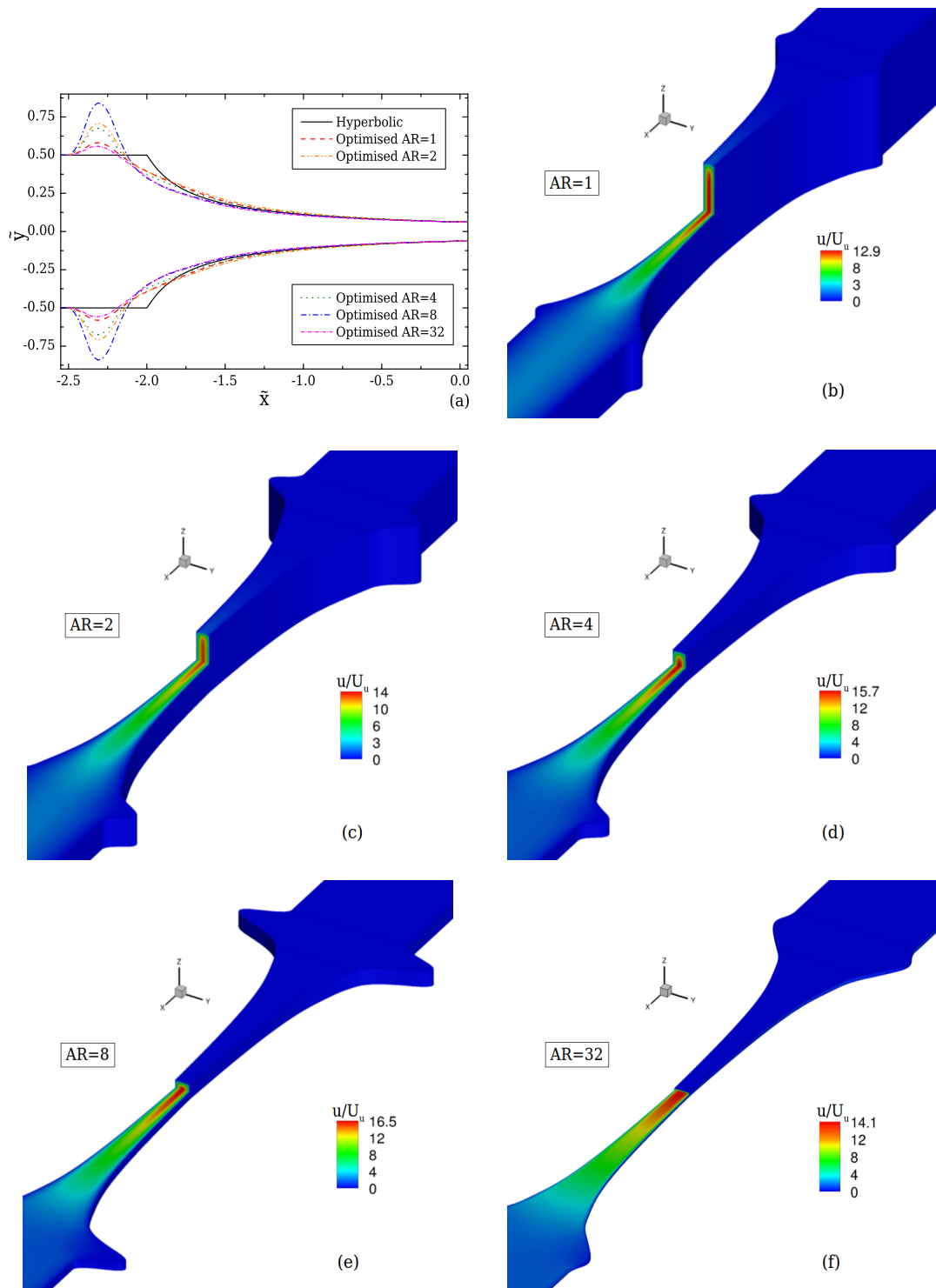


Figure 5.11. (a) Comparison of the channel boundaries obtained from 3D optimisations for creeping flow conditions for $AR = 1, 2, 4, 8$ and 32 and the ideal hyperbolic shape when $l_c = 2w_u$, $l_\varepsilon = w_u$ and $CR = 8$. (b)-(f) Contour-plots of the normalised streamwise velocity for each optimised geometry.

Table 5.2. Mesh characteristics for the 3D optimisations for a geometry of $l_c = 2w_u$, $l_\varepsilon = w_u$ and CR = 8 for AR = 1, 2, 4 and 8.

Mesh	$\delta x_{min}/w_c$	$\delta y_{min}/w_c$	$\delta z_{min}/w_c$	#Computational Cells
AR = 1				
M0	0.045	0.045	0.364	53482
M1	0.023	0.023	0.182	427856
AR = 2				
M0	0.045	0.045	0.182	53482
M1	0.023	0.023	0.091	427856
AR = 4				
M0	0.045	0.045	0.091	53482
M1	0.023	0.023	0.045	427856
AR = 8				
M0	0.045	0.045	0.045	53482
M1	0.023	0.023	0.023	427856
AR = 32				
M0	0.045	0.045	0.011	53482
M1	0.023	0.023	0.006	427856

optimised and the hyperbolic shapes in the first third of the contraction (and at the symmetric end of the expansion), with the differences becoming negligible in the central region $|\tilde{x}| \lesssim 1.3$ (cf. Fig. 5.11a). As shown in Fig. 5.10, using the optimised shapes results in the desired strain-rate profiles along the flow centreline with a maximum deviation of approximately 1% for all five cases.

As in the 2D case, two meshes were employed for each AR, with mesh M0 being used in the optimisation procedure to minimise computational costs and a more refined mesh M1 for assessing the dependence of the optimised solution on the mesh refinement (cf. Table 5.2). Figure 5.12a illustrates the mesh used for obtaining the optimal solution of the design (only a quarter of the geometry is used) for AR = 1, and Fig. 5.12b shows the corresponding refined mesh M1. For AR = 1 and AR = 2 the maximum deviation between the two solutions was approximately 1.0%, for AR = 4 was approximately 0.7%, for AR = 8 was approximately 0.5% and for AR = 32 was approximately 0.8%.

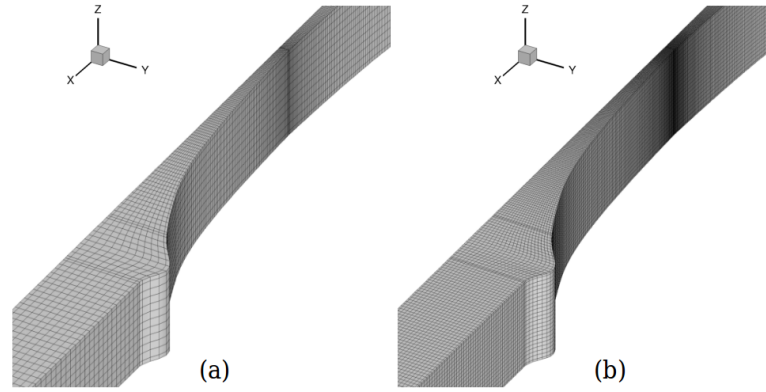


Figure 5.12. Meshes M0 (a) and M1 (b) for the optimised geometry with $l_c = 2w_u$, $l_\varepsilon = w_u$, CR = 8 and AR = 1.

iv) Design Limits

In this section, the operational limits of the 3D configurations presented previously are reported. More specifically, the performance of all designs is examined for increasing Reynolds numbers considering Newtonian fluid flow, using the refined mesh M1. The Reynolds number is defined here as $Re = \rho U_u D_{hu} / \eta_0$, where D_{hu} is the upstream hydraulic diameter defined as $D_{hu} = 2w_u d / (w_u + d)$, with d referring to the depth of the device. Moreover, the performance of the configuration with AR = 1 is investigated for viscoelastic fluids as a function of the Weissenberg number, under creeping flow conditions. The Weissenberg number is here defined as $Wi = \lambda(U_c - U_u) / l_c$.

Figure 5.13a shows the effect of Re on the velocity profile along the centreline obtained for a Newtonian fluid in the optimised geometry for AR = 1. For low Re, the geometry optimised under creeping flow conditions performs well, but it is clear that for $Re \gtrsim 5$ the kinematics in the device start deviating from the target, affecting noticeably the evolution of the resulting strain-rate profiles, as shown in Fig. 5.13b (cf. Appendix B.3 for the remaining aspect ratios). As mentioned previously, all optimisations were conducted considering creeping flow conditions, where the flow field is symmetric upstream and downstream of the contraction. However, entrance and exit effects on the contraction/expansion region become more prominent as Re is increased, resulting in asymmetric behaviour between the converging and diverging parts of the contraction. It should be noted that for the cases of AR = 1, 2 and 4, flow recirculations are ob-

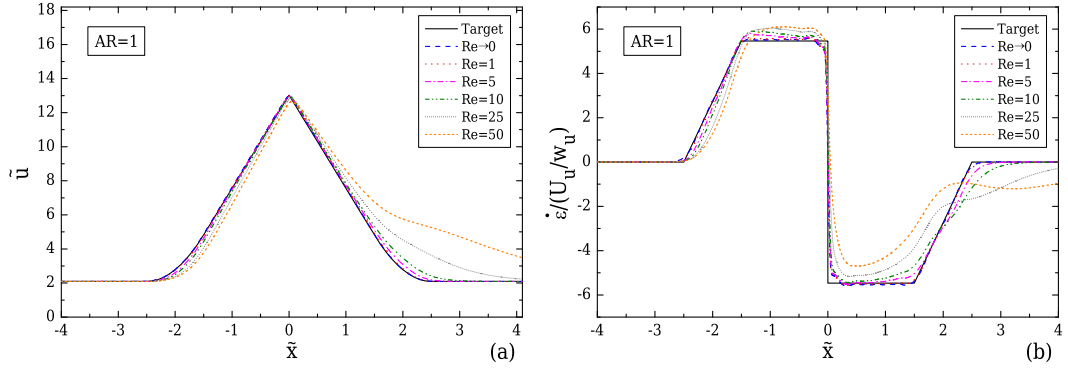


Figure 5.13. Effect of Re on the velocity (a) and strain-rate (b) profiles computed along the flow centreline, for the optimised geometry with $l_c = 2w_u$, $l_\varepsilon = w_u$, $CR = 8$ and $AR = 1$ (Fig. 5.11), considering Newtonian fluid flow.

served downstream of the expansion for $Re \gtrsim 50$, whereas for the other two cases with shallower channels ($AR = 8$ and 32) no recirculations are reported. This behaviour is in agreement with that reported in Oliveira *et al.* [167], where it was shown that the bounding in the direction of the channel depth delays the appearance of recirculations.

Figure 5.14 illustrates the normalised pressure drop, $\Delta P_c/(\eta\dot{\varepsilon}_a)$, between the start and the end of the transition region of the contraction/expansion ($-n_1 - \frac{n_2}{2} \leq \tilde{x} \leq n_1 + \frac{n_2}{2}$) for increasing Reynolds numbers, with $\dot{\varepsilon}_a$ corresponding to the apparent strain-rate evaluated as $\dot{\varepsilon}_a = (U_c - U_u)/l_c = (CR - 1)U_u/l_c$. The inset figures show the normalised pressure profile along the centreline for all Re , calculated based on a reference pressure value, P_{ref} , taken at the beginning of the transition region ($\tilde{x} = -n_1 - \frac{n_2}{2}$) of each geometry. It can be seen that for $Re \lesssim 5$ the increase of the nominal strain-rate results in an almost linear increase in the pressure drop for all cases. However, for higher Re this linearity breaks, and the strain-rate along the centreline becomes asymmetric in the two parts of the design, similar to the behaviour observed in Fig. 5.13 for $AR = 1$. Note that Re is evaluated using the upstream flow conditions, but its value at the contraction will differ for each of the designs. More specifically, since the Reynolds number reported is based on upstream flow conditions, the Reynolds number at the throat is higher for larger AR , justifying the higher deviation of the normalised pressure drops from the equivalent creeping flow value (*dashed line*) for the shallower designs when $Re \gtrsim 5$ (cf. Figs. 5.14c and 5.14d).

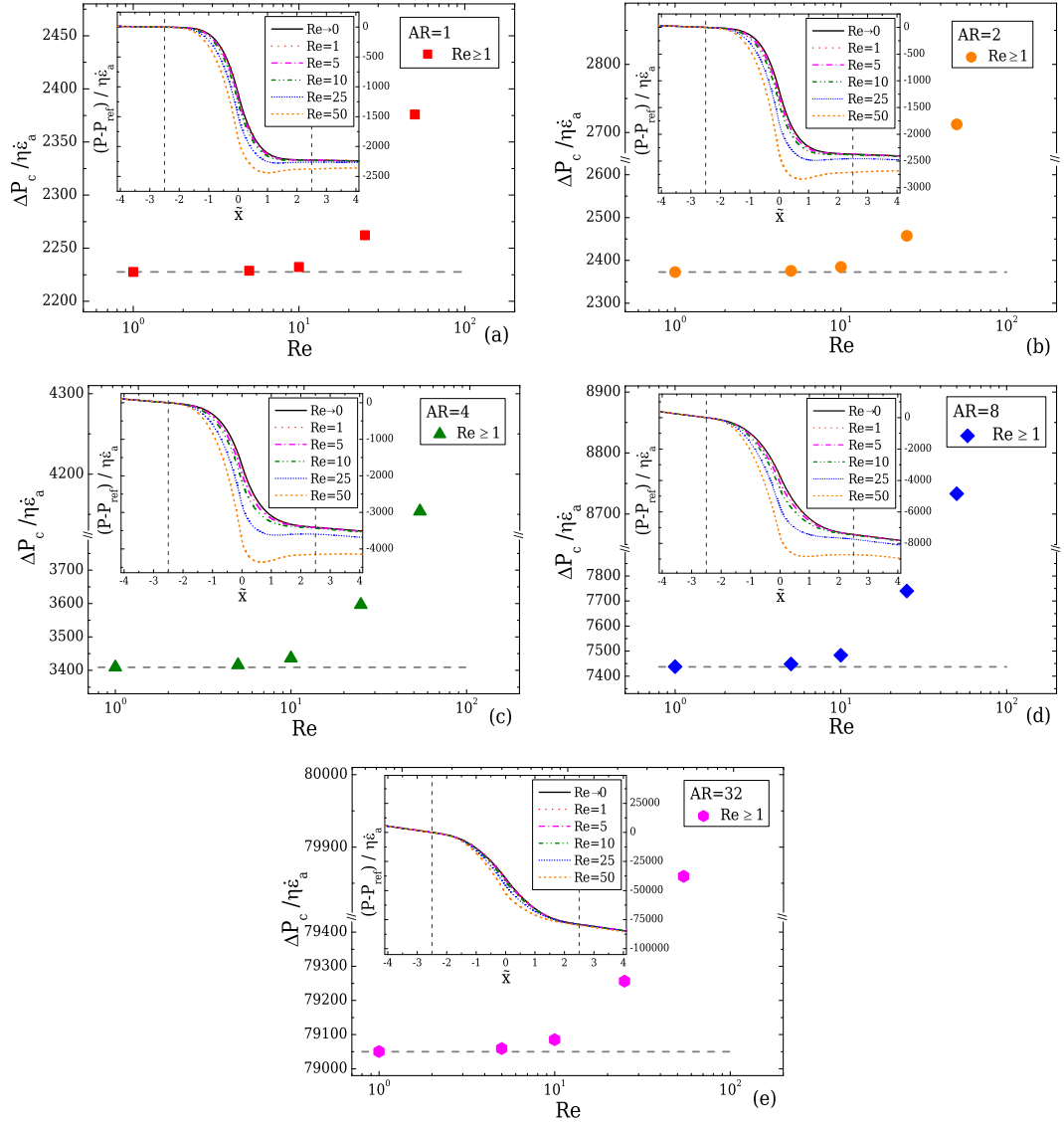


Figure 5.14. Normalised pressure drop for various Re across the contraction for a geometry with $l_c = 2w_u$, $l_e = w_u$, $CR = 8$ and (a) $AR = 1$, (b) $AR = 2$, (c) $AR = 4$ (d) $AR = 8$ and (e) $AR = 32$ with the *horizontal dashed lines* indicating the normalised pressure drop value under creeping flow conditions. The inset figures in (a)-(e) represent the normalised pressure profiles along the centreline for each case, with the *vertical dashed lines* indicating the start and the end of the transition region of the contraction/expansion.

For viscoelastic fluid flows, the effect of elasticity on the velocity field and the limitation of the optimised design for $AR = 1$ is examined by performing simulations of viscoelastic fluid flows at increasing Weissenberg numbers, under creeping flow conditions. As discussed in [Section 5.3](#) two different viscoelastic models are considered, the

Oldroyd-B model ($\varepsilon = 0$, $\beta = 0.5$) and the linear version of the PTT model ($\varepsilon = 0.25$, $\beta = 0.01$). Using the Oldroyd-B model, one is able to investigate the influence of elasticity alone since the model does not predict shear-thinning behaviour. Figure 5.15a shows that in the converging part of the channel a reasonably good approximation to the linear increase in the velocity profile is achieved for the range of Wi tested. However, a gradual increase of Wi leads to progressively higher velocity overshoots close to the throat of the converging/diverging region, where the maximum velocity is reached. The occurrence of velocity overshoots for flows of viscoelastic fluids in contractions, has also been reported by Afonso and Pinho [72] for a PTT model, Alves and Poole [73] for a UCM fluid, and experimentally by Sousa *et al.* [209,210]. This deviation from the target profile for higher Wi is particularly noticeable in the streamwise velocity gradient profiles in Fig. 5.15b, with increasing fluctuations near $\tilde{x} = 0$. It is reported that for $Wi = 0.20$, the strain-rate overshoot leads to a deviation of approximately 74% from the desired constant value. This overshoot clearly affects the behaviour in the diverging part of the channel, and for $Wi \geq 0.05$ the strain-rate in this region can no longer be considered constant. Another fact that can be clearly noticed from the asymmetric profiles between the converging and the diverging part of the contraction is that the strain history affects the velocity profile development. For $Wi \leq 0.02$, the strain-rate can be considered nearly constant, with a maximum deviation of approximately 5% in the beginning of the diverging region.

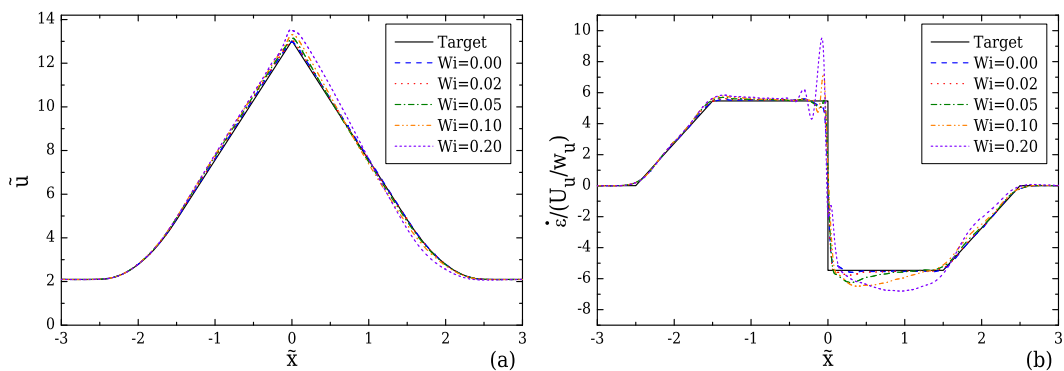


Figure 5.15. Effect of Wi on the velocity (a) and strain-rate (b) profiles along the flow centreline computed for the Oldroyd-B model ($\beta = 0.5$) under creeping flow conditions, for the optimised geometry with $l_c = 2w_u$, $l_\varepsilon = w_u$, $CR = 8$ and $AR = 1$ (Fig. 5.11).

For to the PTT fluid, a different behaviour is reported for increasing Weissenberg numbers as shown in Fig. 5.16. The shear-thinning behaviour predicted by the model results in a more flattened upstream streamwise velocity profile for a PTT fluid when compared to the Newtonian case. For this reason the analysis of the velocity profile along the centreline is accomplished by normalising the data with the fully-developed velocity at the centreline of the upstream channel ($u_{u,fd}$). It can be seen that as the elasticity increases, the normalised velocities in the converging region, shown in Fig. 5.16a, increase as seen previously for the Oldroyd-B model. However, before the fluid approaches the middle of the contraction, the normalised velocities start to decrease, forming a small overshoot upstream of the diverging part in both the velocity and the strain-rate profiles as a consequence of fluid's elasticity. While the fluid flows through the diverging region, the normalised velocities rapidly decrease to smaller values than the target profile, affecting the development of the strain-rate profile (Fig. 5.16b), where an undershoot is observed at the beginning of the diverging part. Both the overshoot and the undershoot become more pronounced with increasing Wi and these deviations should be taken into account when viscoelastic fluids with a shear-thinning response are considered.

Figure 5.17a and Fig. 5.17b present the variation of the normalised pressure profile along the centreline for the Oldroyd-B and the PTT fluids, respectively. It can be seen that both models predict smaller pressure drops across the contraction when compared

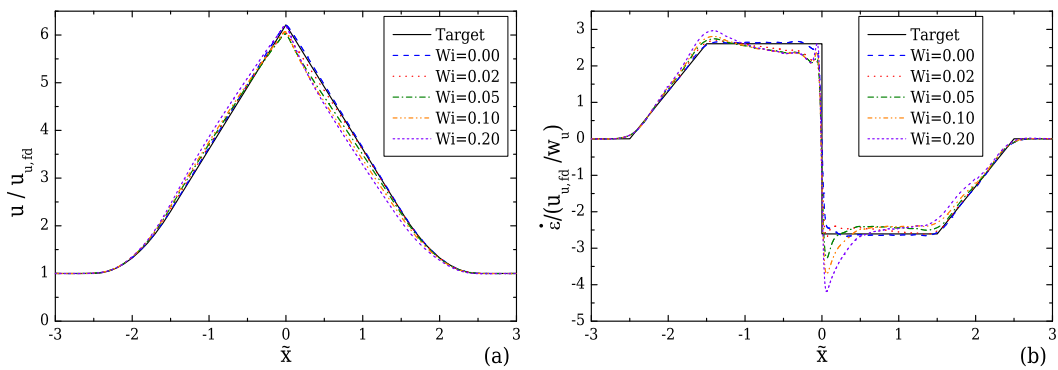


Figure 5.16. Effect of Wi on the velocity (a) and strain-rate (b) profiles along the flow centreline computed for a PTT fluid ($\varepsilon = 0.25, \beta = 0.01$) under creeping flow conditions, for the optimised geometry with $l_c = 2w_u$, $l_\varepsilon = w_u$ and $CR = 8$ for $AR = 1$ (Fig. 5.11).

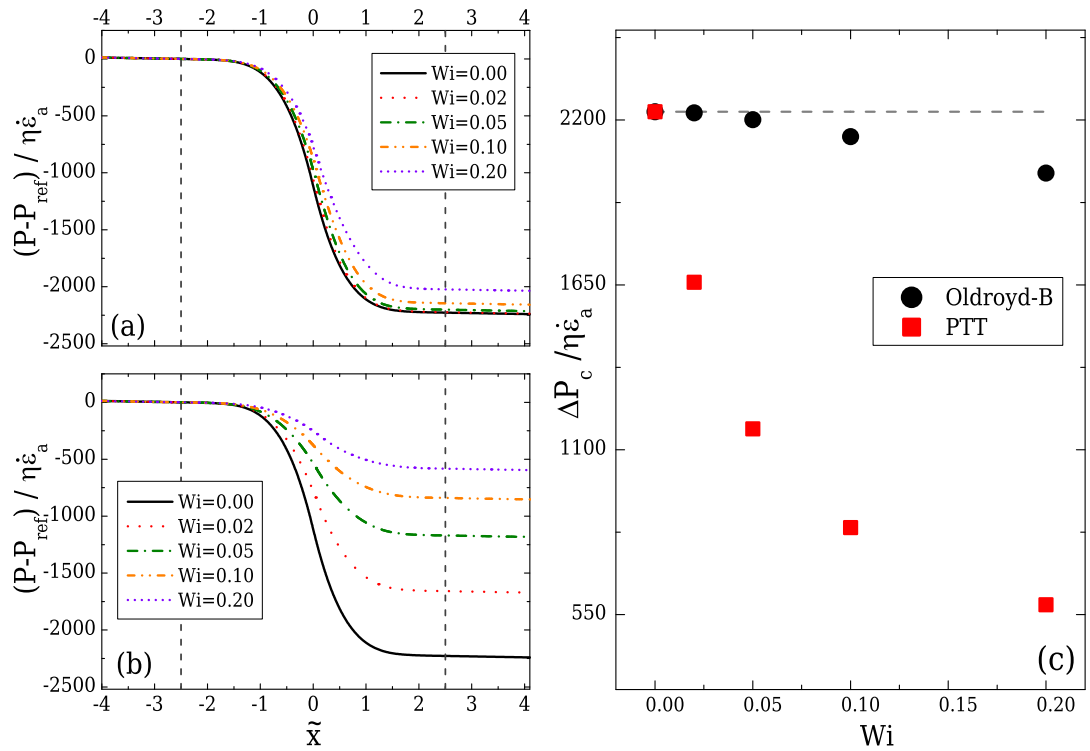


Figure 5.17. Normalised pressure profile along the centreline for the Oldroyd-B model (a), the PTT model (b) and normalised pressure drop across the contraction/expansion region for both models under creeping flow conditions (c), when the optimised geometry with $l_c = 2w_u$, $l_e = w_u$, $CR = 8$ and $AR = 1$ is used. The start and the end of the transition region of the contraction/expansion is indicated by the vertical dashed lines in (a) and (b). The horizontal dashed line in (c) corresponds to the normalised pressure drop for the Newtonian fluid under creeping flow conditions.

to the Newtonian fluid flow. These differences are more pronounced for the PTT fluid as a result of its shear-thinning behaviour. Moreover, the normalised pressure drop between the start and the end of the transition region is decreased for increasing Wi as shown in Fig. 5.17c. Similar behaviour was reported by Binding *et al.* [211], for the flow of an Oldroyd-B fluid through a contraction/expansion geometry. In contrast to numerical findings, experimental measurements for viscoelastic fluid flows in contraction geometries, show pressure drop enhancement and additional flow resistance with the increase of fluid elasticity [17, 172]. This inability of closed-form viscoelastic models to predict the correct pressure drop is a well known drawback of viscoelastic numerical studies [35, 71]. These constitutive models do not contain sufficient information related to the micro-structure of the polymer chains, and it is believed that possible inclusions

at this level will assist in capturing the physics of polymer flows with greater accuracy [212].

5.4.3 Designs for other contraction ratios

For single-stream designs the applied strain-rate can change either by applying a different flow rate at the inlet of the design, or by changing the contraction ratio of the device. The first one is important because the same device can be used, however as it was shown in Section 5.4.2, a limitation exists in terms of Re . This limitation can be surpassed by employing a different design, characterised by another contraction ratio which is also limited by the specific application intended. For example if one desires to investigate the deformation of red blood cells, should take in account the characteristic cell sizes, and decide upon the minimum acceptable CR using this information. Therefore, it was decided to perform a similar investigation for two additional geometries characterised by $CR = 3$ and $CR = 20$ and for an aspect ratio of $AR = 1$. Figure 5.18 illustrates the expected/desired profiles for the normalised velocity and the nominal strain-rates in comparison with the case of $CR = 8$ studied previously.

The configurations here are set to have the same contraction length, $l_c = 2w_u$, and as previously the more realistic target velocity profile is considered, where a smooth transition region of length $l_\varepsilon = w_u$ is employed. Following the optimisation procedure presented in Section 5.2, the performance of the optimised shape is shown in Fig. 5.19a,

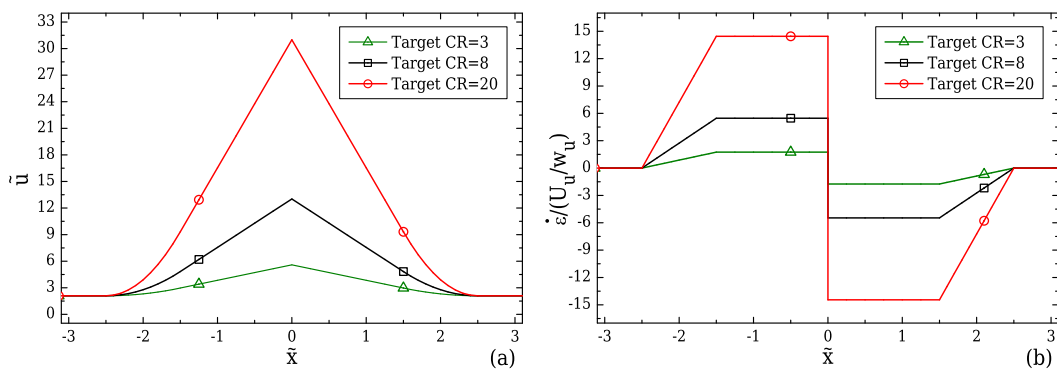


Figure 5.18. Target normalised velocity profiles (a) and nominal strain-rates (b) expected to be produced by the geometries with $CR = 3, 8$ and 20 .

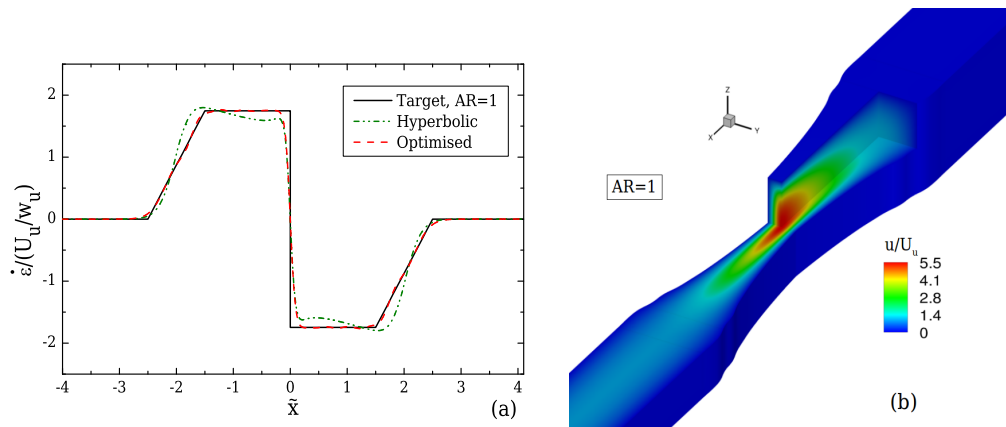


Figure 5.19. Strain-rate profiles along the centreline of the flow for the optimised geometry and the ideal hyperbolic design computed for creeping flow conditions (a) and normalised velocity contours for the optimised shape ($CR = 3$, $l_c = 2w_u$, $l_\epsilon = w_u$ for $AR = 1$).

where the evaluated strain-rate profile along the centreline of the flow is given in contrast with the equivalent performance of the hyperbolic design. Figure 5.19b, demonstrates the three dimensional optimised geometry and the evolution of the normalised stream-wise velocity. Similarly in Fig. 5.20a the performance of the design with $CR = 20$ is given, with the developed strain-rate along the centreline of the flow approaching very well the desired target profile, and in Fig. 5.20b the contours of the normalised developed streamwise velocity field are shown.

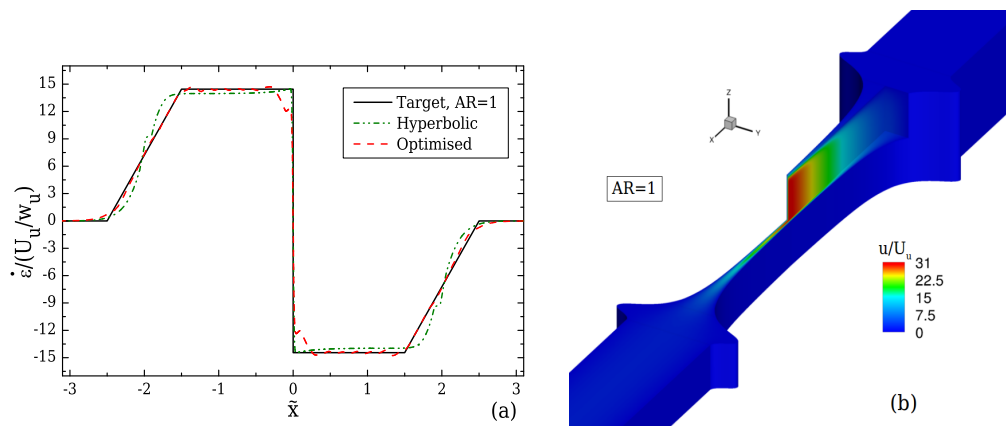


Figure 5.20. Strain-rate profiles along the centreline of the flow for the optimised geometry and the ideal hyperbolic design computed for creeping flow conditions (a) and normalised velocity contours for the optimised shape ($CR = 20$, $l_c = 2w_u$, $l_\epsilon = w_u$ for $AR = 1$).

Table 5.3. Mesh characteristics for the 3D optimisations for the geometries with $l_c = 2w_u$, $l_\varepsilon = w_u$ and $AR = 1$.

Mesh	$\delta x_{min}/w_c$	$\delta y_{min}/w_c$	$\delta z_{min}/w_c$	#Computational Cells
CR = 3				
M0	0.045	0.045	0.273	55902
M1	0.023	0.023	0.136	447216
CR = 20				
M0	0.045	0.045	1.818	66066
M1	0.023	0.023	0.909	528528

During the optimisation procedure the M0 mesh was employed and its characteristics are given in [Table 5.3](#). Therefore, in order to assess the validity of the optimised shapes a more refined mesh M1 was employed (cf. [Table 5.3](#)). The deviation in the evaluation of the strain-rates along the centreline was found to be less than 1% for the case of $CR = 3$ and approximately 1.2% for the case of $CR = 20$. Regarding the final optimised shapes, for the case of $CR = 20$ a boundary shift applied at the transition region extends the boundary approximately 44% compared to the hyperbolic boundary. On the other hand, for the case of $CR = 3$ no significant shift is reported as in all the cases seen so far, but rather the boundary is corrected in order to produce the desired strain-rate profile.

5.4.4 Pressure-driven flow vs Electro-osmotic flow

An attractive advantage of microfluidic devices is that fluid flow forcing can be achieved efficiently in different ways. Arguably, the most common are *pressure-driven* and *electro-osmotic* flows [\[213\]](#). For a pressure-driven flow considered in this thesis the fluid motion is frequently imposed using syringe pumps. This way, a variety of fully-developed velocity profiles are generated, which depend on the cross-sectional aspect ratio as a consequence of fluid-wall interactions, and on the rheology of the fluid. Pressure-driven flows in converging flow configurations, as considered previously, exhibit mixed kinematics: close to the walls, the flow is shear dominated due to the no-slip conditions; along the centreline it is strongly extensional; and the intermediate regions exhibit complex flow kinematics. The shear effects are particularly relevant in the narrow region

of the channel in the middle of the contraction. This physical drawback may affect experimental studies when controlled flow kinematics are required, and thus it is of great importance for experimentalists to know the level of these interactions. In a recent study by the author (Zografos *et al.* [30]) electro-osmotic flow (EOF) conditions have also been considered¹ in the optimisations. This type of flow forcing has found many applications in engineering, biomedicine and chemistry [215]. More specifically, for EOF the charged walls of the microfluidic channel attract the counter ions of the fluid and form an electric double layer (EDL) near the interface. By applying an electric field between the inlet and the outlet of the microchannel, the electrically neutral bulk is set in motion due to the electric force acting on the EDL, generating a plug-like velocity profile. The importance of this flows is that they can overcome the dependence of the velocity profile on the AR, a common characteristic for the pressure-driven flows which can be undesirable for some applications [192]. Furthermore, the characteristic plug-like velocity profile results in reduced shearing effects in the vicinity of the walls, generating a wider region of extensional flow.

When considering EOF the electrical body force per unit volume, \mathbf{F} , is added as an extra term in the momentum equation and is responsible for the motion of the system:

$$\rho \left(\frac{\partial \mathbf{u}}{\partial t} + \mathbf{u} \cdot \nabla \mathbf{u} \right) = -\nabla p + \nabla \cdot \boldsymbol{\tau} + \mathbf{F} \quad (5.11)$$

For the optimisation studies using EOF, the configuration presented in [Section 5.4.2](#) for pressure-driven flow is considered ($l_c = 2w_u$, $l_\varepsilon = w_u$ and $\text{CR} = 8$). It was found that the 2D optimised shape exhibits minor changes relative to the hyperbolic channel, with the latter demonstrating an efficient performance. Moreover, it was shown that in contrast to the pressure-driven cases, where various different shapes have been produced for each aspect ratio considered, the 2D optimised shape could operate with very good performance even when applied to 3D geometries with aspect ratios in the range of

¹ The numerical solver used for the optimisation study with EOF was implemented in OpenFOAM[®] and follows the method described by Afonso *et al.* [214]. The results have been produced by F. Pimenta (FEUP).

$1 \leq AR \leq 8$. The good performance of the hyperbolic shape reported for electro-osmosis is not surprising, since that shape is the analytical solution for a constant strain-rate region assuming potential flow [166]. Although the electric field is irrotational, the velocity is not due to internal pressure gradients and the no-slip conditions at the walls, therefore the similitude between the electric field and the velocity field is broken [216–218]. However, a quasi-potential flow can still be considered, since the added dynamic pressure due to changes in the cross-sectional area of the channel, which reflect on a velocity variation, is relatively small and the electric double layers are thin. This was proved by the reported quasi-linearity of the electric field along the centreline of the contraction/expansion region.

The advantage of having a linear electric field profile at the channel centreline is also a desired feature when considering extensional flows driven by electrophoresis, since electrophoretic motion follows the electric field lines and a constant strain-rate will be imposed. This is further supported by the fact that electrophoretic extension of long molecules, such as λ -DNA, was already performed in hyperbolic micro-contraction devices [219–221].

5.5 Multi-stream designs

In this section two multi-stream configurations are optimised in order to generate homogeneous extensional flow. More specifically, the case of a T-Junction (Section 5.5.1) and the case of a flow-focusing device (Section 5.5.2) are investigated. The first geometry has the ability to generate a stagnation point flow, which has been found very useful for performing elongational studies. The latter geometry relies on the presence of lubricating streams to shape a main stream and generate strong extension in which the shearing effects of fluid-wall interactions are reduced near the region of interest.

5.5.1 T-Junction configuration

Here, the flow in a T-junction is considered as shown in Fig. 5.21, with the two horizontal, opposing, channels being used as flow inlets and the vertical channel as the flow

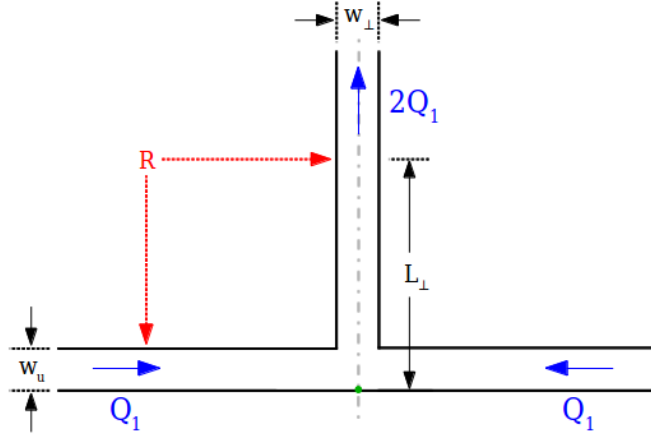


Figure 5.21. Configuration a T-shaped channel. The *dot* illustrates the position of the stagnation point and the *dashed-dotted* line the flow centreline of the channel.

outlet. The same average velocity is imposed on both inlets.

The T-shaped channel considered here is defined by the upstream width, w_u , the downstream width of the vertical segment, w_\perp , and the desired length L_\perp which defines the region to be optimised for homogeneous extension. The length L_\perp is correlated to the upstream width as $L_\perp = n_1 w_u$, and for all the cases studied here the dimensionless factor n_1 is set as $n_1 = 4$. The ratio between the two characteristic widths is called width ratio and is set to be $WR = w_u/w_\perp = 1$.

The target profile along the flow centreline, starts from a zero velocity located exactly at the stagnation point and increases over a length L_\perp up to its maximum value, which corresponds to the fully developed velocity expected at the centreline of the outlet segment:

$$\tilde{v} = \begin{cases} f_1 \tilde{y} & \text{if } 0 \leq \tilde{y} \leq n_1 \\ \tilde{v}_d & \text{if } \tilde{y} \geq n_1 \end{cases} \quad (5.12)$$

where $f_1 = \tilde{v}_d/n_1$. As for the single-stream study, considered in the previous section, all symbols with tilde represent normalised variables such that $\tilde{y} = y/w_u$, $\tilde{v} = v/U_u$ and $\tilde{v}_d = v_d/U_u$, where v_d corresponds to the maximum expected downstream fully-developed velocity and U_u is the average upstream velocity imposed at the inlets. Therefore, the resulting normalised strain-rate profile expected along the flow centreline

is given by ($\dot{\epsilon} = \partial v / \partial y$):

$$\dot{\epsilon} / (U_u / w_u) = \begin{cases} f_1 & \text{if } 0 \leq \tilde{y} \leq n_1 \\ 0 & \text{if } \tilde{y} \geq n_1 \end{cases} \quad (5.13)$$

and has the form of a step profile, as presented in Fig. 5.22b. The target linear velocity profile and the resulting strain-rate profile along the outlet flow centreline is shown in Fig. 5.22. For this configuration the flow centreline coincides with the axis of symmetry, as indicated in Fig. 5.21 and therefore only the half geometry is considered in the 2D optimisations and a quarter of the geometry for the examined 3D case.

The optimisation procedure presented in Section 5.2 is followed here in order to find the most appropriate shape, and all CFD evaluations are performed considering creeping flow conditions. The main difference relative to the optimisations performed for the single-stream designs, is that a sequence of joined lattices is employed here instead of one single lattice considered previously. An example is given in Fig. 5.23. More specifically, Fig. 5.23a illustrates a shape designed by the moving control points. All points considered for generating the evaluated shape are moving along a specified radius R in x, y directions. This choice was made for avoiding possible clashes during the movements of the points of all lattices. The three lattices used need to cooperate in order to maintain the continuity of the boundary shape. Each of the lattices applies a local deformation to the region it embeds. Therefore, if the lattices are not “communicating”

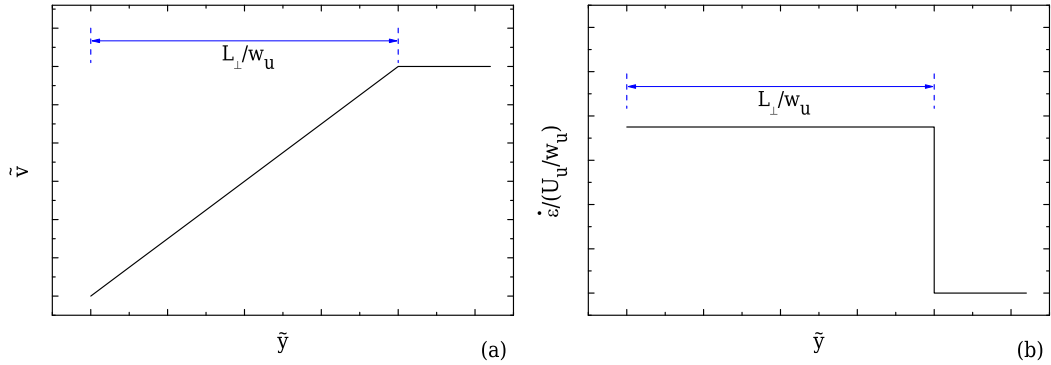


Figure 5.22. Velocity (a) and strain-rate (b) target profiles along the centreline of the flow for $WR = 1$, $L_{\perp} = 4w_u$.

with each other, the possibility of generating cusps at the joint is high. As discussed in Rogers [99], the only way to overcome this problem and transfer information between joint lattices is by generating parallel and collinear segments between them. For the problem studied here position B, which contains three control points for each lattice, is critical. Lattices L_1 and L_3 are mainly responsible for the boundary deformation, while L_2 controls only a single point on this curve. However, as it can be seen in Fig. 5.23, L_2 is required since it controls the inner body correlations between the horizontal and the vertical parts of the domain. The most important choice that helps achieve boundary continuity is the existence of the collinear segments AB and BC, as shown in Fig. 5.23b. This arrangement helps to transfer the appropriate information between L_1 and L_3 . The communication of the three lattices is finally enforced with the use of the parallel segments AE and BD which correlate L_1 with L_2 and L_3 (BD is shared between L_2 and L_3), and BE with CD which correlate L_3 with L_1 and L_2 (BE is shared between L_1 and L_2). That way the shape continuity at the joints of the NURBS lattices is achieved.

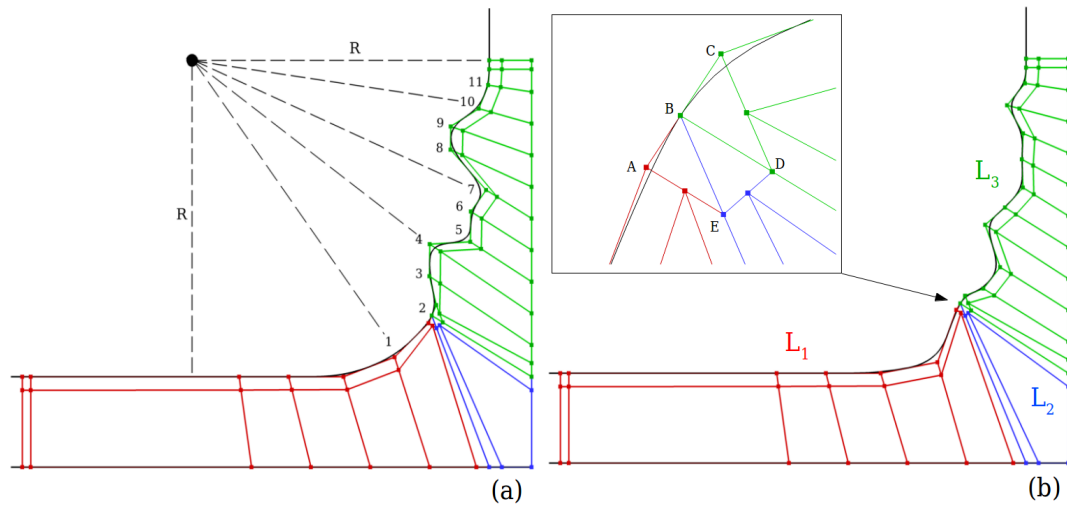


Figure 5.23. Movement of control points for the sequence of the three NURBS lattices used for optimising the T-junction (a) and the merging arrangement of the lattices (L_1 , L_2 and L_3) in order to maintain the continuity of the curve (b).

i) Common configurations

Initially and before performing the optimisation study, three cases of T-shaped channels commonly used are investigated, considering the flow of a Newtonian fluid under creeping flow conditions: a 90° bend configuration, a rounded configuration and a hyperbolic configuration. Figure 5.24 illustrates the performance of the 90° bend T-shaped channel. It can be seen in Fig. 5.24a that the velocity rapidly increases to its maximum upstream value, due to the short transition length of this configuration. The corresponding strain-rate profile along the flow centreline is therefore not constant, as can be seen from Fig. 5.24b.

The boundary of the rounded geometry is constructed by considering a radius $R = 3$ as shown in Fig. 5.25a. For designing the hyperbolic shape the equivalent of the single-stream configuration is considered, assuming that its upstream maximum velocity has the same value with the maximum normalised velocity at $\tilde{y} = 1$ obtained from the target velocity profile of Fig. 5.26a. Then the upstream width is evaluated and a function similar to Eq. (5.9) is employed for constructing the hyperbolic-shaped T-junction.

Figure 5.26 compares the performance of both configurations. For the rounded geometry the velocity profile is initially underestimated, explaining the absence of the overshoot in the strain-rates since the velocity gradients are smoother compared to the hyperbolic and the abrupt. The hyperbolic configuration exhibits a better performance, but there is still an overshoot in the strain-rates and the developed velocity

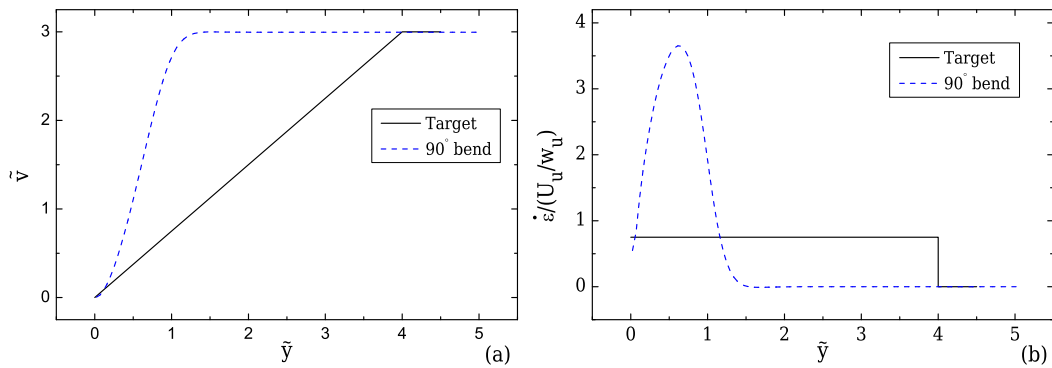


Figure 5.24. Velocity (a) and strain-rate (b) profiles along the centreline of the flow at the outlet of the 2D, 90° bend T-shaped channel with $WR = 1$, under creeping flow conditions.

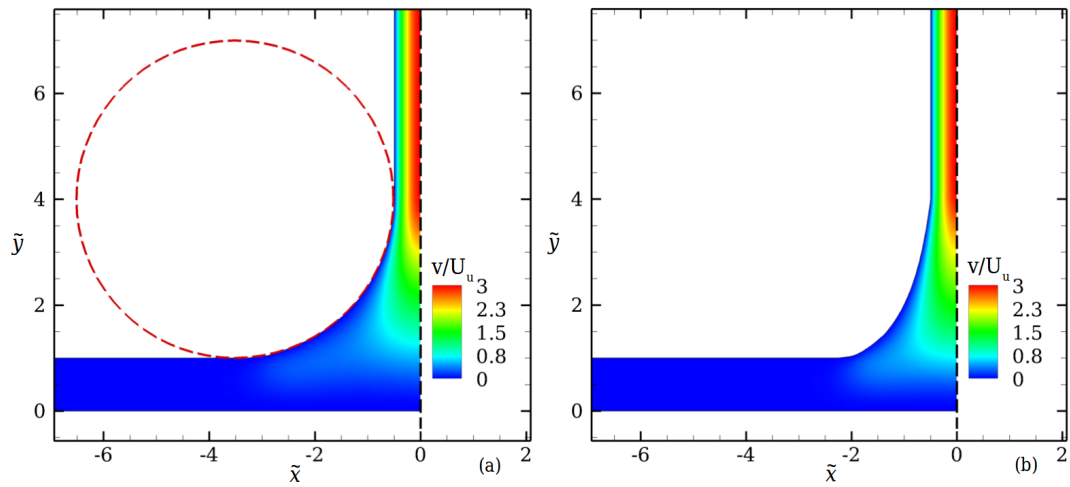


Figure 5.25. Contour-plots of the normalised y -component of the velocity of the rounded (a) and the hyperbolic (b) shaped T-channels in 2D with $WR = 1$ and $L_{\perp} = 4w_u$, under creeping flow conditions. The *dashed* straight line illustrates the position of the symmetry plane.

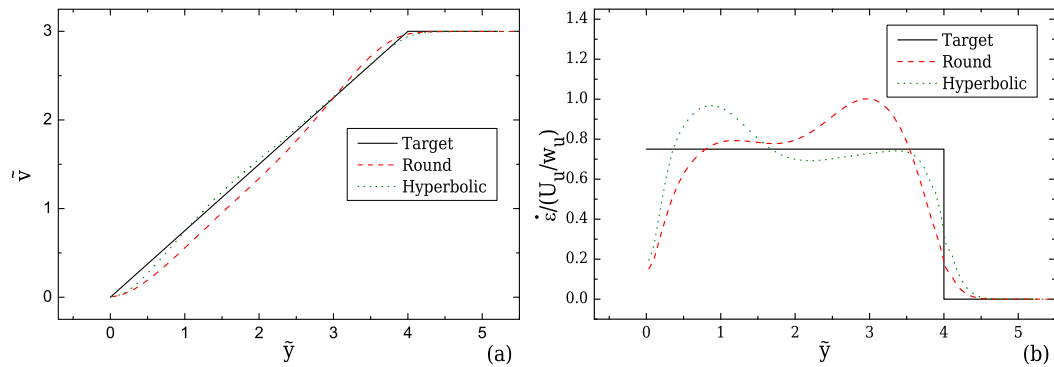


Figure 5.26. Velocity (a) and strain-rate (b) profiles along the centreline of the flow at the outlet of the 2D, rounded and hyperbolic T-channels with $WR = 1$ and $L_{\perp} = 4w_u$, under creeping flow conditions.

profile along the flow centreline fluctuates around the desired target, significantly affecting the strain-rates which cannot be considered constant as shown in Fig. 5.24b.

ii) Optimised T-junction in 2D

Two cases have been considered: the case of a standard T-junction (with a straight and unchanged bottom boundary see Fig. 5.28a) and the case of a T-junction with a cavity, where the shape of the bottom boundary is allowed to change, generating a cavity region (see Fig. 5.28b for an example). For the standard case, 9 control points are

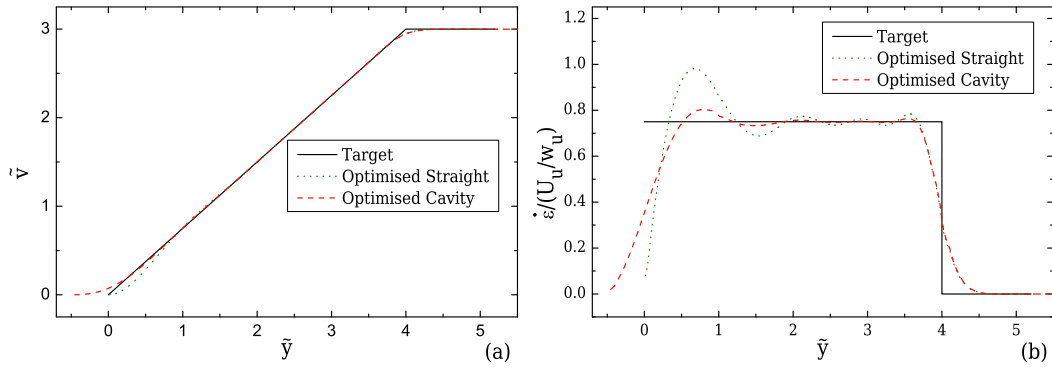


Figure 5.27. Velocity (a) and strain-rate (b) profiles along the centreline of the flow at the outlet channel of the 2D, optimised geometries with straight bottom and an optimised bottom for $WR = 1$ and $L_{\perp} = 4w_u$, under creeping flow conditions.

allowed to move along a radius with $R = 3$, whereas for the T-junction with a cavity, 8 control points are used together with two additional in-line control points located at the bottom boundary are considered for generating the cavity. The optimisations have been performed for a Newtonian fluid when $Re = 0$.

The target velocity profile given by Eq. (5.12) imposes an instantaneous step change in the strain-rate at the end of the desired region, the ability of the optimiser to reduce the inherent strain-rate overshoot is initially examined. Figure 5.27a presents the normalised velocity profiles along the centreline of the flow at the outlet channel, for both optimised cases. It can be seen that in both configurations the existence of a transition length is required, in order for the velocity to start increasing in a continuous manner. The standard case presents a similar behaviour to that produced by the hyperbolic shape (Fig. 5.26), exhibiting a strain-rate overshoot (cf. Fig. 5.27b), since the velocity cannot increase suddenly to the desired value. However, in the present case of the optimised standard T-junction the overshoot decays faster in a smaller span. Furthermore, as illustrated in Fig. 5.28a the optimised geometry exhibits salient corners in the transition boundaries between the inlet and the outlet similar to those in the OSCER (Haward *et al.* [77]). The presence of the salient corners that widen the device locally minimise the developed velocity and shear effects in the region of interest yielding a better approach to the desired kinematics.

The velocity profile considered as the target is inherently challenging both at the

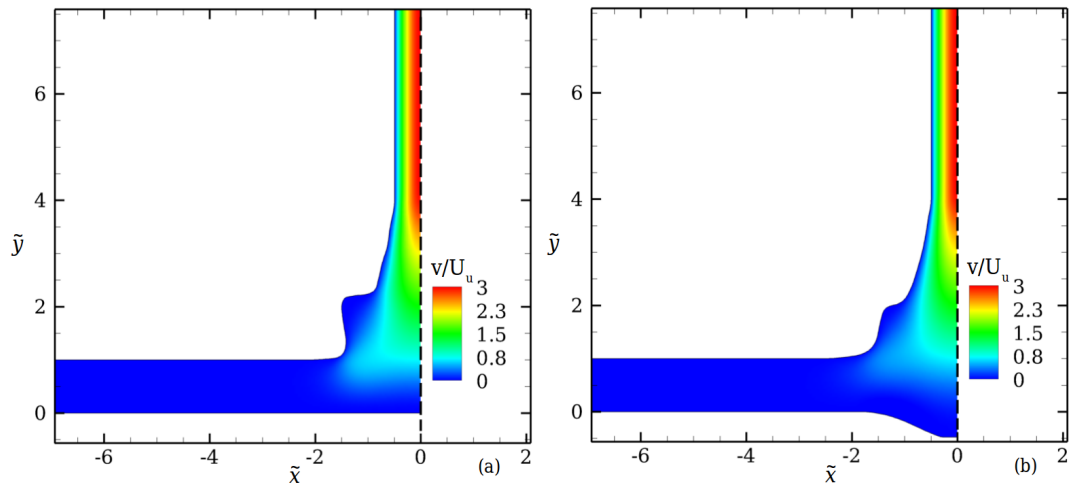


Figure 5.28. Contour-plots of the normalised y -component of the velocity of the optimised T-junction geometries for the optimised standard T-junction (a) and T-junction with cavity (b), in 2D with $WR = 1$ and $L_{\perp} = 4w_u$, under creeping flow conditions. The *dashed* straight line illustrates the position of the symmetry plane.

beginning and at the end of the desired constant strain-rate region. To tackle the challenges associated with the non-continuous velocity gradient at both ends of the homogeneous strain-rate region two approaches have been followed: using a T-junction with a cavity (Fig. 5.28b) or changing the target velocity profile using a smoothing approach similar to that used for the optimisations for the single-stream designs (cf. Section 5.4.1). In the case of the T-junction with a cavity, the optimised shape generated at the transition region between inlet and outlet is similar to the standard case (Fig. 5.28b), but the presence of the bottom cavity significantly reduces the strength of the overshoot (cf. Fig. 5.27a), since the velocity is allowed to develop smoothly along the transition region. This smoother development of the velocity affects the generated shape and the boundary deformations are less steep. Additionally, the generated velocity along the centreline of the flow exhibits less fluctuations around the target profile, compared to the standard geometry. This can also be verified by examining the behaviour of the developed strain-rates shown in Fig. 5.27b. The generation of a cavity however can be undesired for some applications. The reason is that the stagnation point is no longer fixed at the wall but rather is free to move [20]. Thus, as an alternative an appropriate smoothed profile is constructed for optimising geometries that require

a fixed stagnation point.

The desired part of the linear velocity increment is shifted along \tilde{y} in such a way that a transition region l_ε is employed at the beginning of the velocity profile. The velocity will then start increasing smoothly following a second-order polynomial function as shown in Fig. 5.29a. The length of the transition region is correlated to the upstream width by the use of a factor n_2 , such that $l_\varepsilon = n_2 w_u$ and is set as $n_2 = 0.5$. In the same way, a smoother transition region of the same span is also considered at the end of desired linear increase. The modified smoothed velocity profile is expressed in a general form as

$$\tilde{v} = \begin{cases} f_2 \tilde{y}^2 & \text{if } 0 \leq \tilde{y} < n_2 \\ f_1 (\tilde{y} - \frac{n_2}{2}) & \text{if } n_2 \leq \tilde{y} \leq n_1 \\ -f_2 [\tilde{y} - (n_1 + n_2)]^2 + \tilde{v}_d & \text{if } n_1 < \tilde{y} < n_1 + n_2 \\ \tilde{v}_d & \text{if } n_1 + n_2 \leq \tilde{y} \end{cases} \quad (5.14)$$

where, $f_2 = \tilde{v}_d / 2n_1 n_2$. When no smoothing is desired ($n_2 = 0; l_\varepsilon = 0$), the intervals of the smoothed function will drop to zero reproducing the linear velocity profile of Eq. (5.12). The resulting normalised strain-rate profile which corresponds to Eq. (5.14)

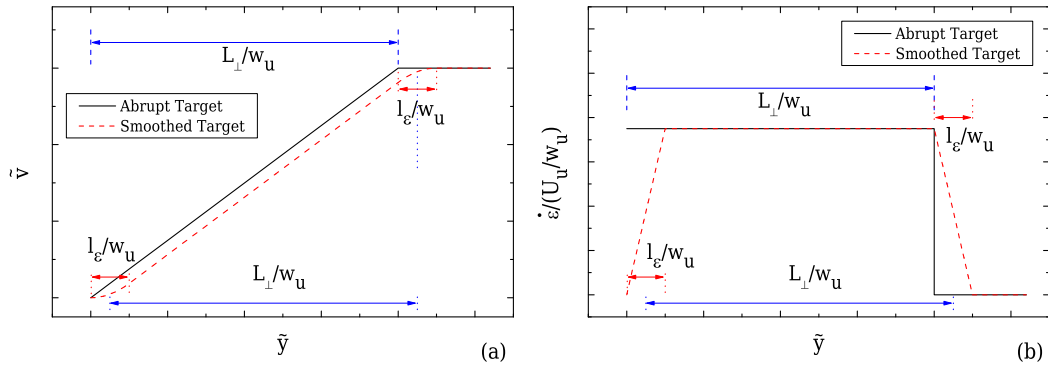


Figure 5.29. Comparison between the original abrupt and the smooth target velocity profiles (a) and corresponding strain-rate profiles (b) along the centreline of the flow at the outlet channel.

is shown in Fig. 5.29b and is expressed by

$$\dot{\varepsilon}/(U_u/w_u) = \begin{cases} 2f_2\tilde{y} & \text{if } 0 \leq \tilde{y} < n_2 \\ f_1 & \text{if } n_2 \leq \tilde{y} \leq n_1 \\ -2f_2[\tilde{y} - (n_1 + n_2)] & \text{if } n_1 < \tilde{y} < n_1 + n_2 \\ 0 & \text{if } n_1 + n_2 \leq \tilde{y} \end{cases} \quad (5.15)$$

Employing the mesh M0 (cf. Table 5.4), the same optimisation procedure is performed considering the modified target velocity profile of Eq. (5.14). In this case 11 control points are responsible for the deformation and the radius is set to be $R = 3.5$ (due to the profile shifting). Figure 5.30 illustrates the performance of the optimised shape, where it can be clearly seen that both the evaluated normalised velocity and the normalised strain-rate profiles approximate very well the desired modified target profiles. The shape that is generated by the optimisation procedure is shown in Fig. 5.31. It is obvious that compared to the shape obtained from the abrupt/linear profile shown in Fig. 5.28a, for this case a smoother boundary with smaller salient corners is obtained. As previously for the case of the converging/diverging channel, the dependence of the optimised solution was done by comparing the results obtained with the mesh M0 used in the optimisation procedure, and those obtained employing a more refined mesh M1 for each of the configurations. The characteristics of both numerical meshes are given in

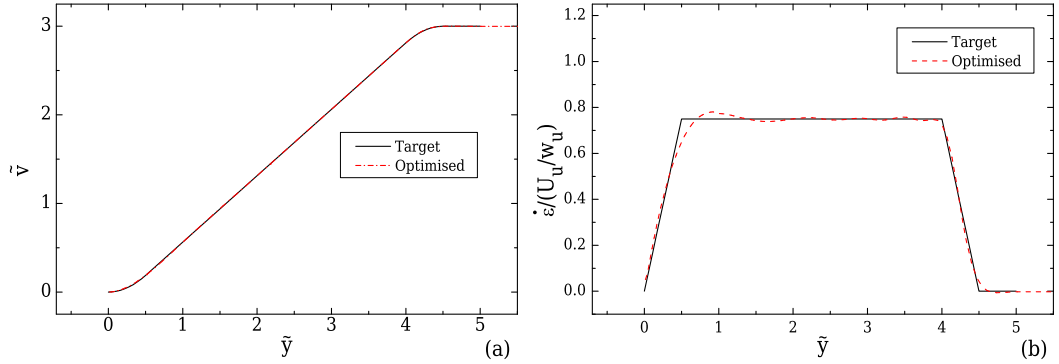


Figure 5.30. Velocity (a) and strain-rate (b) profiles along the centreline of the flow at the outlet channel of the 2D, optimised standard geometry for $WR = 1$, $L_{\perp} = 4w_u$ and $l_{\varepsilon} = 0.5w_u$, considering the modified target velocity profile of Eq. (5.14) under creeping flow conditions.

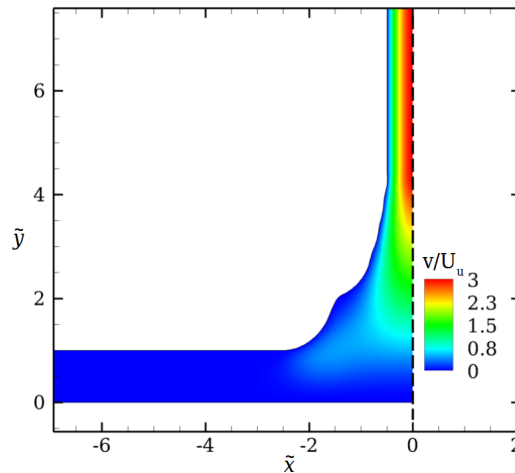


Figure 5.31. Contour-plots of the normalised y -component of the velocity of the optimised standard T-junction in 2D with $WR = 1$, $L_{\perp} = 4w_u$ and $l_{\varepsilon} = 0.5w_u$, under creeping flow conditions when the modified target velocity profile of Eq. (5.14) is used. The dashed straight line illustrates the position of the symmetry plane.

Table 5.4. Mesh characteristics for 2D optimised geometries when $WR = 1$ and $L_{\perp} = 4w_u$.

Mesh	$\delta x_{min}/w_u$	$\delta y_{min}/w_u$	#Computational Cells
M0	0.020	0.029	7980
M1	0.010	0.022	14700

Table 5.4 and it was found that for the two optimised geometries, the solution deviates less than 1%.

iii) Optimised T-junctions in 3D

The optimised shapes presented so far are valid for 2D fluid flows and are not necessarily the best choice for 3D devices with moderate values of depth. In order to investigate the three-dimensional effects due to fluid-wall interactions on the optimised shape of the T-junction configuration, a typical case of a geometry with $AR = 1$ ($AR = w_u/d$) is examined. Using the optimised shape obtained from the 2D optimisation (shown in Fig. 5.31) to design the 3D geometry with $AR = 1$ results in an under-prediction of the target velocities along the majority of the flow centreline, managing to reach the desired centreline velocity value only for a small region near the end of the desired region (displayed in Fig. 5.32a). This obviously affects the strain-rate (cf. Fig. 5.32a)

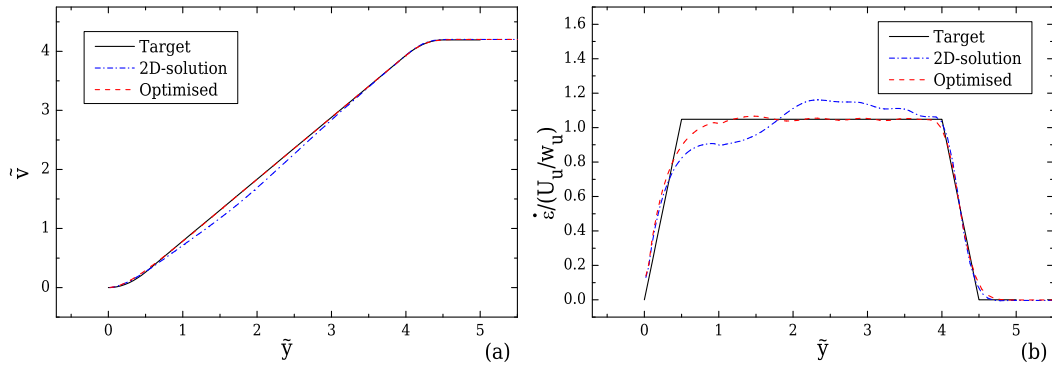


Figure 5.32. Velocity (a) and strain-rate (b) profiles along the centreline of the flow at the outlet channel of the 3D, optimised geometry with straight bottom in and for the 3D geometry designed with the 2D optimised solution for $AR = 1$, $WR = 1$, $L_{\perp} = 4w_u$ and $l_{\varepsilon} = 0.5w_u$, considering the modified target velocity profile of Eq. (5.14) under creeping flow conditions.

as the velocity gradient does not remain constant along the flow centreline. In order to obtain a better approximation to the desired behaviour, optimisations need to be performed for this specific aspect ratio under consideration ($AR = 1$). For an additional study aiming to assess the limiting AR for which the 2D-shape still performs efficiently when applied to 3D geometries please refer to Appendix B.4.

Following the findings from the 2D optimisation study, the velocity profile used as a target in order to evaluate the objective function (cf. Eq. (5.1)) is expressed by the modified smoothed profile given in Eq. (5.14). Similarly to the discussion for the 3D optimisation study performed for the single-stream designs, presented in Section 5.4.2, the target profile is constructed by evaluating the maximum velocity from the fully-developed velocity profiles downstream of region of interest in the outlet channel, using the analytical expression given from Eq. (5.10). For the optimisations only a quarter of the geometry was considered by applying symmetry conditions along xy - and yz -flow centreplanes, in order to reduce the computational cost for each three dimensional CFD evaluation performed by the optimiser. Figures 5.32a and 5.32b display the performance of the optimised design in contrast to the performance of the 2D-solution design applied to the case of $AR = 1$. After optimising the geometry for the specific AR under study, the desired profiles for the velocity and consequently for the strain-rate along the flow centreline, are better approximated. The generated T-junction is

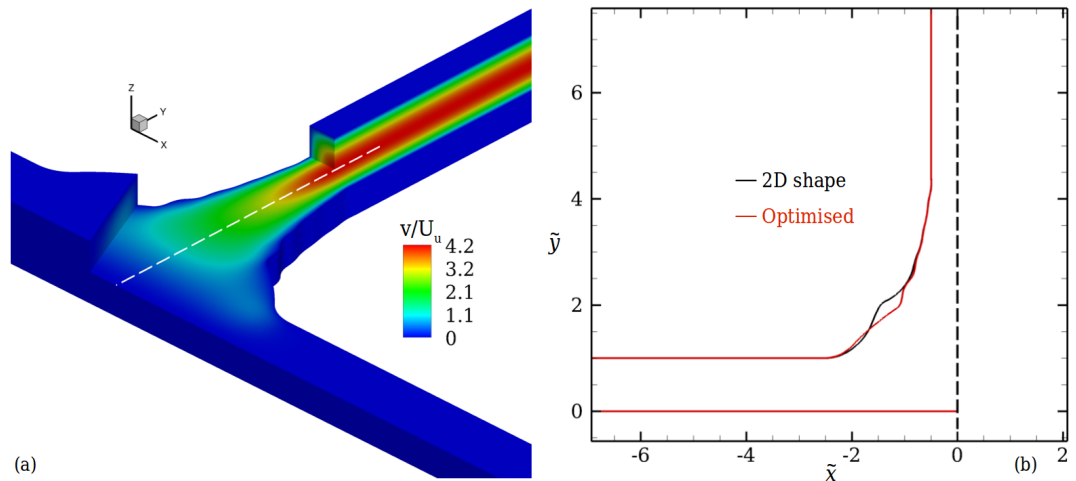


Figure 5.33. Normalised y -component of the velocity contour-plot of the optimised T-junction geometry (a) and comparison with the 2D optimised shape (b), with $AR = 1$, $WR = 1$, $L_{\perp} = 4w_u$ and $l_{\varepsilon} = 0.5w_u$ under creeping flow conditions. The *dashed* straight line illustrates the position of centreline of the flow and the symmetry axis.

shown in Fig. 5.33a together with the normalised contours of the y -component of the velocity, and in Fig. 5.33b a comparison between the 3D and the 2D optimised shapes is presented.

The dependence of the numerical solution on the mesh refinement is evaluated with the use of the more refined mesh M1 (cf. Fig. 5.34b and Table 5.5), where it was found that the maximum deviation in the evaluation of the strain-rates between the two meshes is less than 1%. For the optimisations the numerical mesh M0 shown in

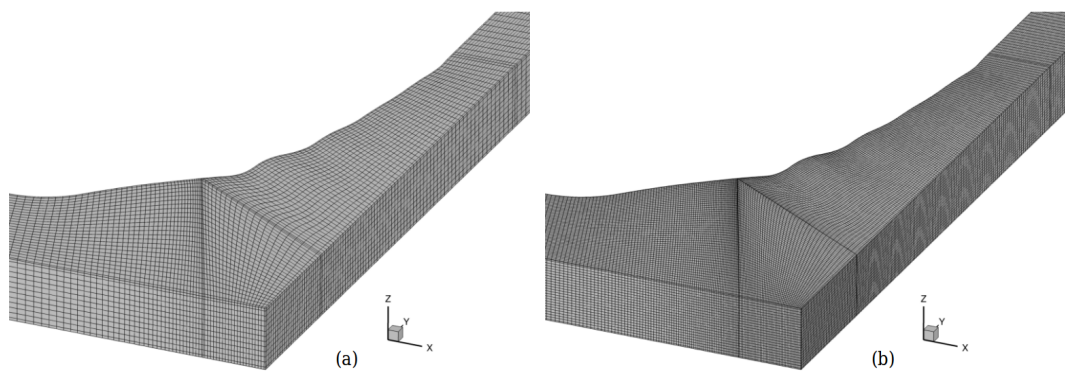


Figure 5.34. Meshes M0 (a) and M1 (b) for the optimised geometry with $AR = 1$, $WR = 1$, $L_{\perp} = 4w_u$ and $l_{\varepsilon} = 0.5w_u$.

Table 5.5. Mesh characteristics for the 3D optimised geometry when $AR = 1$, $WR = 1$, $L_{\perp} = 4w_u$ and $l_{\varepsilon} = 0.5w_u$.

Mesh	$\delta x_{min}/w_u$	$\delta y_{min}/w_u$	$\delta z_{min}/w_u$	#Computational Cells
M0	0.024	0.040	0.042	59400
M1	0.012	0.020	0.021	475200

Fig. 5.34a was used and its characteristics are given in Table 5.5.

iv) Viscoelastic fluid flow in 3D optimised T-junctions

The performance of the optimised T-junction with $AR = 1$ when considering the flow of a viscoelastic fluid is investigated here, employing the M0 mesh. The Weissenberg number used to characterise the viscoelastic fluid flow is defined as $Wi = \lambda U_2/w_{\perp}$, where U_2 is the average velocity at the outlet, perpendicular, channel. The behaviour of the viscoelastic fluids with the same parameters considered in Section 5.4.2 is examined here. Figure 5.35 shows the computed velocity and strain-rate profiles for the Oldroyd-B model ($\varepsilon = 0$) with $\beta = 0.5$. It can be seen that the evaluated velocity along the centreline of the flow, shown in Fig. 5.35a follows the desired behaviour of the target profile in the majority of the optimised region. At the end of the optimised region a small strain-rate overshoot is formed for increasing Weissenberg numbers. The optimised design can perform well up to $Wi = 0.20$, while at $Wi = 0.40$ the strain-rate overshoot

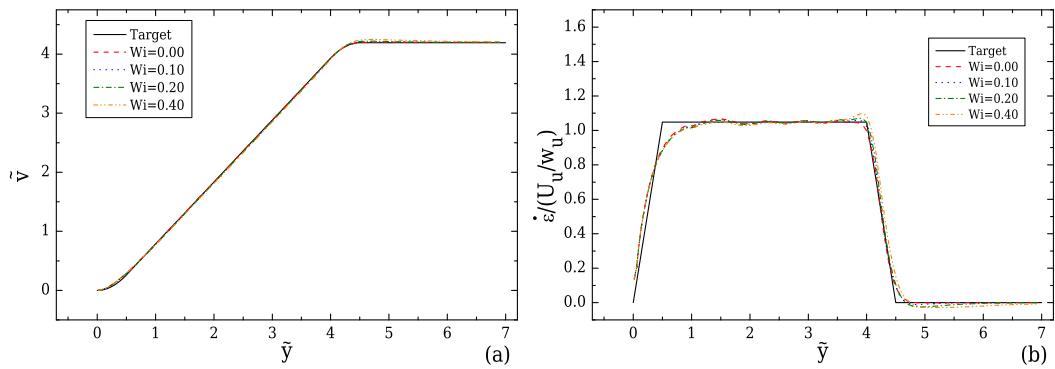


Figure 5.35. Effect of Wi on the velocity (a) and strain-rate (b) profiles along the flow centreline computed for the Oldroyd-B model ($\beta = 0.5$) under creeping flow conditions, for the optimised T-junction with $AR = 1$, $WR = 1$, $L_{\perp} = 4w_u$ and $l_{\varepsilon} = 0.5w_u$.

starts to become more pronounced and above this value care must be taken.

Figure 5.36 illustrates the behaviour of the viscoelastic fluids described by the PTT model with $\varepsilon = 0.25$ and $\beta = 0.01$. Similarly to the case of the PTT fluids in the converging/diverging geometries, here the velocity profiles are shown normalised using the maximum value of the fully developed velocity downstream of the outlet channel, $v_{2,fd}$, in order to be able to use the same target profile for all shear-thinning fluids in the representation. The velocities along the flow centreline for all the PTT fluids, shown in Fig. 5.36a, start to deviate from the target profile almost at the beginning of the desired region overpredicting the target profile, and resulting in the deviation of the strain-rate as shown in Fig. 5.36b. As the fluids approach the end of the optimised region, where the two streams meet, the strain-rate along the flow centreline underpredicts the desired behaviour. In addition to that, a non-monotonic behaviour of the strain-rates for increasing Wi is observed around $\tilde{y} \simeq 4$. This can be explained by the formation of a velocity overshoot around this location, as a consequence of the fluid's elasticity. The inset figure of Fig. 5.36a, shows the obtained velocity profile using the standard normalisation used previously, where the shear-thinning effect upon the velocity profile is now obvious for increasing Weissenberg numbers.

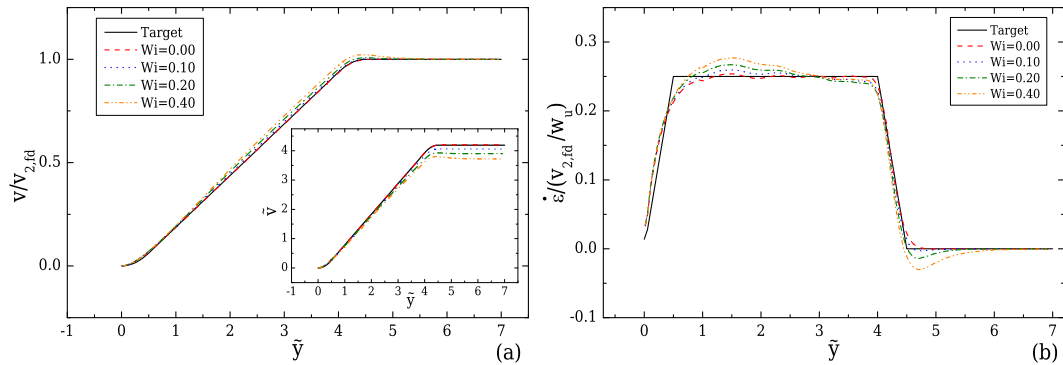


Figure 5.36. Effect of Wi on the velocity (a) and strain-rate (b) profiles along the flow centreline computed for the PTT model ($\beta = 0.01$, $\varepsilon = 0.25$) under creeping flow conditions, for the optimised T-junction with $AR = 1$, $WR = 1$, $L_{\perp} = 4w_u$ and $l_{\varepsilon} = 0.5w_u$.

5.5.2 Flow-focusing configuration

The last multi-stream configuration studied is the flow-focusing set-up with three inlets and one outlet as illustrated in Fig. 5.37. The fluids of interest are imposed from the two opposing horizontal channels and one perpendicular channel, which is exactly opposite to the only outlet channel of the device. In addition to geometrical parameters considered for the case of the T-junction, here the width of the vertical inlet was set to be the same as the horizontal inlets ($w_{\perp} = w_u$). This is arguably the most common design used in literature [201, 202], but geometries with varying values of width ratios have also been considered [200]. Finally, another important ratio for this design is the velocity ratio, VR, defined as the ratio between the imposed average velocity from the horizontal segments, U_1 , and the average velocity at the vertical inlet, U_2 , expressed as $VR = U_1/U_2$.

Figure 5.38 illustrates the contour-plots of the magnitude of the velocity, together with the corresponding flow streamlines for three different velocity ratios, $VR = 10, 20$ and 100 . For all cases, it can be seen that the fluid entering through the horizontal streams shape the vertical stream into a narrower region to a level that depends on

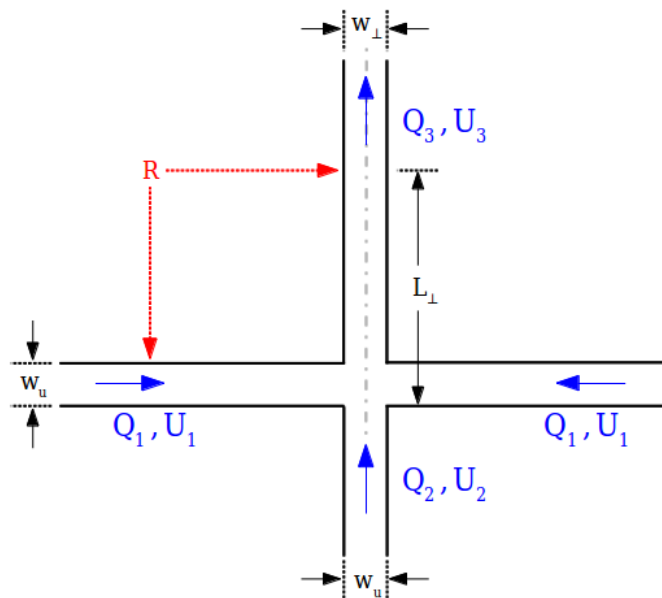


Figure 5.37. Configuration a flow-focusing channel with the *dashed-dotted* line indicating the flow centreline of the channel.

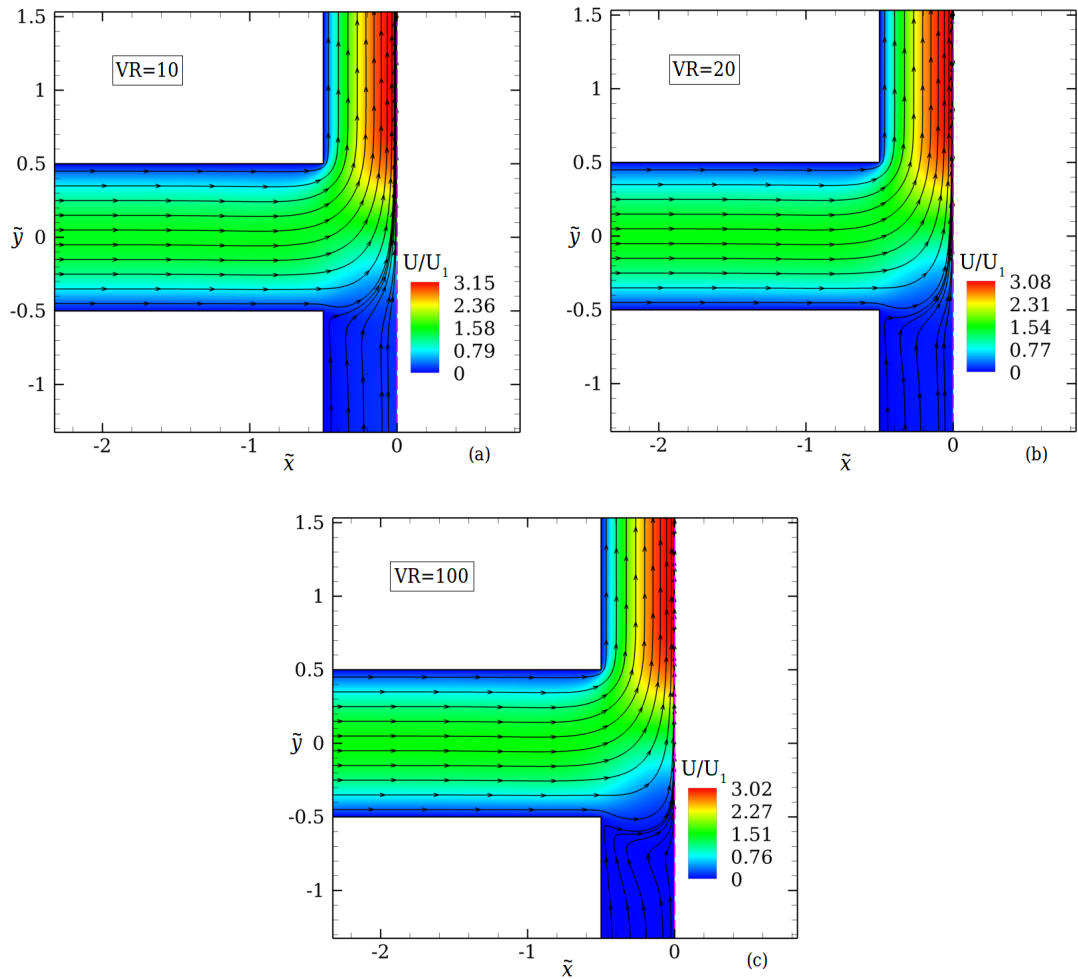


Figure 5.38. Contours of the normalised magnitude of the velocity in a 2D flow-focusing design with $WR = 1$ for $VR = 10$ (a), $VR = 20$ (b) and $VR = 100$ (c) under creeping flow conditions. The *vertical dashed line* indicates the flow field centreline, coinciding with the symmetry axis employed.

the imposed velocity ratio. The higher the velocity ratio, the higher the confinement on the vertical fluid stream. It is interesting to note that the streamlines in the central region of the channel where the vertical and the horizontal flows meet, resemble the converging region of the single-stream designs considered in [Section 5.4](#). One can consider that depending on VR different Hencky strains can be applied to the fluid of interest (imposed through the vertical inlet), generating strong extensional flows with different characteristics using a single device [[21–23](#)]. The qualitative difference of the kinematics relative to single-stream designs is that the converging region is produced

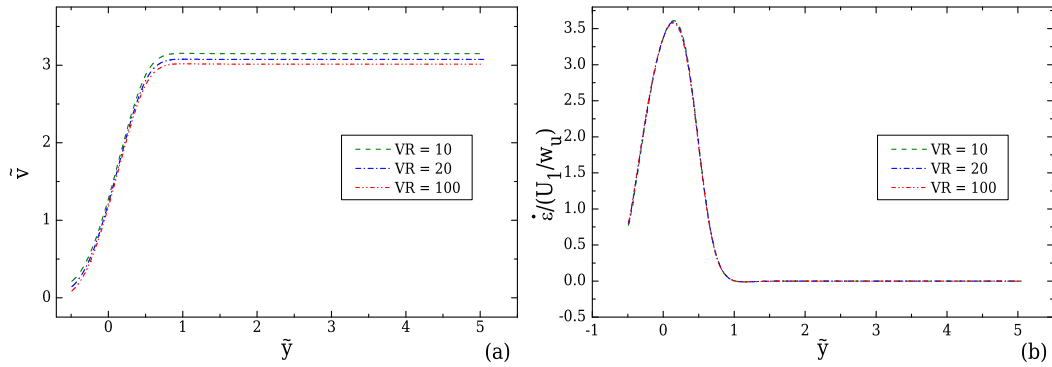


Figure 5.39. Velocity (a) and strain-rate (b) profiles for the abrupt, 2D, flow-focusing geometry with $WR = 1$ considering three different velocity ratios, $VR = 10, 20$ and 100 .

by moving streams and not by converging walls, reducing in this way the effect of shear in the vicinity of the centreline. Furthermore the use of a single geometry to generate various Hencky strains is very attractive from an experimental point of view.

Considering the simplest flow-focusing configuration which is designed by two intersecting segments at 90° (cf. Fig. 5.38), and examining the developed normalised velocity profile and its gradient along the flow centreline for the cases of $VR = 10, 20$ and 100 , shown in Fig. 5.39, a similar behaviour to the case of the T-Junction is displayed. Although the velocity quickly increases to the upstream developed value, the applied strain-rate does not remain constant, peaking just downstream of the centre of the geometry but decaying very rapidly. Therefore, shape optimisations were performed for finding more suitable geometries that can generate homogeneous extensional flow along a defined length L_\perp .

i) Optimised flow-focusing design in 2D

The desired target velocity profile employed is similar to the modified smoothed velocity profile considered in the T-junction optimisations with some minor modifications as

shown in Eq. (5.16) to take into account the third inlet stream:

$$\tilde{v} = \begin{cases} f_2 [\tilde{y} + n_2]^2 + \tilde{v}_2 & \text{if } -n_2 \leq \tilde{y} < 0 \\ f_1 (\tilde{y} + \frac{n_2}{2}) + \tilde{v}_2 & \text{if } 0 \leq \tilde{y} \leq n_1 - n_2 \\ -f_2 [\tilde{y} - n_1]^2 + \tilde{v}_3 & \text{if } n_1 - n_2 < \tilde{y} < n_1 \\ \tilde{v}_3 & \text{if } n_1 \leq \tilde{y} \end{cases} \quad (5.16)$$

where, $f_1 = (\tilde{v}_3 - \tilde{v}_2)/n_1$ and $f_2 = (\tilde{v}_3 - \tilde{v}_2)/2n_1n_2$. The resulting normalised strain-rate profile which corresponds to Eq. (5.16) is then expressed by

$$\dot{\epsilon}/(U_1/w_u) = \begin{cases} f_2 (\tilde{y} + n_2) & \text{if } -n_2 \leq \tilde{y} < 0 \\ f_1 & \text{if } 0 \leq \tilde{y} \leq n_1 - n_2 \\ -2f_2 (\tilde{y} - n_1) & \text{if } n_1 - n_2 < \tilde{y} < n_1 \\ 0 & \text{if } n_1 \leq \tilde{y} \end{cases} \quad (5.17)$$

Based on the findings of previous optimisations, a transition region of the target profiles where the velocity is let to increase smoothly defined by a second order polynomial at the beginning, and is let to decrease smoothly in similar way at the end of the desired region L_\perp is considered. For all the cases studied here the desired constant strain-rate region was set as $L_\perp = 3w_u$, while the same sequence of NURBS lattices as in the T-junction optimisation was employed, using 9 control points.

Three different velocity ratios (VR = 10, 20 and 100) have been investigated for the same geometrical set-up in 2D (WR = 1, $L_\perp = 3w_u$ and $l_\varepsilon = 0.5w_u$), and optimisations have been performed considering creeping flow conditions. Figure 5.40 shows the velocity and strain-rate profiles generated by the optimised shapes for each velocity ratio. It can be seen that the optimised geometries perform well, with both the velocity and the strain-rate profiles being well approximated. The corresponding optimised channels are presented in Fig. 5.41. It is clear that for the cases with higher velocity ratios, the resulting shape at the start of the transition region is wider and smoother overall than in the case with the smaller velocity ratio (VR = 10), in which the fluid going through the central inlet is submitted to a smaller strain. It is interesting to note here that for

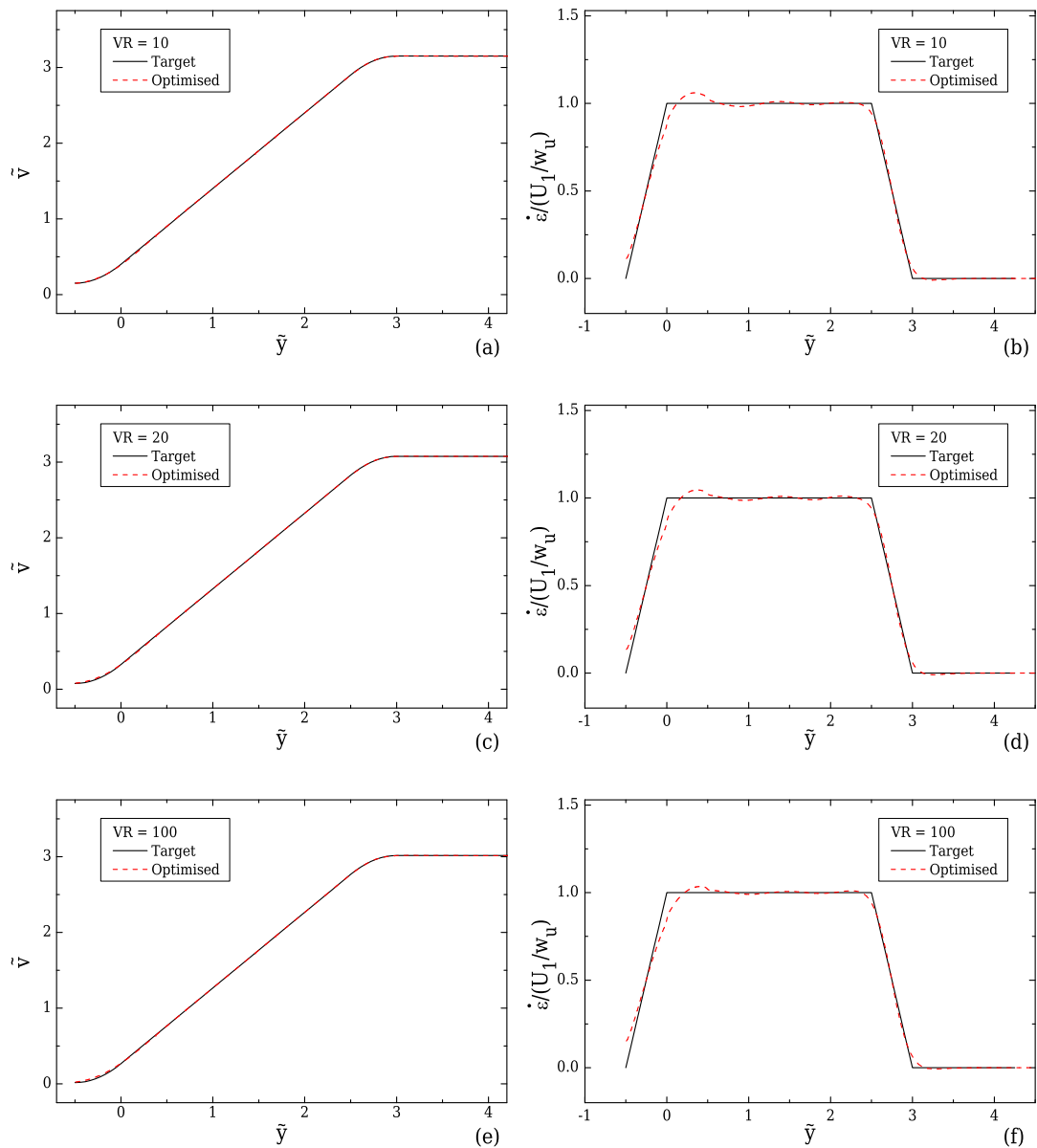


Figure 5.40. Normalised velocity (left hand side column) and strain-rate (right hand side column) profiles along the centreline of the flow for the optimised geometries with $WR = 1$, $L_{\perp} = 3w_u$ and $l_{\varepsilon} = 0.5w_u$ for $VR = 10, 20$ and 100 .

higher VR the flow can be considered equivalent to the case of a T-junction with a cavity of infinite length.

All the optimisations were performed with the use of the numerical mesh M0, with mesh M1 being employed to investigate the dependency of the solution on the mesh

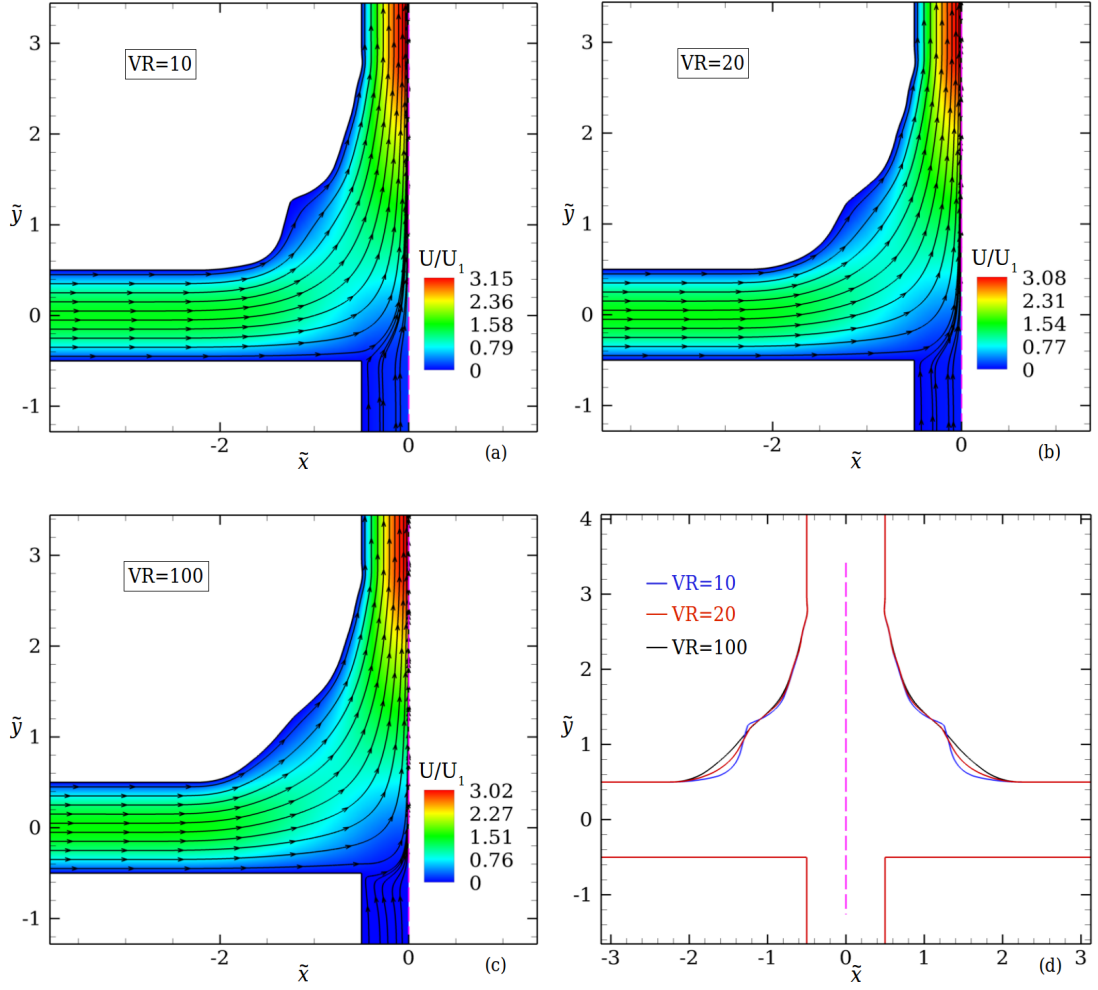


Figure 5.41. Contour-plots of the normalised velocity magnitude and streamlines obtained for the optimised flow focusing geometries under creeping flow conditions with VR=10 (a), VR=20 (b), VR=100 (c) and comparison of the optimised shapes obtained (d) when $WR = 1$, $L_{\perp} = 3w_u$ and $l_{\varepsilon} = 0.5w_u$.

refinement (details given in Table 5.6). It was found that the maximum deviation between the two meshes is approximately 1.2% for the cases of VR = 10 and 20 and

Table 5.6. Mesh characteristics for the 2D optimised geometry when $WR = 1$, $L_{\perp} = 3w_u$ and $l_{\varepsilon} = 0.5w_u$.

Mesh	$\delta x_{min}/w_u$	$\delta y_{min}/w_u$	#Computational Cells
M0	0.040	0.029	16960
M1	0.020	0.015	67840

less than 1% for the case of $VR = 100$.

ii) Optimised flow-focusing design in 3D

As done for all the configurations investigated previously, 3D effects are considered for the case of a flow-focusing device. This study was performed for an aspect ratio of $AR = 1$ considering a velocity ratio of $VR = 20$. Symmetry conditions are applied along xy - and yz -centreplanes to minimise the computational costs and all evaluations are performed for creeping flow conditions.

The 3D optimised shape for $AR = 1$ is shown in Fig. 5.42a together with contour-plot of the normalised velocity magnitude and in Fig. 5.42b a comparison with the optimised shape in 2D is given. Clearly for this aspect ratio ($AR = 1$), three-dimensional effects need to be considered and the transition region needs modifications relative to the 2D case in order to obtain the desired kinematics. As shown in Fig. 5.43, the new optimised shape for the 3D configuration performs much better than when the 2D-shape is used for a 3D flow with $AR = 1$. The velocity profile in the region of interest is well approximated for the new design in contrast to the 2D-shape which slightly underestimates the target profile, as shown in Fig. 5.43a. This obviously affects the

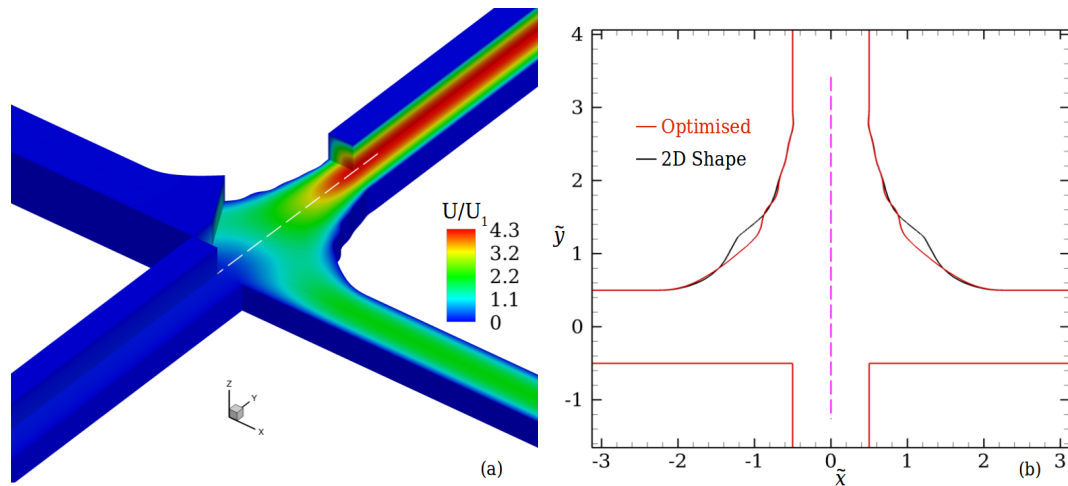


Figure 5.42. Normalised velocity magnitude contour-plot of the 3D optimised, flow-focusing geometry (a) and comparison with the 2D optimised shape (b), with $AR = 1$, $WR = 1$, $VR = 20$, $L_{\perp} = 3w_u$ and $l_{\varepsilon} = 0.5w_u$. The *dashed* straight line illustrates the position of centreline of the flow and the symmetry axis.

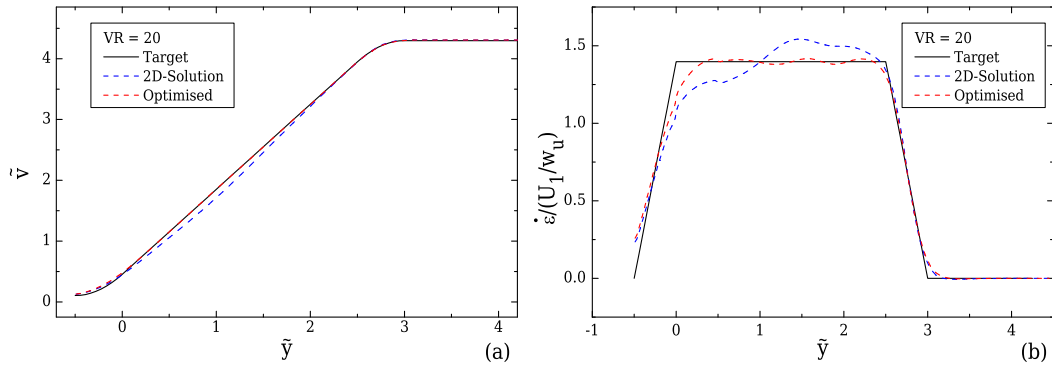


Figure 5.43. Velocity (a) and strain-rate (b) profiles along the centreline of the flow for the 3D, flow-focusing, optimised geometry and for the 3D flow-focusing geometry designed with the shape of the 2D optimised solution for $AR = 1$, $WR = 1$, $VR = 20$, $L_{\perp} = 4w_u$ and $l_{\varepsilon} = 0.5w_u$, under creeping flow conditions.

Table 5.7. Mesh characteristics for the 3D optimised geometry with $AR = 1$, $WR = 1$, $L_{\perp} = 3w_u$ and $l_{\varepsilon} = 0.5w_u$

Mesh	$\delta x_{min}/w_u$	$\delta y_{min}/w_u$	$\delta z_{min}/w_u$	#Computational Cells
M0	0.053	0.042	0.091	93786
M1	0.026	0.021	0.045	750288

streamwise velocity gradient, and therefore the homogeneity of the strain-rate in the region of interest (cf. Fig. 5.43b) is substantially improved with the optimised geometry for the specific AR considered. The numerical results and therefore the produced

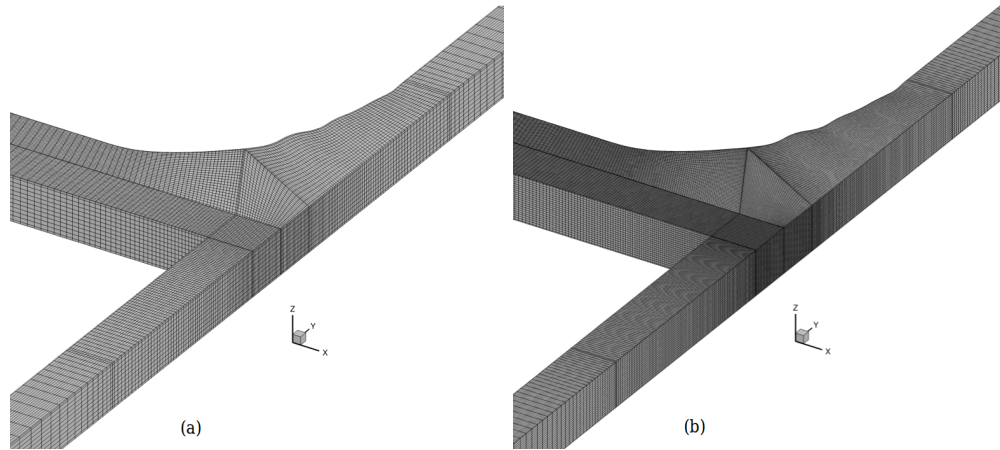


Figure 5.44. Meshes M0 (a) and M1 (b) for the optimised geometry with $AR = 1$, $WR = 1$, $VR = 20$, $L_{\perp} = 3w_u$ and $l_{\varepsilon} = 0.5w_u$.

optimised shape for this case have found to be independent from mesh resolution, since the maximum deviation at the strain-rates between meshes M0 and M1 (cf. Table 5.7 and Fig. 5.44b) which was employed for this purpose is less than 1%.

iii) Different velocity ratios in the 3D optimised flow-focusing design

One of the advantages of using this more complex configuration is to be able to test different Hencky strains using a single device by changing the flow rates in the different branches (equivalent to imposing different contraction ratios [21–23]). As such, ideally one would like to make use of the same optimised configuration for various VR.

To test the limits of the 3D configuration optimised for $VR = 20$ (shown in Fig. 5.42), the strain-rate profiles along the flow centreline for various velocity ratios were compared (cf. Fig. 5.45). It can be seen that the optimised geometry works well for $VR \geq 10$, generating a region of approximately constant strain-rate. When $VR > 20$, there is a small under-prediction for increasing VR, which eventually reaches a plateau. On the other hand, when $VR < 20$ and particularly for the case of $VR = 10$ there is a slight over-prediction of the strain-rates. For low velocity ratios ($VR = 1$) the design fails to produce the desired behaviour. This behaviour can be explained by examining

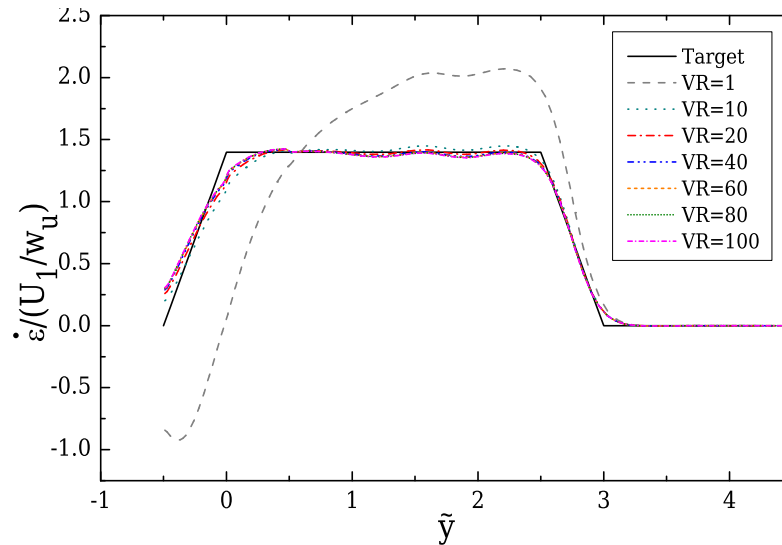


Figure 5.45. Strain-rate profiles along the flow centreline of the 3D optimised flow-focusing geometry with $AR = 1$, $WR = 1$, $L_{\perp} = 3w_u$, $l_{\varepsilon} = 0.5w_u$, optimised for $VR = 20$ under creeping flow conditions, when imposing different velocity ratios.

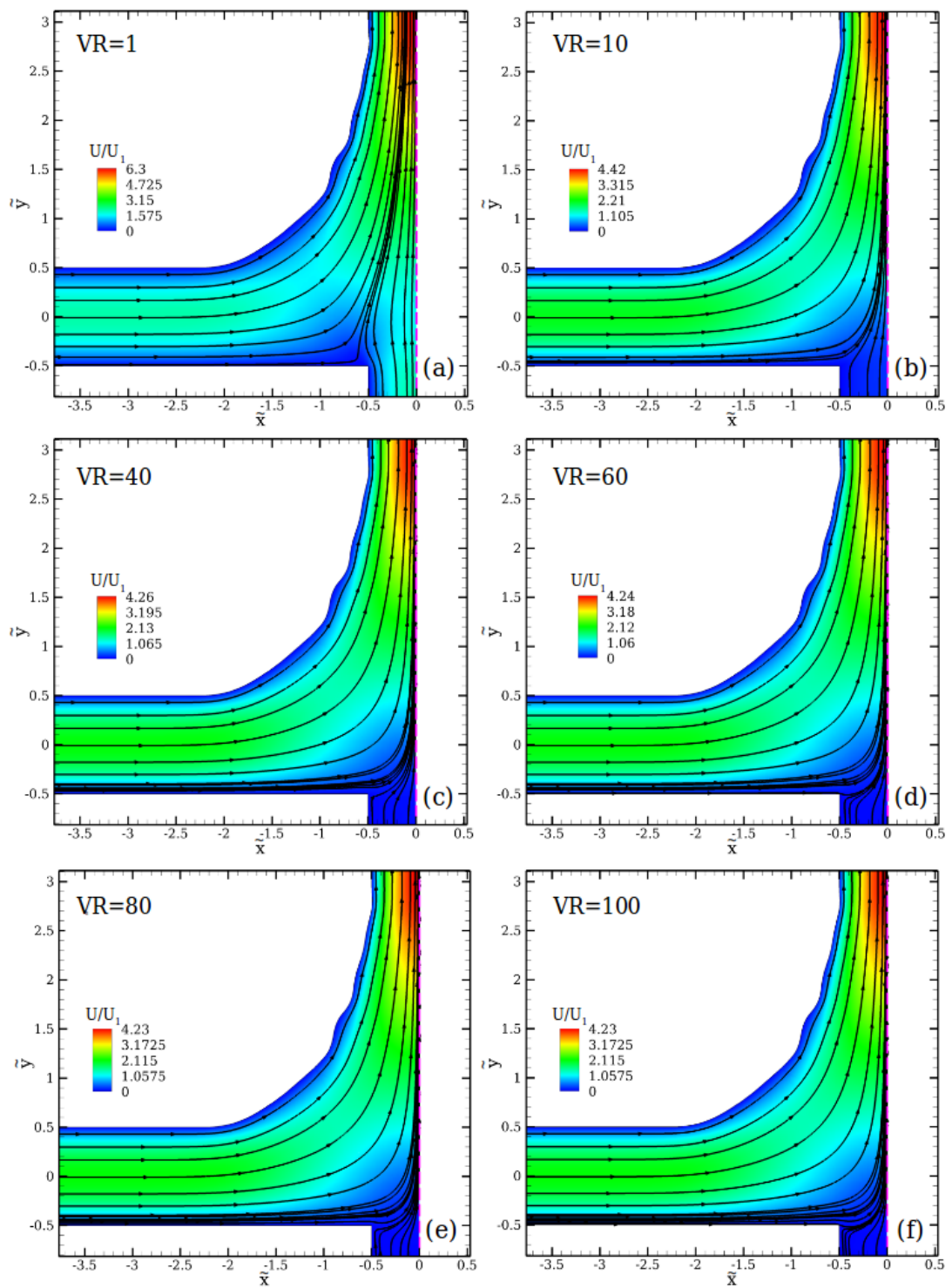


Figure 5.46. Contour-plots of the normalised velocity magnitude and streamlines obtained for the 3D optimised flow focusing geometry with $AR = 1$, $WR = 1$, $L_{\perp} = 3w_u$, $l_{\epsilon} = 0.5w_u$, optimised for $VR = 20$ under creeping flow conditions, when imposing $VR = 1$ (a), $VR = 10$ (b), $VR = 40$ (c), $VR = 60$ (d), $VR = 80$ (e), $VR = 100$ (f).

the flow field shown [Fig. 5.46](#), which illustrates the normalised velocity magnitudes and the streamlines for the different velocity ratios considered.

For the cases with $VR > 20$ shown in [Fig. 5.46\(c\)-\(f\)](#) the generated velocities are not affected significantly by the presence of the vertical, third stream, but are mostly influenced by the horizontal streams. As VR increases, the centreline velocity nearly plateaus as the contribution of the vertical stream to the outlet flow rate becomes negligible, explaining the behaviour of the strain-rates. On the other hand, for $VR = 10$ the slight over-prediction is due to the fact that the third stream influences more the velocity field (cf. [Fig. 5.46\(b\)](#)), and this becomes more notorious for $VR = 1$. Moreover, the diverging streamlines seen for $VR = 1$ when the vertical stream enters the junction result in a decrease of the centreline velocity, which in turn results in the large deviations of strain-rate observed in [Fig. 5.45](#).

It should be noted here, that although the deviations in the strain-rate profiles are small for $VR \geq 10$, the optimiser is expected to generate slightly different shapes for each VR to reduce these deviations, similarly to what is seen for the 2D case.

iv) **Viscoelastic fluid flow in 3D optimised flow-focusing design**

The performance of the 3D optimised device for a velocity ratio of $VR = 20$ when viscoelastic fluid flows are considered, is investigated using M0. [Figure 5.47](#) shows the performance predicted for an Oldroyd-B fluid with $\beta = 0.50$, as considered in all previous cases. Although a direct comparison with the case of the optimised T-junction is not possible because the optimised lengths considered (L_{\perp}) are different, a similar behaviour is observed. As noticed previously, a strain-rate overshoot is formed at the end of the optimised region for progressively increasing Weissenberg numbers (cf. [Fig. 5.47b](#)). However, in contrast to the T-junction, it can be seen here that as Wi is increased the existence of the vertical stream starts to affect slightly the generated strain-rate profile also at the beginning. These effects produced from the existence of the vertical stream on the flow field are expected and as reported in Oliveira *et al.* [21], an instability is expected to occur in this region above a critical Weissenberg number. From the results presented it can be seen that the optimised design can perform well

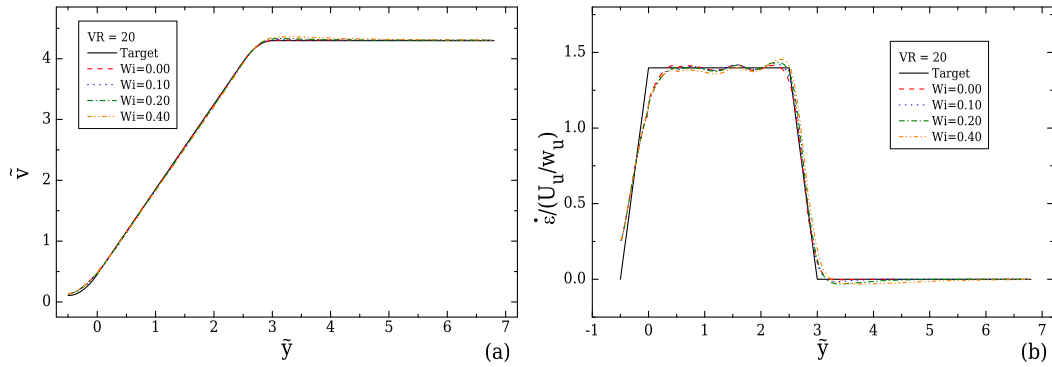


Figure 5.47. Effect of Wi on the velocity (a) and strain-rate (b) profiles along the flow centreline computed for the Oldroyd-B model ($\beta = 0.50$) under creeping flow conditions, for the optimised geometry with $AR = 1$, $WR = 1$, $VR = 20$, $L_{\perp} = 3w_u$ and $l_{\varepsilon} = 0.5w_u$.

up to $Wi = 0.20$, but after this value the velocity overshoot becomes more pronounced.

For the case of the PTT fluid, shear-thinning effects affect both the velocity and the strain-rate profiles along the flow centreline, resulting in the profiles shown in Fig. 5.48. Both profiles are normalised considering the maximum evaluated velocity in downstream of the optimised region in the outlet channel, while the inset figure in Fig. 5.48a considers the previous normalisation where the shear-thinning effects are obvious ($\dot{\epsilon}$ would reduce due to shear thinning if normalised by (U_1/w_u)). The behaviour for the PTT fluid is similar to what is seen for the T-Junction case. The velocity profile overpredicts the desired target, forming an overshoot around $\tilde{y} = 2.5$ for increasing Wi ,

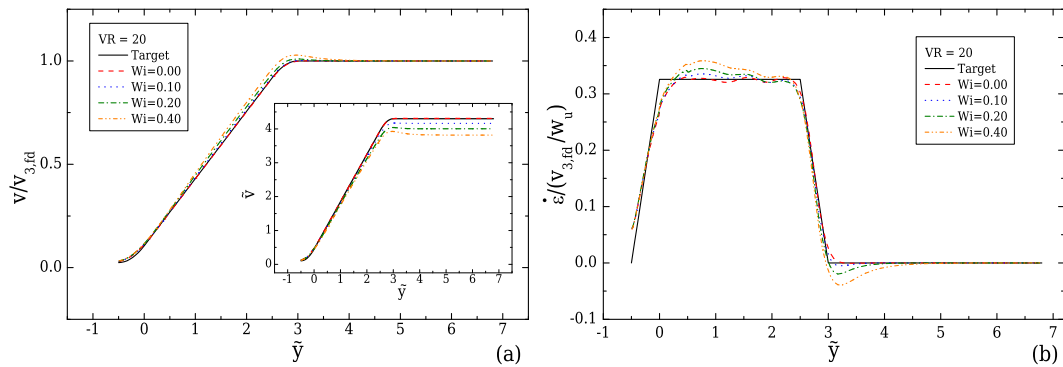


Figure 5.48. Effect of Wi on the velocity (a) and strain-rate (b) profiles along the flow centreline computed for the PTT model ($\varepsilon = 0.25$ and $\beta = 0.50$) under creeping flow conditions, for the optimised geometry with $AR = 1$, $WR = 1$, $VR = 20$, $L_{\perp} = 3w_u$ and $l_{\varepsilon} = 0.5w_u$.

which is verified by the non-monotonic behaviour of the strain-rate around this point, and is then followed by a strain-rate undershoot.

5.6 Synopsis

The study of complex fluid systems, under extensional flow conditions can provide a variety of important information, both in terms of the characterisation of viscoelastic fluids and the individual behaviour of particles, such as cells, fibres, proteins and DNA, but often require flows with well defined and known characteristics, to allow or simplify their analysis. The optimised geometries in this work give the ability to generate a wide region of homogeneous strain-rate and can be interesting platforms for studies of cell and droplet deformation, or stretching of single molecules (e.g. DNA, proteins) under uniform controlled extensional flows. In addition, these optimised configurations have the potential to be used for performing measurements of the extensional properties of complex fluids. All geometries have advantages and disadvantages, and the choice of the geometry to be used depends strongly on the application. Single-stream, converging/diverging designs with their inherent simplicity require the control of only one stream, whereas for multi-stream designs the control of more than two streams is mandatory but they provide more flexibility.

The major purpose of this study was the generation of optimised configurations that are able to generate flows with region of homogeneous extension. In this chapter, various configurations able to handle one or more fluid streams were investigated and optimised designs have been proposed for this purpose. It was shown that commonly used shapes, defined by known geometrical functions, such as hyperbolic, rounded and 90° intersections, will not necessarily present the ideal desired behaviour. It was shown that CFD calculations associated with an optimisation methodology have great potential to overcome the typical *trial-and-error* approach, saving time and reducing costs by improving designs prior to fabrication.

In this chapter, converging-diverging geometries, T-junctions and flow-focusing devices have been considered. The shape of various single-stream, converging/diverging

geometries defined by different aspect ratios and different contraction ratios has been optimised in order to generate a region of constant strain-rate along the centreline, under creeping flow conditions. It was shown that for the case of $CR = 8$ in the 2D limit when the contraction region is long enough, the optimised geometries approach an ideal hyperbolic shape. In this case, the optimisation procedure is only useful to control the strain-rate profile of the transition region at the contraction entrance and expansion exit. However, such limits are seldom used in practice in lab-on-a-chip devices, for which the well-known hyperbolic shape is not the most suitable configuration for producing homogeneous extensional flows. As the contraction becomes shorter, entrance and exit effects of the contraction affect the strain-rate profile, an issue also shown experimentally by Oliveira *et al.* [74] and Ober *et al.* [166]. This drawback is surpassed with the optimised geometry exhibiting transition regions at the start and at the end of the contraction/expansion, which become larger for short lengths.

For three dimensional converging/diverging configurations in which a variable aspect ratio along the contraction is introduced, the effects on the velocity development are even more intense. It was shown that for all 3D devices with different contraction ratios ($3 \leq CR \leq 20$) and different aspect ratios ($1 \leq AR \leq 32$), different optimised shapes are generated which significantly improve the performance relative to the ideal hyperbolic shape, and are unique for each contraction and aspect ratio. This outcome is important and may be useful as a guideline to help experimentalists better decide upon the appropriate shape to be used depending on the application.

All 3D configurations obtained for $CR = 8$ and $1 \leq AR \leq 32$ were found to perform well up to $Re \approx 5$ for Newtonian fluids. Additionally, for the viscoelastic fluids studied using the design of $AR = 1$, it was demonstrated that when they exhibit significant shear-thinning (PTT model), the configuration optimised for Newtonian fluid flow needs to be used with care, especially in what concerns the diverging region, where it fails to produce a constant strain-rate along the flow centreline even for low Weissenberg numbers. On the other hand, for a constant viscosity viscoelastic fluid (Oldroyd-B) the design can be used accurately in the full converging/diverging region up to $Wi = 0.02$ (remember Wi was defined based on the apparent strain rate), or

even higher if interested in the converging region alone. Use beyond these limits would require optimisations for the particular fluid/flow condition under consideration.

Another type of design that can be used for performing studies related to extensional properties are the multi-stream configurations. Two different arrangements have been investigated: a T-junction and a flow-focusing design. For both cases it was shown that the simplest 90° configurations cannot be used for extensional studies, since the velocity gradient peaks and rapidly decays along the intersecting regions. Additionally, for the T-junction it was shown that a rounded and a hyperbolic boundary shape also do not perform ideally.

The study of the T-Junction geometry was performed considering two different objective functions. The first was characterised by a sudden increase of the velocity right after the stagnation point, and the second was employing a smoother transition region both at the start and at the end of the desired constant strain-rate region. It was shown that the first case could be approximated well only if a cavity is generated, indicating that the existence of a transition region for the velocity development is mandatory. However due to the fact that in T-junctions with cavities the stagnation point is free, the modified profile was employed in order to optimise effectively a geometry with an unchanged boundary and a fixed stagnation point at the wall. Using the modified smoothed profile, both 2D and 3D arrangements have been optimised. For moderate depths of the device, the 2D optimal shape cannot be used and optimisations need to be performed in order to obtain a more liable design. The 3D optimised configuration demonstrated good performance for Newtonian fluids and for constant viscosity viscoelastic fluids (Oldroyd-B model) up to a $Wi = 0.20$. After this value and for higher Weissenberg numbers, the formation of the overshoot in the strain-rate profiles at the end of the optimised region needs to be taken into consideration. On the contrary, for shear-thinning viscoelastic fluids (PTT model) it was shown that the strain-rates along the flow centreline do not remain constant and different optimisation strategy should be employed.

Moving to the flow-focusing configuration, three cases with different velocity ratios, $VR = 10, 20$ and 100 , have been studied in 2D and it was shown that each one of them

requires a slightly different boundary shape for obtaining a constant strain-rate along the centreline of the prescribed region. The case with $VR = 20$ was also investigated in 3D, and similarly to the T-Junction it was found that the 2D shape cannot be used for a geometry with $AR = 1$ and shape optimisations are needed. Moreover, the same 3D design was used for investigating its limits in terms of different velocity ratios. It was shown that the configuration can operate efficiently for $VR \geq 10$, exhibiting only small deviations in the strain rates. Therefore the optimised geometry can be employed for generating homogeneous extensional flows of different Hencky strains. On the other hand, for small velocity ratios ($VR = 1$) the design fails to produce the desired behaviour. The examination of the viscoelastic fluids described by the Oldroyd-B model showed a similar response with the one observed in the 3D optimised T-junction, with the design operating well up to $Wi = 0.20$. After this value the overshoot in the strain-rates at the end of the optimised region becomes more pronounced and in addition, the incoming stream from the perpendicular inlet channel starts to affect the desired behaviour at the beginning of the optimised region. For the viscoelastic fluids described by the PTT model, the shear-thinning behaviour of the fluid does not allow the generation of the desired behaviour, resulting in a response similar to that observed for the flow of the same fluid in the 3D optimised T-junction.

Although these single- and multi-stream geometries discussed have in common the generation of homogeneous extension along the flow centreline, the flow within the designs exhibits significant differences. The simplest design of the converging/diverging configurations has the advantage of controlling only one stream in order to produce the desired flow conditions. Therefore the ease with which one can control the flow conditions, makes these channels well suited for example in analysing the stretch of molecules. For the T-Junctions one needs to control two streams and has the ability to generate a stagnation point flow, where molecules can be trapped in, exhibiting infinite stretch. Moreover, the use of two streams can be exploited to further investigate mixing techniques. Finally, with the use of a flow-focusing device, one can resemble flows of converging/diverging geometries with various Hencky strain values, by controlling the three imposed streams in different ways [21–23]. As shown the two horizontal streams

shape the third, vertical stream and in this way a region with strong extension can be generated where shear effects are reduced relative to the converging/diverging designs.

“Any method which simultaneously possess accuracy, stability algorithmic simplicity, and an easily comprehended physical interpretation would seem to be optimal.”

B.P. Leonard

Chapter 6

From single-phase to two-phase

In this chapter, the implementation of a two-phase solver on top of the single-phase solver discussed in [Chapter 3](#) exploiting the already established capabilities of the single-phase solver for the simulation of viscoelastic fluid flows is presented. The Phase Field method is employed and the Cahn-Hilliard equation is considered for describing the transport of a binary fluid system. The ultimate aim is to be able to study three dimensional flow problems using two-phase systems, with either Newtonian and non-Newtonian phases or a combination of both. Although the two phase solver is implemented in such a way to allow problems with viscoelastic fluids for flow in three dimensions, in this thesis it has only been validated for two-dimensional binary fluid flows with Newtonian phases, employing appropriate test-cases.

6.1 Introduction

In order to investigate and analyse the complex dynamics of a multiphase system, various numerical techniques have been proposed and used effectively. They are distinguished in two major categories [56, 222], the *interface tracking* methods and the *interface capturing* methods. Tracking methods such as front-tracking [223], immersed

boundary [224, 225] and boundary integral methods [226], consider a moving boundary which tracks and defines a sharp interface between the different fluids. Thus, the interface is explicitly described by a moving computational boundary with the interfacial conditions used as boundary conditions. These methods are very accurate since they model the surface directly, however, they usually require a large amount of computational resources for storing and processing the appropriate information. Furthermore, because of mesh movement-reconstruction these methods present singularity issues and fail to capture morphological changes such as droplet breakup and coalescence [227–229].

On the other hand, when interface capturing techniques are employed, the numerical mesh is static (fixed-grid methods) and the interface is captured based on the variation of an artificial scalar field, which is used for distinguishing between the different phases. These methods instead of analysing the flow of two fluid systems separated by an interface, they consider the system as one single fluid with variable properties, overcoming the discontinuity across fluid-fluid interface, and treat the interfacial tension as a body force. The Volume of Fluid (VOF) [230, 231], the Level Set (LS) [232, 233] and the Phase Field (PF) [234, 235] are all examples of the interface capturing methods. The scalar quantity used as a phase indicator in all these methods, here represented by the generic variable C , is commonly allowed to vary in the range $0 \leq C \leq 1$ (or sometimes $-1 \leq C \leq 1$) at the interface between the two fluids. Away from the interface, in the bulk phases, the phase indicator remains constant, with 0 denoting the bulk of fluid- A and 1 indicating the bulk of fluid- B . For VOF and PF, this scalar quantity is usually related to a volume fraction or a mass concentration, whereas for LS it is a purely geometrical variable defined as the signed distance function from the interface contour.

Here, the Phase Field method is considered for simulating two-phase flows and is implemented on top of the single phase CFD solver used, described in [Section 3.3](#). The birth of PF theory goes back to 1893, when the first model and the basic ideas were introduced by van der Waals [236]. In his studies, van der Waals presented a new approach for the investigation of liquid-liquid interfaces, arguing that the molecules which compose both phases are in rapid movement both in the bulk of each fluid and

their boundary layer. Thus, in contrast to Gibbs theory [237], in which the interface between two fluids is considered as a “property-barrier”, resulting in a discontinuity between the different fluid properties, van der Waals suggested that alternatively the interface should be treated as a transition region where the properties are allowed to vary continuously, resulting in a *diffuse-interface*. The profile of this transition region was determined by the minimisation of the free energy of the interface as discussed later in Section 6.2. Following this approach, Cahn and Hilliard [238,239] extended the diffuse-interface theory and proposed a time-dependent evolution equation for investigating problems with pure diffusion. Following that, Hohenberg and Halperin [240] introduced the convective Cahn-Hilliard equation known as Model H for binary liquids with equal densities.

In contrast to other approaches for simulating multiphase systems, diffuse-interface models become attractive for three main reasons. Their continuum approach of the interface smooths the inherent discontinuities of sharp interface models [227,228], facilitating studies that are related to morphological changes of the interface, such as droplet breakup and coalescence. In addition, they consist of a “friendlier” numerical environment able to handle and simulate demanding cases that are related to non-Newtonian fluids, in which the use of rheological models increases the challenges from a numerical point of view. Finally, their greater advantage is arguably the fact that interface tracking can be completely avoided and the evaluation of interface curvature and interface normals are not required [241], resulting also in an easier numerical implementation in three dimensions.

Various Phase Field models have been proposed for studying interfacial phenomena and morphological changes [227,242–244]. Anderson *et al.* [234] reviewed the applications of the diffuse-interface models and examined the physical phenomena to which they can be applied successfully. Later, Kim [235] reviewed recent development of the phase fields models for multi-component flows and discussed their coupling with the Navier-Stokes equations.

This chapter is arranged as follows. In Section 6.2 the theory of the Phase Field method is presented, leading to the Cahn-Hilliard differential equation which accounts

for the existence of the second phase. In [Section 6.3](#), the numerical implementation of all the terms of the Cahn-Hilliard equation is presented and in [Section 6.4](#) the efficiency of the implementation is investigated, considering various test-cases appropriate for two-phase flows code validations.

6.2 Phase Field theory

6.2.1 Phase field approach

The majority of the continuum surface methods (i.e. VOF, LS) are based on the performance of each appropriate surface tension model used. On the contrary, PF models are based on the free energy of the fluid, first introduced and modelled by van der Waals. For an isothermal and immiscible two-phase system, the free energy density f can be expressed by [\[236\]](#):

$$f = \epsilon^{-1}\sigma\alpha\psi(C) + \frac{1}{2}\epsilon\sigma\alpha|\nabla C|^2 \quad (6.1)$$

where C is allowed to vary in the range $0 < C < 1$ and represents the mass concentration of the system, ϵ , is the surface thickness, σ , is the surface tension coefficient and α , is a constant parameter that will be defined below and depends on the chosen range of the variation of C . Finally, $\psi(C)$ is a *double well* function of the mass concentration defined as

$$\psi(C) = \frac{1}{4}C^2(1 - C)^2 \quad (6.2)$$

and has two energy minima located in the vicinity of each phase, as shown in [Fig. 6.1](#). The double well function is the simplest non-singular function [\[245\]](#) of the mass concentration and is arguably one of the most frequently considered expressions in PF models [\[227\]](#), as it reduces the numerical difficulties associated with common approaches that exhibit a singular behaviour [\[246, 247\]](#).

The two terms on the right hand side of [Eq. \(6.1\)](#) represent two counteracting processes. The bulk energy density, $\epsilon^{-1}\sigma\alpha\psi(C)$, influenced by the double well function, corresponds to a “phobic” behaviour which forces the system to remain separated in two domains with pure components corresponding to $C = 0$ and $C = 1$. On the contrary, the

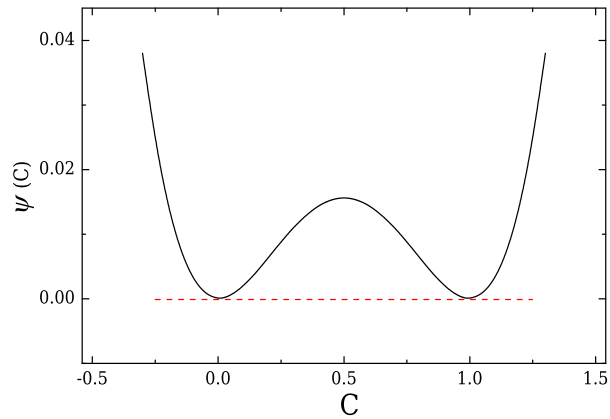


Figure 6.1. Double well function for the free energy density model in Eq. (6.1).

energy of the system due to phase gradients, $\frac{1}{2}\epsilon\sigma\alpha|\nabla C|^2$, represents the interactions between the two components, restraining the “phobic” behaviour and enhancing a “philic” response. In other words, the first term enhances the immiscibility of the two components and the second promotes their mixing [227, 228].

The rate of change of the free energy of the system enclosed in a domain V , $F = \int_V f dV$, with respect to the mass concentration C , defines the chemical potential, ϕ [239]:

$$\phi = \frac{\delta F}{\delta C} = \epsilon^{-1}\sigma\alpha\psi'(C) - \epsilon\sigma\alpha\nabla C^2 \quad (6.3)$$

Considering that the diffuse interface is at equilibrium (equal counteracting effects), the chemical potential is zero and thus for a one dimensional, simple flat interface profile, Eq. (6.3) yields the solution profile for C [58, 243]:

$$C(x) = 0.5 + 0.5 \tanh\left(\frac{x}{2\sqrt{2\epsilon}}\right) \quad (6.4)$$

In this way the concentration is allowed to vary smoothly across the interface as is shown in Fig. 6.2. Considering the profile of Eq. (6.4) a concentration variation from 0.05 to 0.95 results in a width $\delta = 4\sqrt{2\epsilon}\tanh^{-1}(0.9)$ [235, 243]. For all numerical simulations with the PF method, δ is related to the desired number of cells, k , used for discretising the interface thickness [235, 245]. For a numerical (uniform) grid with characteristic cell

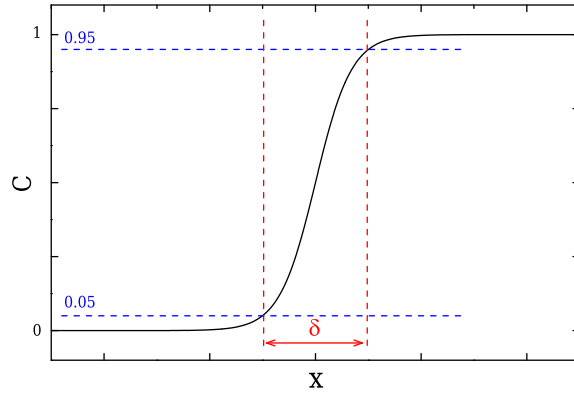


Figure 6.2. Concentration profile at the interface of the two fluids given from Eq. (6.4). The *dashed-red lines* indicate the width of the interface and the

size h ¹, the interface width is defined as $\delta = hk$ and thus, the interface thickness is correlated to the numerical mesh as $\epsilon = hk/(4\sqrt{2} \tanh^{-1}(0.9))$.

For an isothermal fluid system, the surface tension can be expressed as the integral of the free energy density through the interface per unit area [228, 248]. Considering the simplest form of a flat interface, the surface tension is then given by

$$\sigma = \epsilon\sigma\alpha \int_{-\infty}^{+\infty} \left(\frac{\partial C}{\partial x} \right)^2 dx \quad (6.6)$$

yielding that

$$\epsilon\alpha \int_{-\infty}^{+\infty} \left(\frac{\partial C}{\partial x} \right)^2 dx = 1 \quad (6.7)$$

As mentioned previously, the constant parameter α is defined by the choice of the range which, C , is allowed to vary [235]. Here, $C \in [0, 1]$ and the solution of Eq. (6.7) using Eq. (6.4) results in $\alpha = 6\sqrt{2}$.

¹ The grid size on each direction is defined as

$$h_x = L_x/N_x \quad ; \quad h_y = L_y/N_y \quad ; \quad h_z = L_z/N_z \quad (6.5)$$

where L_x, L_y, L_z are the desired domain lengths on each direction and N_x, N_y, N_z the number of cells used for discretising the domain in each direction.

6.2.2 Governing equations

The extension of Van der Waals approach to time dependent diffusional problems was proposed by Cahn and Hilliard [238, 239] in their studies for a binary fluid. They proposed that the rate of change of the concentration, C , depends on the gradients of the chemical potential (defined in Eq. (6.3)):

$$\frac{\partial C}{\partial t} = \nabla \cdot (M \nabla \phi) \quad (6.8)$$

where M is the mobility, a parameter that controls the magnitude of the diffusion term and naturally takes place at the molecular level. Furthermore, Eq. (6.8) has been extended in order to model advection problems for incompressible, immiscible flows, introducing the convective Cahn-Hilliard equation [242, 249]:

$$\frac{\partial C}{\partial t} + \mathbf{u} \cdot \nabla C = \nabla \cdot (M \nabla \phi) \quad (6.9)$$

where \mathbf{u} is the velocity vector. Clearly, the rate of change of the concentration was replaced by its material derivative, taking into account the convection of the concentration. The convective Cahn-Hilliard equation models the creation, evolution and dissolution of phase field interfaces, which are controlled by diffusion [227, 250] and is implemented here given its ability to deal with systems composed by more than one phase. Additionally, for solving the partial differential equation, Eq. (6.9), the boundary conditions considered are zero-gradient at the walls of the domain [58, 243]:

$$\mathbf{n} \cdot \nabla C = 0 \quad (6.10)$$

$$\mathbf{n} \cdot M \nabla \phi = 0 \quad (6.11)$$

where \mathbf{n} is the unit vector normal to the domain boundary.

Considering a two-phase (binary) fluid system the continuity and the incompressible Navier-Stokes equation are:

$$\nabla \cdot \mathbf{u} = 0 \quad (6.12)$$

$$\rho \left(\frac{\partial \mathbf{u}}{\partial t} + \mathbf{u} \cdot \nabla \mathbf{u} \right) = -\nabla p + \nabla \cdot \boldsymbol{\tau} + \rho \mathbf{g} + \mathbf{f}_{\text{st}} \quad (6.13)$$

where ρ is the density, p the pressure, $\boldsymbol{\tau}$ the extra stress tensor, \mathbf{g} the gravitational acceleration and the last term, \mathbf{f}_{st} , is added to account for the forces due to surface tension.

The modelling of the surface tension in the Navier-Stokes equation is key to a successful numerical code, and various models have been proposed for that reason [227, 228, 241, 244, 245]. Here, the work of Badalassi *et al.* [243] and Ding *et al.* [58] is adopted and the surface tension is evaluated based on the gradients of the concentration across the interface:

$$\mathbf{f}_{\text{st}} = \phi \nabla C \quad (6.14)$$

The advantage of this approach is that it is easier to implement since there is no need to evaluate gradient normals and additionally it has shown very good performance compared to the LS method [251].

To summarise, the concentration is set to take values in the range $[0, 1]$, indicating either the bulk of each phase (when $C = 0$ or $C = 1$) or the interface between them for intermediate values of C . For a binary fluid composed of fluids A and B , the physical properties of each fluid such as the density, ρ , and the viscosity, η , should remain constant in the bulk of each phase and vary across the interface. Here, both properties are considered as a linear function of the concentration and are expressed by

$$\rho(C) = \rho_A C + \rho_B (1 - C) \quad (6.15)$$

$$\eta(C) = \eta_A C + \eta_B (1 - C) \quad (6.16)$$

6.2.3 Considerations for the Cahn-Hilliard equation

Before presenting the numerical implementation and the way the Cahn-Hilliard equation is discretised, it is interesting to discuss some features of the method, which distinguish PF from other methods such as VOF and LS, and are important for the accuracy and the final outcome. It is clear that the key for a successful use of the PF method

relies greatly in the treatment of two important parameters, the interface thickness and the mobility. Both ϵ and M are physical properties and their choice will affect the final outcome significantly. More specifically, the thickness can be estimated experimentally and is typically of the order $\epsilon \sim 10^{-9}$ m [229], whereas a magnitude of the mobility is estimated to vary in the range $10^{-17} \lesssim M \lesssim 10^{-13} \text{ m}^5\text{s}^{-1}\text{J}^{-1}$, from liquid to gas phases respectively [248, 252].

Currently it is unrealistic for a numerical mesh used in CFD calculations to have a grid size, h , of the same order of magnitude of ϵ or smaller, and to use values of M of the order of physical mobility as these approach the machine accuracy. Thus, it becomes clear that these quantities can only be considered under a numerical point of view rather than physical and their choice is crucial for the accuracy of the method. In the literature, the interface thickness is usually related to the numerical grid by the Cahn number, $\text{Cn} = \epsilon/L$, where L is a characteristic length. A basic disadvantage of PF methods is the relatively wide interfaces they produce [227]. Thus, ideally one should consider small Cahn numbers (for $\text{Cn} \ll 1$, the sharp interface limit is approached). However, this dramatically increases the computational cost and therefore other techniques, such as adaptive mesh refinement would be ideal to employ [57].

Considering the dimensionless space, $r^* = r/L$, the dimensionless velocity, $u^* = u/U$, and the dimensionless time, $t^* = t/T_c$, where $T_c = L/U$ is a characteristic time, and U a characteristic velocity, Eq. (6.9) can be expressed in a dimensionless form as

$$\frac{U}{L} \frac{\partial C}{\partial t^*} + \frac{U}{L} \mathbf{u}^* \cdot \nabla C = \frac{M_c \phi_c^*}{L^2} \nabla^2 \phi^* \quad (6.17)$$

or

$$\frac{\partial C}{\partial t^*} + \mathbf{u}^* \cdot \nabla C = \frac{1}{\text{Pe}} \nabla^2 \phi^* \quad (6.18)$$

where, $\phi^* = \phi/\phi_c$ is a dimensionless chemical potential, M_c , is a characteristic value for the mobility and ϕ_c is a characteristic chemical potential, that can be defined by rearranging Eq. (6.3) to write:

$$\phi = \phi_c (\alpha \psi'(C) - \epsilon^2 \alpha \nabla C^2) \quad (6.19)$$

resulting to $\phi_c = \sigma\epsilon^{-1}$, which has units of Nm^{-2} . Furthermore, Eq. (6.17) illustrates the existence of two characteristic times, a convective time $t_{conv} = \frac{L}{U}$ and a diffusive time $t_{diff} = \frac{L^2}{M_c\phi_c}$. The ratio of the diffusive to the convective time yields the characteristic *Peclet number*, Pe , defined as $Pe = \frac{LU\epsilon}{M_c\sigma}$. In Section 6.4, when presenting the various test cases, the effect of these parameters are considered in detail, since they evidently affect the characteristic time scales of the problem.

6.3 Numerical Implementation

The collocated grid approach described in Ferziger and Peric [59], for the Finite Volume method is adopted here, consistent with the in-house single-phase solver. The following sections describe the discretisation procedure followed for implementing the terms of Cahn-Hilliard equation (Eq. (6.9)), the force term added in the momentum equation to account for surface tension effects and the boundary conditions considered.

6.3.1 The Cahn-Hilliard equation

Using Eq. (6.2) in Eq. (6.3), the expression of the chemical potential that needs to be discretised is

$$\phi = \epsilon^{-1}\sigma\alpha [C^3 - 1.5C^2 + 0.5C] - \epsilon\sigma\alpha\nabla^2C \quad (6.20)$$

Evidently, the combination of Eq. (6.20) and Eq. (6.9) will produce a gradient of fourth order, which makes the discretisation of Eq. (6.9) very complex. In order to surpass this difficulty, the chemical potential is explicitly evaluated at each computational cell of the discretised domain using Eq. (6.20) and the current concentration values. Then, together with the mobility they are used for the evaluation of a general diffusive flow rate of Eq. (6.9). It should be mentioned that mobility is either considered as a constant, $M = M_c$, similarly to Yue *et al.* [228] and Yue *et al.* [57], or as a second order function of the concentration $M = M_cC(1 - C)$ as in Kim [244] and Ding *et al.* [58]. Here it is implemented as $M = M_c[C(1 - C)]^\gamma$, where γ can only take values of 0 or 1, to be able to examine both problems with constant or variable mobility respectively. The diffusive

flow rate of the Cahn-Hilliard equation is expressed as

$$\mathbf{q} = M\nabla\phi \quad (6.21)$$

and is considered as a source term in equation Eq. (6.9). For a Cartesian coordinate system it is expressed in terms of its components for each of the three directions as

$$\mathbf{q} = q_1\mathbf{e}_1 + q_2\mathbf{e}_2 + q_3\mathbf{e}_3 = M\frac{\partial\phi}{\partial x_i}\mathbf{e}_i \quad (6.22)$$

with \mathbf{e}_i representing the normal vector in each direction. Hence the diffusion term of the Cahn-Hilliard equation can be written in Cartesian coordinates using Einstein notation as

$$\nabla \cdot \mathbf{q} = \frac{\partial q_i}{\partial x_i} \quad (6.23)$$

Following that, the complete form of Eq. (6.9), using Einstein notation, can be written as

$$\frac{\partial C}{\partial t} + u_i \frac{\partial C}{\partial x_i} = \frac{\partial q_i}{\partial x_i} \quad (6.24)$$

Employing the coordinate transformation rules for expressing the time and spatial derivatives in generalised coordinates [59], each term of Eq. (6.24) is transformed as follows:

- Inertia term

$$\frac{\partial C}{\partial t} = \frac{1}{J} \frac{\partial}{\partial t} (CJ) \quad (6.25)$$

- Convection term

$$\frac{\partial}{\partial x_i} (u_i C) = \frac{1}{J} \frac{\partial}{\partial \xi_l} (C u_i \beta^{li}) \quad (6.26)$$

- Diffusion term

$$\frac{\partial q_i}{\partial x_i} = \frac{1}{J} \frac{\partial}{\partial \xi^l} (q_i \beta^{li}) \quad (6.27)$$

where, J is the Jacobian and β^{li} the cofactors of the coordinate transformation matrix, introduced in Section 3.2. Hence, Eq. (6.24) is written for a generalised coordinate

system as

$$\frac{\partial}{\partial t} (CJ) + \frac{\partial}{\partial \xi_l} (Cu_i \beta^{li}) = \frac{\partial}{\partial \xi^l} (q_i \beta^{lj}) \quad (6.28)$$

Additionally, the components of the diffusive flow rate from Eq. (6.22) in each direction are transformed in generalised coordinates and expressed in Einstein notation for a Cartesian coordinate system as

$$q_i = M \frac{\partial \phi}{\partial x_i} = \frac{M}{J} \frac{\partial \phi}{\partial \xi^l} \beta^{li} \quad (6.29)$$

and in expanded form for each one of the components as

$$\begin{aligned} q_1 &= \frac{M}{J} \left[\frac{\partial \phi}{\partial \xi^1} \beta^{11} + \frac{\partial \phi}{\partial \xi^2} \beta^{21} + \frac{\partial \phi}{\partial \xi^3} \beta^{31} \right] \\ q_2 &= \frac{M}{J} \left[\frac{\partial \phi}{\partial \xi^1} \beta^{12} + \frac{\partial \phi}{\partial \xi^2} \beta^{22} + \frac{\partial \phi}{\partial \xi^3} \beta^{32} \right] \\ q_3 &= \frac{M}{J} \left[\frac{\partial \phi}{\partial \xi^1} \beta^{13} + \frac{\partial \phi}{\partial \xi^2} \beta^{23} + \frac{\partial \phi}{\partial \xi^3} \beta^{33} \right] \end{aligned} \quad (6.30)$$

Each component q_1 , q_2 and q_3 of the diffusive flow rate contains a product of the rate of change of the chemical potential along each direction with the appropriate cofactor.

Since the finite volume approach is adopted and in order to discretise the Cahn-Hilliard equation, Eq. (6.28) is integrated over each numerical cell of volume V_P :

$$\int_{V_P} \frac{\partial}{\partial t} (CJ) dV_P + \int_{V_P} \frac{\partial}{\partial \xi_l} (Cu_i \beta^{li}) dV_P = \int_{V_P} \frac{\partial}{\partial \xi^l} (q_i \beta^{li}) dV_P \quad (6.31)$$

or alternatively:

$$\int_{V_P} \frac{\partial}{\partial t} (CJ) dV_P + \underbrace{\int_{V_P} \frac{\partial}{\partial \xi_l} (Cu_i \beta^{li} - q_i \beta^{li}) dV_P}_{= 0} = 0 \quad (6.32)$$

Using Gauss theorem, which transforms the volume integral of a vector divergence to a surface integral, the convection-diffusion integral of Eq. (6.32) (underline term) can be approximated by the sum of the six integrals evaluated on the cell faces, given in a general form:

$$I_{V_P} = I_e + I_w + I_n + I_s + I_t + I_b \quad (6.33)$$

where e, w, n, s, t and b indicate each of the six-faces of the computational cell P. These face integrals represent the flux of the transporting quantity, \mathbf{C} , through the control volume surfaces and all of them can be approximated similarly to the case of the east surface as

$$I_e = \int_{A_e} \mathbf{C} \cdot \mathbf{n} dA_e \simeq C_e A_e \quad (6.34)$$

resulting to the approximation of the total flux as

$$I_{V_P} \simeq C_e A_e - C_w A_w + C_n A_n - C_s A_s + C_t A_t - C_b A_b \quad (6.35)$$

Examining a single control volume cell, P, as the one shown in Fig. 6.3 in two dimensions, based on mass conservation, the outward flux through its east face, $I_{e,P}$, will be the same as the inward flux from the west face of its east neighbour, $I_{w,E}$. This is important in terms of numerical implementation since only three integrals of Eq. (6.33) need to be evaluated at each computational cell, particularly I_e, I_n and I_s , therefore reducing the computational needs [59, 86].

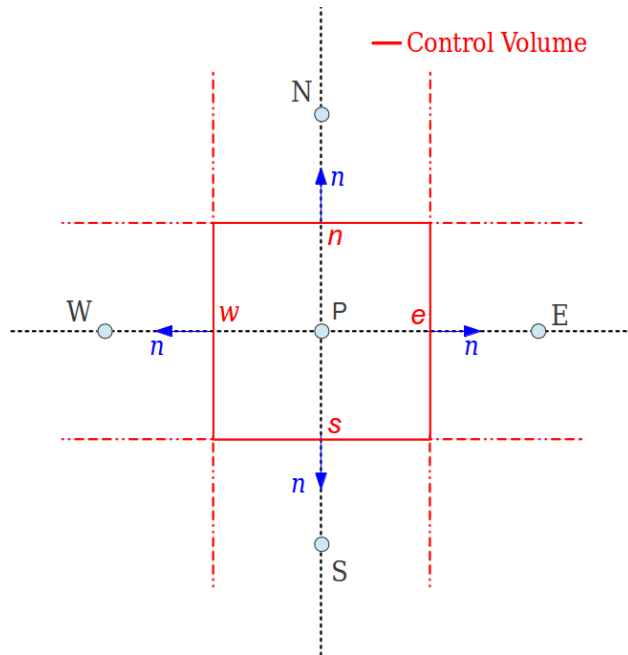


Figure 6.3. Two dimensional representation of a control volume.

Similarly to the majority of textbooks considering finite volume techniques [59, 60, 64], the convection-diffusion integral is considered as a sum of the convection term and the diffusion term as

$$I = I^C + I^D \quad (6.36)$$

and treated separately. Substituting the integrals of Eq. (6.33) with its counterparts from Eq. (6.36) the desired discretisation of the Cahn-Hilliard partial differential equation will be produced, and are examined separately below.

- **Inertia term**

$$\int_{V_P} \frac{\partial}{\partial t} (CJ) dV_P = \left(\frac{C^n - C^{n-1}}{\Delta t} \right)_P V_P \quad (6.37)$$

where, C^n and C^{n-1} , are the cell-centred solutions of the concentration at the current and previous time step respectively. For all the following discretisations, both the convective and the diffusive terms are using concentration values computed at the current time, following the fully-implicit considerations of the single-phase solver. For that reason, the index n is dropped to avoid confusion and only the previous time step level will be indicated if needed.

- **Convection term**

$$I^C = \int_{V_P} \frac{\partial}{\partial \xi_l} (Cu_i \beta^{li}) dV_P \quad (6.38)$$

Analysing the convection term inside the integral to its components:

$$\begin{aligned} \frac{\partial}{\partial \xi_l} (Cu_i \beta^{li}) &= \frac{\partial}{\partial \xi_1} (Cu_1 \beta^{11} + Cu_2 \beta^{12} + Cu_3 \beta^{13}) \\ &+ \frac{\partial}{\partial \xi_2} (Cu_1 \beta^{21} + Cu_2 \beta^{22} + Cu_3 \beta^{23}) + \frac{\partial}{\partial \xi_3} (Cu_1 \beta^{31} + Cu_2 \beta^{32} + Cu_3 \beta^{33}) \end{aligned} \quad (6.39)$$

Then integrating over the control volume, each one of the first order derivatives is expressed as

$$\begin{aligned}
 \int_{V_P} \frac{\partial}{\partial \xi_1} (Cu_i \beta^{li}) dV_P &= (Cu_i \beta^{1i} A)_e - (Cu_i \beta^{1i} A)_w \\
 \int_{V_P} \frac{\partial}{\partial \xi_2} (Cu_i \beta^{li}) dV_P &= (Cu_i \beta^{2i} A)_n - (Cu_i \beta^{2i} A)_s \\
 \int_{V_P} \frac{\partial}{\partial \xi_3} (Cu_i \beta^{li}) dV_P &= (Cu_i \beta^{3i} A)_t - (Cu_i \beta^{3i} A)_b
 \end{aligned} \tag{6.40}$$

resulting to the total contribution of the convective terms:

$$I^C = (Cu_i b^{1i})_w^e + (Cu_i b^{2i})_s^n + (Cu_i b^{3i})_b^t = \sum_{f=1}^6 \left(\sum_i \hat{C}_{fu_i} b^{li} \right) \tag{6.41}$$

where as discussed in [Section 3.3.2](#), the convected variable \hat{C}_f indicates that a different approach is employed for evaluating the convective variable at the cell face. The evaluation of the convective terms is done in the same way as presented in [Section 3.3.3](#).

- **Diffusion term**

The diffusion term of the generalised Cahn-Hilliard [Eq. \(6.31\)](#) is

$$I^D = \int_{V_P} \frac{\partial}{\partial \xi^l} (q_i \beta^{li}) dV_P \tag{6.42}$$

Expanding the diffusion term inside the integral to its components:

$$\begin{aligned}
 \frac{\partial}{\partial \xi^l} (q_i \beta^{li}) &= \frac{\partial}{\partial \xi^1} (q_1 \beta^{11} + q_2 \beta^{12} + q_3 \beta^{13}) + \frac{\partial}{\partial \xi^2} (q_1 \beta^{21} + q_2 \beta^{22} + q_3 \beta^{23}) \\
 &\quad + \frac{\partial}{\partial \xi^3} (q_1 \beta^{31} + q_2 \beta^{32} + q_3 \beta^{33})
 \end{aligned} \tag{6.43}$$

Then by integrating the expanded differential equation for the diffusion terms over a control volume, the diffusion component of [Eq. \(6.36\)](#) will be

$$\begin{aligned}
 I^D &= \left[(q_1 \beta^{11} + q_2 \beta^{12} + q_3 \beta^{13}) A \right]_w^e + \left[(q_1 \beta^{21} + q_2 \beta^{22} + q_3 \beta^{23}) A \right]_s^n \\
 &\quad + \left[(q_1 \beta^{31} + q_2 \beta^{32} + q_3 \beta^{33}) A \right]_b^t
 \end{aligned} \tag{6.44}$$

Following the notation of Oliveira *et al.* [27] and similarly to the form of the discretised equations in Section 3.3.2, the diffusion term of the Cahn-Hilliard equation is treated as a source term and is expressed in a generalised discretised form as

$$\int_{V_P} \frac{\partial}{\partial \xi^l} (q_i \beta^{li}) dV_P = \sum_{f=1}^6 b_f^{fi} q_i = S_{C\text{-diffusion}} \quad (6.45)$$

For the reasons discussed previously only the integrals on east (I_e^D), north (I_n^D) and top (I_t^D) faces need to be calculated numerically and their evaluation is described below. The integral on the east face is expressed as

$$I_e^D = (q_1 b^{11})_e + (q_2 b^{12})_e + (q_3 b^{13})_e \quad (6.46)$$

with each one of the components q_1 , q_2 and q_3 given in Eq. (6.30) need to be evaluated on the east surface. As mentioned previously, for all three components, q_l , the first-order derivatives of ϕ are the same and therefore need to be evaluated only once, and then multiplied by the appropriate cofactor b^{li} . Considering initially the derivative in the direction normal to the surface, the use of central differencing scheme will give (cf. Fig. 6.4)

$$\left(\frac{\partial \phi}{\partial \xi^1} \right)_e = \frac{\phi_E - \phi_P}{\delta \xi_e^1} \quad (6.47)$$

where the quantities ϕ_P and ϕ_E required are taken directly from the stored values on the cell centre (P) and its east neighbour (E) with $\delta \xi_e^1$ corresponding to the grid spacing along the direction ξ^1 . On the other hand, the evaluation of the cross-diffusion components $\partial \phi / \partial \xi^2$ and $\partial \phi / \partial \xi^3$ of Eq. (6.30) on the east face, is not as straight-forward as in the case of the normal derivatives. They are approximated on the east surface as

$$\left(\frac{\partial \phi}{\partial \xi^2} \right)_e = \left(\frac{\phi_n - \phi_s}{\delta \xi_e^2} \right)_e = \frac{\phi_{ne} - \phi_{se}}{\delta \xi_e^2} \quad (6.48)$$

and

$$\left(\frac{\partial \phi}{\partial \xi^3} \right)_e = \left(\frac{\phi_t - \phi_b}{\delta \xi_e^3} \right)_e = \frac{\phi_{te} - \phi_{be}}{\delta \xi_e^3} \quad (6.49)$$

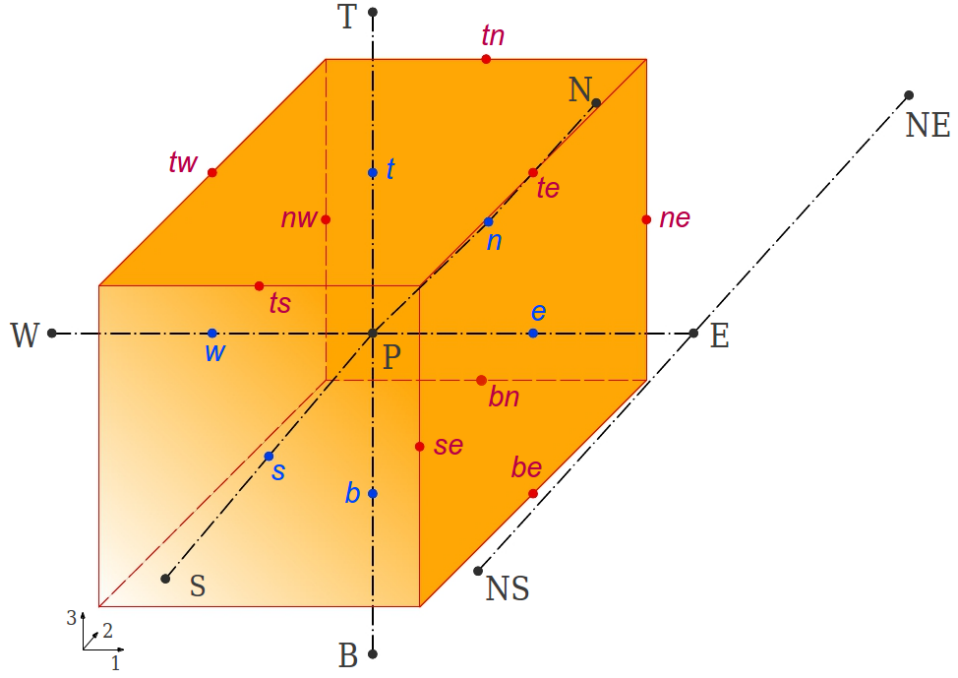


Figure 6.4. Three dimensional representation of a control volume. Cell centres are indicated by *black-dots*, cell faces by *blue-dots* and edge centres by *red-dots*

where the values ϕ_{ne} , ϕ_{se} , ϕ_{te} and ϕ_{be} , located at the centres of each edge (cf. *red-dots* on the edges in Fig. 6.4) are unknown and they will be approximated using interpolation between known neighbouring values. Using Eqs. (6.47) to (6.49) inside Eq. (6.30) all three components of the diffusive flow rate needed for the evaluation of the diffusion component of the total east-face integral Eq. (6.34), are discretised as

$$\begin{aligned}
 q_{1,e} &= \left(\frac{M}{\delta V} \right)_e \left[(\phi_E - \phi_P) b_e^{11} + (\phi_{ne} - \phi_{se}) b_e^{21} + (\phi_{te} - \phi_{be}) b_e^{31} \right] \\
 q_{2,e} &= \left(\frac{M}{\delta V} \right)_e \left[(\phi_E - \phi_P) b_e^{12} + (\phi_{ne} - \phi_{se}) b_e^{22} + (\phi_{te} - \phi_{be}) b_e^{32} \right] \\
 q_{3,e} &= \left(\frac{M}{\delta V} \right)_e \left[(\phi_E - \phi_P) b_e^{13} + (\phi_{ne} - \phi_{se}) b_e^{23} + (\phi_{te} - \phi_{be}) b_e^{33} \right]
 \end{aligned} \tag{6.50}$$

where δV_e , is a pseudo differential volume² at the face of the cell [27, 59].

²The relationship results from the product of the Jacobian and the grid spacings along each direction:

$$J \delta \xi^1 \delta \xi^2 \delta \xi^3 = \delta V$$

Starting from the evaluation of the cross-diffusion term along the second direction, $\partial\phi/\partial\xi^2$, the numerator of Eq. (6.48) can be evaluated using linear interpolation between the two neighbouring computational cells along direction-1 (cf. Fig. 6.4):

$$(\phi_n - \phi_s)_e = (\phi_n - \phi_s)_P(1 - F_{X,P}) + (\phi_n - \phi_s)_E F_{X,P} \quad (6.51)$$

where F_X is the appropriate interpolation factor related to grid spacing³. Clearly the value of ϕ , needs to be evaluated on the north and south sides of cell P and its east neighbour, cell E. By performing again linear interpolation between the P-cell and the one that shares the side under consideration (N or S), the values of the chemical potential are evaluated as

$$\begin{aligned} (\phi_n)_P &= \phi_N F_{Y,P} + \phi_P(1 - F_{Y,P}) \\ (\phi_s)_P &= \phi_P F_{Y,S} + \phi_S(1 - F_{Y,S}) \end{aligned} \quad (6.52)$$

and similarly for the E-cell (using the value stored in NE and SE cells)

$$\begin{aligned} (\phi_n)_E &= \phi_{NE} F_{Y,E} + \phi_E(1 - F_{Y,E}) \\ (\phi_s)_E &= \phi_E F_{Y,SE} + \phi_{SE}(1 - F_{Y,SE}) \end{aligned} \quad (6.53)$$

Substituting Eqs. (6.52) and (6.53) inside Eq. (6.51) the final discretised form of the the cross-diffusion term along the second direction ξ_2 is

$$\begin{aligned} (\phi_n - \phi_s)_e &= \left[\phi_P(1 - F_{Y,P} - F_{Y,S}) + \phi_N F_{Y,P} - \phi_S(1 - F_{Y,S}) \right] (1 - F_{X,P}) + \\ &\quad \left[\phi_E(1 - F_{Y,E} - F_{Y,SE}) + \phi_{NE} F_{Y,E} - \phi_{SE}(1 - F_{Y,SE}) \right] F_{X,P} \end{aligned} \quad (6.54)$$

³The interpolation factors for each direction are:

$$F_{X,P} = \frac{Pe}{Pe + eE} \quad ; \quad F_{Y,P} = \frac{Pn}{Pn + nN} \quad ; \quad F_{Z,P} = \frac{Pt}{Pt + tT}$$

For the evaluation of the cross-diffusion term along the third direction, $\partial\phi/\partial\xi^3$, the same procedure is followed with the numerator of Eq. (6.49) evaluated as

$$(\phi_t - \phi_b)_e = (\phi_t - \phi_b)_P(1 - F_{X,P}) + (\phi_t - \phi_b)_E F_{X,P} \quad (6.55)$$

Where now the value of ϕ needs to be evaluated on the top and bottom sides of P and its east neighbour, E. For the P-cell, they are evaluated as

$$\begin{aligned} (\phi_t)_P &= \phi_T F_{Z,P} + \phi_P(1 - F_{Z,P}) \\ (\phi_b)_P &= \phi_P F_{Z,B} + \phi_B(1 - F_{Z,B}) \end{aligned} \quad (6.56)$$

and in the same manner for the E-cell as

$$\begin{aligned} (\phi_t)_E &= \phi_{TE} F_{Z,E} + \phi_E(1 - F_{Z,E}) \\ (\phi_b)_E &= \phi_E F_{Z,BE} + \phi_{BE}(1 - F_{Z,BE}) \end{aligned} \quad (6.57)$$

Substituting Eqs. (6.56) and (6.57) inside Eq. (6.55) the final discretised form of the the cross-diffusion term along the third direction ξ_3 is defined as

$$\begin{aligned} (\phi_t - \phi_b)_e &= \left[\phi_P(1 - F_{Z,P} - F_{Z,B}) + \phi_T F_{Z,P} - \phi_B(1 - F_{Z,B}) \right] (1 - F_{X,P}) + \\ &\quad \left[\phi_E(1 - F_{Z,E} - F_{Z,BE}) + \phi_{TE} F_{Z,E} - \phi_{BE}(1 - F_{Z,BE}) \right] F_{X,P} \end{aligned} \quad (6.58)$$

Substituting the discretised Eqs. (6.54) and (6.58) for the cross-diffusion terms inside Eq. (6.50), all three components are now consisted by known values of the chemical potential ϕ and the diffusive flow rate components on the east side are able to calculated numerically.

The same procedure should be followed for having the discretised expressions for the diffusion integrals on the north (n) and top (t) faces, resulting in equivalent relationships. For completeness, only the important relationships are given below. Starting from the n -face integral:

$$I_n^D = (q_1 b^{21})_n + (q_2 b^{22})_n + (q_3 b^{23})_n \quad (6.59)$$

where the first order derivatives are expressed as

$$\left(\frac{\partial\phi}{\partial\xi^1}\right)_n = \left(\frac{\phi_e - \phi_w}{\delta\xi^1}\right)_n ; \left(\frac{\partial\phi}{\partial\xi^2}\right)_n = \frac{\phi_N - \phi_P}{\delta\xi_n^2} ; \left(\frac{\partial\phi}{\partial\xi^3}\right)_n = \left(\frac{\phi_t - \phi_b}{\delta\xi^3}\right)_n \quad (6.60)$$

with each component of the diffusion flow rate expressed as

$$\begin{aligned} q_{1,n} &= \left(\frac{M}{\delta V}\right)_n \left[(\phi_{ne} - \phi_{nw})b_n^{11} + (\phi_N - \phi_P)b_n^{21} + (\phi_{tn} - \phi_{bn})b_n^{31} \right] \\ q_{2,n} &= \left(\frac{M}{\delta V}\right)_n \left[(\phi_{ne} - \phi_{nw})b_n^{12} + (\phi_N - \phi_P)b_n^{22} + (\phi_{tn} - \phi_{bn})b_n^{32} \right] \\ q_{3,n} &= \left(\frac{M}{\delta V}\right)_n \left[(\phi_{ne} - \phi_{nw})b_n^{13} + (\phi_N - \phi_P)b_n^{23} + (\phi_{tn} - \phi_{bn})b_n^{33} \right] \end{aligned} \quad (6.61)$$

where the cross-derivatives are discretised as

$$\begin{aligned} (\phi_e - \phi_w)_n &= \left[\phi_P(1 - F_{X,P} - F_{X,W}) + \phi_E F_{X,P} - \phi_W(1 - F_{X,W}) \right] (1 - F_{Y,P}) + \\ &\quad \left[\phi_N(1 - F_{X,N} - F_{X,NW}) + \phi_{NE} F_{X,N} - \phi_{NW}(1 - F_{X,NW}) \right] F_{Y,P} \end{aligned} \quad (6.62)$$

$$\begin{aligned} (\phi_t - \phi_b)_n &= \left[\phi_P(1 - F_{Z,P} - F_{Z,B}) + \phi_T F_{Z,P} - \phi_B(1 - F_{Z,B}) \right] (1 - F_{Y,P}) + \\ &\quad \left[\phi_N(1 - F_{Z,N} - F_{Z,BN}) + \phi_{TN} F_{Z,N} - \phi_{BN}(1 - F_{Z,BN}) \right] F_{Y,P} \end{aligned} \quad (6.63)$$

Similarly for the t-face integral:

$$I_t^D = (q_1 b^{31})_t + (q_2 b^{32})_t + (q_3 b^{33})_t \quad (6.64)$$

the first order derivatives are expressed as

$$\left(\frac{\partial\phi}{\partial\xi^1}\right)_t = \left(\frac{\phi_e - \phi_w}{\delta\xi^1}\right)_t ; \left(\frac{\partial\phi}{\partial\xi^2}\right)_t = \left(\frac{\phi_n - \phi_s}{\delta\xi^2}\right)_t ; \left(\frac{\partial\phi}{\partial\xi^3}\right)_t = \frac{\phi_T - \phi_P}{\delta\xi_t^3} \quad (6.65)$$

with the discretised terms:

$$\begin{aligned}
 q_{1,t} &= \left(\frac{M}{\delta V}\right)_t \left[(\phi_{te} - \phi_{tw})b_t^{11} + (\phi_{tn} - \phi_{ts})b_t^{21} + (\phi_T - \phi_P)b_t^{31} \right] \\
 q_{2,t} &= \left(\frac{M}{\delta V}\right)_t \left[(\phi_{te} - \phi_{tw})b_t^{12} + (\phi_{tn} - \phi_{ts})b_t^{22} + (\phi_T - \phi_P)b_t^{32} \right] \\
 q_{3,t} &= \left(\frac{M}{\delta V}\right)_t \left[(\phi_{te} - \phi_{tw})b_t^{13} + (\phi_{tn} - \phi_{ts})b_t^{23} + (\phi_T - \phi_P)b_t^{33} \right]
 \end{aligned} \tag{6.66}$$

and the cross-derivatives expressed as

$$\begin{aligned}
 (\phi_e - \phi_w)_t &= \left[\phi_P(1 - F_{X,P} - F_{X,W}) + \phi_E F_{X,P} - \phi_W(1 - F_{X,W}) \right] (1 - F_{Z,P}) + \\
 &\quad \left[\phi_T(1 - F_{X,T} - F_{X,TW}) + \phi_{TE} F_{X,T} - \phi_{TW}(1 - F_{X,TW}) \right] F_{Z,P}
 \end{aligned} \tag{6.67}$$

$$\begin{aligned}
 (\phi_n - \phi_s)_t &= \left[\phi_P(1 - F_{Y,P} - F_{Y,S}) + \phi_N F_{Y,P} - \phi_S(1 - F_{Y,S}) \right] (1 - F_{Z,P}) + \\
 &\quad \left[\phi_T(1 - F_{Y,T} - F_{Y,TS}) + \phi_{TN} F_{Y,T} - \phi_{TS}(1 - F_{Y,TS}) \right] F_{Z,P}
 \end{aligned} \tag{6.68}$$

The linear interpolations performed assist in discretising Eq. (6.44) and additionally express all unknown terms of the cross-derivatives to already evaluated values of the cell centres. The interpolations between the two nearest computational cells results in a scheme that is second order accurate [59, 60].

A general diffusive flow rate (Eq. (6.21)) was considered in order to overcome the inherent difficulty of the Cahn-Hilliard equation to treat numerically the fourth order derivatives of the concentration. For completing this section, the discretisation of the Laplacian term of the concentration in Eq. (6.20) is addressed. The values of the chemical potential are evaluated on each cell-centre P:

$$\phi_P = \left(\varepsilon^{-1} \sigma \alpha [C^3 - 1.5C^2 + 0.5C] - \varepsilon \sigma \alpha \nabla^2 C \right)_P \tag{6.69}$$

The concentration is straight-forward to calculate using the stored values on each control volume centre, C_P . On the contrary the Laplacian term is calculated based on a

second order approximation ⁴ using neighbouring nodal values:

$$\left(\nabla^2 C\right)_P = \left(\frac{\partial^2 C}{\partial x_i^2}\right)_P = \frac{C_E + C_W + C_N + C_S + C_T + C_B - 6C_P}{\Delta h^2} \quad (6.70)$$

where Δh , is the grid size of the uniform mesh along all three directions. By contrast to the previous analysis, the Laplacian term is discretised considering a Cartesian coordinate system. This choice is not affecting the results of the test cases performed in order to validate the two-phase solver implementation. The reason is due to the fact that all numerical tests performed in [Section 6.4](#) are based on orthogonal meshes, and thus the generalised coordinate system will reproduce the Cartesian system. However, for studies that consider more complex geometries (cf. [Chapter 5](#)) the second order derivatives at each direction should be expressed in generalised coordinates so as to be applicable for non-orthogonal meshes. For doing this, 27 terms that represent the Laplacian in the generalised coordinate system need to be discretised [\[253\]](#).

Arranging all discretised terms together, and similarly to the approach described in [Chapter 3](#), the linear algebraic system solved numerically is:

$$a_P C_P - \sum_F a_F C_F = S_{u_i} + \frac{V_P}{\Delta t} C_P^{n-1} \quad (6.71)$$

As discussed in [Section 3.3.6](#), once the velocity field is corrected based on the SIMPLEC algorithm procedure then the transport of any other property is evaluated. Therefore, the discretised Cahn-Hilliard equation is solved directly after the correction of pressures and velocities. Similarly to the momentum algebraic equations, the matrices of [Eq. \(6.71\)](#) are pre-conditioned by an incomplete LU decomposition and solved with the bi-conjugate gradient method.

⁴As an example, for the x_1 -direction:

$$\left(\frac{\partial^2 C}{\partial x_1^2}\right)_P = \frac{\left(\frac{\partial C}{\partial x_1}\right)_e - \left(\frac{\partial C}{\partial x_1}\right)_w}{\Delta x_1} = \frac{C_E + C_W - 2C_P}{\Delta x_1^2}$$

6.3.2 The force term

In continuum surface modelling, the surface tension is usually evaluated by a product of an interface gradient and the surface curvature [254]. For all approaches of this kind, the effects of the surface force are taken into account by considering a form of a volume force, \mathbf{f}_{st} , which is added in the momentum equation (cf. Eq. (6.13)). For the PF method, various different approaches have been proposed for evaluating the effects of the surface forces [58, 227, 241, 244]. Here, the product of the chemical potential, ϕ , and the gradient of the concentration, C , is used (given by Eq. (6.14)).

Following the same concepts as in Section 6.3.1, the expression of the surface tension force is transformed in generalised coordinates as

$$\mathbf{f}_{st} = \phi \frac{\partial C}{\partial x_i} = \phi \frac{1}{J} \frac{\partial C}{\partial \xi_l} \beta^{li} \quad (6.72)$$

Each of the force term components acting along each one of the three directions will be added as a source term in the appropriate component of the momentum equation, in a similar fashion as the pressure gradients were treated. Moreover, the Jacobian appearing in Eq. (6.72) is dropped out, since it is cancelled out from the remaining terms in the generalised momentum equation and is only evaluated together with the gravity terms. Hence, the contribution of the surface tension force along direction $i = 1$ corresponding to the u -component of the momentum equation, is written:

$$\phi \frac{\partial C}{\partial \xi_l} \beta^{l1} = \phi \left[\frac{\partial C}{\partial \xi_1} \beta^{11} + \frac{\partial C}{\partial \xi_2} \beta^{21} + \frac{\partial C}{\partial \xi_3} \beta^{31} \right] \quad (6.73)$$

After integrating over the finite control volume P , the discretised form of Eq. (6.73) is:

$$\int_{V_P} \phi \frac{\partial C}{\partial \xi_l} \beta^{l1} dV_P = \phi_P \left[(C_e - C_w) b_P^{11} + (C_n - C_s) b_P^{21} + (C_t - C_b) b_P^{31} \right] \quad (6.74)$$

The concentration values on each face of the control volume, e , w , n , s , t and b , are estimated by the same interpolation practice mentioned before, using the known values

of the cell centres. For example on the west and east faces it reads:

$$\begin{aligned} C_e &= F_{X,P}C_E + (1 - F_{X,P})C_P \\ C_w &= F_{X,W}C_P + (1 - F_{X,W})C_W \end{aligned} \quad (6.75)$$

Similarly, the discretised components of the surface force which act along the remaining two directions, added to the v -momentum ($i = 2$) and w -momentum ($i = 3$) sources respectively, are presented below for completeness:

$$\int_{V_P} \phi \frac{\partial C}{\partial \xi_l} \beta^{l2} dV_P = \phi_P \left[(C_e - C_w)b_P^{12} + (C_n - C_s)b_P^{22} + (C_t - C_b)b_P^{32} \right] \quad (6.76)$$

$$\int_{V_P} \phi \frac{\partial C}{\partial \xi_l} \beta^{l3} dV_P = \phi_P \left[(C_e - C_w)b_P^{13} + (C_n - C_s)b_P^{23} + (C_t - C_b)b_P^{33} \right] \quad (6.77)$$

Hence, it is clear that the values of the chemical potential are known, and for all three directions the evaluation is done on the cell centres P. Following the notation of Oliveira *et al.* [27] and similarly to the form of the discretised equations in Section 3.3.2, the discretised term related to the surface forces is added in the momentum sources and expressed in a generalised form as

$$\int_{V_P} \phi \frac{\partial C}{\partial \xi_l} \beta^{li} dV_P = \sum_{l=1}^3 \phi_P b^{li} [\Delta C]_l^P = S_{u_i-st} \quad (6.78)$$

Moreover the total sources in the momentum equation presented in Section 3.3.2 (see Eq. (3.32)) are updated as

$$S_{u_i} = S_{u_i-pressure} + S_{u_i-stress} + S_{u_i-gravity} + S_{u_i-st} + S_{u_i-diffusion} \quad (6.79)$$

6.3.3 The boundary conditions

The numerical implementation of the Cahn-Hilliard equation is concluded with the implementation of the boundary conditions. The boundaries are considered as numerical cells with zero width and thus, the boundary faces of each boundary cell should be addressed with the appropriate boundary values for each variable. As mentioned in

Section 6.2.2, the wall boundary conditions considered for the Cahn-Hilliard equations are zero gradients for the concentration and the chemical potential (cf. Eqs. (6.10) and (6.11)) on the boundary normal direction. The same treatment was adopted for all four different types of boundaries (inlet, outlet, wall and symmetry). Following that, it suffices to declare explicitly that the face centre has the same value as the boundary cell centre:

$$\begin{aligned}C_f &= C_{P,bnd} \\ \phi_f &= \phi_{P,bnd}\end{aligned}\tag{6.80}$$

where f indicates the boundary face centre along the appropriate direction (e, w, n, s, t or b). Having said that, the evaluation of the concentration gradients at the boundaries, resulting from the surface force as discussed in the previous section, are explicitly taken as being equal to zero, obeying directly Eq. (6.80).

Concluding, since for all the following validation cases the mobility was considered as a function of the concentration ($M = M_c[C(1 - C)]$, $\gamma = 1$), the same practice was followed, with the boundary face having the same value as the boundary cell centre.

6.4 Validation

In this section, the implementation of the Cahn-Hilliard equation for considering two-phase flows is validated. Two main categories of test cases are considered. In Section 6.4.1 the implementation for cases with zero surface tension is examined, where the convective terms are solely investigated. Then, in Section 6.4.2 the effects of the surface tension are included and the complete discretisation is examined. It should be noted that although the discretisation is accomplished for three dimensions (3D), all subsequent validation cases performed consider a two-dimensional (2D) system.

6.4.1 Test-cases with non-active surface tension

In this section, the implementation and the accuracy of the discretisation schemes for the convective terms is examined when the surface tension coefficient is set to zero ($\sigma = 0$). For this case, the chemical potential turns to zero everywhere (cf. Eq. (6.20))

and thus, only the term for the advection of the concentration remains in Eq. (6.9) (or in Eq. (6.28) for the generalised coordinate system). Moreover, the values of the characteristic mobility, M_c , and the interface thickness ϵ , have no impact in the calculations since there is no diffusion term. Physically, a value of zero surface tension means that effectively the fluids of interest are the same.

i) **Stretching Element**

The validation of the two-phase solver begins with the investigation of the accuracy of the discretisation schemes used for the convective terms of the CH equation. The numerical schemes considered and tested are the third order accurate schemes discussed in Section 3.3.3, the QUICK by Leonard [87], the SMART by Gaskell and Lau [92] and CUBISTA by Alves *et al.* [93]. Their performance is investigated considering the test-case of the stretching element [55]. This test-case is very well known in validations of two-phase solvers and has been used in various studies [241, 255–258]

A circular element placed inside a square domain, is deformed by a velocity field defined by the stream function:

$$\Psi = \frac{1}{\pi} \sin^2(\pi x) \sin^2(\pi y) \cos(\pi t/T_f) \quad (6.81)$$

where T_f corresponds to the total time of the numerical experiment. The velocity field generated by the stream function will initially stretch the circular element at $t = 0$ s, while the Leveque temporal cosine term $\cos(\pi t/T_f)$ [259] will progressively decrease its intensity until the velocity field is completely reversed, and the element is forced back to its initial position. The velocity vector is related to the stream function by

$$\mathbf{u}(u, v) = \left(-\frac{\partial \Psi}{\partial y}, \frac{\partial \Psi}{\partial x} \right) \quad (6.82)$$

and thus, the velocities along each direction x, y , are given by

$$\begin{aligned} u &= -2 \sin^2(\pi x) \sin(\pi y) \cos(\pi y) \cos(\pi t/T_f) \\ v &= 2 \sin^2(\pi y) \sin(\pi x) \cos(\pi x) \cos(\pi t/T_f) \end{aligned} \quad (6.83)$$

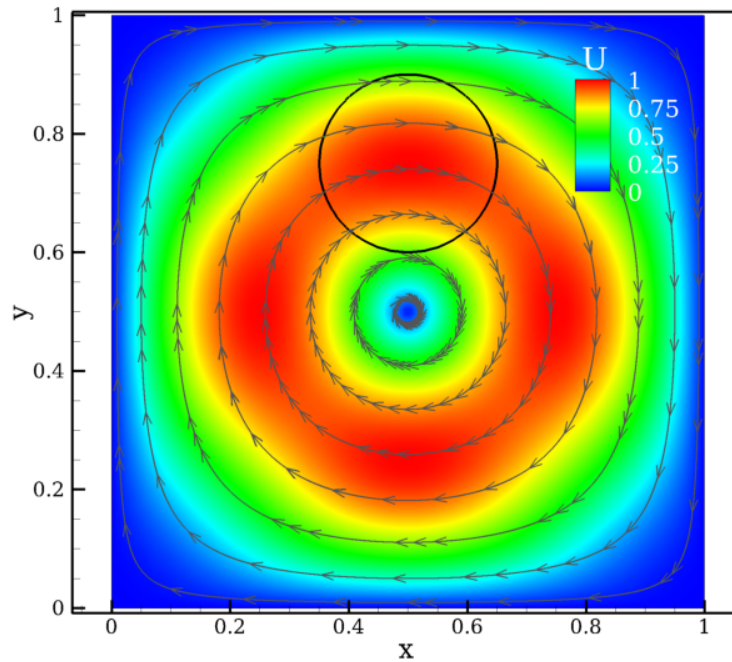


Figure 6.5. Domain initialisation for the stretching element case. The contour corresponds to the magnitude of velocity from Eq. (6.83) and the black circle indicates the drop interface based on the 0.5-contour at $t = 0$ s.

At $t = 0$ s, the centre of the circular drop with a radius $R = 0.15$ m, is positioned at $(x_0, y_0) = (0.5, 0.75)$, as shown in Fig. 6.5 together with the magnitude of the velocity field calculated from Eq. (6.83). The total time of the simulation is $T_f = 4$ s. For this study, three uniform numerical meshes are employed M128, M256 and M512 (cf. Table 6.1), with the interface always resolved by five computational cells ($k = 5$). The time steps used are fixed: $\Delta t = 5.0 \times 10^{-4}$ s for the M128, $\Delta t = 2.5 \times 10^{-4}$ s for the M256 and $\Delta t = 1.25 \times 10^{-4}$ s for the M512.

In Fig. 6.6, the results computed with the numerical mesh M128 and the SMART scheme are examined for various times. The contours correspond to the u -velocity and the circle is produced by the 0.5-contour of the concentration, indicating the interface location. When $0 \text{ s} \leq t \leq T_f/2$, the velocity field is stretching the circular body and transforms it into a thin filament, forcing it to move spirally to the middle of the domain. At the same time, the intensity of the field decreases because of the temporal cosine in Eq. (6.83), reaching a zero-velocity field at $t = T_f/2 = 2$ s. Then, for $T_f/2 \leq t \leq T_f$, the velocity field is reversed with its intensity progressively increasing,

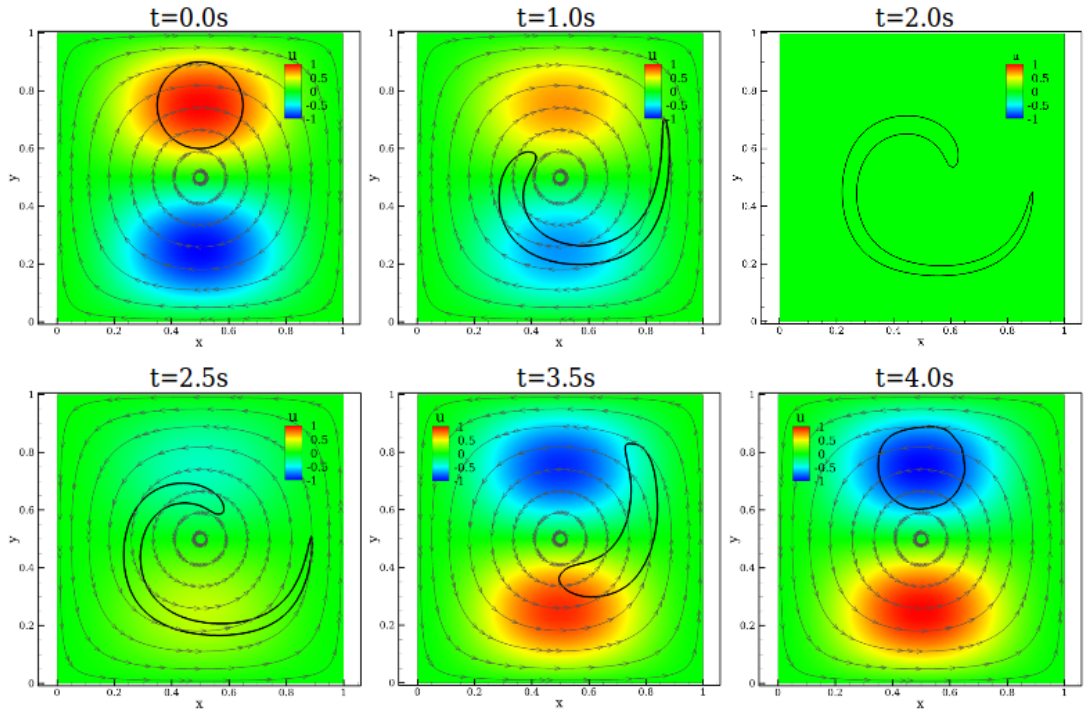


Figure 6.6. Stretching of the 0.5-contour of the circular element in time for the M128 mesh, using the SMART scheme for convection. The contours correspond to u -velocity calculated from Eq. (6.83).

while the thin filament is expected to shrink back to its initial circular form. At the final position $T_f = 4$ s, the shape differences compared to its initial form are evaluated and the numerical scheme for the advection terms which presents the best performance, managing to recover the initial shape, is chosen as the most appropriate to be used.

Figure 6.7 illustrates the performance of each numerical scheme for every mesh used, comparing their behaviour at two different times: $t = 2$ s, corresponding to the deformation of the element into a filament at half-time (Figs. 6.7a, 6.7c and 6.7e); and at the final time at $t = 4$ s, when the body has shrank back to its initial location (Figs. 6.7b, 6.7d and 6.7f). It can be seen that as expected, all schemes increase their accuracy as the mesh size is increased. More specifically, the “tail” of the filament is better resolved at $t = 2$ s, when the finer grid is used for all schemes. On the other hand, when the coarser mesh is used it can be seen that SMART (Fig. 6.7a) and QUICK (Fig. 6.7e) resolve better the tail compared to CUBISTA. All schemes perform similarly when the intermediate mesh is considered, M256, and almost identical for the

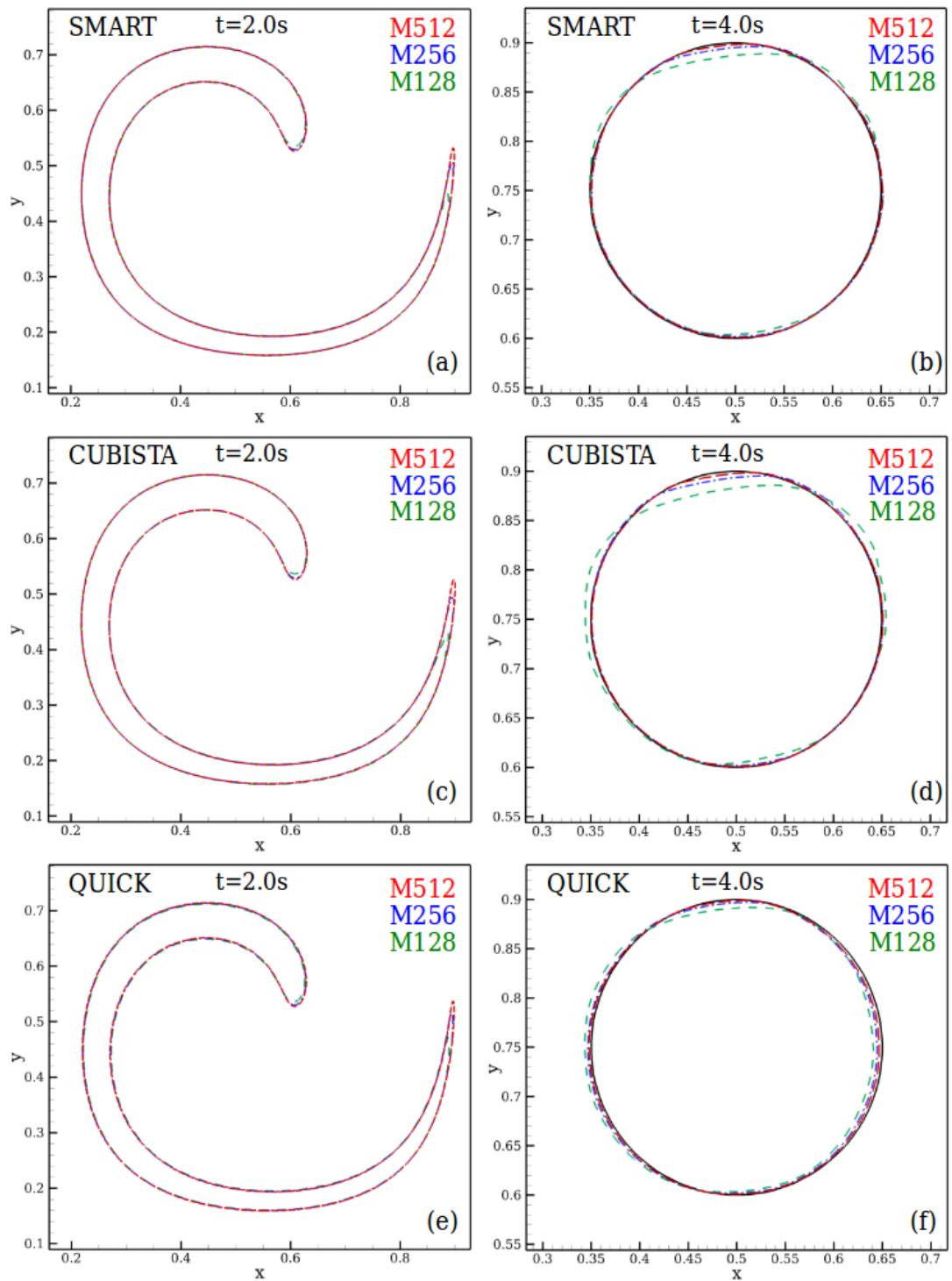


Figure 6.7. Performance of all the convective schemes for all numerical meshes at times $t = 2$ s and $t = 4$ s.

most refined, M512, as it can be seen in Fig. 6.8a.

To quantify the deviation between the actual final shape (at $t = 4$ s) of the element and the initial area it should recover, the areas enclosed by the 0.5-contour are determined at $t = 0$ s (S_0) and at $t = 4$ s (S_{T_f}) and evaluate the deviation, E_s , as

$$E_S = \frac{|S_{T_f} - S_0|}{S_0} \quad (6.84)$$

The deviation is reported in Table 6.1 for the various schemes and mesh used. It can be seen that for the coarser mesh, CUBISTA performs well in terms of preserving the area inside the 0.5-contour, however the final shape shown in Fig. 6.7d is much more distorted than for the SMART (Fig. 6.7b) and QUICK schemes (Fig. 6.7f). Furthermore, comparing the results obtained with SMART and CUBISTA, Fig. 6.8b, compares the final shape for all schemes for the most refined mesh M512. Although the differences

Table 6.1. Performance of all numerical schemes for each computational mesh considered, for the stretching test of a circular element with $R = 0.15$ m.

Mesh	Cn	h/ϵ	E_S^{SMART}	E_S^{CUBISTA}	E_S^{QUICK}	Cells
M128	0.031	0.60	1.66%	0.46%	1.84%	16,384
M256	0.016	0.60	0.54%	0.63%	1.03%	65,536
M512	0.008	0.60	0.35%	0.42%	0.66%	262,144

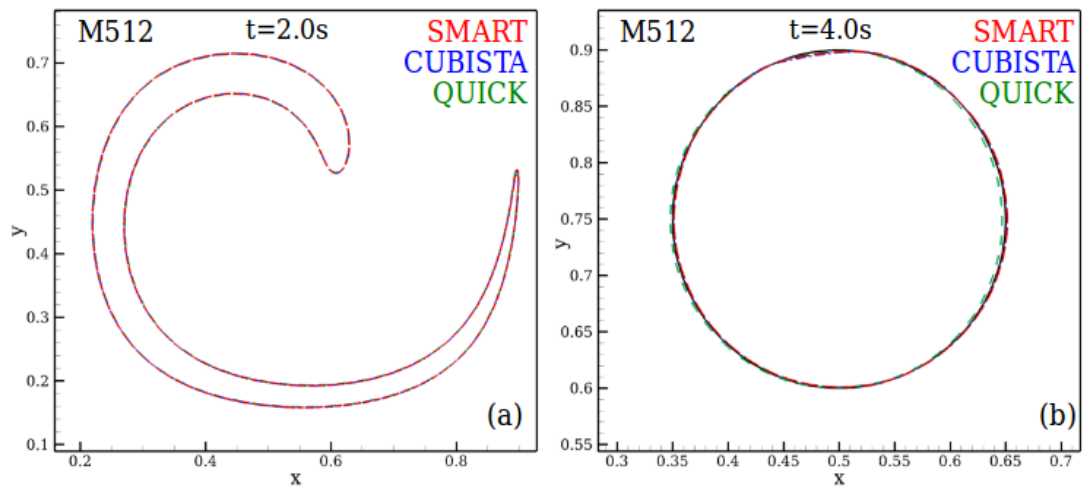


Figure 6.8. Performance of all the convective schemes for the most refined grid, M512, at times $t = 2$ s and $t = 4$ s.

are not noticeable and it can be seen that the results obtained with QUICK present the largest deviations in terms of shape after reversal. It was expected that both SMART and CUBISTA would perform better than QUICK, since both schemes are upgraded versions of QUICK and take advantage of its good performance [61], omitting some of its downsides. For the intermediate and the more refined meshes, the SMART scheme exhibits the best overall behaviour. This is explained by its less diffusive and more compressive nature compared to CUBISTA and therefore its enhanced ability to approximate sharp fronts, by better preserving its inherent third accuracy [93].

Based on these results, the SMART scheme was chosen for evaluating the convective

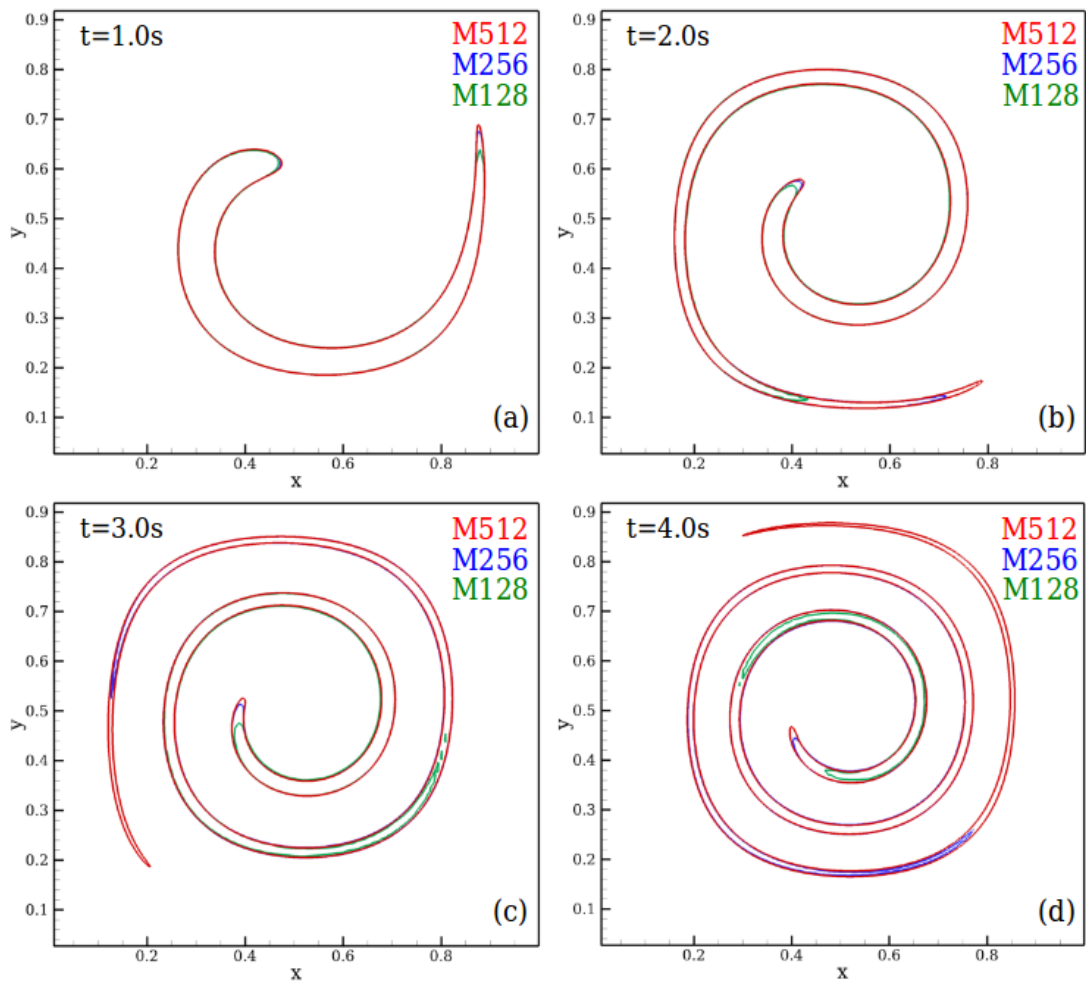


Figure 6.9. Stretching of the circular element without reversing the velocity field by removing the cosine term from Eqs. (6.81) and (6.83) for all grids using the SMART scheme at times $t = 1$ s, $t = 2$ s, $t = 3$ s and $t = 4$ s.

terms in all following test-cases used, for the validation of the two-phase implementation. However, when it comes to numerical studies of viscoelastic fluids, Alves *et al.* [93] showed that CUBISTA is more robust and exhibits faster convergence rates for higher grid accuracy than the SMART scheme. Therefore, since this numerical implementation is intended for possible use in studies of two-phase systems that also consider viscoelastic elements, the performance of the numerical schemes for treating the convective terms, is recommended to be re-evaluated.

Finally, using the SMART scheme the stretching test was repeated for the three numerical meshes, but this time the temporal cosine term was removed from Eqs. (6.81) and (6.83), studying therefore the problem of infinite stretching by a non-time varying velocity field. Figure 6.9, presents the results obtained at four different times, $t = 1$ s, $t = 2$ s, $t = 3$ s and $t = 4$ s for all meshes. Mesh refinement is particularly important in this case as the element becomes more stretched. Large differences are observed between the various meshes especially at the tail region, and these differences are accentuated as the experiment evolves in time and the element thins. For the coarse mesh (M128) some break-up events of the interface are observed (cf. figs 6.9c and 6.9d) near the filament's tail, due to the insufficient number of cells used to resolve the interface. When the intermediate mesh (M256) is used the differences with the most refined (M512) are clear only at the filament's tail at (cf. Fig. 6.9b,c,d).

ii) Rayleigh-Taylor instability

The existence of a perturbation along the interface between two fluids A and B , as shown in Fig. 6.10, where fluid- A is heavier than fluid- B , will result in an instability known as the Rayleigh-Taylor instability. Commonly, fluid- A lies above fluid- B and depending on the density difference between the two fluids, the instability driven by the effect of the gravitational field will evolve in different ways. The density difference for this test-case is represented by the Atwood number, $At = (\rho_A - \rho_B)/(\rho_A + \rho_B)$.

This problem has been extensively studied in two-phase flow studies [58,227,235,258,260,261], and is now established as one of the benchmarks for examining the capability of a numerical implementation to track the evolution of the interface. Additionally, the

ability of the numerical code to capture effectively the occurring instabilities, indicates its potential use for investigating more complex problems.

Tryggvason [260], investigated numerically and reported the evolution of Rayleigh-Taylor instability for inviscid, incompressible fluids with zero surface tension for $At = 0.5$ and $At \simeq 1$. Later Guermond *et al.* [261], considered a viscous and incompressible two-phase system with variable density, and found good agreement with the previous studies. Ding *et al.* [261] and Chiu *et al.* [258], performed similar investigations using PF method and they also reported good agreement.

Here, both cases of $At = 0.5$ and $At \simeq 1$ with fluids of the same viscosity are examined. More specifically this means that for the case of $At = 0.5$ the density ratio is set as $\lambda_\rho = \rho_A/\rho_B = 3$, and for $At \simeq 1$, λ_ρ was set to 300 (which is large enough to yield less than 1% error in the Atwood number). The Reynolds number is fixed at $Re = \rho_A w^{3/2} g^{1/2} / \eta = 3000$, where g is the gravitational acceleration, η , is the viscosity of the fluids ($\eta = \eta_A = \eta_B$) and w is the width of the domain. At this high value of Re , is guaranteed that viscous effects are small compared to inertial effects and therefore,

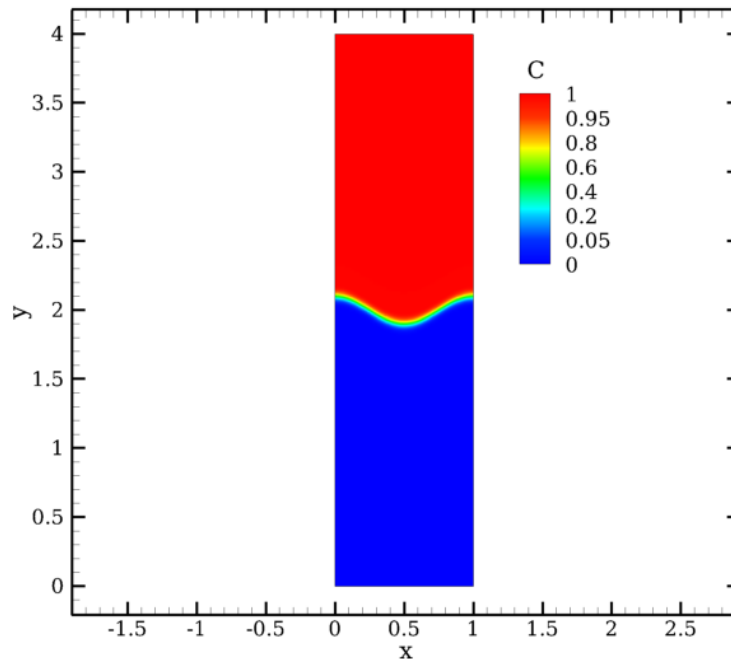


Figure 6.10. Contour-plot of the concentration for the initialisation of the Rayleigh-Taylor instability problem. The top fluid (A , red) is heavier than the bottom fluid (B , blue).

the comparison with the results of the inviscid case of Tryggvason [260] is possible, similarly to what was done in Guermond *et al.* [261] and Ding *et al.* [58]. As shown in Fig. 6.10 the domain is rectangular with the height (h_y) equal to four times the width (w). Symmetry conditions are applied at $x = 0$ and $x = w/w = 1$, whereas wall boundaries are considered for $y = 0$ and $y = h_y/w = 4$.

At time $t = 0$ s, the initial state of the interface is described by a perturbation applied at the concentration field as

$$C(x, y, 0) = 0.5 + 0.5 \tanh\left(\frac{y - y_{int} - 0.1 \cos(2\pi x)}{2\sqrt{2}\epsilon}\right) \quad (6.85)$$

where y_{int} would be the desired position for the 0.5-contour if there was no perturbation, and here is set as $y_{int} = 2$. The interface thickness, ϵ , is resolved using five computational cells ($k = 5$) and is evaluated from the expression $\epsilon = hk/(4\sqrt{2} \tanh^{-1}(0.9))$, where h is the grid spacing.

All previous studies on the problem of Rayleigh-Taylor instability, report their results using a dimensionless time $\tilde{t} = t\sqrt{Atg/w}$. In order to compare the results from the simulations performed here with these studies, the same time scale is adopted. Fig. 6.11 displays the evolution of the Rayleigh-Taylor instability at different dimensionless times for $At = 0.5$ using the most refined mesh, M200 (cf. Table 6.2 for details). The contour patterns at each time-frame compare qualitatively well with previous studies [58, 235, 258, 261]. Initially the heavier fluid falls downwards forming a “spike” or finger and the lighter fluid rises forming bubble-like fronts. At $\tilde{t} = 1.26$, the first stage of the heavier fluid roll-up appears, evolving to two symmetric counter-rotating vortices at $\tilde{t} = 1.51$ and $\tilde{t} = 1.76$. At later times when $\tilde{t} > 1.76$, these vortices become more unstable, generating new pairs of vortices, while the front of the heavier fluid keeps moving downwards. The fact that the instabilities appearing on the left and right side of the neck of the falling fluid after $\tilde{t} = 1.51$, are symmetric, indicates the good performance of the numerical implementation. Moreover, Fig. 6.12 illustrates the evolution the interface positions of the 0.5-contour, in terms of the top y -position of the rising lighter fluid and the lower y -position of the falling heavier fluid. The results are com-

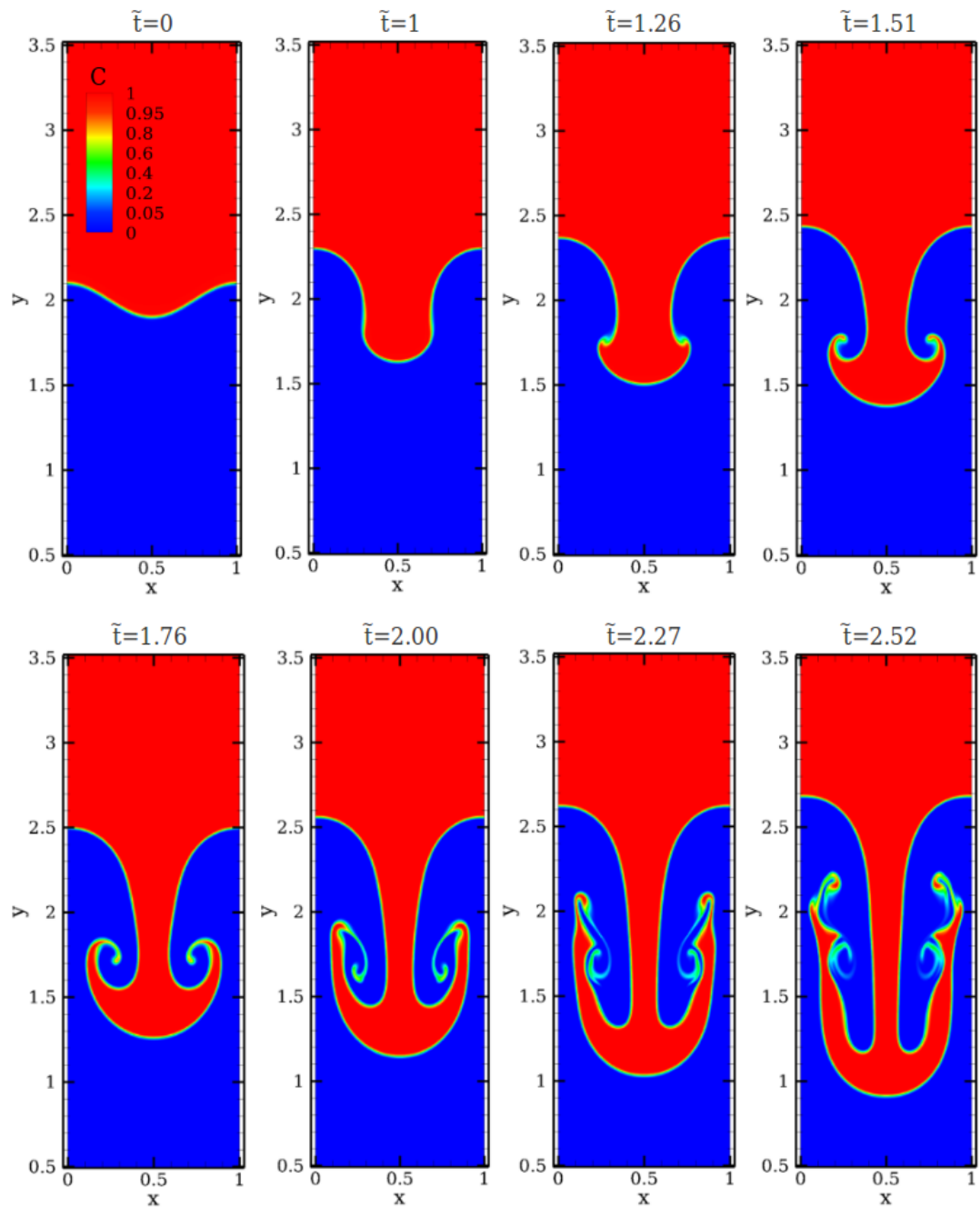


Figure 6.11. Contour-plots of the concentration at different dimensionless times for the Rayleigh-Taylor instability when $At = 0.5$ for the M200.

Table 6.2. Mesh characteristics for the Rayleigh-Taylor instability study.

Mesh	h	ϵ (m)	Cn	Cells
M064	0.0156	0.0094	0.009	16,384
M128	0.0078	0.0047	0.005	65,536
M200	0.0050	0.0030	0.003	160,000

pared with the numerical study performed by Ding *et al.* [58] and clearly a very good agreement exists between the two studies.

Three different uniform meshes have been used (details in Table 6.2) in order to examine the grid-dependency of the numerical solution with $h = \delta x/N_x = \delta y/N_y$, where N_x and N_y are the number of cells used in each direction respectively. The results for all grids are juxtaposed in Fig. 6.12 and it can be seen that the solution is mesh independent.

For larger Atwood numbers (larger density ratios), the flow patterns differ from the case of moderate numbers. Figure 6.13 presents the evolution of the pattern for the case of $At \simeq 1$, considering $\lambda_\rho = 300$, $\lambda_\eta = 1$ and $Re = 3000$. Again the three numerical meshes detailed in Table 6.2 are considered.

In contrast with the previous case of $At = 0.5$, when $At \simeq 1$, no vortices are

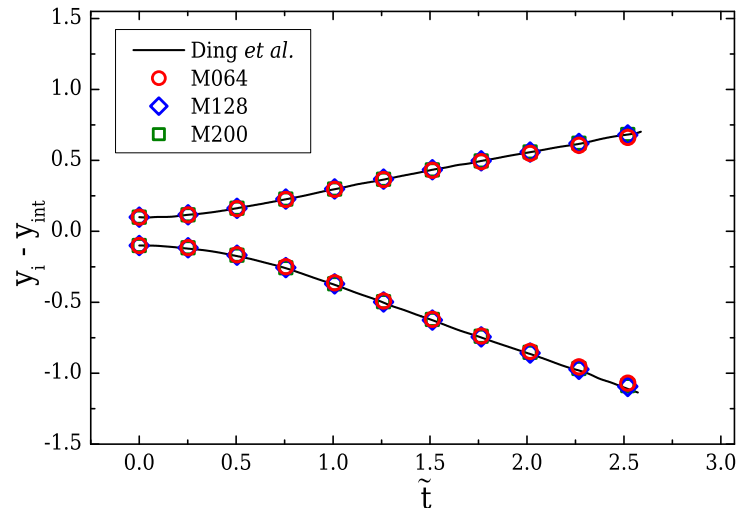


Figure 6.12. Front positions for the lighter and heavier fluids at different dimensionless times, for the Rayleigh-Taylor instability when $At = 0.5$ for all numerical meshes considered (cf. Table 6.2), compared with the solution from Ding *et al.* [58].

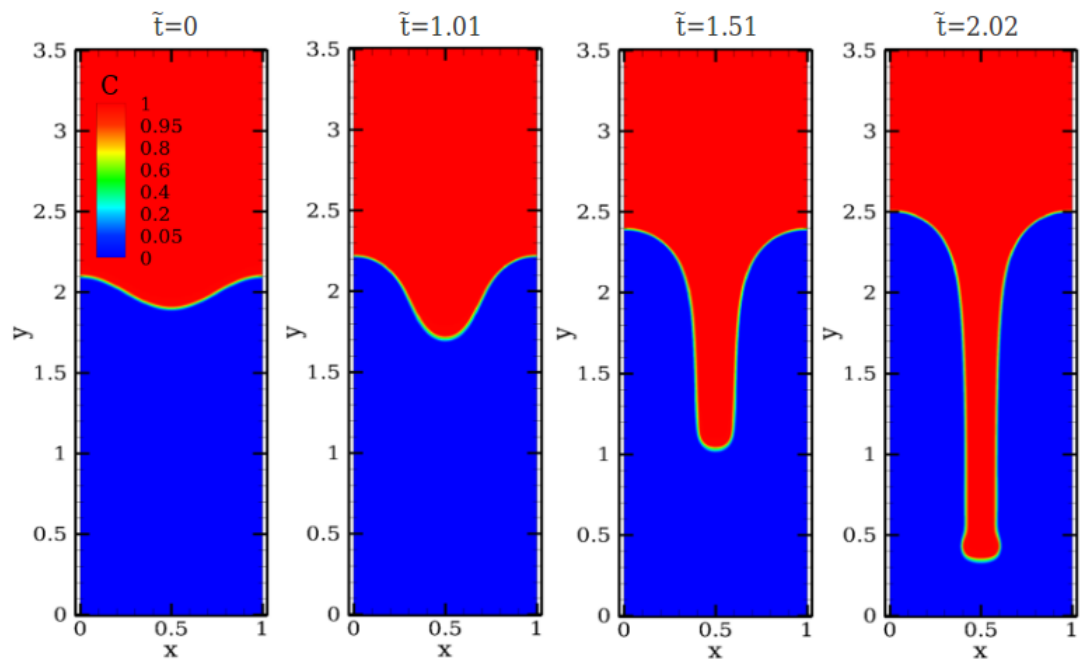


Figure 6.13. Contour-plots of the concentration at different dimensionless times for the Rayleigh-Taylor instability when $At = 1$ for the M200.

generated and as the heavier fluid is falling downwards, only a narrow spike is formed [260], while the lighter fluid is rising in a similar way as previously. In Fig. 6.14, the positions of the fronts of the two fluids are reported. It can be seen that the positions

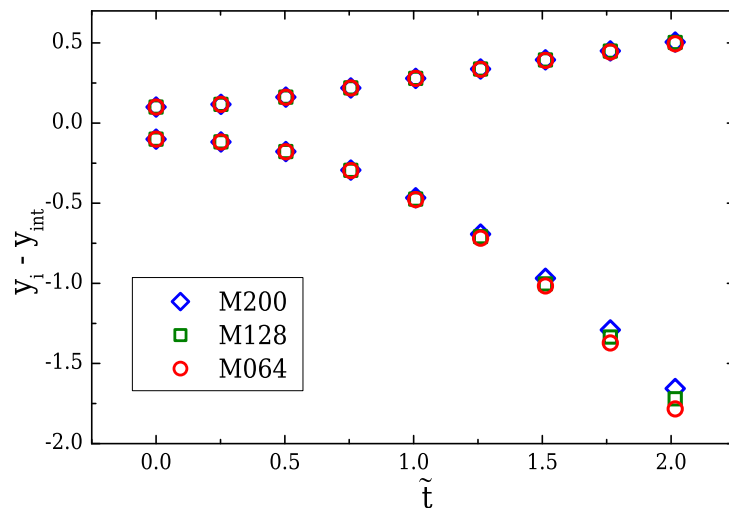


Figure 6.14. Front positions for the lighter and heavier fluids at different dimensionless times, for the Rayleigh-Taylor instability when $At = 1$ for all numerical meshes considered (cf. Table 6.2)

of the rising light fluid are mesh independent. However, this is not the case for the front of the heavier fluid. In this case, at the early stages all meshes perform equivalently, but at late times ($\tilde{t} > 1.5$) a deviation is observed. A possible reason explaining this behaviour is the use of a constant time stepping method. As the fluid is falling, its velocity progressively increases (much faster than in the case of the rising fluid) and the combination of time step value and low mesh resolution may not be appropriate for capturing efficiently these last stages.

6.4.2 Test-cases considering active surface tension

In this section the surface tension forces are taken into account ($\sigma \neq 0$) and the numerical implementation for both the diffusion and the convection terms is validated. In contrast with the results presented in [Section 6.4.1](#), where only cases of fluids with different densities have been discussed, here cases where both fluids have different viscosities are also reported.

i) Young-Laplace equation

One of the most important numerical tests for validating implementations of two-phase flow solvers is the problem of a quiescent circular drop at rest while surrounded by a matrix fluid. The aim of this test-case is the satisfactory verification of the Young-Laplace equation and has been widely used in the past as a benchmark case [56]. According to the Young-Laplace law, when a three-dimensional drop is surrounded by an immiscible fluid and the system is at equilibrium state, the pressure drop, ΔP , across the interface can be estimated by

$$\Delta P = \sigma \left(\frac{1}{R_1} + \frac{1}{R_2} \right) \quad (6.86)$$

where R_1 and R_2 are the principal radii of curvature.

In order to validate the numerical implementation presented in [Section 6.3](#), simulations of a quiescent drop are performed, where only a quarter of a 2D, $[0, 1] \times [0, 1]$ square, domain is considered, as shown in figure [Fig. 6.15](#). All the sides of the square

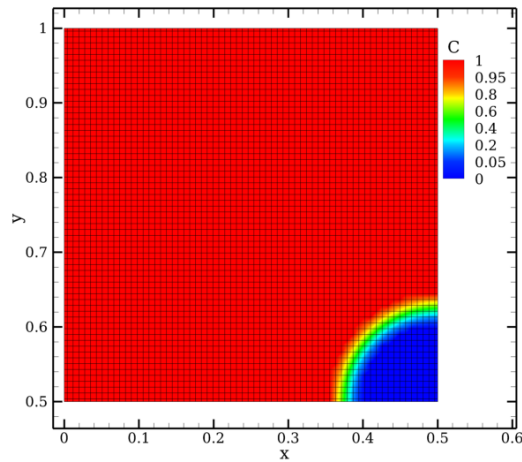


Figure 6.15. Domain initialisation for the M064 mesh (cf. Table 6.3) for validating Young-Laplace formula (Eq. (6.86)).

are treated with symmetry boundary conditions and the centre of the two-dimensional drop is located at the centre of the square domain. Since this study is for two dimensions, the drop can be considered as an infinite cylinder ($R_2 \rightarrow \infty$). Thus, Eq. (6.86) can be modified for predicting the pressure drop in the 2D-case:

$$\Delta P = \frac{\sigma}{R_1} \quad (6.87)$$

where R_1 is the drop radius.

Since there is no flow in the domain, the convective terms in both the Cahn-Hilliard (Eq. (6.9)) and the Navier-Stokes equation (Eq. (6.13)) are negligible. Hence with this case, the efficiency of the discretisation scheme of the diffusion terms of the Cahn-Hilliard equation is examined. As for the momentum equation, since the velocity field is zero, the stress-field is also negligible resulting in a problem that is driven by the balance between the pressure drop, ΔP , and the surface forces, \mathbf{f}_{st} . It should be mentioned that the decreased amount of parameters involved in this test-case, assist in examining the discretisations of the surface tension in the momentum equation and the diffusion term of the Cahn-Hilliard equation, without additional effects due to convection.

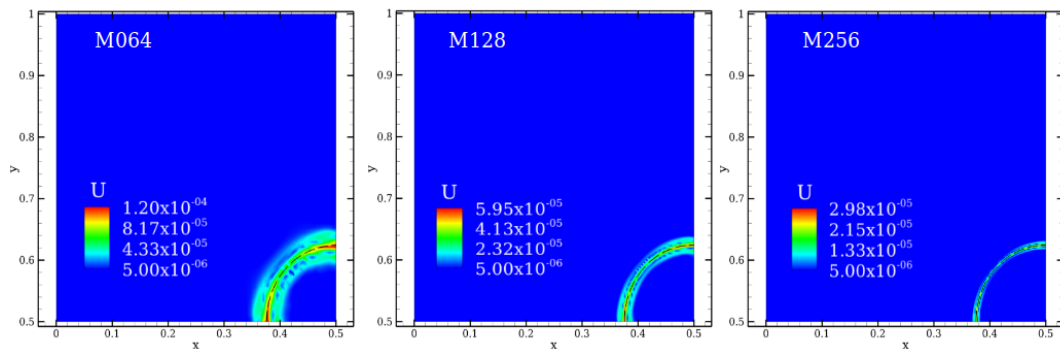
Initially, a 2D droplet with a radius $R = 0.125$ m, is surrounded by a matrix fluid of the same viscosity and same density. Hence the viscosity and density ratios are set

Table 6.3. Mesh characteristics for the Young-Laplace test-case for $R = 0.125$ m and $\sigma = 0.1$ Nm⁻¹.

Mesh	h	ϵ (m)	Cn	t_{diff} (s)	ΔP (Pa)	Cells
M064	0.0078	0.0047	0.038	108.4	0.796	4,096
M128	0.0039	0.0024	0.019	54.2	0.792	16,384
M256	0.0020	0.0012	0.009	27.1	0.791	65,536

$\lambda_\eta = \eta_d/\eta_c = 1$ and $\lambda_\rho = \rho_d/\rho_c = 1$ respectively, with η_d and ρ_d corresponding to the viscosity and the density of the dispersed phase, and η_c and ρ_c to the viscosity and the density of the continuous phase. The surface tension coefficient is set to be $\sigma = 0.1$ Nm⁻¹, resulting in an expected value for the pressure drop from Eq. (6.87), $\Delta P = 0.8$ Pa. Three uniform meshes ($\delta_x = \delta_y$) have been employed in order to simulate this case, with the thickness always defined using five computational cells and a value for the characteristic mobility of $M_c = 6.76 \times 10^{-6}$ m⁵s⁻¹J⁻¹. Table 6.3, illustrates the results of the simulations. It can be seen that the expected pressure drop is well approximated, with a maximum deviation smaller than 1%.

The majority of surface tension simulation methods which belong in interface capturing techniques, suffer from parasitic velocities, commonly known as *spurious currents* [244]. Figure 6.16 illustrates this numerical artefact, and it is clear that the magnitude of the velocities decreases as the mesh size increases. However, the spurious velocities developed are very small and do not affect significantly the evaluation of the pressure drop.

**Figure 6.16.** Contour plot of the velocity magnitude for the various meshes considered (details in Table 6.3). The *dashed* line indicates the position of the interface (0.5-contour).

As discussed in [Section 6.2.3](#) the existence of a characteristic diffusion time needs to be considered when using PF methods. Kim [235], suggested that the cells resolving the interface should be in the range $4 \leq k \leq 8$; it was pointed out that if k is very small, then the calculation of higher order derivatives will be difficult and interface gradients will not be analysed with increased accuracy. On the other hand, if a large number of cells is used then the interface becomes more diffuse and wider, deviating from its natural form and the desired sharp interface limit, resulting in unrealistic results. [Table 6.3](#), reports that by selecting to use always the same resolution of the interface ($k = 5$) while the mesh size is increased, the characteristic diffusion time decreases and concurrently, the Cahn number indicates that the sharp interface limit is approached.

In order to assess the performance of the implemented two-phase for varying ϵ (and consequently k) and M_c parameters, the same set-up is considered and a set of test-cases is conducted. Initially, the variation of the interface resolution (k) is examined, while the mobility remains constant. [Table 6.4](#) illustrates the numerical results for the evaluation of Young-Laplace formula.

When the thickness is resolved by three cells ($k = 3$), clearly the gradients along the interface are not evaluated correctly, a fact that leads to a large under-prediction of the expected ΔP . Conversely, as the resolution increases it can be seen that the pressure drop approximation is improved with the better solution occurring for $k = 7$. Interestingly, as the mesh size is increased (M256) and the diffusion time remains constant by controlling ϵ to be the same ($k = 20$) with the base mesh (M064), the evaluated

Table 6.4. Variation of the interface resolution, k , for the case of a quiescent drop with $R = 0.125$ m, $\sigma = 0.1$ Nm⁻¹ and $M_c = 6.76 \times 10^{-6}$ m⁵s⁻¹J⁻¹.

k	ϵ (s)	Cn	h/ϵ	t_{diff} (s)	ΔP (Pa)	Deviation
M128						
3	0.0014	0.011	0.36	32.5	0.673	15.91%
5	0.0024	0.019	0.60	54.2	0.792	0.99%
7	0.0033	0.026	0.84	75.9	0.798	0.23%
10	0.0047	0.038	1.20	108.4	0.804	0.43%
M256						
20	0.0047	0.038	2.40	108.4	0.808	0.97%

Table 6.5. Variation of the characteristic mobility M_c for the case of a quiescent drop with $R = 0.125$ m, $\sigma = 0.1$ Nm⁻¹ and a constant interface resolution, $k = 5$.

M_c^* (m ³ sKg ⁻¹)	ϵ (m)	Cn	h/ϵ	t_{diff} (s)	ΔP (Pa)	Deviation
M128						
1.69×10^{-6}	0.0024	0.019	0.60	216.8	0.791	1.10%
3.38×10^{-6}	0.0024	0.019	0.60	108.4	0.791	1.08%
1.35×10^{-5}	0.0024	0.019	0.60	27.1	0.792	1.07%
2.70×10^{-5}	0.0024	0.019	0.60	13.6	0.792	1.01%

pressure drop deviates more. This finding is in accordance with Kim [235], and thus the suggestion to treat the interface with a limited number of cells.

In order to examine the way the characteristic mobility is affecting the quality of the results, the interface resolution is kept constant and analysed by 5 cells ($k = 5$), whereas the mobility varies in the range $M_c/4 \leq M_c^* \leq 4M_c$. Table 6.5 shows that there is no significant change in the final result, where for all the cases ΔP is equivalently approximated. It should be mentioned that for all the cases examined, the same time step was used, $\Delta t = 5.0 \times 10^{-4}$ s, except from the case of $M_c^* = 4M_c$ which produces the smaller diffusion time and therefore the time step was reduced to half, $\Delta t = 2.5 \times 10^{-4}$ s.

This set of numerical test-cases focusing on the effect of the parameters of the PF method is concluded with the analysis of the variation of both k and M_c simultaneously. The aim of this last test-case is to perform the same numerical experiment done so far, while the characteristic diffusion times for all the cases presented in Table 6.4 are matched to the characteristic diffusion time of M064. To do this, the characteristic mobility varies as shown in Table 6.6. Comparing the pressure drop values between

Table 6.6. Variation of the interface resolution, k , and the characteristic mobility, M_c , for the case of a quiescent drop with $R = 0.125$ m, $\sigma = 0.1$ Nm⁻¹.

k	M_c (m ³ sKg ⁻¹)	ϵ (m)	Cn	h/ϵ	t_{diff} (s)	ΔP (Pa)	Deviation
M128							
3	2.03×10^{-6}	0.0014	0.011	0.36	108.4	0.673	15.90%
5	3.38×10^{-6}	0.0024	0.019	0.60	108.4	0.791	1.08%
7	4.73×10^{-6}	0.0033	0.026	0.84	108.4	0.798	0.23%
10	6.76×10^{-6}	0.0047	0.038	1.20	108.4	0.804	0.43%

Tables 6.4 and 6.6 for each case, clearly the matching of the diffusion time is not affecting significantly the final outcome, indicating that the treatment of the resolution of the interface thickness remains the most important to be taken into account.

The performance of the two-phase implementation was also assessed using the M064 mesh for different values of the surface tension coefficient, while the radius remains constant ($R = 0.125$ m). From Eq. (6.87) it is obvious that ΔP is a linear function of σ . The surface forces acting normal to the interface are forcing the pressure to higher values inside the circular droplet to balance. Figure 6.17a illustrates that the evaluation of the pressure drop is very well approximated as σ varies. Conversely, Eq. (6.87) indicates that if the surface coefficient remains fixed ($\sigma = 0.1$ Nm^{-1}) but the radius increases, the surface curvature decreases and lower pressure is required inside the drop for balancing the surface forces. This reciprocal relationship between ΔP and R is shown in Fig. 6.17b together with the results from the numerical simulations.

Another important characteristic of Equation (6.87) is its independence from possible viscosity and density differences between the two fluids. Hence, the performance of the two-phase solver is examined for a range of viscosity ratios $1 \leq \lambda_\eta \leq 1000$ and density ratios $1 \leq \lambda_\rho \leq 1000$, for fixed values of σ and R , as previously. The results shown in Fig. 6.18 are in very good agreement with the expected theoretical pressure drop for all the cases examined. More specifically, Fig. 6.18a illustrates the solver performance when the fluids have the same viscosity ($\lambda_\eta = 1$), but their density varies. Conversely,

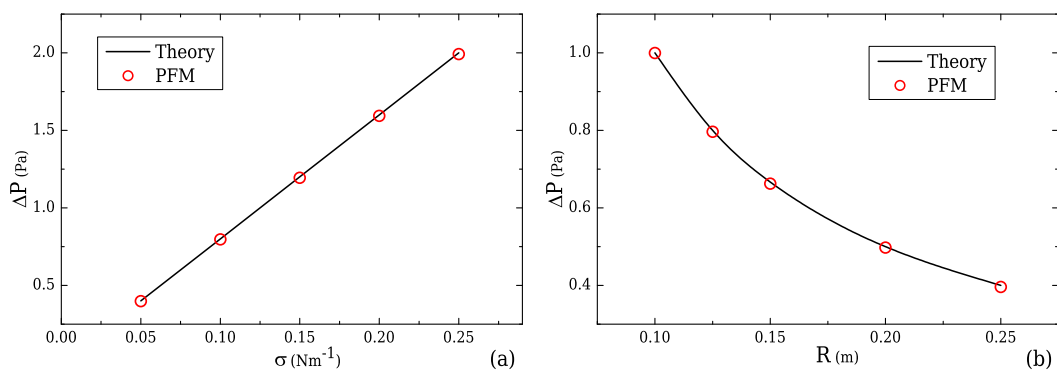


Figure 6.17. Evaluation of Young-Laplace formula (Eq. (6.87)) for different surface tension coefficient values for a fixed $R = 0.125$ m (a) and for different radii for a fixed $\sigma = 0.1$ Nm^{-1} (b).

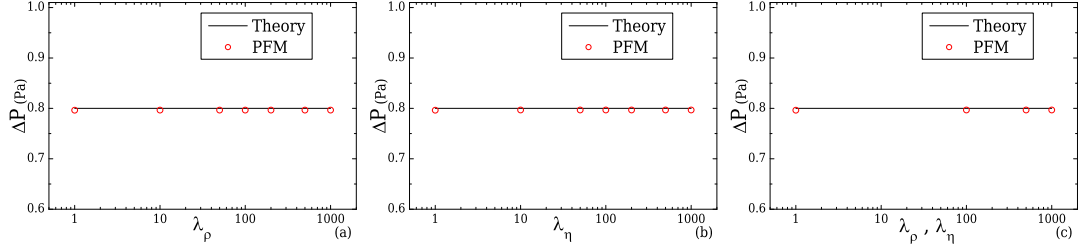


Figure 6.18. Evaluation of Young-Laplace formula (Eq. (6.87)) for a range of density ratios, λ_ρ , when $\lambda_\eta = 1$ (a) for a range of viscosity ratios, λ_η , when $\lambda_\rho = 1$ (b) and when both λ_ρ and λ_η vary (c), for $R = 0.125$ m and $\sigma = 0.1$ Nm⁻¹.

Fig. 6.18b shows the results when $\lambda_\rho = 1$, while the fluids have different viscosities. Finally, in Fig. 6.18c the evaluation of the pressure drop along the interface is shown when both properties vary in the same way.

Concluding, in order to test any potential errors during the implementation of the two-phase solver, the case when $\sigma = 0$ was also conducted and the simulation converged immediately without any changes in the initialisation. This behaviour is expected since $\sigma = 0$ corresponds to the same fluid and since the surface forces are zero, the pressure drop along the interface should also be zero.

ii) Oscillating droplet

The quiescent drop case discussed previously can indicate important coding errors that may have occurred during the implementation, or even more importantly in the choice of inaccurate discretisations. However, in this case the evaluation is done in the absence of convection. In order to investigate also the performance of the convective terms, the oscillation test-case is employed.

Initially at $\tilde{t} = 0$, a square 2D drop is set in the middle of a square domain, as shown in the first contour-plot of Fig. 6.19, and then is let to evolve in time. The dimensionless time is defined as $\tilde{t} = t/T_f$ where, t is the current time under examination and T_f is the total time of the simulation. The four corners of the square are described by higher concentration gradients, coinciding with the demand of locally higher levels of curvature. Since the surface tension is proportional to the interface curvature, the initial square-shaped drop will deform due to surface tension imbalance along the interface,

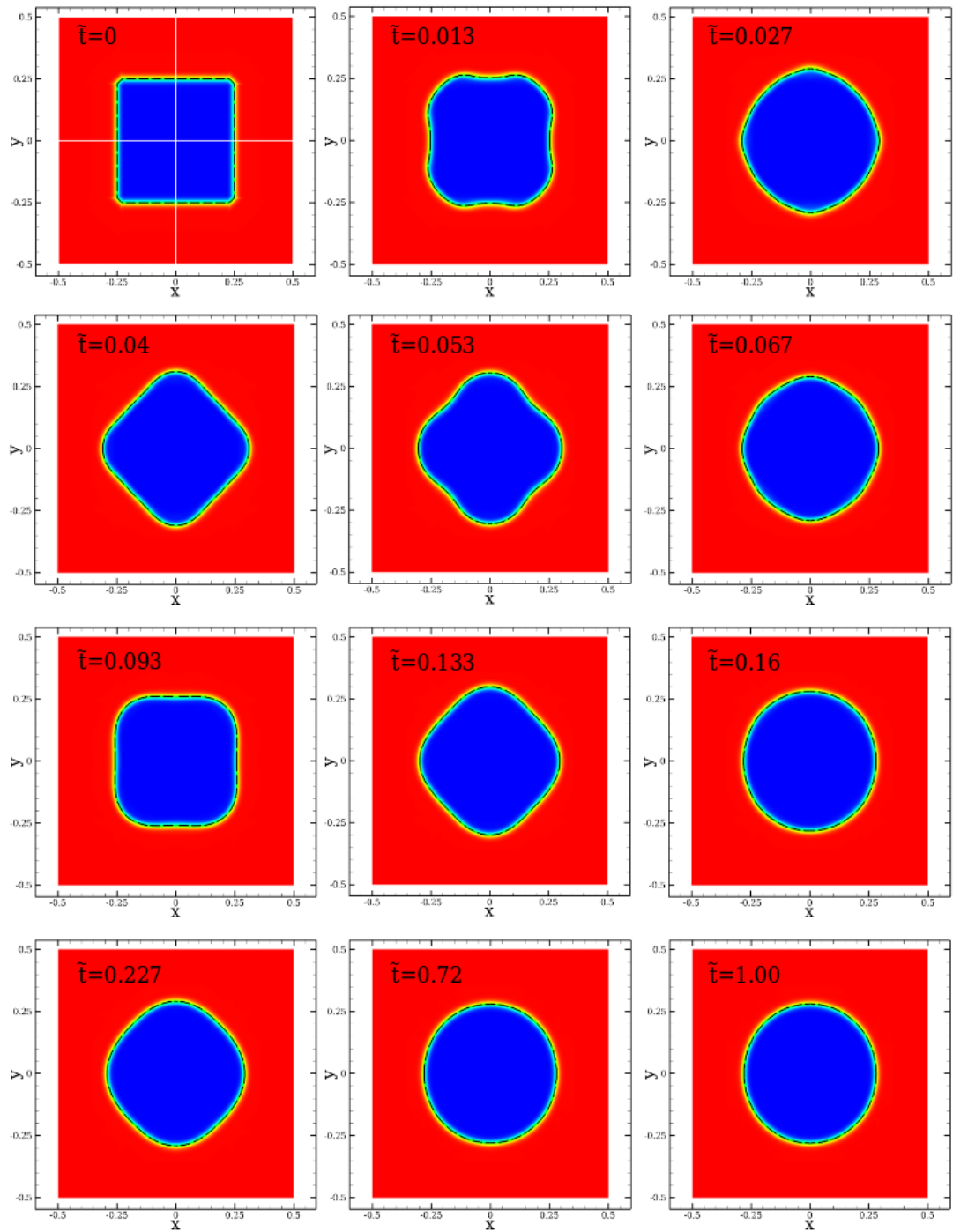


Figure 6.19. Contour-plots of the concentration of the oscillatory droplet at different dimensionless times when $\lambda_\rho = \lambda_\eta = 100$, $\sigma = 0.01 \text{ Nm}^{-1}$ and $M_c = 6.76 \times 10^{-6} \text{ m}^5 \text{ s}^{-1} \text{ J}^{-1}$. The *long-dashed* line indicates the 0.5-contour where the interface position is considered.

which as a result will trigger a pressure imbalance in the momentum equation. As a consequence an oscillatory behaviour will take place, with the drop changing forms and its oscillation decaying in time, until it reaches an equilibrium state, obtaining a circular shape [254,262].

The M064 (cf. Table 6.3) mesh is employed for qualitatively investigating the behaviour described above. Only a quarter of the geometry is considered, corresponding to the top left quarter, indicated in the first contour at $\tilde{t} = 0$ of Fig. 6.19. The initial shape of the drop is defined by a square with sides $\alpha = 0.5$ m. All the boundaries of the numerical domain are treated with symmetry boundary conditions and the time step was set to $\Delta t = 1 \times 10^{-3}$ s. The surface tension coefficient is set as $\sigma = 0.01$ Nm⁻¹, the characteristic mobility as $M_c = 6.76 \times 10^{-6}$ m⁵s⁻¹J⁻¹ and $\lambda_\rho = \lambda_\eta = 100$.

The contour-plots of Fig. 6.19 at different dimensionless times illustrate the square-shaped droplet oscillatory movement in time. It can be seen that the droplet deforms into various shapes, where for each time frame a new position with higher curvature is generated, resulting in regions where the pressure has higher values. Figure 6.20 illustrates the generated velocity and pressure field around the droplet for four different time-frames. The left half-part of each contour-plot shows the distribution of the velocity magnitude, while the symmetric right half-part presents the pressure variation in the two-phase system. The contour-plots related to pressure distribution are coloured based on the pressure maximum value at equilibrium. For the time-frames $\tilde{t} = 0.013$, $\tilde{t} = 0.053$ and $\tilde{t} = 0.133$, the pressure varies along the interface and generates the velocity field shown in the left-half. It is obvious that, as the experiment evolves in time, the velocity field exhibits smaller values and the oscillation decays, yielding a circular droplet at $\tilde{t} = 1.00$. At equilibrium, the pressure field varies only across the interface, corroborating the expected behaviour. In the numerical results, the droplet final radius is $R = 0.281$ m. For this radius, Eq. (6.87) estimates the pressure drop across the interface is to be $\Delta P = 0.0356$ Pa, while the numerical results indicate $\Delta P = 0.0352$ Pa representing 1.1% deviation. The above results are satisfactory and, as was reported in Liu *et al.* [256], the CH equation reveals a very good performance.

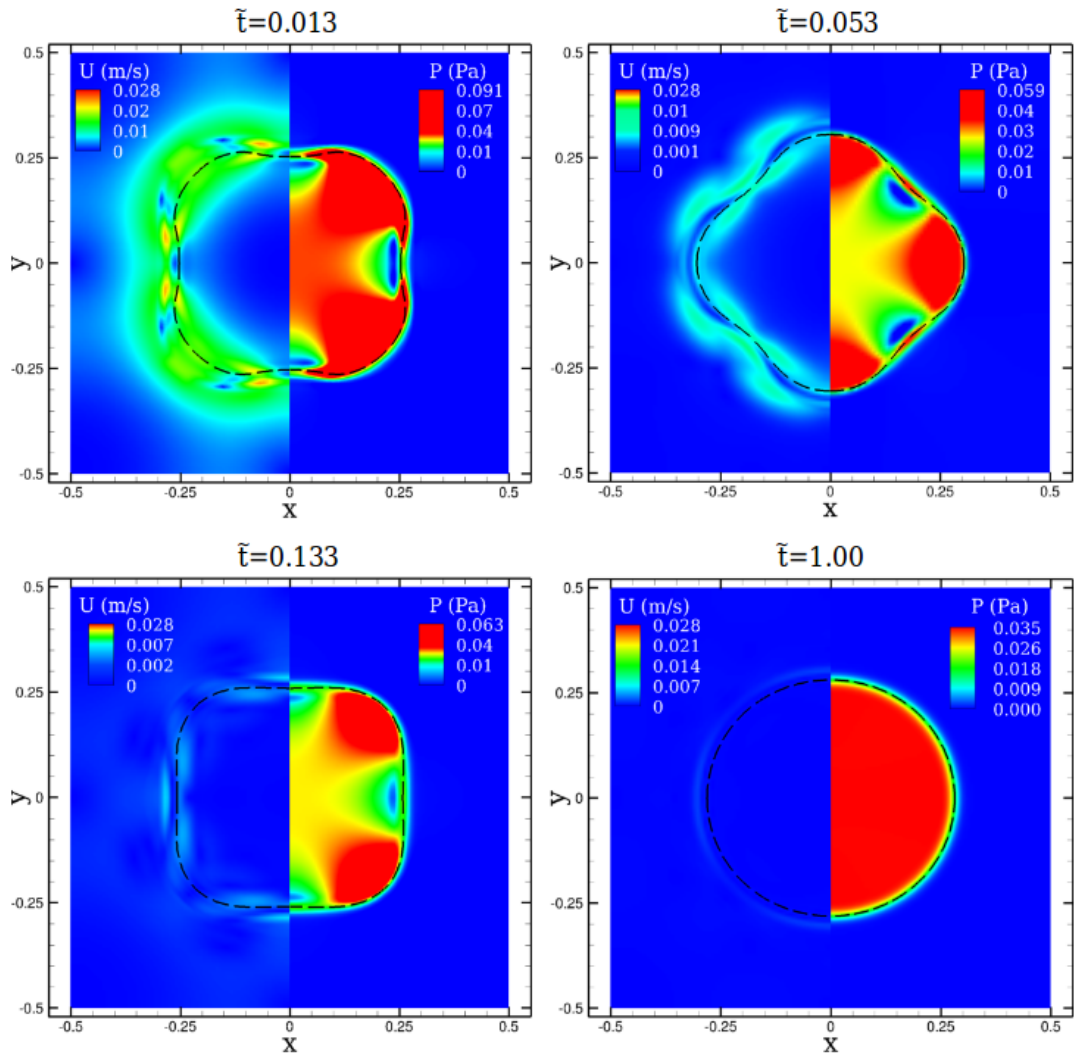


Figure 6.20. Combined contour-plots of the velocity magnitude (left-part) and the pressure distribution (right-part) for each frame at different dimensionless times $\lambda_\rho = \lambda_\eta = 100$, $\sigma = 0.01 \text{ Nm}^{-1}$ and $M_c = 6.76 \times 10^{-6} \text{ m}^5 \text{ s}^{-1} \text{ J}^{-1}$. The *long-dashed* line indicates the 0.5-contour where the interface position is considered.

iii) Droplet deformation under constant shear

One of the most commonly considered studies for validating two-phase flow implementations is the study of the droplet deformation under shear. For this test-case, the drop is placed between two parallel plates that move with constant velocities in opposite directions as shown in Fig. 6.21a. Thus, the drop is deformed with the deformation depending on the viscosity ratio, λ_η , and the capillary number, Ca , which represents

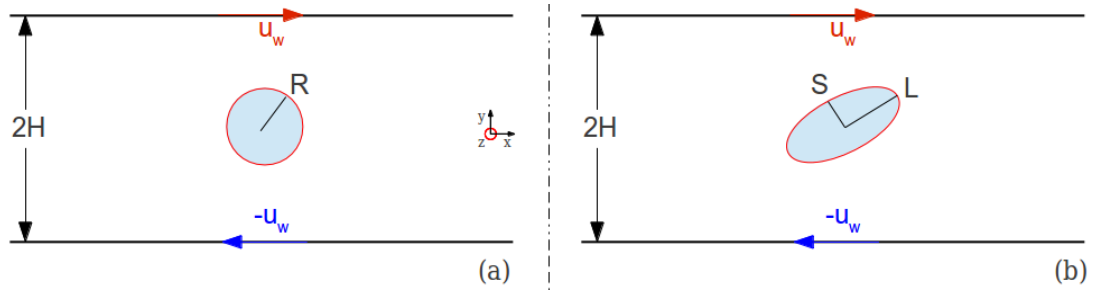


Figure 6.21. Configuration for the shear deformation test-case. The drop is positioned in between the two parallel plates ($y = 0$) that move in opposite directions with the same velocity (a), and deforms under constant shear obtaining an ellipsoidal form (b).

a measure of the viscous to surface tension effects. Taylor [180] found that for a liquid drop surrounded by a matrix liquid of equal viscosity ($\lambda_\eta = 1$), its deformation under constant shear takes an ellipsoidal form and can be expressed by the deformation parameter:

$$D = \frac{L - S}{L + S} \quad (6.88)$$

where L is the longest and S the shortest axes of the ellipsoidal deformation (cf. Fig. 6.21b). Additionally he expressed the deformation parameter as a function of the capillary number as

$$D = \frac{35}{32} \text{Ca} \quad (6.89)$$

However, Eq. (6.89) is applicable for real dimensions (3D), which is not the case examined here since only the 2D equivalent problem is studied.

Figure 6.21, illustrates the problem configuration. The distance between the two plates is $2H$ and in between, at $y = 0$, a drop of radius R is placed. The fully developed velocity field, generated by the opposite movement of the two plates, is applied as an initial condition. The analytical velocity profile along y -direction is given by

$$u = \frac{u_w}{H} y \quad (6.90)$$

where the characteristic shear-rate is $\dot{\gamma} = u_w/H$.

The case examined in order to validate the performance of the solver is similar to the case studied by Chinyoka *et al.* [263]. The Newtonian drop is set with an initial

radius $2H/R = 8$, while the Newtonian matrix fluid has the same viscosity and the same density as the drop ($\lambda_\eta, \lambda_\rho = 1$). The capillary number is defined as $\text{Ca} = \eta_c \gamma R / \sigma$, whereas the Reynolds number is defined as $\text{Re} = \rho_c \gamma R^2 / \eta_c$. Both dimensionless numbers are defined based on the viscosity η_c , and the density, ρ_c , of the matrix fluid; for this case are $\text{Ca} = 0.6$ and $\text{Re} = 0.3$. The boundary walls at $y = H$ and $y = -H$, are moving with equal but opposite velocities of magnitude $u_w = 0.5 \text{ ms}^{-1}$ (cf. Fig. 6.21). The right and left boundaries of the domain are treated with symmetry boundary conditions. The choice of these conditions will generate a flow field that rotates clockwise inside the numerical domain and for that reason the domain is chosen long enough, to avoid any disturbances from the boundaries to affect the region of interest.

For this study, three meshes have been employed for each of the two different approaches considered. For the first approach, the interfacial thickness is always defined by five cells, $k = 5$, resulting in decreasing Cahn numbers ($\text{Cn} = \epsilon/R$) and different diffusion times. For the second approach, the thickness is maintained, resulting in a constant Cn number and the same diffusion times for the three meshes. For all the cases studied, the characteristic mobility was defined as $M_c = 6.76 \times 10^{-6} \text{ m}^5 \text{ s}^{-1} \text{ J}^{-1}$, unless stated otherwise.

Table 6.7 presents the relevant information for each mesh considered in the constant resolution approach. Figure 6.22 shows the history of the deformation for the 0.5-contour, applied by the generated velocity field in dimensionless time, defined as $\tilde{t} = t\dot{\gamma}$. The deforming drop follows the behaviour reported by Chinyoka *et al.* [263], with the deformation increasing in time similarly for all meshes tested (the solution obtained for the most refined mesh deviates approximately 1% from Chinyoka *et al.* [263]). Figure 6.23a, illustrates the drop deformation based on the 0.5-contour at four dimen-

Table 6.7. Mesh characteristics for the study of the droplet deformation under constant shear with $k = 5$.

Mesh	ϵ (s)	Cn	h/ϵ	t_{diff} (s)	Cells
M128	0.0047	0.038	0.60	108.4	50,688
M180	0.0034	0.027	0.60	77.1	90,000
M256	0.0024	0.019	0.60	54.2	166,912

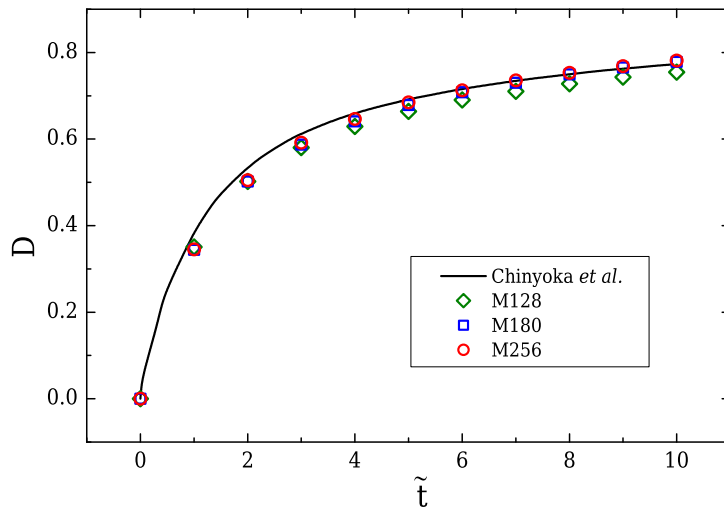


Figure 6.22. Drop deformation in dimensionless time, evaluated using Eq. (6.88), for all numerical grids of Table 6.7, compared with the solution from Chinyoka *et al.* [263].

sionless times $\tilde{t} = 0$, $\tilde{t} = 3$, $\tilde{t} = 7$ and $\tilde{t} = 10$, and Fig. 6.23b shows the development of the velocity streamlines around the deformed drop at $\tilde{t} = 10$. Obviously, the presence of the drop changes the velocity field which is no longer uniform (Eq. (6.90)): the matrix fluid flowing towards the poles of the drop is forced to change direction and flow backwards, whereas the rest flows around the deformed interface and constantly increases the deformation. The development of the stresses along the interface is responsible for

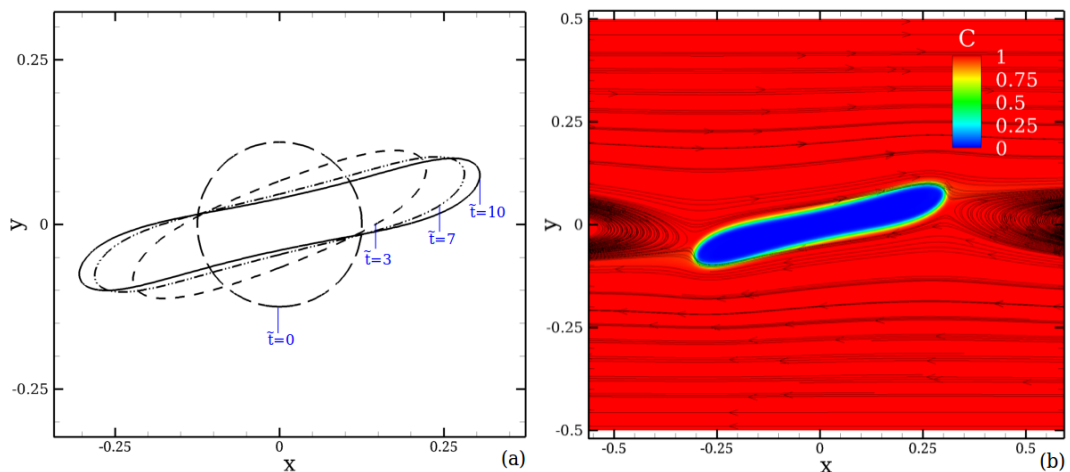


Figure 6.23. Drop deformation indicated by the 0.5-contour for various dimensionless times (a), and contour-plot of concentration together with the streamlines at $\tilde{t} = 10$ (b), for $Ca = 0.6$ and $Re = 0.3$ when $k = 5$ for M256.

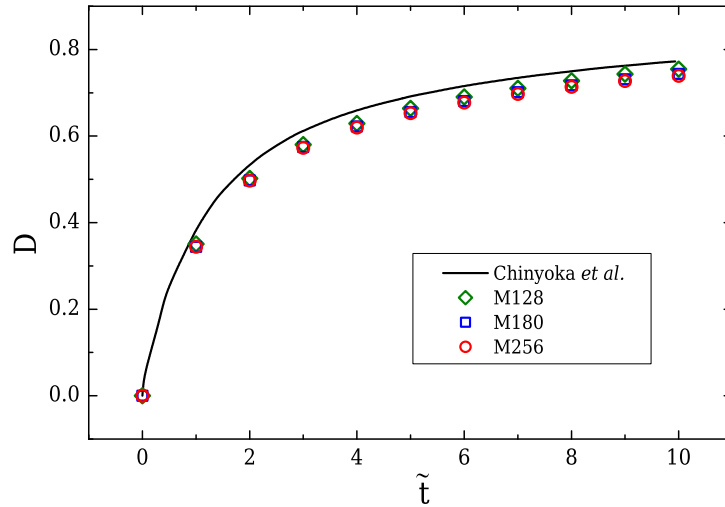


Figure 6.24. Drop deformation in dimensionless time, evaluated using Eq. (6.88), for all numerical grids of Table 6.7, compared with the solution from Chinyoka *et al.* [263].

the history and the trend of the deformation. Therefore, this deformation is expected to vary differently in time depending on the viscosity ratio λ_η , Ca and Re, which directly impact the stress field.

The case in which ϵ is set to be constant for all numerical meshes, resulting in the same t_{diff} and Cn number, is evaluated next. Table 6.8 presents the relevant information for each mesh. Considering the same conditions as in the previous approach, the evolution of the drop deformation in time is shown in Figure 6.24. Although the history of the deformation follows a similar trend, the deformation presented by Chinyoka *et al.* [263] is under-predicted for increasing mesh size. Furthermore increasing the mesh size does not improve the results, with the deformation deviating approximately 4% at $\tilde{t} = 10$ for M256. Figure 6.25a illustrates the deformation of the droplet in time, based on the deformation of the 0.5-contour and Fig. 6.25b displays the variation of

Table 6.8. Mesh characteristics for the study of the droplet deformation under constant shear with constant interface thickness, ϵ .

Mesh	ϵ (s)	Cn	h/ϵ	t_{diff} (s)	Cells
M128	0.0047	0.038	0.60	108.4	50,688
M180	0.0047	0.038	0.85	108.4	90,000
M256	0.0047	0.038	1.20	108.4	166,912

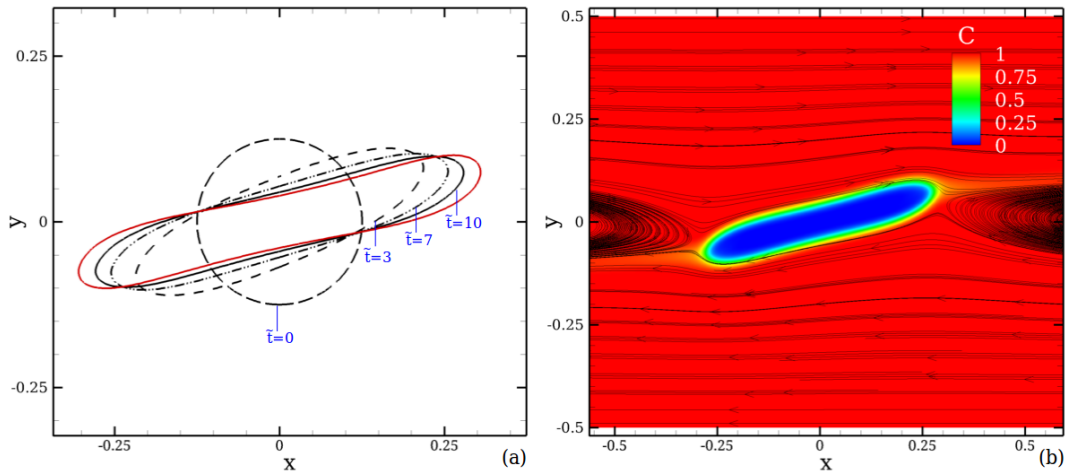


Figure 6.25. Drop deformation indicated by the 0.5-contour in dimensionless times with the arrow pointing the direction of the deformation (a), and contour-plot of concentration together with the streamlines at $\tilde{t} = 10$ (b), for $Ca = 0.6$ and $Re = 0.3$ when ϵ is constant ($k = 20$) for the M256. The red shape in (a) corresponds to the case of $k = 5$ at $\tilde{t} = 10$.

the concentration together with the streamlines. The point to highlight in this case is that for larger thickness resolution of the interface (for static and uniform meshes), the contours are more diffusive. This behaviour has been mentioned by Kim [235], suggesting that the interface for static (non-adaptive) meshes should not be resolved by a large number of cells, and by Komrakova *et al.* [264], reporting that the thicker the interface the larger the “contamination” of the area around the drop. Similar findings were reported by Akhlaghi *et al.* [251] for the developed velocity profiles of the phases for a one directional stratified flow. Both PF and LS could not approach the correct values as long as C_n was fixed and h was increasing, but they showed increased accuracy as $C_n \rightarrow 0$, where the sharp interface limit is approached.

The deformations presented in Figs. 6.22 and 6.24, indicate that depending on the choice of the interface thickness resolution, k , different results will be produced. More specifically, for the results produced by M256 for the two cases presented above, a relative difference of approximately 5% exists between the solutions for the final deformation at $\tilde{t} = 10$. This behaviour was expected and has first pointed out in Section 6.2.3 and the non-dimensionalisation of the CH equation. As the mesh size h is decreased (more fine mesh) and the interfacial resolution, k , remains the same, the

diffusion time is also decreased. Additionally, since the interface thickness ϵ for PF is related to a physical property, it should not change during the numerical experiments, as it would not during a real experiment. Figure 6.26 illustrates the contour variation along the interface for each approach. In Fig. 6.26a it can be seen that for each mesh the contour variation is different as the interface thickness becomes progressively small, with the 0.5-contour for the more refined meshes M180 and M256 displaying a similar deformation history. Conversely, in Fig. 6.26b it can be seen that as the mesh refinement increases, a solution independent of the numerical grid is obtained (M256), with the variation of all contours being similar and progressively better since gradients along the interface are better analysed.

An important fact is that the cases of Fig. 6.26b are characterised by a thickness value which is unrealistically large (see concentration contour in Fig. 6.25b). Conversely, the approach of the fine mesh M256 shown in Fig. 6.26a corresponds to a small Cahn number and therefore is the only one of all the discussed cases that approaches the desired sharp interface limits. That way, the major disadvantage of PF methods compared to its counterparts, LS and VOF, is evident. Either large interfaces are generated, deviating from real dimensions, or high computational demands are required for adequately analysing the thickness by considering small Cn numbers.

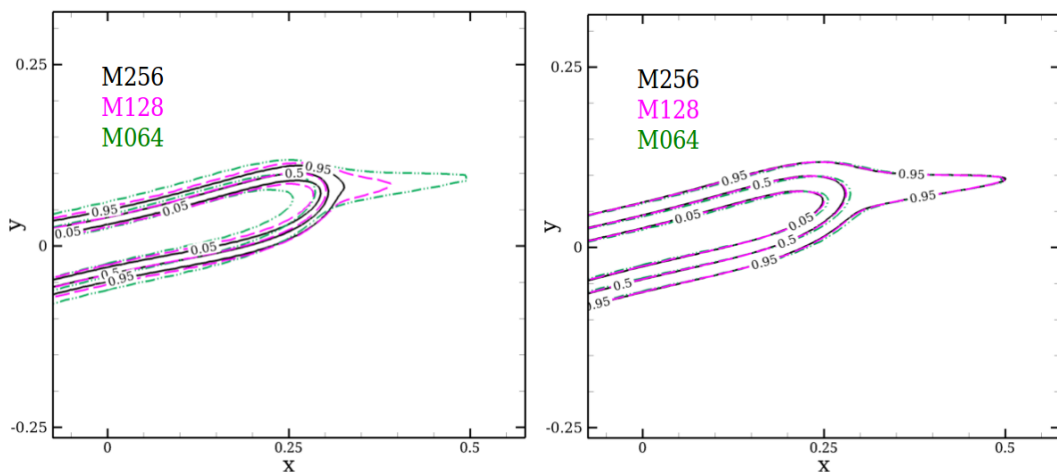


Figure 6.26. Behaviour of the contour-lines at $\tilde{t} = 10$ for all three meshes when $k = 5$ (a) and for constant ϵ (b), for $Ca = 0.6$, $Re = 0.3$.

6.5 Synopsis

The implementation of a two-phase solver built on top of an in-house single-phase solver was examined, considering a range of different test-cases for validation purposes. The solver adopts the Phase Field method presented in [Section 6.2](#), and the Cahn-Hilliard equation ([Eq. \(6.9\)](#)) was employed for adding the elements related to the second phase.

When the surface tension coefficient is set to zero ($\sigma = 0$), the diffusion term in the Cahn-Hilliard equation is dropped out and the PF method is similar to VOF and LS. Additionally, the force term, \mathbf{f}_{st} , in the momentum equation (cf. [Eq. \(6.13\)](#)) is vanishing and therefore, the implementation should perform equally for all methods. The advantage of examining test-cases with $\sigma = 0$ is the evaluation of the convection terms alone, without any additional effects. More importantly, and as illustrated in [Section 6.4](#), the efficiency and the accuracy of PF method depends on the best possible treatment of the interface [\[227\]](#). Unlike VOF and LS methods, here the relevant parameter has physical significance (cf. [Section 6.2.3](#)). In [Section 6.4.1](#), the case of the element stretching was studied. The outcome of this numerical experiment was the use of the SMART scheme for the convective terms in all the remaining test-cases, since it illustrated the best performance in terms of accuracy and mass-loss. It was shown that the best performances were reported for SMART and CUBISTA, with the later being more diffusive. However, Alves *et al.* [\[93\]](#), showed that when considering viscoelastic simulations, CUBISTA performs better in terms of convergence comparing to SMART, and therefore, it is recommended to re-evaluate their performance when viscoelastic elements are considered. Furthermore, it was shown that the two phase solver is capable of capturing interesting two phase phenomena, such as the Rayleigh-Taylor instability for different Atwood numbers. It would be interesting to expand the investigation of this problem to cases where one or both phases are characterised by viscoelastic fluids.

When $\sigma \neq 0$, the diffusion term and the surface forces are active and the implementation was tested for three test-cases in [Section 6.4.2](#). For these cases the interface thickness, ϵ , and the variable mobility, $M(C)$, are taken into consideration and affect the final outcome. The Young-Laplace equation was evaluated, a test-case that can in-

dicating various possible mistakes and drawbacks in the implementation. The advantage is that the drop is quiescent, meaning that there is no influence in the system from convection. Therefore, this problem offers the ability to investigate solely the interactions between the pressure gradient and the surface forces. For all interface capturing methods, the convective terms near the interface are not exactly zero because of spurious velocities [244]. Their existence may produce fluid motion near the surface that is not negligible, but rather affects the quality of the results and needs to be investigated. For this implementation however, it was seen that their presence at the interface is not affecting the final result. Moreover, a set of different initialisations was studied, illustrating how the use of different values of ϵ , can influence significantly the final outcome. The best approximations were accomplished for $k = 5$ or $k = 7$, satisfying at the same time the need for a “thin” interface. On the other hand, when ϵ is analysed by a small number of cells it was shown that the gradients are not calculated correctly, leading to large deviations and additionally, when k is large the interface is non-physically large leading to unreliable results as reported in Kim [235]. Moreover, the evaluated pressure drops were found to be less affected by the variations in the characteristic value of mobility, M_c , and the Young-Laplace formula was well approximated. Finally, for a range of different viscosity ratios, $1 < \lambda_\mu < 1000$, and density ratios, $1 < \lambda_\rho < 1000$, as well as for other combinations of R and σ , the performance was found to be very good.

When effects from convection are also accounted for (oscillating droplet and droplet deformation), the solver performs satisfactory, illustrating adequate capturing of the expected physics. Initially, for the case of the oscillating droplet the square-shaped droplet was successfully driven to an equilibrium state, obtaining a circular shape and at the same time the correct pressure difference, expected from the Young-Laplace formula, at this final state was developed. During the intermediate stages, the drop changed shape, obtaining an oscillatory movement towards the equilibrium state as expected [254, 256, 262].

The final test-case conducted for validation purposes was the case of the droplet deformation under constant shear. The study of this case revealed some characteristics of the PF method that should be treated carefully. As the grid becomes more refined

($h \rightarrow 0$) and the interfacial resolution, k , is resolved by the same number of cells, the diffusion time is decreased (ϵ decreases) and raises the question whether the same problem is being investigated. On the other hand, keeping k constant while $h \rightarrow 0$, large interfaces are generated. Hence, since the interface thickness used in PF methods is related to a physical quantity, unlike the case of VOF and LS methods, is it realistic to treat it as such? Two different approaches were presented: the same numbers of cells were used, resulting in decreasing Cahn numbers; Cn was fixed for all meshes (k increases). Both approaches resulted in a drop deformation which followed the expected trend, with the case of constant k producing more realistic contours of concentration across the interface, since in this way the sharp interface limit is approached ($Cn \rightarrow 0$).

The problems occurring from the interface definition can be minimised in two ways. The use of an adaptive meshing method could assist in better resolving the interface without changing the actual and desired value of ϵ , providing simultaneously a better resolution for the gradients of each quantity along the interface. Another way, is the modification of the serial two-phase solver into a parallel version, which will improve the ability to run more computationally demanding problems and thus, make it possible to reach smaller Cn numbers even when using a uniform mesh. In fact, when studying two-phase flows, code parallelisation seems mandatory due to the increased computational needs. This is even more important for effectively studying 3D two-phase flows, where the additional third direction further increases the complexity and the problem becomes more time demanding.

*“..The water flowing
The endless river
Forever and ever..”*
High Hopes - Pink Floyd

Chapter 7

Conclusions & Future work

7.1 Thesis conclusions

The work developed in this thesis aims to contribute to the investigation and development of complex fluid flow systems related in Lab-on-a-chip devices. It was conceptually divided in two main topics: the numerical design of geometrical configurations for studying flows of Newtonian and non-Newtonian fluids under specific and well defined conditions required for different applications; the implementation of a two-phase solver integrated into an already available in-house single-phase CFD solver for viscoelastic fluid flows.

7.1.1 Design of microfluidic components

Two different techniques were employed in this thesis for designing microfluidic components. The first was inspired by biomimetic principles for generating bifurcating networks, that are able to provide good control of the shear-stress gradients and the flow resistance in various generations. The second utilised shape optimisation techniques aiming to produce the appropriate configurations for generating homogeneous extensional flows.

i) Biomimetic design for shear flow networks

A biomimetic design rule appropriate for designing planar microfluidic bifurcating networks of rectangular cross-section with constant depth for investigating the flow of power-law fluids was proposed. Based on the biomimetic principle proposed by Emerson *et al.* [139] and Barber and Emerson [140], the corresponding theory was further extended here to consider power-law fluids. The design rule produces the appropriate dimensions for each generation of the microfluidic network depending on the fluid to be used, on the desired aspect ratio and the branching parameter. The branching parameter provides extra flexibility and allows one to control how the wall shear-stress varies along the branching network. In addition, when the design follows the length proportionality, the biomimetic rule is able to provide additional information related to the hydraulic resistance along the network.

The theoretical rule proposed was tested numerically considering three different values of the branching parameter for generating networks with four consecutive generations and an inlet aspect ratio of $\alpha = 0.5$. Initially, the branching parameter value was set equal to unity ($X = 1$), yielding bifurcating configurations able to maintain uniform shear-stress gradients (equal average wall shear-stresses at each generation), while the hydraulic resistance is expected to increase linearly along the network. Initially the flow of a Newtonian fluid was investigated under creeping flow conditions, demonstrating a very good agreement with the expected behaviour. Next, a range of power-law fluids was examined, varying from shear-thinning to shear-thickening behaviour ($n = [0.2, 2.0]$). The customised networks for each power-law fluid were found to exhibit small differences relative to the proposed Newtonian-designed geometry. Therefore, the latter could be employed to investigate the response of the power-law fluids. This universality introduces an important advantage of the design for experimental measurements, since the same configuration can be used for the Newtonian and all power-law fluids tested.

The ability of the biomimetic design rule to produce channels with specific shear-stress gradients has also been examined for a case of positive gradients ($X = 1.25$) and a case with negative gradients ($X = 0.75$), both under creeping flow conditions.

Considering three fluids, a Newtonian ($n = 1$), a shear-thinning ($n = 0.6$) and a shear-thickening ($n = 1.6$) fluid, it was shown that a universal configuration does not exist and the design of each network is unique. Thus, when contemplating to employ configurations of this type, experimentalists should design bifurcating networks with the appropriate customised widths for the fluids to be used. As an alternative, under creeping flow conditions one can use these channels as dual-performance networks, where by reversing the flow field the gradients are also reversed.

The assumption of creeping flow conditions is generally a good approximation for lab-on-a-chip devices, however since “truly” creeping conditions cannot be attained in reality, the limits of the universal design in terms of Reynolds numbers were also investigated. For a Newtonian ($n = 1$), a shear-thinning ($n = 0.6$) and a shear-thickening ($n = 1.6$) fluid it was found that when $Re_0^* \gtrsim 30$ the numerical results start to deviate from the expected behaviour and the associated errors should be taken into account.

ii) Microchannel shape optimisation for homogeneous extensional flow

Shape optimisation techniques have been employed to design microfluidic devices able to generate a region of homogeneous extensional flow. The investigated configurations were classified in two categories depending on the number of inlet fluid streams: the single-stream and the multi-stream designs. The optimisation procedure considered creeping flow conditions and relies on the combination of the single-phase solver, a mesh deformation procedure and a derivative free optimiser.

The fact that contraction-expansion geometries are ubiquitous and able to generate strong extensional flows motivated the studies related to shape optimisation of this single-stream configuration, where for all geometries of different contraction ratios examined their efficiency has been significantly improved. Particularly for the case of $CR = 8$, 2D and 3D channels of different aspect ratios have been optimised. It was shown that when considering 2D fluid flows, the optimised shape performance is equivalent to the well known hyperbolic design, being improved only at the transition region (entrance and exit of the contraction-expansion region). On the contrary, for 3D flows the optimised shapes exhibit a significantly improved performance for all the aspect

ratios considered ($1 \leq \text{AR} \leq 32$) when compared to the hyperbolic shape, resulting in a larger region of constant strain-rate along the flow centreline.

All designs proposed have been examined numerically regarding their operational limits in terms of Reynolds numbers for Newtonian fluids, and it was found that they operate well for $\text{Re} \lesssim 5$. Additionally, for viscoelastic fluids where the design with $\text{AR} = 1$ was employed, it was shown that for increasing Weissenberg numbers a velocity overshoot is observed in the throat of the design. The design illustrated good performance in the whole contraction-expansion region up to $\text{Wi} = 0.02$ for constant viscosity viscoelastic fluids. For higher Wi the strain-rate profile deviates from the desired performance in the diverging part, being clearly affected by the strain history. Moreover, these configurations fail to operate efficiently for highly shear-thinning viscoelastic fluids, where the strain-rate profiles were found to deviate from the desired performance for all Wi examined and this shear dependent viscosity would need to be considered in the optimisation.

The different features introduced by the usage of multi-stream designs and their ability to generate homogeneous extensional flows motivated the optimisation of T-shaped and flow-focusing channels. When standard designs of these channels are used they do not provide the desired performance. Improved designs have been proposed based on the optimisation procedure both for 2D and 3D flows. For 2D flows in T-junctions it was shown that good solutions which result in constant strain-rate along the flow centreline can be obtained, either by generating a cavity and a free stagnation flow or by modifying the considered objective function. For a 3D T-junction with $\text{AR} = 1$, optimised with a modified objective function, it was shown that the optimised design can be used up to $\text{Wi} = 0.2$ for constant viscosity viscoelastic fluids. For increasing values of Weissenberg number a velocity overshoot was seen to be formed at the end of the optimised region where a contraction flow is resembled. On the contrary, for shear-thinning viscoelastic fluids the design was not operating efficiently, and similarly to the single-stream design, this characteristic needs to be accounted in the optimisation.

Good solutions were achievable both for 2D and 3D flow-focusing designs using a modified velocity target profile similarly to the T-junction optimisations. For the

2D case, three different velocity ratios between the vertical and the horizontal inlets ($VR = 10$, $VR = 20$ and $VR = 100$) were investigated, and it was shown that slightly different shapes are produced for each velocity ratio in order to obtain a constant strain-rate along the flow centreline. In addition, a 3D configuration was optimised for $AR = 1$ and $VR = 20$. The design was able to generate constant strain-rate along the flow centreline for Newtonian fluids under creeping flow conditions. Different velocity ratios were considered in order to investigate the limits of the design for exploiting the ability to test different Hencky strains using the same configuration. It was shown that for $VR \geq 10$ the design manages to generate the desired behaviour, which can be very interesting for practical applications. However, for the case with $VR = 1$ it was shown that the design fails to generate constant or nearly constant strain-rate profile along the flow centreline and shape optimisation should be considered. Moreover, when viscoelastic fluid flows are examined, the 3D design presented a good performance for constant viscosity viscoelastic fluids up to $Wi = 0.2$, but, similar to the behaviour observed for the T-junction, is not illustrating the desired performance for shear-thinning fluids viscoelastic fluids.

In all single- and multi-stream cases considered the shapes obtained exhibit local salient corners similarly to what has been found for the cross-slot configuration [190, 192]. Close to the walls, shear effects reduce the stretching of fluid elements and the presence of stagnant regions of the salient corners help “self-lubricate” the flow [77]. However, important differences exist between these designs. Single-stream designs are simpler to use and this makes them more flexible configurations for extensional flow applications. The nominal strain-rate can be easily controlled by adjusting the volumetric flow rate at the desired levels. On the contrary, attaining a constant strain-rate along the flow centreline in a multi-stream design, depends on the accurate control of the entangled streams. However, multi-stream configurations provide features that single-streams designs are unable to offer. Employing a T-junction one can generate a stagnation point flow, providing the advantage of producing strong extension around the stagnation region. If one chooses to use a flow-focusing design, may exploit the two important features of this set-up: the two opposed jets can act as lubricant fluids,

minimising the shear effect due to fluid-wall interactions on the vertically imposed, third stream; they can resemble a variety of single-stream, converging flows described by different Hencky strain values by only adjusting in an appropriate way the imposed streams [21–23].

7.1.2 Two-phase solver

A two phase solver based on the Phase Field method has been implemented on top of an in-house single phase CFD solver appropriate for studying viscoelastic fluid flows. The appropriate elements describing the second phase based on the Cahn-Hilliard equation [238, 239] have been adapted in the context of the single-phase solver, following the finite volume method, and were implemented to consider three dimensional problems. The solver has so far only been validated for two dimensional problems, illustrating a very good performance for all cases considered. The test-cases chosen were subdivided in two categories, those in which the surface forces are negligible and those in which surface forces influence the dynamics of the investigated system.

The cases with non-active surface forces provided significant information both in terms of numerical and performance aspects, e.g. based on these test cases the most appropriate higher order numerical scheme used to discretise the convective terms of the Cahn-Hilliard equations was selected. The purely numerical test-case of the stretching element was used, in which only the convective CH equation is solved for a prescribed velocity field. It was found that the SMART scheme is the most accurate and thus, it was used in all the remaining test-cases. Using this finding, the investigation of the test-case of the Rayleigh-Taylor instability, for which the momentum, the continuity and the Cahn-Hilliard equations were solved, demonstrated a very good agreement with previous studies in literature.

A number of other test cases where the surface forces were included in the mechanisms of the two-phase system have been employed for the validation of the two-phase solver. Starting from the simplest case of a quiescent drop, the solution of the problem showed a good balance between the pressure forces and the surface forces. Moreover, a good estimation of the Young-Laplace formula was found for various radius and sur-

face tension coefficients, viscosity and density ratios. The simplicity of this test-case assisted further in the investigation of the influence of the PF parameters, illustrating the significance of a good evaluation of the interface thickness. This feature was further investigated in the drop deformation under shear, where the importance of the physical interpretation of this quantity on the results was discussed. The validity of the numerical implementation was further supported by the fact that the square drop experiences the expected oscillating behaviour, attaining a circular shape and predicting correctly the expected pressure drop from the Young - Laplace equation.

7.2 Future work

The numerical studies performed in this thesis and the microfluidic designs proposed can assist in a range of future studies to investigate the behaviour of Newtonian and complex fluid systems. The given details for a number of geometries, focusing either on shear or extensional characteristics, can be used in order to fabricate the desired microchannels and perform interesting experiments. More specifically, it would be of great importance to validate experimentally the applicability of bifurcating networks for power-law fluids that are designed using the biomimetic rule. The preliminary experimental investigation is encouraging, and various things that should be attended to have been indicated. In particular, it would be worth to consider the use of the customised bifurcating networks as sensors for testing shear sensitive materials such as cells, vesicles and individual polymers molecules as the design allows for testing a range of shear-stresses in the same device. This characteristic would be particularly interesting in cases where the cumulative effect of shear is important. Moreover, exploiting the advantage of generating different conditions in the same network by just splitting differently the flow in the first junction, allows one to examine simultaneously the behaviour of the same sample under different flow conditions. Studies related to mixing or separation of species using this type of configurations could be interesting. For example examination of the capability of these networks to perform blood-plasma separation. A combination of the appropriate branching parameter, together with the

imposition of different flow rates at the branches of the network may result a desired level of separation. Moreover, the study of viscoelastic fluid flow should be examined both numerically and experimentally. For example, imposing the viscoelastic fluid from the last generations and driving it to the parent segment, may result instabilities due to the shear-stress gradients and the streamline curvature, that can be exploited in order for the channel to act as a passive micro-mixer.

The performance of the optimised shapes for single-stream and multi-stream geometries as possible platforms to investigate homogeneous extensional flows, should be evaluated experimentally. These geometries can be useful for further studies related to cell/droplet responses and as possible micro-rheometers. However, before this happens it is crucial to analyse in detail the pressure and stress fields. Additionally, in the case of multi-stream configurations the operational limits for the T-Junction and the flow-focusing designs have not yet been investigated and should be considered in terms of increasing Re for Newtonian fluids. This is needed since the dynamics in these geometries are more complex than the single-stream designs and thus, their performance should be tested in detail. Additionally, performing optimisations in order to find shapes for different width ratios, but more importantly for different aspect ratios would be beneficial.

The implementation of the two-phase solver was motivated by the need to investigate numerically two-phase problems that are related to non-Newtonian fluids. The solver has been validated so far only for Newtonian fluids, whereas its performance when handling cases where at least one of the phases is non-Newtonian should be considered. Furthermore, the two phase solver was implemented in three dimensions but its performance has only been validated for 2D cases. The interest in 3D two-phase flows is great (e.g. for simulations of microfluidic devices) and this validation should be performed.

Before the 3D validation, the performance of the current version should be investigated when non-uniform meshes are employed, since refinement in regions with large changes are highly needed and so far only uniform meshes have been considered. This, together with the inclusion of adaptive meshing techniques is expected to improve the

performance of the current solver. However, the most important upgrade of the current version would be the translation of the computationally serial version of the code, to a version that performs parallel computations. The 3D validation in serial will consume many computational resources¹, since the requirements for high grid resolution will be increased. Moreover, this upgrade will benefit further the study of two-phase flows that include a non-Newtonian phase, where the inclusion of the additional constitutive relation increases further the needs for accuracy and thus grid resolution. It would be of great interest to investigate two-phase flows considering the biomimetic networks or the optimised geometries. Obviously, improvements of the type mentioned in the two-phase solver will permit numerical studies related to these and other geometries.

¹The required calculations for a 3D geometry will be $N_{3D} = (n + 1)N_{2D}$, where N_{2D} are those required for the 2D case, and n corresponds to each new cell that is added along the third direction.

Appendices

Appendix A

Biomimetic Design

A.1 Biomimetic design other aspect ratios

The following tables present the geometrical parameters of planar bifurcating networks computed after solving the set of Eqs. (4.24), (4.25) and (4.31) for the biomimetic design rule presented in Section 4.3, considering power-law indices of $n = 0.6, 1.0$ and

Table A.1. Geometrical parameters and dimensions of planar bifurcating networks with inlet aspect ratio $\alpha_0 = 0.2$ obtained for Newtonian ($n = 1.0$) and power-law fluids ($n = 0.6, 1.6$) for $X = 1$.

i	w_i (μm)	d_i (μm)	α_i	D_{hi} (μm)	a^*	b^*
$n = 1.0$						
0	625.0	125.0	0.200	208.3	0.3475	0.8444
1	312.9	125.0	0.399	178.6	0.2661	0.7573
2	171.5	125.0	0.729	144.6	0.2189	0.6890
3	106.3	125.0	1.176	114.9	0.2139	0.6803
$n = 0.6$						
0	625.0	125.0	0.200	208.3	0.3475	0.8444
1	307.5	125.0	0.407	177.8	0.2642	0.7549
2	167.7	125.0	0.745	143.3	0.2180	0.6874
3	104.4	125.0	1.198	113.8	0.2143	0.6811
$n = 1.6$						
0	625.0	125.0	0.200	208.3	0.3475	0.8444
1	316.8	125.0	0.395	179.3	0.2674	0.7589
2	174.3	125.0	0.717	145.6	0.2196	0.6902
3	107.7	125.0	1.160	115.7	0.2136	0.6798

Table A.2. Geometrical parameters and dimensions of planar bifurcating networks with inlet aspect ratio $\alpha_0 = 0.3$ obtained for Newtonian ($n = 1.0$) and power-law fluids ($n = 0.6, 1.6$) for $X = 1$.

i	w_i (μm)	d_i (μm)	α_i	Dh_i (μm)	a^*	b^*
$n = 1.0$						
0	416.7	125.0	0.300	192.3	0.2991	0.7954
1	217.6	125.0	0.574	158.8	0.2328	0.7113
2	128.5	125.0	0.973	126.7	0.2121	0.6772
3	83.8	125.0	1.492	100.3	0.2230	0.6957
$n = 0.6$						
0	416.7	125.0	0.300	192.3	0.2991	0.7954
1	214.8	125.0	0.582	158.0	0.2318	0.7098
2	126.8	125.0	0.986	125.9	0.2121	0.6771
3	83.0	125.0	1.507	99.7	0.2235	0.6966
$n = 1.6$						
0	416.7	125.0	0.300	192.3	0.2991	0.7954
1	219.7	125.0	0.569	159.3	0.2335	0.7124
2	129.7	125.0	0.964	127.3	0.2122	0.6773
3	84.4	125.0	1.481	100.8	0.2226	0.6951

1.6 for a branching parameter $X = 1$. [Table A.1](#) shows the geometrical parameters for

Table A.3. Geometrical parameters and dimensions of planar bifurcating networks with inlet aspect ratio $\alpha_0 = 1.0$ obtained for Newtonian ($n = 1.0$) and power-law fluids ($n = 0.6, 1.6$) for $X = 1$.

i	w_i (μm)	d_i (μm)	α_i	Dh_i (μm)	a^*	b^*
$n = 1.0$						
0	125.0	125.0	1.000	125.0	0.2121	0.6771
1	81.9	125.0	1.527	98.9	0.2243	0.6978
2	56.3	125.0	2.220	77.6	0.2537	0.7413
3	39.5	125.0	3.162	60.1	0.2928	0.7885
$n = 0.6$						
0	125.0	125.0	1.000	125.0	0.2121	0.6771
1	82.0	125.0	1.524	99.0	0.2242	0.6977
2	56.6	125.0	2.209	77.9	0.2532	0.7406
3	39.9	125.0	3.133	60.5	0.2917	0.7873
$n = 1.6$						
0	125.0	125.0	1.000	125.0	0.2121	0.6771
1	81.8	125.0	1.528	98.9	0.2243	0.6979
2	56.1	125.0	2.228	77.4	0.2540	0.7417
3	39.3	125.0	3.183	59.8	0.2936	0.7894

an inlet aspect ratio $\alpha_0 = 0.2$, [Table A.2](#) for $\alpha_0 = 0.3$ and [Table A.3](#) for $\alpha_0 = 1.0$.

Appendix B

Optimised designs

B.1 Converging/diverging geometry compared to converging/abrupt

The study presented in [Section 5.4](#) is entirely focused on symmetric contraction/expansion geometries. As mentioned in the main text, the reason of this choice is based on the fact that this configuration provides a constant strain-rate along the entire length of the contraction/expansion with a positive strain-rate in the converging region and a negative value in the expansion region, where the stretching and relaxation processes can be analysed under homogeneous flow conditions. On the other hand,

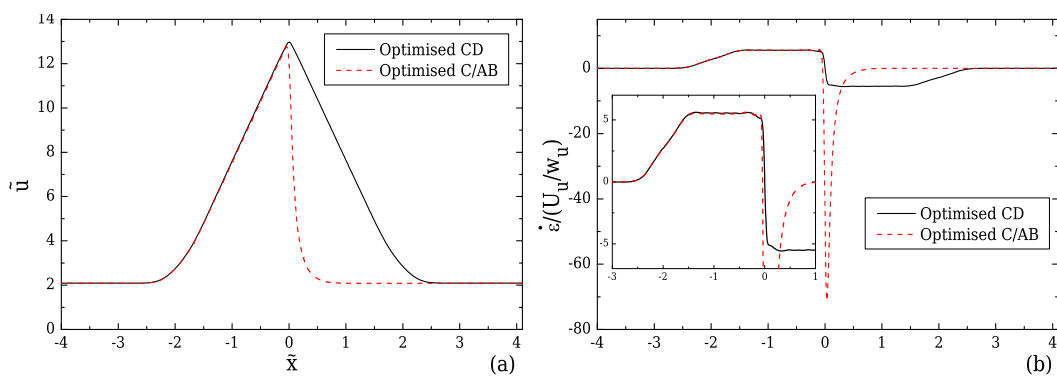


Figure B.1.1. Velocity (a) and strain-rate (b) profiles along the centreline of the flow for the optimised converging-diverging (*solid line*) and converging-abrupt geometries (*dashed line*) for $AR = 1$, $CR = 8$, $l_c = 2w_u$, $l_\varepsilon = w_u$ at $Re = 1$.

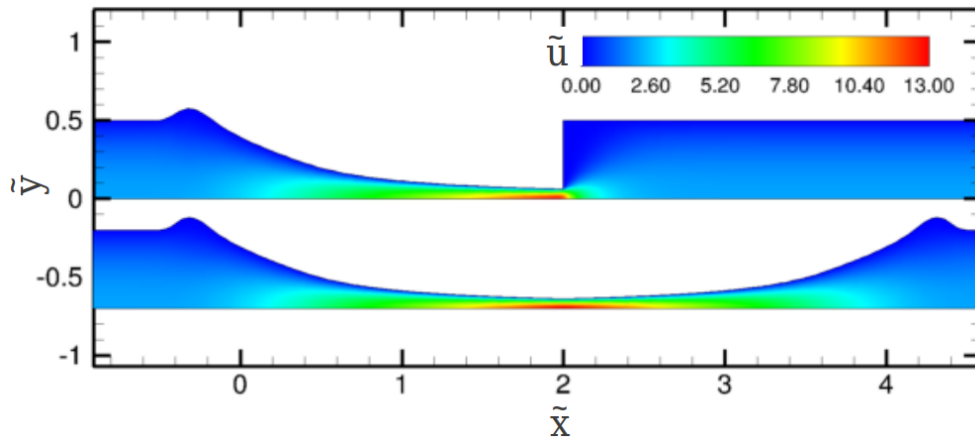


Figure B.1.2. Normalised velocity contour-plots for the optimised converging-abrupt (top-figure) and converging-diverging (bottom-figure) geometries at $Re = 1$.

a smooth contraction/abrupt expansion configuration similar to Oliveira *et al.* [74], would generate a large undershoot of the strain-rate in the vicinity of the expansion plane (as shown in Figure B.1.1b), due to the sudden decrease of the velocity along the centreline as shown in Figure B.1.1a. This behaviour would not be ideal for devices intended to produce homogeneous extension. Figure B.1.2 demonstrates the contour-plots of the normalised velocity on the streamwise direction for both designs.

B.2 Linear target profile

The study presented in Section 5.4.1 was performed considering a smoothed velocity profile at the transition region at the start and at the end of the contraction/expansion region. Here, the effect of the use of an abrupt transition profile at the start of the contraction and at the end of the expansion region on the shape of the optimised design and its performance is presented. The optimised solution when the abrupt transition is used as target, obtained for $n_2 = 0$ in Eq. (5.7), is shown in Fig. B.2.1a and the computed strain-rate profiles along the flow centreline are presented in Fig. B.2.1b. The zoomed inset of Fig. B.2.1a shows that the fluid velocity at the entrance of the converging region, and similarly at the end of the diverging part of the contraction, has higher values than the desired target. Therefore, the optimiser is searching for a solution to decrease their difference, in order to approximate the abrupt transition of the velocity

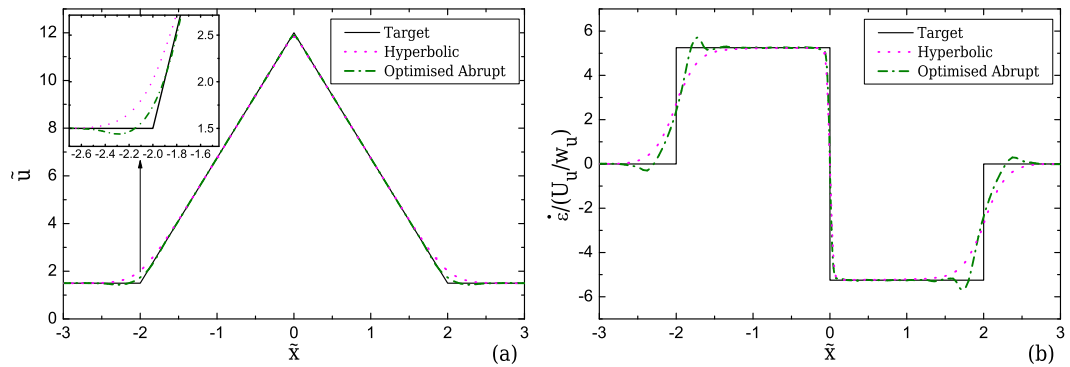


Figure B.2.1. Velocity (a) and strain-rate (b) profiles computed for creeping flow conditions along the centreline of the flow for the optimised geometry considering an abrupt transition profile and the ideal hyperbolic design (2D, $CR = 8$, $l_c = 2w_u$, $l_\varepsilon = 0$). The target velocity profile is represented as a *continuous line*.

profile in the best possible way, and thus minimise the value of the objective function Eq. (5.1). In this case, the boundary of the optimised device is shifted generating a bump, as shown in Fig. B.2.2. It is clear that even for the optimised geometry the instantaneous step changes in the strain-rate profile are difficult to attain (Fig. B.2.1b). As expected, the choice of the smoothed velocity profile used as target has a significant impact on the final shape of the optimised geometry, where the boundary shifting is significantly reduced as shown in Fig. B.2.2.

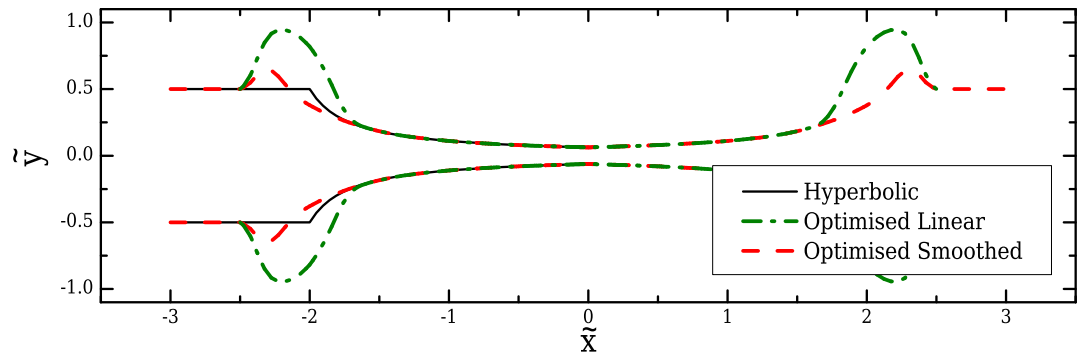


Figure B.2.2. Comparison between the optimised shapes obtained considering the abrupt transition profile (2D, $CR = 8$, $l_c = 2w_u$, $l_\varepsilon = 0$), the smoothed transition profile (2D, $CR = 8$, $l_c = 2w_u$, $l_\varepsilon = w_u$) and the ideal hyperbolic function.

B.3 Velocity profiles for increasing Re for other aspect ratios

The performance of the remaining, three dimensional, optimised converging/diverging geometries, discussed in Section 5.4.2, in terms of velocity and strain profiles along the flow centreline for increasing Reynolds numbers, are shown in Figs. B.3.1 to B.3.4. More specifically, Fig. B.3.1 corresponds to the design with $AR = 2$, Fig. B.3.2 to the design with $AR = 4$, Fig. B.3.3 to the design with $AR = 8$ and Fig. B.3.4 to the design with $AR = 32$.

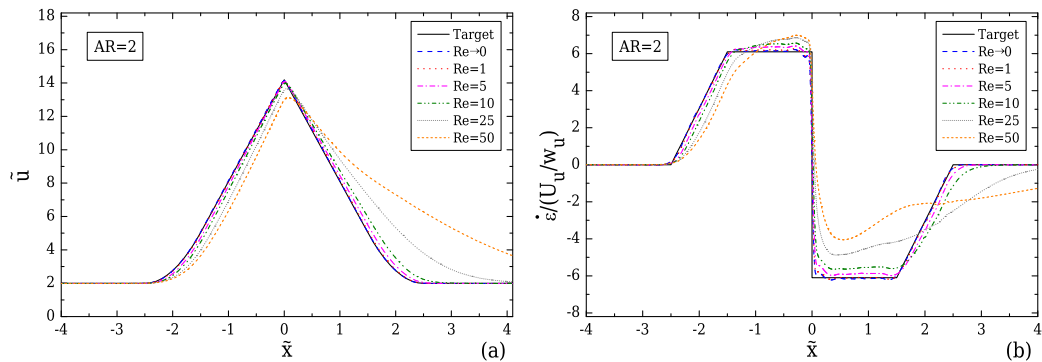


Figure B.3.1. Effect of Re on the velocity (a) and strain-rate (b) profiles computed along the flow centreline, for the optimised geometry with $l_c = 2w_u$, $l_\varepsilon = w_u$, $CR = 8$ for $AR = 2$ (Fig. 5.11c), considering Newtonian fluid flow.

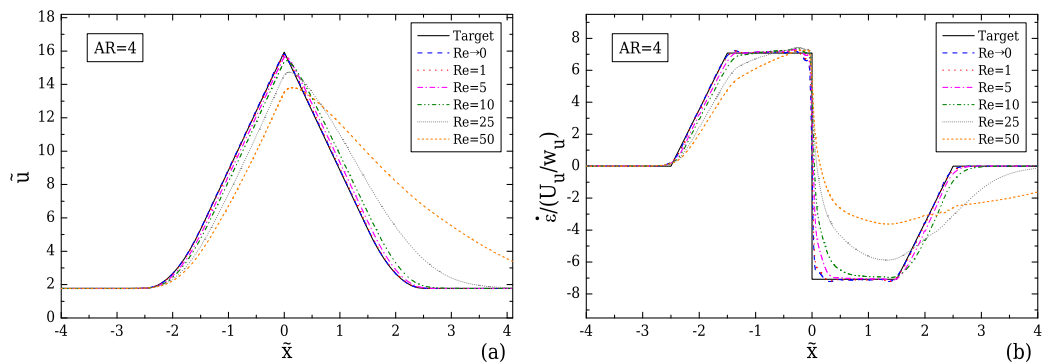


Figure B.3.2. Effect of Re on the velocity (a) and strain-rate (b) profiles computed along the flow centreline, for the optimised geometry with $l_c = 2w_u$, $l_\varepsilon = w_u$, $CR = 8$ for $AR = 4$ (Fig. 5.11d), considering Newtonian fluid flow.

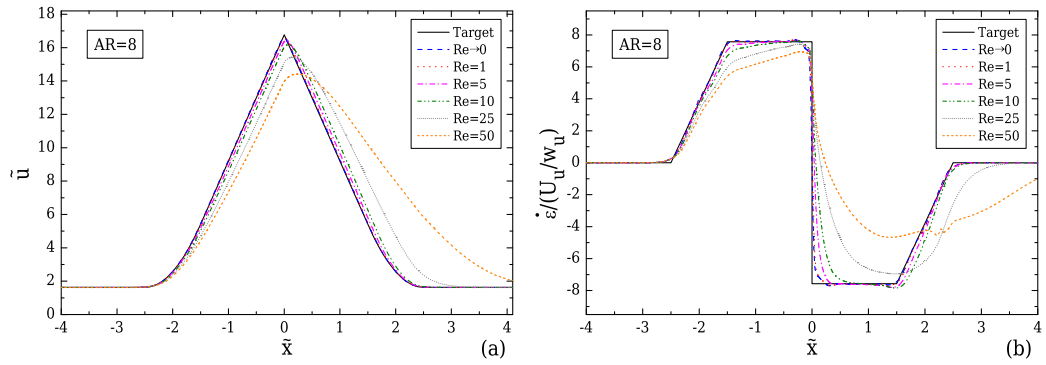


Figure B.3.3. Effect of Re on the velocity (a) and strain-rate (b) profiles computed along the flow centreline, for the optimised geometry with $l_c = 2w_u$, $l_\varepsilon = w_u$, $CR = 8$ for $AR = 8$ (Fig. 5.11e), considering Newtonian fluid flow.

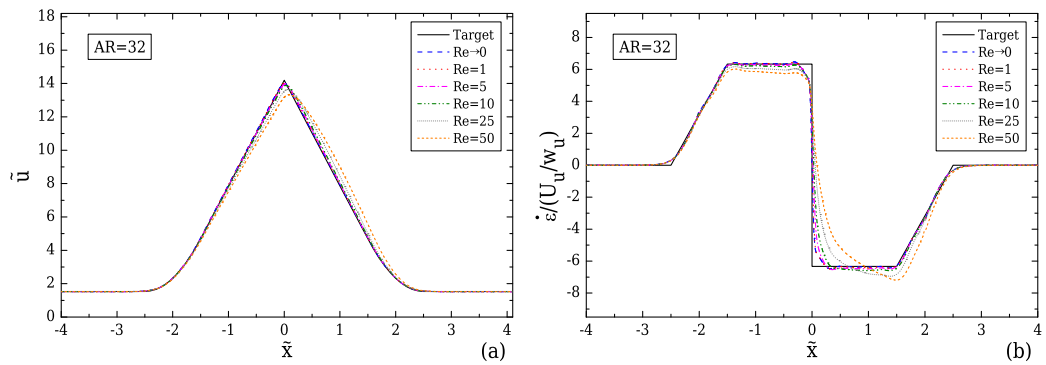


Figure B.3.4. Effect of Re on the velocity (a) and strain-rate (b) profiles computed along the flow centreline, for the optimised geometry with $l_c = 2w_u$, $l_\varepsilon = w_u$, $CR = 8$ for $AR = 32$ (Fig. 5.11f), considering Newtonian fluid flow.

B.4 Other aspect ratios for the 2D optimised shape for a T-junction

The optimised shape for a 2D T-junction geometry when the modified smooth velocity profile is used (Eq. (5.14)), presented in Section 5.5.1, will not necessarily perform ideally for 3D geometries since the kinematics of each geometry strongly depend from the value of the aspect ratio used. Figure B.4.1 illustrates the performance of the 2D shape for various aspect ratios in the range $0.1 \leq AR \leq 2$. It can be seen that for the case of $AR = 0.1$ the strain-rate profile is well approximated. However, when the depth of the device starts to decrease and becomes smaller than the width, the strain-rate

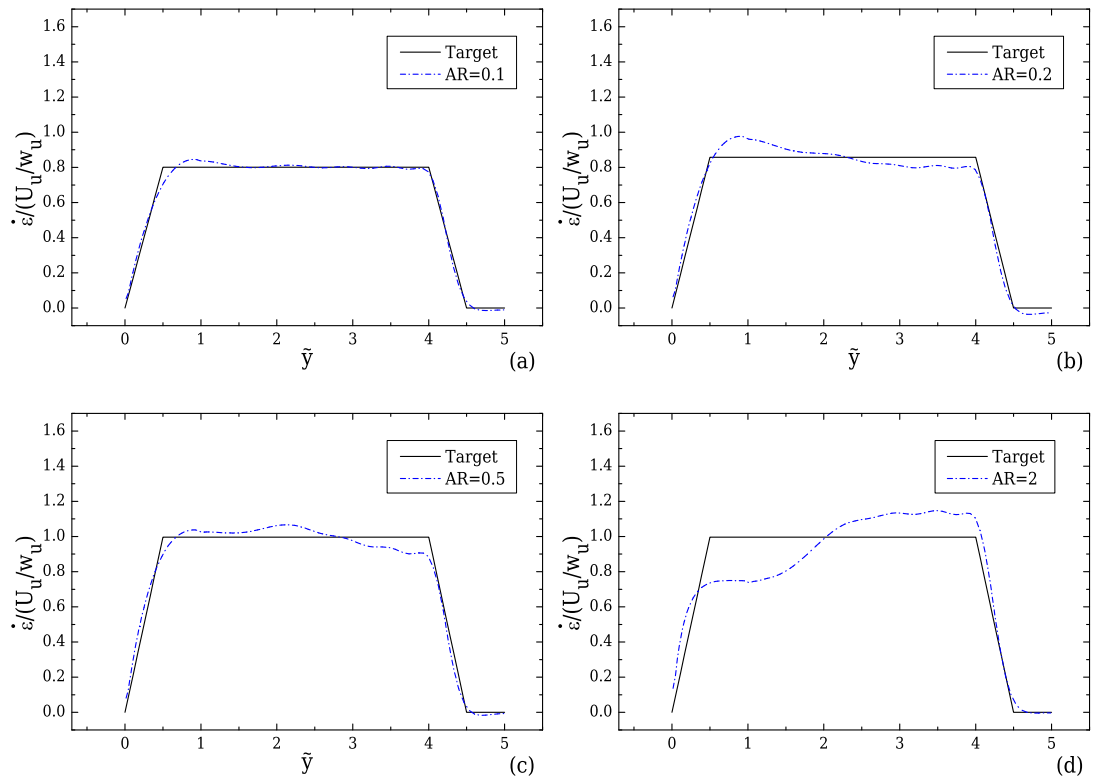


Figure B.4.1. Effect of the aspect ratio ($AR = w_u/d$) on the strain-rate profile computed along the flow centreline. The 3D geometries are designed using the 2D optimised shape for $AR = 0.1, 0.2, 0.5$ and 2 with $WR = 1$, $L_{\perp} = 4w_u$ and $l_{\varepsilon} = 0.5w_u$ considering creeping flow conditions.

profile will not obtain the desired behaviour and therefore, the 2D shape should not be used. Additionally this primary investigation is for the specific case of $WR = 1$, $L_{\perp} = 4w_u$ and $l_{\varepsilon} = 0.5w_u$ and therefore the limits for other configurations will be different.

Bibliography

- [1] J. F. V. Vincent, O. A. Bogatyreva, N. R. Bogatyrev, A. Bowyer, and A. K. Pahl, “Biomimetics: its practice and theory,” *J. R. Soc. Interface*, vol. 3, pp. 471–482, 2006.
- [2] H. A. Stone, A. D. Stroock, and A. Ajdari, “Engineering flows in small devices: Microfluidics toward a lab-on-a-chip,” *Annu. Rev. Fluid Mech.*, vol. 36, pp. 381–411, 2004.
- [3] G. M. Whitesides, “The origins and the future of microfluidics.,” *Nature*, vol. 442, pp. 368–373, 2006.
- [4] M. Faivre, M. Abkarian, K. Bickraj, and H. A. Stone, “Geometrical focusing of cells in a microfluidic device: An approach to separate blood plasma,” *Biorheology*, vol. 43, pp. 147–159, 2006.
- [5] H. W. Hou, A. A. S. Bhagat, W. C. Lee, S. Huang, J. Han, and C. T. Lim, “Microfluidic devices for blood fractionation,” *Micromachines*, vol. 2, pp. 319–343, 2011.
- [6] L. Choucha-Snouber, C. Aninat, L. Grsicom, G. Madalinski, C. Brochot, P. E. Poleni, F. Razan, C. G. Guillouzo, C. Legallais, A. Corlu, and E. Leclerc, “Investigation of Ifosfamide Nephrotoxicity Induced in a Liver–Kidney Co-Culture Biochip,” *Biotechnol. Bioeng.*, vol. 110, pp. 597–608, 2013.

- [7] D. Huh, B. D. Matthews, A. Mammoto, M. Montoya-Zavala, H. Y. Hsin, and D. E. Ingber, “Reconstituting Organ-Level Lung Functions on a Chip,” *Science*, vol. 328, pp. 1662–1668, 2010.
- [8] R. Riahi, A. Tamayol, S. A. M. Shaegh, A. M. Ghaemmaghami, M. R. Dokmeci, and A. Khademhosseini, “Microfluidics for advanced drug delivery systems,” *Curr. Opin. Chem. Eng.*, vol. 7, pp. 101–112, 2015.
- [9] M. S. N. Oliveira, M. A. Alves, and F. T. Pinho, *Microfluidic Flows of Viscoelastic Fluids*, ch. 6, pp. 131–174. Wiley-V C H Verlag GMBH, 2012.
- [10] C. J. Pipe and G. H. McKinley, “Microfluidic rheometry,” *Mechanics Research Communications*, vol. 36, pp. 110–120, 2009.
- [11] F. J. Galindo-Rosales, L. Campo-Deaño, P. C. Sousa, V. M. Ribeiro, M. S. N. Oliveira, M. A. Alves, and F. T. Pinho, “Viscoelastic instabilities in micro-scale flows,” *Exp. Therm. Fluid. Sci.*, vol. 59, pp. 128–139, 2014.
- [12] A. Groisman and S. R. Quake, “A Microfluidic Rectifier: Anisotropic Flow Resistance at Low Reynolds Numbers,” *Phys. Rev. Lett.*, vol. 92, p. 094501, 2004.
- [13] P. C. Sousa, F. T. Pinho, M. S. N. Oliveira, and M. A. Alves, “High performance microfluidic rectifiers for viscoelastic fluid flow,” *RSC Advances*, vol. 2, pp. 920–929, 2012.
- [14] J. Zilz, R. J. Poole, M. A. Alves, D. Bartolo, B. Levache, and A. Lindner, “Geometric scaling of a purely elastic flow instability in serpentine channels,” *J. Fluid. Mech.*, vol. 712, pp. 203–218, 2012.
- [15] J. Zilz, C. Schäfer, C. Wagner, R. J. Poole, M. A. Alves, and A. Lindner, “Serpentine channels: micro-rheometers for fluid relaxation times,” *Lab. Chip.*, vol. 14, pp. 351–358, 2013.
- [16] L. E. Rodd, T. P. Scott, D. V. Boger, J. J. Cooper-White, and G. H. McKinley, “The inertio-elastic planar entry flow of low-viscosity elastic fluids in micro-fabricated geometries,” *J. Non-Newton. Fluid Mech.*, vol. 129, pp. 1–22, 2005.

- [17] S. Nigen and K. Walters, “Viscoelastic contraction flows: comparison of axisymmetric and planar configuration,” *J. Non-Newton. Fluid Mech.*, vol. 102, pp. 343–359, 2002.
- [18] S. Drost and J. Westerweel, “Interaction effects in multi-outlet viscoelastic contraction flow,” *J. Non-Newton. Fluid Mech.*, vol. 213, pp. 31–38, 2014.
- [19] P. C. Sousa, F. T. Pinho, M. S. N. Oliveira, and M. A. Alves, “Purely elastic flow instabilities in microscale cross-slot devices,” *Soft Matter*, vol. 11, pp. 8856–8862, 2015.
- [20] J. Soulages, M. S. N. Oliveira, P. C. Sousa, M. A. Alves, and G. H. McKinley, “Investigating the stability of viscoelastic stagnation flows in T-shaped microchannels,” *J. Non-Newton. Fluid Mech.*, vol. 163, pp. 9–24, 2009.
- [21] M. S. N. Oliveira, F. T. Pinho, R. J. Poole, P. J. Oliveira, and M. A. Alves, “Purely elastic flow asymmetries in flow-focusing devices,” *J. Non-Newton. Fluid Mech.*, vol. 160, pp. 31–39, 2009.
- [22] M. S. N. Oliveira, F. T. Pinho, and M. A. Alves, “Divergent streamlines and free vortices in Newtonian fluid flows in microfluidic flow-focusing devices,” *J. Fluid Mech.*, vol. 771, pp. 171–191, 2012.
- [23] M. S. N. Oliveira, F. T. Pinho, and M. A. Alves, “Extensional flow of Newtonian and boger fluids through a flow focusing microdevice,” in *3rd Micro and Nano Flows Conference*, Thessaloniki, Greece, 22–24th August, 2011.
- [24] A. Huerre, V. Miralles, and M. Jullien, “Bubbles and foams in microfluidics,” *Soft Matter*, vol. 10, pp. 6888–6902, 2014.
- [25] S. L. Anna, “Droplets and bubbles in microfluidic devices,” *Annu. Rev. Fluid Mech.*, vol. 28, pp. 285–309, 2016.
- [26] C. G.F. and S. L. Anna, “Microfluidic methods for generating continuous droplet streams,” *J. Phys. D Appl. Phys.*, vol. 40, pp. R319–R336, 2007.

- [27] P. J. Oliveira, F. T. Pinho, and G. A. Pinto, “Numerical simulation of non-linear elastic flows with a general collocated finite-volume method,” *J. Non Newton. Fluid Mech.*, vol. 79, pp. 1–43, 1998.
- [28] K. Zografos, R. W. Barber, D. R. Emerson, and M. S. N. Oliveira, “A design rule for constant depth microfluidic networks for power-law fluids,” *Microfluid Nanofluid*, vol. 19, pp. 737–749, 2015.
- [29] K. Zografos, R. W. Barber, D. R. Emerson, and M. S. N. Oliveira, “Constant depth microfluidic networks based on a generalised Murray’s law for Newtonian and power-law fluids,” in *Proceedings of the 4th Micro and Nano Flows Conference*, 2014.
- [30] K. Zografos, F. Pimenta, M. A. Alves, and M. S. N. Oliveira, “Microfluidic converging/diverging channels optimised for homogeneous extensional deformation,” *Biomicrofluidics*, vol. 10, no. 043508, 2016.
- [31] R. B. Bird, R. C. Armstrong, and O. Hassager, *Dynamics of polymeric liquids. Volume 1: Fluid Dynamics*. John Wiley & Sons, New York, 1987.
- [32] M. Reiner, “The Deborah Number,” *Phys. Today*, vol. 17, p. 1, 1964.
- [33] H. A. Barnes, J. F. Hutton, and K. Walters, *An introduction to rheology*. Elsevier, Amsterdam, 1989.
- [34] F. A. Morrison, *Understanding Rheology*. Oxford University Press, Inc., 2001.
- [35] R. G. Owens and T. N. Phillips, *Computational Rheology*. Imperial College Press, 2002.
- [36] D. V. Boger, “A highly elastic constant-viscosity fluid,” *J. Non-Newton. Fluid Mech.*, vol. 3, pp. 87–91, 1977.
- [37] F. M. White, *Viscous Fluid Flow, 3rd Edition*. McGraw-Hill, 2006.

- [38] Y. S. Lee, E. D. Wetzel, and N. J. Wagner, “The ballistic impact characteristics of Kevlar woven fabrics impregnated with a colloidal shear thickening fluid,” *J. Mater. Sci.*, vol. 38, pp. 2825–2833, 2003.
- [39] M. J. Decker, C. J. Halbach, C. H. Nam, N. J. Wagner, and E. D. Wetzel, “Stab resistance of shear thickening fluid (STF)-treated fabrics,” *Compos. Sci. Technol.*, vol. 67, pp. 565–578, 2007.
- [40] F. A. Morrison, *An introduction to fluid mechanics*. Cambridge University Press, New York, 2013.
- [41] J. C. Maxwell, “On the Dynamical Theory of Gases,” *Phil. Trans. R. Soc. Lond.*, vol. 157, pp. 49–88, 1867.
- [42] J. Oldroyd, “An approach to non-Newtonian fluid mechanics,” *J. Non-Newton. Fluid*, vol. 14, pp. 9–46, 1984.
- [43] A. Morozov and S. E. Spagnolie, “Introduction to complex fluids,” in *Complex Fluids in Biological Systems*, pp. 3–52, Springer, 2015.
- [44] G. Prilutski, R. K. Gupta, T. Sridhar, and M. E. Ryan, “Model viscoelastic liquids,” *J. Non-Newton. Fluid Mech.*, vol. 12, pp. 233–241, 1983.
- [45] D. F. James, “Boger Fluids,” *Annu. Rev. Fluid Mech.*, vol. 41, pp. 129–142, 2009.
- [46] N. Phan-Thien and R. I. Tanner, “A new constitutive equation derived from network theory,” *J. Non-Newton. Fluid Mech.*, vol. 2, pp. 353–365, 1977.
- [47] N. Phan-Thien, “A nonlinear network viscoelastic model,” *J. Rheol.*, vol. 22, pp. 259–283, 1978.
- [48] M. A. Alves, F. T. Pinho, and P. J. Oliveira, “Study of steady pipe and channel flows of a single-mode Phan-Thien-Tanner fluid,” *J. Non-Newton. Fluid Mech.*, vol. 101, pp. 55–76, 2001.

- [49] P. J. Oliveira and F. T. Pinho, “Analytical solution for fully developed channel and pipe flow of Phan-Thien-Tanner fluids,” *J. Fluid. Mech.*, vol. 387, pp. 271–280, 1999.
- [50] R. B. Bird, R. C. Armstrong, and O. Hassager, *Dynamics of polymeric liquids. Volume 2: Kinetic Theory*. John Wiley & Sons, New York, 1987.
- [51] R. J. Poole, “The Deborah and Weissenberg numbers,” *Rheol. Bull.*, vol. 53, pp. 32–39, 2012.
- [52] J. L. White, “Dynamics of viscoelastic fluids, melt fracture and the rheology of fiber spinning,” *J. Appl. Polymer Sci.*, vol. 8, pp. 2339–2357, 1964.
- [53] G. H. McKinley, “Dimensionless groups for understanding free surface flows of complex fluids,” *SOR Reology Bulletin*, vol. 74, 2005.
- [54] J. Dealy, “Weissenberg and Deborah numbers - Their definition and use,” *Rheol. Bull.*, vol. 79, pp. 14–18, 2010.
- [55] A. Prosperetti and G. Tryggvason, eds., *Computational methods for multiphase flow*. Cambridge University Press, 2006.
- [56] Y. Zhang and H. Liu, *Microdroplet technology: principles and emerging applications in biology and chemistry*, ch. Physics of Multiphase Microflows and Microdroplets, pp. 1–21. Springer New York, 2012.
- [57] P. Yue, C. Zhou, and J. J. Feng, “Spontaneous shrinkage of drops and mass conservation in phase-field simulations,” *J. Comput. Phys.*, vol. 223, pp. 1–9, 2007.
- [58] H. Ding, P. D. M. Spelt, and C. Shu, “Diffuse interface model for incompressible two-phase flows with large density ratios,” *J. Comput. Phys.*, vol. 226, pp. 2078–2095, 2007.
- [59] J. H. Ferziger and M. Perić, *Computational Methods for Fluid Dynamics*. Springer Berlin Heidelberg, 2002.

- [60] S. V. Patankar, *Numerical Heat Transfer and Fluid Flow*. McGraw-Hill, 1980.
- [61] F. Moukalled, L. Mangani, and M. Darwish, *The finite volume method in computational fluid dynamics*. Springer International Publishing, 2016.
- [62] M. Schäfer, *Computational Engineering - Introduction to Numerical Methods*. Springer Berlin Heidelberg, 2006.
- [63] P. Sölin, *Partial Differential Equations and the Finite Element Method*. Blackwell Science Publ, Osney Mead, Oxford OX2 0EL, England, 2006.
- [64] W. Malalasekera and H. Versteeg, *An Introduction to fluid dynamics. The finite Volume method*. Longman Scientific & Technical, 1995.
- [65] M. A. Alves, *Laminar flow of viscoelastic fluids: numerical, theoretical and experimental analysis*. PhD thesis, (in portuguese), Faculty of Engineering, Universidade do Porto, 2004.
- [66] P. J. Oliveira, *Computer modeling of multidimensional multiphase flow and applications to T-Junctions*. PhD thesis, Imperial Colege, University of London, 1992.
- [67] P. J. Oliveira and F. T. Pinho, “Numerical procedure for the computation of fluid flow with arbitrary stress-strain relationship,” *Numer. Heat Tr. B-Fund.*, vol. 35, pp. 295–315, 1999.
- [68] P. J. Oliveira, “Method for time-dependent simulations of viscoelastic flows: vortex shedding behind cylinder,” *J. Non-Newton. Fluid Mech.*, vol. 101, pp. 113–137, 2001.
- [69] P. J. Oliveira, “Asymmetric flows of viscoelastic fluids in symmetric planar expansion geometries,” *J. Non-Newton. Fluid Mech.*, vol. 114, pp. 33–63, 2003.
- [70] P. J. Oliveira, “Asymmetric flows of viscoelastic fluids in symmetric planar expansion geometries,” *J. Non-Newton. Fluid Mech.*, vol. 114, pp. 33–63, 2003.

- [71] M. A. Alves, P. J. Oliveira, and F. T. Pinho, “Benchmark solutions for the flow of Oldroyd-B and PTT fluids in planar contractions,” *J. Non-Newton. Fluid Mech.*, vol. 110, pp. 45–75, 2003.
- [72] A. Afonso and F. T. Pinho, “Numerical investigation of the velocity overshoots in the flow of viscoelastic fluids inside a smooth contraction,” *J. Non-Newton. Fluid Mech.*, vol. 139, pp. 1–20, 2006.
- [73] M. A. Alves and R. J. Poole, “Divergent flow in contractions,” *J. Non-Newton. Fluid Mech.*, vol. 144, pp. 140–148, 2007.
- [74] M. S. N. Oliveira, M. A. Alves, F. T. Pinho, and G. H. McKinley, “Viscous Flow through microfabricated hyperbolic contractions,” *Exp. Fluids*, vol. 43, pp. 437–451, 2007.
- [75] R. J. Poole, M. A. Alves, P. J. Oliveira, and F. T. Pinho, “Plane sudden expansion flows of viscoelastic liquids,” *J. Non-Newton. Fluid Mech.*, vol. 146, pp. 79–91, 2007.
- [76] R. J. Poole, F. T. Pinho, M. A. Alves, and P. J. Oliveira, “The effect of expansion ratio for creeping expansion flows of UCM fluids,” *J. Non-Newton. Fluid Mech.*, vol. 163, pp. 35–44, 2009.
- [77] S. J. Haward, M. S. N. Oliveira, M. A. Alves, F. T. Pinho, and G. H. McKinley, “Optimised cross-slot flow geometry for microfluidic extensional rheometry,” *Physical Review Letters*, vol. 109, 2012.
- [78] S. Dhinakaran, M. S. N. Oliveira, F. T. Pinho, and M. A. Alves, “Steady flow of power-law fluids in a 1:3 planar sudden expansion,” *J. Non-Newtonian Fluid Mech*, vol. 198, pp. 48–58, 2013.
- [79] F. A. Cruz, R. J. Poole, A. M. Afonso, F. T. Pinho, P. J. Oliveira, and M. A. Alves, “Influence of channel aspect ratio on the onset of purely-elastic flow instabilities in three-dimensional planar cross-slots,” *J. Non-Newton. Fluid Mech.*, vol. 227, pp. 65–79, 2016.

- [80] G. A. Pinto, “Development of a numerical simulation program for the calculation of laminar flows with non-linear elastic fluids,” Master’s thesis, University of Porto, 1996.
- [81] S. V. Patankar and D. B. Spalding, “Calculation procedure for heat, mass and momentum-transfer in three-dimensional parabolic flows,” *Int. J. Heat Mass Tran.*, vol. 15, pp. 1787–1806, 1972.
- [82] J. P. Van Doormal and G. D. Raithby, “Enhancements of the SIMPLE method for predicting incompressible fluid flows,” *Numer. Heat Transfer*, vol. 7, pp. 147–163, 1984.
- [83] M. Peric, R. Kessler, and G. Scheuerer, “Comparison of finite volume numerical method with staggered and colocated grids,” *Comput. Fluids*, vol. 16, pp. 389–403, 1988.
- [84] M. Peric, I. Demirdzic, and Z. Lilek, “A colocated finite volume method for predicting flows at all speeds,” *Int. J. Numer. Meth. Fl.*, vol. 16, pp. 1029–1050, 1993.
- [85] C. M. Rhie and W. L. Chow, “Numerical study of the turbulent flow past an airfoil with trailing edge separation.,” *AIAA J.*, vol. 21, pp. 1525–1532, 1983.
- [86] M. Peric, *A finite volume method for the prediction of three-dimensional fluid flow in complex ducts*. PhD thesis, Imperial College, University of London, 1985.
- [87] B. P. Leonard, “A stable and accurate convection modeling procedure based on quadratic upstream interpolation,” *Computer Methods in Applied Mechanics and Engineering*, vol. 19, pp. 59–98, 1979.
- [88] A. Harten, “High resolution schemes for hyperbolic conservation laws,” *J. Comput. Phys.*, vol. 49, pp. 357–393, 1983.
- [89] B. P. Leonard, “Simple high-accuracy resolution program for convective modelling of discontinuities.,” *Int. J. Numer. Meth. Fl.*, vol. 8, pp. 1291–1318, 1988.

- [90] B. P. Leonard, “The ULTIMATE conservative difference scheme applied to unsteady one-dimensional advection,” *Comput. Method. Appl. M.*, vol. 88, pp. 17–74, 1991.
- [91] M. S. Darwish and F. H. Moukalled, “Normalized variable and space formulation methodology for high-resolution schemes,” *Numer. Heat Tr. B-Fund.*, vol. 26, pp. 79–96, 1994.
- [92] P. H. Gaskell and A. K. C. Lau, “Curvature compensated convective transport: SMART, a new boundedness preserving transport algorithm,” *Int. J. Numer. Meth. Fl.*, vol. 8, pp. 617–641, 1988.
- [93] M. A. Alves, P. J. Oliveira, and F. T. Pinho, “A convergent and universally bounded interpolation scheme for the treatment of advection,” *Int. J. Numer. Meth. Fluids*, vol. 41, pp. 47–75, 2003.
- [94] P. K. Khosla and S. G. Rubin, “A diagonally dominant second order accurate implicit scheme,” *Comput. Fluids*, vol. 2, pp. 207–209, 1974.
- [95] W. J. Minkowycz, E. M. Sparrow, and J. Y. Murthy, eds., *Handbook of numerical heat transfer (second edition)*. John Wiley & Sons, Inc., 2006.
- [96] R. I. Issa and P. J. Oliveira, “Numerical prediction of phase separation in two phase flow through T-junctions,” *Comput. Fluids*, vol. 23, pp. 347–372, 1994.
- [97] J. F. Thomson, B. K. Soni, and N. P. Weatherill, *Handbook of Grid Generation*. CRC Press LLC, 1999.
- [98] P. J. Oliveira, *Manual for MESH3D: A three-dimensional mesh generator*.
- [99] D. F. Rogers, *An Introduction To Nurbs*. Elsevier, 2001.
- [100] L. Piegl and W. Tiller, *The Nurbs Book*. Springer, 1996.
- [101] W. K. Anderson and V. Venkatakrishnan, “Aerodynamic design optimization on unstructured grids with a continuous adjoint formulation,” *Comput. Fluids*, vol. 28, pp. 443–480, 1999.

- [102] K. C. Giannakoglou, "Design of optimal aerodynamic shapes using stochastic optimization methods and computational intelligence," *Prog. Aerosp. Sci.*, vol. 38, pp. 43–76, 2002.
- [103] S. Pierret and R. A. Van den Braembussche, "Turbomachinery Blade Design Using a Navier-Stokes Solver and Artificial Neural Network," *J. Turbomach.*, vol. 121, pp. 326–332, 1999.
- [104] G. E. Farin, *Curves and surfaces for computer aided geometric design*. Academic Press, 1996.
- [105] T. W. Sederberg and S. R. Parry, "Free Form Deformation of Solid Geometric Models," *Computer Graphics*, vol. 20, pp. 151–160, 1986.
- [106] J. F. Hughes and H. Kaufman, "Direct Manipulation of Free - Form Deformations," *Computer Graphics*, pp. 177–184, 1992.
- [107] H. J. Lamousin and W. N. Waggenspack, "NURBS-based free-form deformations," *IEEE Comput. Graph.*, vol. 14, pp. 59–65, 1994.
- [108] C. D. Boor, "On calculating with B-splines," *Journal of Approximation Theory*, vol. 6, pp. 50–62, 1972.
- [109] T. J. R. Hughes, J. A. Cottrell, and Y. Bazilevs, "Geometric analysis: CAD, finite elements, NURBS, exact geometry and refinement," *Comput. Methods Appl. Mech. Engrg.*, vol. 194, pp. 4135–4195, 2005.
- [110] T.-Y. Yu and B. K. Soni, "Application of NURBS in numerical grid generation," *Computer-Aided Design*, vol. 27, pp. 147–157, 1995.
- [111] A. M. Shih, T.-Y. Yu, S. Gopalsamy, Y. Ito, and B. Soni, "Geometry and mesh generation for high fidelity computational simulations using non-uniform rational B-splines.," *Applied Numerical Mathematics*, vol. 55, p. 368–381, 2005.
- [112] E. Dimas and D. Briassoulis, "3D geometric modelling based on NURBS: a review," *Advances in Engineering Software*, vol. 30, p. 741–751, 1999.

- [113] D. Terzopoulos and H. Qin, “Dynamic NURBS with Geometric Constraints for Interactive Sculpting,” *ACM Transactions on Graphics*, vol. 13, pp. 103–136, 1994.
- [114] T. J. R. Hughes, A. Reali, and G. Sangalli, “Duality and unified analysis of discrete approximations in structural dynamics and wave propagation: Comparison of p-method finite elements with k-method NURBS,” *Comput. Methods Appl. Mech. Engrg.*, vol. 197, p. 4104–4124, 2008.
- [115] D. Wang and J. Xuan, “An improved NURBS-based isogeometric analysis with enhanced treatment of essential boundary conditions,” *Comput. Methods Appl. Mech. Engrg.*, vol. 199, pp. 2425–2436, 2010.
- [116] K. A. McCulloh, J. S. Sperry, and F. R. Adler, “Water transport in plants obeys Murray’s Law,” *Nature*, vol. 421, pp. 939–942, 2003.
- [117] P. Domachuk, K. Tsioris, F. G. Omenetto, and D. L. Kaplan, “Bio-microfluidics: Biomaterials and Biomimetic Designs,” *Adv. Mater.*, vol. 22, pp. 249–260, 2010.
- [118] X. J. Li, A. S. Popel, and G. E. Karniadakis, “Blood-plasma separation in Y-shaped bifurcating microfluidic channels: a dissipative particle dynamics simulation study,” *Phys. Biol.*, vol. 9, no. 026010, 2012.
- [119] S. Tripathi, A. Prabhakar, N. Kumar, S. G. Singh, and A. Agrawal, “Blood plasma separation in elevated dimension T-shaped microchannel,” *Biomed. Microdevices*, vol. 15, pp. 415–425, 2013.
- [120] S. Yang, A. Undar, and J. D. Zahn, “A microfluidic device for continuous, real time blood plasma separation,” *Lab Chip*, vol. 6, pp. 871–880, 2006.
- [121] J. A. Potkay, M. Magnetta, A. Vinson, and B. Cmolik, “Bio-inspired, efficient, artificial lung employing air as the ventilating gas,” *Lab Chip*, vol. 11, pp. 2901–2909, 2011.
- [122] T. Kniazeva, A. A. Epshteyn, J. C. Hsiao, E. S. Kim, V. B. Kolachalama, J. L. Charest, and J. T. Borenstein, “Performance and scaling effects in a multilayer mi-

- crofluidic extracorporeal lung oxygenation device.,” *Lab Chip*, vol. 12, pp. 1686–1695, 2012.
- [123] Q. Zhang and R. H. Austin, “Applications of Microfluidics in Stem Cell Biology,” *BioNanoScience.*, vol. 2, pp. 277–286, 2012.
- [124] D. Huh, Y. Torisawa, G. A. Hamilton, H. J. Kim, and D. E. Ingber, “Microengineered physiological biomimicry: Organs-on-Chips,” *Lab Chip*, vol. 12, pp. 2156–2164, 2012.
- [125] A. Hasan, A. Paul, N. E. Vrana, X. Zhao, A. Memic, Y. S. Hwang, M. R. Dokmeci, and A. Khademhosseini, “Microfluidic techniques for development of 3D vascularized tissue,” *Biomaterials*, vol. 35, pp. 7308–7325, 2014.
- [126] D. Pinho, T. Yaginuma, and R. Lima, “A microfluidic device for partial cell separation and deformability assessment.,” *BioChip J.*, vol. 7, pp. 367–374, 2013.
- [127] R. Lima, S. Wada, S. Tanaka, M. Takeda, T. Ishikawa, K. I. Tsubota, Y. Imai, and T. Yamaguchi, “In vitro blood flow in a rectangular PDMS microchannel: experimental observations using a confocal micro-PIV system,” *Biomed Microdevices*, vol. 10, pp. 153–167, 2008.
- [128] T. M. DesRochers, E. Palma, and D. L. Kaplan, “Tissue-engineered kidney disease models.,” *Adv Drug Deliver Rev*, vol. 69, pp. 67–80, 2014.
- [129] S. K. W. Dertinger, D. T. Chiu, N. L. Jeon, and G. M. Whitesides, “Generation of gradients having complex shapes using microfluidic networks,” *Anal. Chem.*, vol. 73, pp. 1240–1246, 2001.
- [130] N. L. Jeon, S. K. W. Dertinger, D. T. Chiu, I. S. Choi, A. D. Stroock, and G. M. Whitesides, “Generation of solution and surface gradients using microfluidic systems,” *Langmuir*, vol. 16, pp. 8311–8316, 2000.
- [131] Y. X. Hu, X. R. Zhang, and W. C. Wang, “Simulation of the generation of solution gradients in microfluidic systems using the lattice Boltzmann method,” *Ind. Eng. Chem. Res.*, vol. 50, pp. 13932–13939, 2011.

- [132] D. B. Weibel and G. M. Whitesides, “Applications of microfluidics in chemical biology,” *Curr. Opin. Chem. Biol.*, vol. 10, pp. 584–591, 2006.
- [133] J. J. Brandner, “Microstructure devices for process intensification: Influence of manufacturing tolerances and design,” *Appl Therm Eng*, vol. 59, pp. 745–752, 2013.
- [134] W. X. Liao, N. Wang, T. S. Wang, J. Xu, X. D. Han, Z. Y. Liu, X. M. Zhang, and W. X. Yu, “Biomimetic microchannels of planar reactors for optimized photocatalytic efficiency of water purification,” *Biomicrofluidics*, vol. 10, p. 014123, 2016.
- [135] C. D. Murray, “The physiological principle of minimum work: I. The vascular system and the cost of blood volume,” *Proc. Natl. Acad. Sci. USA*, vol. 12, pp. 207–214, 1926.
- [136] H. S. Damiri and H. K. Bardaweel, “Numerical design and optimization of hydraulic resistance and wall shear stress inside pressure-driven microfluidic networks,” *Lab Chip*, vol. 10, pp. 4187–4196, 2015.
- [137] A. Bejan, “The constructal law of organization in nature: tree-shaped flows and body size,” *J. Exp. Biol.*, vol. 208, pp. 1677–1686, 2005.
- [138] A. Bejan and S. Lorente, “Constructal theory of generation of configuration in nature and engineering,” *J. Appl. Phys.*, p. doi: 10.1063/1.2221896, 2006.
- [139] D. R. Emerson, K. Cieslicki, X. J. Gu, and R. W. Barber, “Biomimetic design of microfluidic manifolds based on a generalised Murray’s law,” *Lab Chip*, vol. 6, pp. 447–454, 2006.
- [140] R. W. Barber and D. R. Emerson, “Optimal design of microfluidic networks using biologically inspired principles,” *Microfluid Nanofluid*, vol. 4, pp. 179–191, 2008.
- [141] A. B. Metzner and J. C. Reed, “Flow of non-Newtonian fluids - correlation of the laminar, transition and turbulent flow regimes,” *A.I.Ch.E.*, vol. 1, pp. 434–440, 1955.

- [142] W. Kozicki, C. H. Chou, and C. Tiu, “Non-Newtonian flow in ducts of arbitrary cross-sectional shape,” *Chem. Eng. Sci.*, vol. 21, pp. 665–679, 1966.
- [143] W. M. Rohsenow, J. P. Hartnett, and Y. Cho, eds., *Handbook of heat transfer*. McGraw-Hill, 1998.
- [144] J. Hartnett and M. Kostic, “Heat transfer to Newtonian and non-Newtonian fluids in rectangular ducts,” *Adv Heat Transfer*, vol. 19, pp. 247–356, 1989.
- [145] Y. Son, “Determination of shear viscosity and shear rate from pressure drop and flow rate relationship in a rectangular channel,” *Polymer*, vol. 48, pp. 632–637, 2007.
- [146] B. J. West, *Fractal physiology and chaos in medicine*. World Scientific, Singapore, 1990.
- [147] X. B. Liu, M. Wang, J. Meng, E. Ben-Naim, and Z. Y. Guo, “Minimum entransy dissipation principle for optimization of transport networks,” *Int. J. Nonlin. Sci. Num. Sim.*, vol. 11, pp. 113–120, 2010.
- [148] X. D. Shan, M. Wang, and Z. Y. Guo, “Geometry optimization of self-similar transport network,” *Math. Probl. Eng.*, no. 421526, 2011.
- [149] B. J. Kirby, *Micro- and Nanoscale Fluid Mechanics: Transport in Microfluidic Devices*. Cambridge University Press, 2010.
- [150] W. H. Press, S. A. Teukolsky, W. T. Vetterling, and B. P. Flannery, *Numerical Recipes in Fortran 77: The art of scientific computing*. Cambridge University Press, 1992.
- [151] J. Fidalgo, *Private communication*, 2016.
- [152] P. Pakdel and G. H. Mckinley, “Elastic instability and curved streamlines,” *Phys. Rev. Lett.*, vol. 77, pp. 2459–2462, 1996.

- [153] F. J. Galindo-Rosales, M. S. N. Oliveira, and M. A. Alves, “Microdevices for extensional rheometry of low viscosity elastic liquids: a review,” *Microfluid Nanofluid*, vol. 14, pp. 1–19, 2013.
- [154] S. J. Haward, “Microfluidic extensional rheometry using stagnation point flow,” *Biomicrofluidics*, vol. 10, no. 043401, 2016.
- [155] E. K. Sackmann, A. L. Fulton, and D. J. Beebe, “The present and future role of microfluidics in biomedical research,” *Nature*, vol. 507, pp. 181–189, 2014.
- [156] P. C. Sousa, F. T. Pinho, M. A. Alves, and M. S. N. Oliveira, “A review of hemorheology: Measuring techniques and recent advances,” *Korea-Aust. Rheol. J.*, vol. 28, pp. 1–22, 2016.
- [157] L. Shui, J. C. T. Eijkel, and A. van den Berg, “Multiphase flow in microfluidic systems - Control and applications of droplets and interfaces,” *Adv. Colloid Interface Sci.*, vol. 133, pp. 35–49, 2007.
- [158] G. Velve-Casquillas, M. L. Berre, M. Piel, and P. T. Tran, “Microfluidic tools for cell biological research,” *Nano Today*, vol. 5, pp. 28–47, 2010.
- [159] M. K. Mulligan and J. P. Rothstein, “The effect of confinement-induced shear on drop deformation and breakup in microfluidic extensional flows,” *Phys. Fluids*, vol. 23, no. 022004, 2011.
- [160] D. J. Mai, C. Brockman, and C. M. Schroeder, “Microfluidic systems for single DNA dynamics,” *Soft Matter*, vol. 8, pp. 10560–10572, 2012.
- [161] D. R. Gossett, H. T. K. Tse, S. A. Lee, Y. Ying, A. G. Lindgren, O. O. Yang, J. Rao, A. T. Clark, and D. D. Carlo, “Hydrodynamic stretching of single cells for large population mechanical phenotyping,” *Proc. Natl. Acad. Sci. U.S.A.*, vol. 109, no. 7630, 2012.
- [162] J. P. Rothenstein and G. H. McKinley, “The axisymmetric contraction-expansion: The role of extensional rheology on vortex growth dynamics and the enhanced pressure drop,” *J. Non-Newton. Fluid Mech.*, vol. 98, pp. 33–63, 2001.

- [163] O. Hassager, “Working group on numerical techniques (Vth Workshop on Numerical Methods in Non-Newtonian Flow),” *J. Non-Newton. Fluid Mech.*, vol. 29, pp. 2–5, 1988.
- [164] D. V. Boger, “Circular entry flows of inelastic and viscoelastic fluids,” *In: Mujumdar A. S. , Mashelkar R. A. (eds) Advances of transport processes, vol 2. Wiley Eastern, New Delhi*, pp. 43–98, 1987.
- [165] L. E. Rodd, J. J. Cooper-White, D. V. Boger, and G. H. McKinley, “Role of the elasticity number in the entry flow of dilute polymer solutions in micro-fabricated contraction geometries,” *J. Non-Newton. Fluid Mech.*, vol. 143, pp. 170–191, 2007.
- [166] T. J. Ober, S. J. Haward, C. J. Pipe, J. Soulages, and G. H. McKinley, “Microfluidic extensional rheometry using a hyperbolic contraction geometry,” *Rheol Acta*, vol. 52, pp. 529–546, 2013.
- [167] M. S. N. Oliveira, L. E. Rodd, G. H. McKinley, and M. A. Alves, “Simulations of extensional flow in microrheometric devices,” *Microfluid Nanofluid*, vol. 5, pp. 809–826, 2008.
- [168] F. N. Cogswell, “Converging flow and stretching flow: a compilation,” *J. Non-Newton. Fluid Mech.*, vol. 4, pp. 23–38, 1978.
- [169] F. N. Cogswell, “Measuring the extensional rheology of polymer melts,” *T. Soc. Rheol.*, vol. 16, pp. 383–403, 1972.
- [170] D. F. James, G. M. Chandler, and S. J. Armour, “A converging channel rheometer for the measurement of extensional viscosity,” *J. Non-Newton. Fluid Mech.*, vol. 35, pp. 421–443, 1990.
- [171] G. H. McKinley, L. E. Rodd, M. S. N. Oliveira, and J. J. Cooper-White, “Extensional flows of polymer solutions in microfluidic converging/diverging geometries,” *J. Cent. South Univ. T.*, vol. 14, pp. 6–9, 2007.

- [172] L. Campo-Deaño, F. J. Galindo-Rosales, F. T. Pinho, M. A. Alves, and M. S. N. Oliveira, “Flow of low viscosity Boger fluids through a microfluidic hyperbolic contraction,” *J. Non-Newton. Fluid Mech.*, vol. 166, pp. 1286–1296, 2011.
- [173] P. C. Sousa, F. T. Pinho, M. S. N. Oliveira, and M. A. Alves, “Extensional flow of blood analog solutions in microfluidic devices,” *Biomicrofluidics*, vol. 5, no. 014108, 2011.
- [174] R. O. Rodrigues, D. Pinho, V. Faustino, and R. Lima, “A simple microfluidic device for the deformability assessment of blood cells in a continuous flow,” *Biomed. Microdevices*, vol. 17, no. 108, 2015.
- [175] S. S. Lee, Y. Yim, K. H. Ahn, and S. J. Lee, “Extensional flow-based assessment of red blood cell deformability using a hyperbolic converging microchannel,” *Biomed. Microdevices*, vol. 11, pp. 1021–1027, 2009.
- [176] T. Yaginuma, M. S. N. Oliveira, R. Lima, T. Ishikawa, and T. Yamaguchi, “Human red blood cell behavior under homogeneous extensional flow in a hyperbolic-shaped microchannel,” *Biomicrofluidics*, vol. 7, no. 054110, 2013.
- [177] T. Wu and J. J. Feng, “Simulation of malaria-infected red blood cells in microfluidic channels: Passage and blockage,” *Biomicrofluidics*, vol. 7, no. 044115, 2013.
- [178] B. Keshavarz and G. H. McKinley, “Micro-scale extensional rheometry using hyperbolic converging/diverging channels and jet breakup,” *Biomicrofluidics*, vol. 10, no. 043502, 2016.
- [179] B. Keshavarz, V. Sharma, E. C. Houze, M. R. Koerner, J. R. Moore, P. M. Cotts, P. Threlfall-Holmes, and G. H. McKinley, “Studying the effects of elongational properties on atomization of weakly viscoelastic solutions using Rayleigh Ohnesorge Jetting Extensional Rheometry (ROJER),” *J. Non-Newton. Fluid Mech.*, vol. 222, pp. 171–189, 2015.

- [180] G. I. Taylor, “The formation of emulsions in definable fields of flow,” *Proc. R. Soc. Lond.*, vol. 146, p. 501–523, 1934.
- [181] S. D. Hudson, F. R. Phelan, M. D. Handler, J. T. Cabral, K. B. Migler, and E. J. Amis, “Microfluidic analog of the four-roll mill,” *Appl. Phys. Lett.*, vol. 85, pp. 335–337, 2004.
- [182] J. S. Lee, R. Dylla-Spears, N. P. Teclemariam, and S. J. Muller, “Microfluidic four-roll mill for all flow types,” *Appl. Phys. Lett.*, vol. 90, no. 074103, 2007.
- [183] P. E. Arratia, C. C. Thomas, J. Diorio, and J. P. Gollub, “Elastic instabilities of polymer solutions in cross-channel Flow,” *Phys. Rev. Lett.*, vol. 96, no. 144502, 2006.
- [184] S. J. Haward, T. J. Ober, M. S. N. Oliveira, M. A. A. MA, and G. H. McKinley, “Extensional rheology and elastic instabilities of a wormlike micellar solution in a microfluidic cross-slot device,” *Soft Matter*, vol. 8, pp. 536–555, 2012.
- [185] R. J. Poole, M. A. Alves, and P. J. Oliveira, “Purely elastic flow assymetries,” *Phys. Rev. Lett.*, vol. 99, no. 164503, 2007.
- [186] A. M. Afonso, F. T. Pinho, and M. A. Alves, “Purely elastic instabilities in three-dimensional cross-slot geometries,” *J. Non-Newton. Fluid Mech.*, vol. 165, pp. 743–751, 2010.
- [187] R. Dylla-Spears, J. E. Townsend, L. Jen-Jacobson, L. L. Sohn, and S. J. Muller, “Single-molecule sequence detection via microfluidic planar extensional flow at a stagnation point,” *Lab Chip*, vol. 2010, pp. 1543–1549, 2010.
- [188] S. Cha, T. Shin, S. S. Lee, W. Shim, G. Lee, S. J. Lee, Y. Kim, and J. M. Kim, “Cell Stretching Measurement Utilizing Viscoelastic Particle Focusing,” *Anal. Chem.*, vol. 84, no. 10471, 2012.
- [189] S. J. Haward, R. J. Poole, M. A. Alves, P. J. Oliveira, N. Goldenfeld, and A. Q. Shen, “Tricritical spiral vortex instability in cross-slot flow,” *Phys. Rev. E*, vol. 93, no. 031101, 2016.

- [190] M. A. Alves, “Design a cross-slot flow channel for extensional viscosity measurements,” in *AIP Conf Proc*, vol. 1027, pp. 240–242, 2008.
- [191] S. J. Haward, A. Jaishankar, M. S. N. Oliveira, M. A. Alves, and G. H. McKinley, “Extensional flow of hyaluronic acid solutions in an optimized microfluidic cross-slot device,” *Biomicrofluidics*, vol. 7, no. 044108, 2013.
- [192] F. J. Galindo-Rosales, M. S. N. Oliveira, and M. A. Alves, “Optimized cross-slot microdevices for homogeneous extension,” *RSC Adv.*, vol. 4, pp. 7799–7804, 2014.
- [193] D. R. Link, S. L. Anna, D. A. Weitz, and H. A. Stone, “Geometrically mediated breakup of drops in microfluidic devices,” *Phys. Rev. Lett.*, vol. 92, no. 054503, 2004.
- [194] J. Husny and J. J. Cooper-White, “The effect of elasticity on drop creation in T-shaped microchannels,” *J. Non-Newton. Fluid Mech.*, vol. 137, pp. 121–136, 2006.
- [195] M. C. Jullien, M. J. Tsang Mui Ching, C. Cohen, L. Menetrier, and P. Tabeling, “Droplet breakup in microfluidic T-junctions at small capillary numbers,” *Phys. Fluids*, vol. 21, no. 072001, 2009.
- [196] J. Tang and P. S. Doyle, “Electrophoretic stretching of DNA molecules using microscale T junctions,” *Appl. Phys. Lett.*, vol. 90, no. 224103, 2007.
- [197] W. B. Zimmerman, J. M. Rees, and T. J. Craven, “Rheometry of non-Newtonian electrokinetic flow in a microchannel T-junction,” *Microfluid Nanofluid*, vol. 2, pp. 481–492, 2006.
- [198] N. A. Mouheb, A. Montillet, C. Sollicec, C. Sollicec, J. Havlica, P. Legentilhomme, J. Comiti, and J. Tihon, “Flow characterization in T-shaped and cross-shaped micromixers,” *Microfluid Nanofluid*, vol. 10, pp. 1185–1197, 2011.
- [199] N. A. Mouheb, D. Malsch, A. Montillet, C. Sollicec, and T. Henkel, “Numerical and experimental investigations of mixing in T-shaped and cross-shaped micromixers,” *Chem. Eng. Sci.*, vol. 68, pp. 278–289, 2012.

- [200] B. Steinhaus and A. S. R. Sureshkumar, “Dynamics of viscoelastic fluid filaments in microfluidic devices,” *Phys. Fluids*, vol. 19, no. 073103, 2007.
- [201] P. E. Arratia, J. P. Gollub, and D. J. Durian, “Polymeric filament thinning and breakup in microchannels,” *Phys. Rev. E.*, vol. 77, no. 036309, 2008.
- [202] T. Cubaud and T. G. Mason, “High-viscosity fluid threads in weakly diffusive microfluidic systems,” *New J. Phys*, vol. 11, no. 075029, 2009.
- [203] Q. B. Xu, M. Hashimoto, T. T. Dang, T. Hoare, D. S. Kohane, G. M. Whitesides, R. Langer, and D. G. Anderson, “Preparation of monodisperse biodegradable polymer microparticles using a microfluidic flow-focusing device for controlled drug delivery,” *Small*, vol. 5, pp. 1575–1581, 2009.
- [204] S. Le Digabel, “Algorithm 909: NOMAD: Nonlinear optimization with the MADS algorithm,” *ACM T. Math. Software*, vol. 37, pp. 1–15, 2011.
- [205] C. Audet and J. E. Dennis Jr., “Mesh adaptive direct search algorithms for constrained optimization,” *SIAM Journal on Optimization*, vol. 17, pp. 188–217, 2006.
- [206] C. Audet, S. Le Digabel, and C. Tribes, “NOMAD user guide,” Tech. Rep. G-2009-37, Les cahiers du GERAD, 2009.
- [207] P. J. Oliveira, “On the numerical implementation of nonlinear viscoelastic models in a finite-volume method,” *Numer Heat Transfer*, vol. 40, pp. 283–301, 2001.
- [208] D. F. James, “Flow in a converging channel at moderate Reynolds numbers,” *AIChE Journal*, vol. 37, pp. 59–64, 1991.
- [209] P. C. Sousa, P. M. Coelho, M. S. N. Oliveira, and M. A. Alves, “Three-dimensional flow of Newtonian and Boger fluids in square–square contractions,” *J. Non-Newton. Fluid Mech.*, vol. 160, pp. 122–139, 2009.
- [210] P. C. Sousa, P. M. Coelho, M. S. N. Oliveira, and M. A. Alves, “Effect of the contraction ratio upon viscoelastic fluid flow in three-dimensional square–square contractions,” *Chem. Eng. Sci.*, vol. 66, pp. 998–1009, 2011.

- [211] D. M. Binding, P. M. Phillips, and T. N. Phillips, "Contraction/expansion flows: The pressure drop and related issues," *J. Non-Newton. Fluid Mech.*, vol. 137, pp. 31–38, 2006.
- [212] J. P. Rothenstein and G. H. McKinley, "Inhomogeneous transient uniaxial extensional rheometry," *J. Rheol.*, vol. 46, pp. 1419–1443, 2002.
- [213] A. Webster, J. Greenman, and S. J. Haswell, "Development of microfluidic devices for biomedical and clinical application," *J. Chem. Technol. Biotechnol.*, vol. 86, pp. 10–17, 2011.
- [214] A. M. Afonso, F. T. Pinho, and M. A. Alves, "Electro-osmosis of viscoelastic fluids and prediction of electro-elastic flow instabilities in a cross slot using a finite-volume method," *J. Non-Newton. Fluid Mech.*, vol. 179-180, pp. 55–68, 2012.
- [215] X. Wang, C. Cheng, S. L. Wang, and S. R. Liu, "Electroosmotic pumps and their applications in microfluidic systems," *Microfluid Nanofluid*, vol. 6, pp. 145–162, 2009.
- [216] E. B. Cummings, S. K. Griffiths, R. H. Nilson, and P. H. Paul, "Conditions for similitude between the fluid velocity and electric field in electroosmotic flow," *Anal. Chem.*, vol. 72, pp. 2526–2532, 2000.
- [217] J. G. Santiago, "Electroosmotic flows in microchannels with finite inertial and pressure forces," *Anal. Chem.*, vol. 73, pp. 2353–2365, 2001.
- [218] J. G. Santiago, "Comments on the conditions for similitude in electroosmotic flows," *J. Colloid Interf. Sci.*, vol. 310, pp. 675–677, 2007.
- [219] J. W. Larson, G. R. Yantz, Q. Zhong, R. Charnas, C. M. D'Antoni, M. V. Gallo, K. A. Gillis, L. A. Neely, K. M. Phillips, G. G. Wong, S. R. Gullans, and R. Gilmanshin, "Single DNA molecule stretching in sudden mixed shear and elongational microflows," *Lab Chip*, vol. 6, pp. 1187–1199, 2006.

- [220] G. C. Randall, K. M. Schultz, and P. S. Doyle, “Methods to electrophoretically stretch DNA: microcontractions, gels, and hybrid gel-microcontraction devices,” *Lab Chip*, vol. 6, pp. 516–525, 2006.
- [221] X. Hu, S. N. Wang, and L. J. Lee, “Single-molecule DNA dynamics in tapered contraction-expansion microchannels under electrophoresis,” *Phys. Rev. E.*, vol. 79, no. 041911, 2009.
- [222] T. Tezduyar, “Interface-tracking and interface-capturing techniques for finite element computation of moving boundaries and interfaces,” *Comput. Method Appl. M.*, vol. 195, p. 2983–3000, 2006.
- [223] G. Tryggvason, B. Bunner, A. Esmaeeli, D. Juric, N. Al-Rawahi, W. Tauber, J. Han, S. Nas, and Y. J. Jan, “A front-tracking method for the computations of multiphase flow,” *J. Comput. Phys.*, vol. 169, pp. 708–759, 2001.
- [224] C. Peskin, “The fluid dynamics of heart valves: Experimental, theoretical, and computational methods,” *Annu. Rev. Fluid Mechanics*, vol. 14, p. 235, 1982.
- [225] R. Mittal and G. Iaccarino, “Immersed boundary methods,” *Annu. Rev. Fluid Mechanics*, vol. 37, pp. 239–261, 2005.
- [226] T. Y. Hou, J. S. Lowengrub, and M. J. Shelley, “Boundary integral methods for multicomponent fluids and multiphase materials,” *J. Comput. Phys.*, vol. 169, pp. 302–362, 2001.
- [227] D. Jacqmin, “Calculation of Two-Phase Navier–Stokes Flows Using Phase-Field Modeling,” *J. Comput. Phys.*, vol. 155, pp. 96–127, 1999.
- [228] P. Yue, J. J. Feng, C. Liu, and J. Shen, “A diffuse-interface method for simulating two-phase flows of complex fluids,” *J. Fluid Mech.*, vol. 515, pp. 293–317, 2004.
- [229] F. Magaletti, F. Picano, M. Chinappi, L. Marino, and C. M. Casciola, “The sharp-interface limit of the Cahn–Hilliard/Navier–Stokes model for binary fluids,” *J. Fluid Mech.*, vol. 714, pp. 95–126, 2013.

- [230] C. W. Hirt and D. B. Nichols, “Volume of fluid (VOF) method for the dynamics of free boundaries,” *J. Comput. Phys.*, vol. 39, pp. 201–225, 1981.
- [231] R. A. Figueiredo, C. M. Oishi, A. M. Afonso, I. V. M. Tasso, and J. A. Cuminato, “A two-phase solver for complex fluids: Studies of the Weissenberg effect,” *Int. J. Multiphas. Flow*, vol. 84, pp. 98–115, 2016.
- [232] J. A. Sethian and P. Semerka, “Level set methods for fluid interfaces,” *Annu. Rev. Fluid Mechanics*, vol. 35, pp. 341–372, 2003.
- [233] M. Sussman, P. Smereka, and S. Osher, “A level set approach for computing solutions to incompressible two-phase flows,” *J. Comput. Phys.*, vol. 114, pp. 146–159, 1994.
- [234] D. M. Anderson and G. B. Wheeler, “Diffuse-interface methods in fluid mechanics,” *Annu. Rev. Fluid Mechanics*, vol. 30, pp. 139–165, 1998.
- [235] J. Kim, “Phase-Field Models for Multi-Component Fluid Flows,” *Comput. Method Appl. M.*, vol. 12, pp. 613–661, 2012.
- [236] J. D. Van der Waals, “The thermodynamic theory of capillarity flow under the hypothesis of a continuous variation of density. English translation by J. S. Rowlinson,” *J. Stat. Phys.*, vol. 20, pp. 197–244, 1979.
- [237] J. Gibbs, “On the equilibrium of heterogeneous substances,” *Trans. Conn. Acad. Sci.*, vol. III, pp. 108–248, 1875.
- [238] J. W. Cahn and J. E. Hilliard, “Free Energy of a Nonuniform System. 1. Interfacial Free Energy,” *J. Chem. Phys.*, vol. 28, pp. 258–267, 1958.
- [239] J. W. Cahn and J. E. Hilliard, “Free Energy of a Nonuniform System. 3 Nucleation in a two-component incompressible fluid,” *J. Chem. Phys.*, vol. 31, pp. 688–699, 1959.
- [240] P. C. Hohenberg and B. I. Halperin, “Theory of dynamic critical phenomena,” *Rev. Mod. Phys.*, vol. 49, pp. 435–479, 1977.

- [241] Y. Sun and C. Beckermann, “Sharp interface tracking using the phase-field equation,” *J. Comput. Phys.*, vol. 220, pp. 626–653, 2007.
- [242] L. K. Antanovskii, “A phase field model of capillarity,” *Phys. Fluids.*, vol. 7, pp. 747–753, 1995.
- [243] V. E. Badalassi, H. D. Ceniceros, and S. Banerjee, “Computation of multiphase systems with phase field models,” *J. Comput. Phys.*, vol. 190, pp. 371–397, 2003.
- [244] J. Kim, “A continuous surface tension force formulation for diffuse-interface models,” *J. Comput. Phys.*, vol. 204, pp. 784–804, 2005.
- [245] A. A. Donaldson, D. M. Kirpalani, and A. Macchi, “Diffuse interface tracking of immiscible fluids: Improving phase continuity through free energy density selection,” *Int. J. Multiphase Flow*, vol. 37, pp. 777–787, 2011.
- [246] Y. Oono and S. Puri, “Study of phase-separation dynamics by use of cell dynamical systems. I. Modeling,” *Phys. Rev. A.*, vol. 38, pp. 434–453, 1988.
- [247] R. H. Nochetto, M. Paolini, and C. Verdi, “A dynamic mesh algorithm for curvature dependent evolving interfaces,” *J. Comput. Phys.*, vol. 123, pp. 296–310, 1996.
- [248] D. Jacqmin, “Contact-line dynamics of a diffuse fluid interface,” *J. Fluid Mech.*, vol. 402, pp. 57–88, 2000.
- [249] M. Gurtin, D. Polignone, and J. Vinals, “Two-phase binary fluids and immiscible fluids described by an order parameter,” *Math. Mod. Meth. Appl. S.*, vol. 6, pp. 815–831, 1996.
- [250] P. W. Bates and P. C. Fife, “The Dynamics of Nucleation for the Cahn-Hilliard Equation,” *SIAM J. Appl. Math.*, vol. 53, pp. 990–1008, 1993.
- [251] H. A. Amiri and A. Hamouda, “Evaluation of level set and phase field methods in modeling two phase flow with viscosity contrast through dual-permeability porous medium,” *Int. J. Multiphas Flow*, vol. 52, pp. 22–34, 2013.

- [252] V. V. Khataavkar, P. D. Anderson, P. C. Duineveld, and H. E. H. Meijer, “Diffuse-interface modelling of droplet impact,” *J. Fluid Mech.*, vol. 581, pp. 97–127, 2007.
- [253] L. Caretto, *Coordinate transformations - Notes on engineering analysis*. California State University, Northridge, 2010.
- [254] J. U. Brackbill, D. B. Kothe, and C. Zemach, “A continuum method for modeling surface tension,” *J. Comput. Phys.*, vol. 100, pp. 335–354, 1992.
- [255] W. Yue, C. L. Lin, and V. C. Patel, “Numerical simulation of unsteady multidimensional free surface motions by level set method,” *Int. J. Numer. Meth. Fl.*, vol. 42, pp. 853–884, 2003.
- [256] C. Liu and J. Shen, “A phase field model for mixture of two incompressible fluids and its approximation by a Fourier-spectral method,” *Physica D*, vol. 179, pp. 211–228, 2003.
- [257] X. Yang, J. J. Ashley, J. Lowengrub, X. Zheng, and V. Cristini, “An adaptive coupled level-set/volume-of-fluid interface capturing method for unstructured triangular grids,” *J. Comput. Phys.*, vol. 217, pp. 364–394, 2006.
- [258] P. H. Chiu and Y. T. Lin, “A conservative phase field method for solving incompressible two-phase flows,” *J. Comput. Phys.*, vol. 230, pp. 185–204, 2011.
- [259] R. J. Leveque, “High-resolution conservative algorithms for advection in incompressible flow,” *Siam J. Numer. Anal.*, vol. 33, pp. 627–665, 1996.
- [260] G. Tryggvason, “Numerical simulations of the Rayleigh-Taylor instability,” *J. Comput. Phys.*, vol. 75, pp. 253–282, 1988.
- [261] J. L. Guermond and L. Quartapelle, “A projection FEM for variable density incompressible flows,” *J. Comput. Phys.*, vol. 165, pp. 167–188, 2000.
- [262] M. Zhang, “Simulation of surface tension method in 2D and 3D with smoothed particle hydrodynamics method,” *J. Comput. Phys.*, vol. 229, pp. 7238–7259, 2010.

- [263] T. Chinyoka, Y. Y. Renardy, M. Renardy, and D. B. Khismatullin, “Two-dimensional study of drop deformation under simple shear for Oldroyd-B fluids,” *J. Non-Newton. Fluid Mech.*, vol. 130, pp. 45–56, 2005.
- [264] A. Komrakova, O. Shardt, D. Eskin, and J. Derksen, “Lattice Boltzmann simulations of drop deformation and breakup in shear flow,” *Int. J. Multiphase Flow*, vol. 126, pp. 150–159, 2015.